

Modelling of transient phenomena in gas discharges

Citation for published version (APA):

Brok, W. J. M. (2005). *Modelling of transient phenomena in gas discharges*. [Phd Thesis 1 (Research TU/e / Graduation TU/e), Applied Physics and Science Education]. Technische Universiteit Eindhoven.
<https://doi.org/10.6100/IR595133>

DOI:

[10.6100/IR595133](https://doi.org/10.6100/IR595133)

Document status and date:

Published: 01/01/2005

Document Version:

Publisher's PDF, also known as Version of Record (includes final page, issue and volume numbers)

Please check the document version of this publication:

- A submitted manuscript is the version of the article upon submission and before peer-review. There can be important differences between the submitted version and the official published version of record. People interested in the research are advised to contact the author for the final version of the publication, or visit the DOI to the publisher's website.
- The final author version and the galley proof are versions of the publication after peer review.
- The final published version features the final layout of the paper including the volume, issue and page numbers.

[Link to publication](#)

General rights

Copyright and moral rights for the publications made accessible in the public portal are retained by the authors and/or other copyright owners and it is a condition of accessing publications that users recognise and abide by the legal requirements associated with these rights.

- Users may download and print one copy of any publication from the public portal for the purpose of private study or research.
- You may not further distribute the material or use it for any profit-making activity or commercial gain
- You may freely distribute the URL identifying the publication in the public portal.

If the publication is distributed under the terms of Article 25fa of the Dutch Copyright Act, indicated by the "Taverne" license above, please follow below link for the End User Agreement:

www.tue.nl/taverne

Take down policy

If you believe that this document breaches copyright please contact us at:

openaccess@tue.nl

providing details and we will investigate your claim.

Modelling of Transient Phenomena in Gas Discharges

Wouter Brok

Copyright © 2005 by W.J.M. Brok

Typeset in L^AT_EX 2_ε using the Vim editor. Figures made with Gnuplot and Xfig.

Cover design by Janne Brok: Radioactief verval, geregistreerd met een xt-schrijver. Aquarel met Oost-Indische inkt (1995).

Printed by PrintPartners Ipskamp, Enschede.

This research was financially supported by the Philips Research Laboratories, Eindhoven, The Netherlands.

CIP-DATA LIBRARY TECHNISCHE UNIVERSITEIT EINDHOVEN

Brok, Woutherus Johannes Maria

Modelling of transient phenomena in gas discharges / by Woutherus Johannes Maria Brok. – Eindhoven : Technische Universiteit Eindhoven, 2005. – Proefschrift.

ISBN 90-386-2291-0

NUR924

Trefwoorden : plasmafysica / gasontladingen / lichtbronnen / Monte Carlo methoden / vloeistofmodellen / computersimulaties

Subject headings : plasma physics / gas discharges / light sources / Monte Carlo methods / fluid models / computer simulations / electric breakdown / ignition

Modelling of Transient Phenomena in Gas Discharges

PROEFSCHRIFT

ter verkrijging van de graad van doctor aan de
Technische Universiteit Eindhoven, op gezag van de
Rector Magnificus, prof.dr.ir. C.J. van Duijn, voor een
commissie aangewezen door het College voor
Promoties in het openbaar te verdedigen
op woensdag 5 oktober 2005 om 16.00 uur

door

Woutherus Johannes Maria Brok

geboren te 's-Hertogenbosch

Dit proefschrift is goedgekeurd door de promotoren:

prof.dr.ir. M. Haverlag
en
prof.dr.ir. G.M.W. Kroesen

Copromotor:
dr. J.J.A.M. van der Mullen

*aan mijn ouders
en aan Sveta*

Contents

1	General introduction	1
1.1	Gas discharges	2
1.1.1	When discharged through an exhausted receiver	2
1.1.2	Steady-state modes of operation	5
1.1.3	Breakdown	7
1.2	Gas discharge modelling	8
1.2.1	The Boltzmann equation	8
1.2.2	Expansion methods	11
1.2.3	Fluid methods	12
1.2.4	Sampling methods	13
1.2.5	Combinations of the above	14
1.3	Electron locality	14
1.4	This thesis	16
	Bibliography	16
2	Monte Carlo code	19
2.1	Introduction	20
2.2	Theory	22
2.2.1	Random numbers	23
2.2.2	Free path	24
2.2.3	Equations of motion	27
2.2.4	Selecting the process	29
2.2.5	Scattering	31
2.3	Code design and implementation	39
2.3.1	Classes and objects	39
2.3.2	Random number generator	41
2.3.3	Structure of the Monte Carlo code	41
2.3.4	Species, particles and swarms	42
2.3.5	Processes	43
2.3.6	Environment	46
2.3.7	Statistics	47
2.3.8	FlightControl	47

References	51
2.A Probability calculus	53
2.A.1 Probability distribution	53
2.A.2 Cumulative distribution	53
2.A.3 Sampling of $p(x)$ with random numbers	54
2.B Centre of mass frame	55
2.C Scattering matrix	57
3 Fluid – Monte Carlo coupling	61
3.1 Introduction	62
3.2 Coupling Monte Carlo and fluid models	62
3.2.1 Basic fluid model	63
3.2.2 Input from Monte Carlo	64
3.2.3 Hybrid models in literature	65
3.3 The md2d-mc hybrid model	68
3.3.1 Fluid \rightarrow MC communication	69
3.3.2 Fluid \leftarrow MC communication	73
3.3.3 Control of the Monte Carlo module	74
3.4 Conclusions	75
References	75
4 Breakdown between parabolic electrodes	79
4.1 Introduction	80
4.1.1 Experimental setup and iCCD images	81
4.2 The models	81
4.2.1 Model applicability	83
4.3 Pre-breakdown light flash	84
4.3.1 Results	85
4.3.2 Discussion	85
4.4 Crossing of ionisation front	87
4.4.1 Results	87
4.4.2 Discussion	89
4.5 Conclusions	91
References	91
5 Model of ionisation wave propagation	95
5.1 Introduction	96
5.2 Description of the model	98
5.2.1 Volume description	99
5.2.2 Wall-interaction description	101
5.2.3 System under consideration	103
5.2.4 Input data for the model	103
5.3 Simulation results	106

5.3.1	Breakdown evolution	106
5.3.2	Parameter variations	112
5.4	Discussion	113
5.4.1	Phenomenological behaviour	113
5.4.2	Influence of control parameters	118
5.4.3	Validity of fluid model assumptions	120
5.4.4	Later phases in breakdown and more cfl-like systems	120
5.5	Conclusions	122
	References	123
6	Model of dc and ac breakdown in Ar–Hg	127
6.1	Introduction	128
6.2	The model	128
6.2.1	Model description	129
6.2.2	Species and reactions	130
6.3	DC breakdown	131
6.3.1	Results	131
6.3.2	Discussion	135
6.4	AC breakdown	138
6.4.1	Results	138
6.4.2	Discussion	141
6.5	Conclusions	142
	References	143
7	Numerical description of the plasma needle	145
7.1	Introduction	146
7.2	The model	147
7.2.1	Model description	147
7.2.2	Species and reactions	148
7.2.3	Needle geometry and circuit	148
7.3	Results	149
7.3.1	Discharge characteristics	150
7.3.2	Influence of distance and applied voltage	152
7.3.3	Effect of current restriction	152
7.4	Discussion	153
7.4.1	Comparison to experiments	154
7.4.2	Reaction kinetics	155
7.4.3	Effect of current restriction	157
7.5	Conclusions	158
	References	159

8	Concluding remarks	163
8.1	Introduction	164
8.2	General remarks concerning the code	164
8.3	Breakdown	164
8.3.1	Parabolic electrodes	165
8.3.2	Discharge tubes	165
8.4	The plasma needle	166
	References	167
	Summary	169
	Samenvatting	173
	Dankwoord	177
	Curriculum Vitae	179

1

General introduction

The variety and complexity of the electrical phenomena which occur when matter is present in the electric field are in marked contrast to the simplicity of the phenomena when the ether alone is involved.

J.J. Thomson, *The Discharge of Electricity Through Gases*, 1898.

1.1 Gas discharges

This thesis deals with the numerical modelling of transient phenomena in gas discharges. In the following we will introduce the subject by first giving a short historical overview of the early development of discharge physics, by describing various operational modes of the classical steady-state discharge and by briefly touching upon the subject of breakdown. Subsequently, various approaches to discharge modelling are discussed and arguments are given for the development of the models described in this thesis.

1.1.1 When discharged through an exhausted receiver . . .

“... this stream often divides itself into a variety of beautiful rivulets, which are continually changing their course, uniting and dividing again in the most pleasing manner”.¹

This line was written by Joseph Priestley (1733–1804) in his *History of Electricity* (1769) and gives an account of the earliest interest in man-made gas discharges. This subject started to receive attention in the 18th century: Sir Isaac Newton (1643–1727) and contemporaries were among the first to report the light that is emitted by the electrical discharges that were created by charging due to friction. The nature of electricity, however, remained poorly explained until experimental observations lead Benjamin Franklin (1706–1790) to his theory of a single electric fluid, “self-repulsive and diffused in definite quantities through all bodies” [1] in 1747. This electrical fire could be transmitted via a spark between two objects with a relative shortage and surplus of the fire. Franklin’s theory was disputed by Robert Symmer (1707–1763) who instead proposed a theory of “two electric fluids, each self-repulsive, but both mutually attractive” [1] in 1759.

The experiments conducted in those times were possible because of the *Leiden jar*, invented by Pieter van Musschenbroek (1692–1761) in 1745, and the further development of the *friction machine*, which, in rudimentary form, was introduced by Otto von Guericke (1602–1686) in 1663. This technology allowed natural philosophers to generate and store significant amounts of electric charge and conduct their experiments.

The development of machines that could create discharges continued when friction machines were replaced by the more efficient *influence machines* (see figure 1.1) such as those designed by Giuseppe Belli (1791–1860), August Töpler (1836–1912), Wilhelm Holtz (1836–1913) and James Wimshurst (1832–1903). However, the development of the first battery, the *voltaic pile* by Alessandro Volta (1745–1827) in 1800, the *dynamo* in 1821 by Michael Faraday (1791–1867), and the *induction coil* in 1851 by Heinrich Ruhmkorff (1803–1877) really facilitated the leap in the understanding of electricity and gas discharges.

With the work of Heinrich Geissler (1814–1879), the first evacuated ($\sim 10^3$ Pa) glass tubes became available in 1855 for scientific study of discharges in a more controlled environment. Michael Faraday, Julius Plücker (1801–1868), William Crookes (1823–1919) and others conducted experiments with *discharge tubes* containing various gases at different

¹The ‘exhausted receiver’ in this experiment is a glass vessel, pumped towards vacuum. The top has been closed off with cement. A wire inserted through this cement was connected to a source of static electricity, which discharged inside the vessel and thereby created filaments of light.

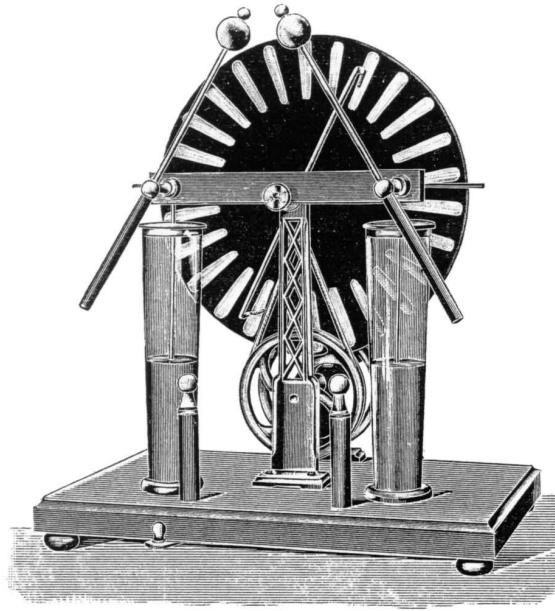


Figure 1.1: Illustration of a Wimshurst machine, taken from reference [2]. Via an ingenious principle, two counter-rotating discs are used to separate charge into Leyden jars. This type of influence machine was used to demonstrate Geissler tubes to the public.

pressures (see figure 1.2 for a schematic picture of a discharge in such a tube). They observed the light emitted by these discharges and noted that different chemical substances radiated in different colours and, moreover, that the discharges often displayed a complex structure.

During such an experiment in 1858, Plücker observed phosphorescence in the glass at the end of the tube opposite to the cathode. The *cathode rays* that caused this phosphorescence were further investigated by Crookes, who, by 1875, had developed better vacuum pumps that could reduce pressure to ~ 0.1 Pa. Experiments done on the cathode rays in these high vacuum *Crookes tubes* eventually lead to the discovery of *x-rays* by Wilhelm Conrad Röntgen (1845–1923) in 1895 and to the discovery of the *electron* by Joseph John Thomson (1856–1940) in 1897 [3].

Meanwhile, in 1889, Friedrich Paschen (1865–1947) published a paper [4] in which he investigated the minimum potential that is necessary to generate a spark in the gap between the two electrodes in discharge tubes. Curves of this potential as a function of pressure are nowadays called *Paschen curves* (see the right hand plot in figure 1.4 on page 7). He furthermore noted that these curves are invariant to the product pd , in which p is the pressure and d is the distance between the electrodes. Around the same time, A.G. Stoletov (1839–1896) noticed that the discharge current as a function of pressure shows a maximum and that this point is invariant to pd .

In 1909, Sir John Townsend (1868–1957) proposed the theory of *ionisation by collision* to explain the development of currents in gases. He was thereby able to explain many

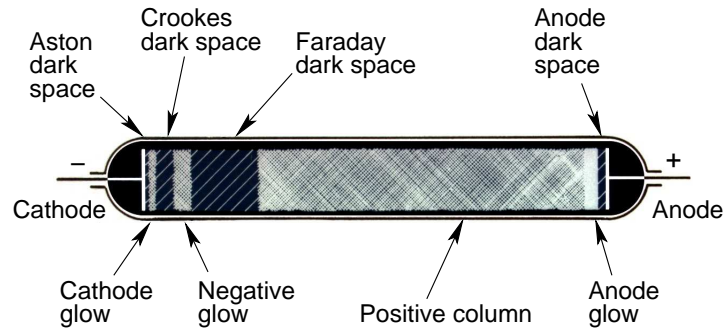


Figure 1.2: Illustration of the light emitted by a discharge tube, redrawn from reference[6]. Although not indicated here, the positive column often shows moving or stationary striations.

phenomena in connection with the discharge of electricity through gas, including the observations of Paschen and Stoletov. He introduced a coefficient α to describe the average number of electrons that is produced by one electron moving through a centimetre of gas. One electron released at the cathode and its progeny in the discharge volume cause an *avalanche* of ionisation. This results in $e^{\alpha d}$ electrons to reach the anode at a distance d from the cathode [5].

Rapid advances in particle physics then culminated in the explanation of atomic structure by Niels Bohr (1885–1962) in 1922. The understanding of the properties of particles and their interactions in a discharge has since been further developed by many researchers. This is in fact still happening, albeit largely focused on very detailed phenomena, mostly related to industrial applications of discharges.

Here we will not further list these advances but instead mention that nowadays [7, 8, 9, 6, 10, 11, 12, 13, 14] it is known that a gas discharge consists of a mixture of neutral atoms, molecules, electrons and ions. These species interact with one another, with electric and magnetic fields, with light, and with material surfaces. Gas discharges can be generated in many ways other than discharging a capacitor. Therefore, the term gas discharge now refers to any flow of current through an ionised gas [13]. The part of the discharge, in which positive and negative charges add up to form a charge neutral region, is referred to as a plasma.

In the present day the elementary processes are generally well understood. However, the question of how these processes interact to determine the more macroscopic phenomena in gas discharges is what drives research. The many possible configurations, the interactions of the discharge with itself and its surroundings, both at microscopic and macroscopic length scales, all give rise to a myriad of applications of discharges. Among these are lighting, material processing, propulsion and chemical analysis. New types of discharges keep emerging and give rise to new applications and technologies.

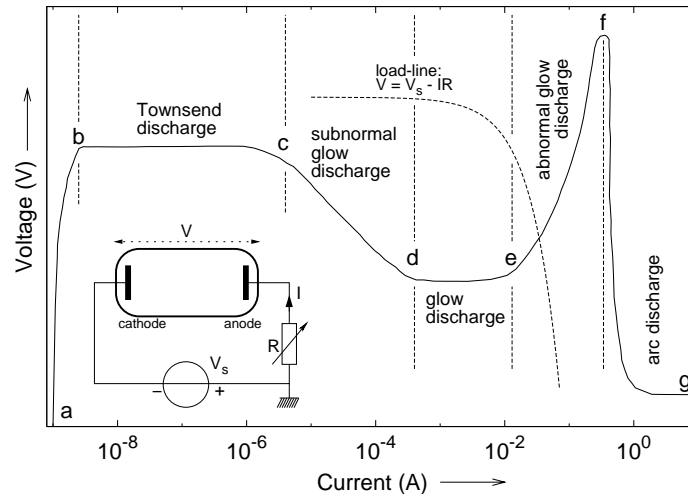


Figure 1.3: The current-voltage characteristics of a DC discharge [9]. Note that the range for the current is merely illustrative. The point at which the discharge operates is the crossing point of this characteristic with the load-line, $V = V_s - IR$. The exemplary load-line that is drawn in this plot is curved due to the logarithmic scale.

1.1.2 Steady-state modes of operation

In order to further introduce the subject of gas discharges, we will briefly describe the various operational modes of what can be called the *canonical gas discharge*: a discharge generated at low pressures between two parallel electrodes at constant potential [9, 13].

These modes can be distinguished in the current-voltage characteristic of this discharge over a wide range of currents. Such a characteristic is sketched for a low pressure (less than a few Torr or a few 100 Pa) discharge in figure 1.3. This curve could be experimentally found by carefully changing the value of the impedance in series with the discharge in order to select its operating point on the curve.

photo electric currents (a – b): due to cosmic and other sources of radiation, erratic electrons are created inside the discharge region and at the electrode surfaces. These electrons give rise to a tiny current when a voltage V is applied. No significant ionisation takes place and the fact that the discharge relies on external sources of ionisation means that it is not self-sustained.

Townsend discharge (b – c): the electric field $E = V/d$ is high enough for electrons to cause an appreciable avalanche of ionisation. The ions that result from this avalanche drift towards the cathode and release new electrons in secondary emission processes. In the steady-state, the number of ionisation events $e^{\alpha d}$ per electron released at the cathode causes the number of ions that arrives at the cathode surface to produce exactly enough secondary electrons to allow the discharge to sustain itself. This is expressed by $e^{\alpha d} - 1 = 1/\gamma$, in which $1/\gamma$ is the number of ions necessary to pro-

duce one secondary electron. Even the slightest increase in the voltage for which this equality holds (the *breakdown voltage*) would result in a larger current and therefore this part of the current-voltage characteristic is practically flat. The ionisation coefficient α/p is a function of the reduced electric field strength E/p [5]. As a result, the breakdown voltage is a function of pd as well. This is shown in figure 1.4. Since hardly any light is emitted from the discharge, this mode is often called a ‘dark discharge’.

subnormal glow discharge (c – d): near the cathode a positive space charge exists due to the difference in mobilities of the light electrons and heavy ions. In this mode of operation, the space charge has become of sufficient density to be able to affect the electric field $E(x)$ and thereby to concentrate the potential drop more and more towards the cathode in what is called a *cathode fall*. Since $\alpha/p = f(E/p)$, the total ionisation yield, given by $\exp(\int_0^d \alpha(x)dx)$, increases in this example with the formation of the cathode fall. This allows the voltage to decrease for increasing current. Note that the current is now not only determined by the external resistor, but by the discharge as well. This region is often unstable and can give rise to temporal and spatial pattern formation [15].

glow discharge (d – e): when the current is allowed to increase further, the discharge extends over the electrode surface, while keeping a constant current density. The extent of the current interval across which this mode exists depends on the surface area and shape of the electrode.

abnormal glow discharge (e – f): the entire surface of the electrode is now covered by the discharge. The only way in which the current can be increased is by increasing the cathode fall, so that secondary electrons travel across a larger potential difference and therefore cause more ionisation.

arc discharge (f – g): at even larger currents, the discharge voltage drops again and an arc discharge is established. Entirely different processes like gas heating, radiative cooling and constriction start playing a role in the discharge volume. Ion bombardments heat the cathode to such a degree that thermal electron emission becomes more important than secondary emission and the cathode fall can decrease again.

As illustrated in figure 1.2, the light emitted by a glow discharge (c – f) can exhibit more structure than caused by the positive space charge layer in front of the cathode alone. If the conditions are suitable, different luminous zones and striations, similar to those in a Franck and Hertz experiment, can be observed in glow discharges in long tubes [16]. These phenomena are related to the fact that electrons do not collide enough to be in a local equilibrium with the field. Instead, they gain energy while moving collectively through a potential drop in the tube and lose it at once in excitation or ionisation.

The extra complication introduced by such *non-local* electron behaviour remains a challenge in modern discharge physics. While the evidence is clearly visible in some discharge tubes, non-local electron behaviour is often important in less illustrative conditions and forms in part the background of some of the work presented in this thesis.

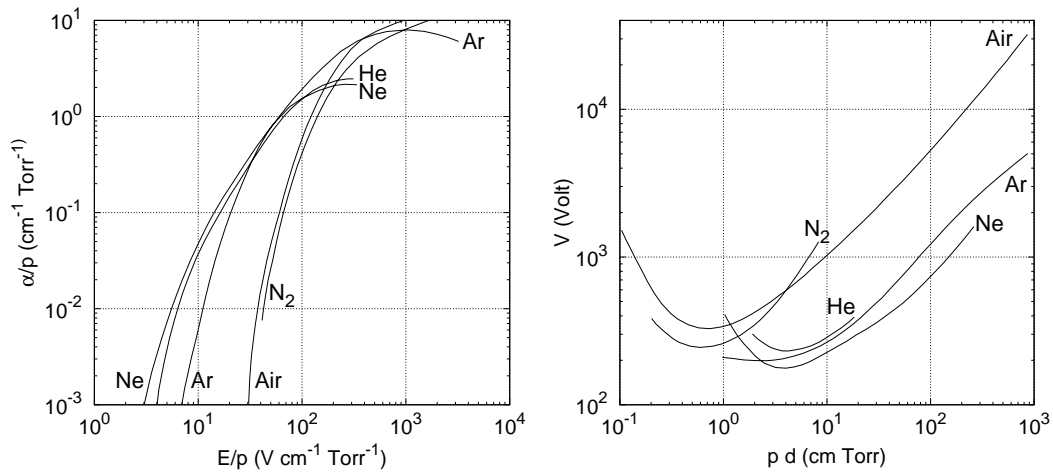


Figure 1.4: *On the left:* the dependence of α/p on the reduced electric field strength E/p is shown for various gases [11]. *On the right:* the Paschen curves for these gases [13]. The minimum in the Paschen curve is called Stoletov's point.

1.1.3 Breakdown

The discharges considered in this thesis can, in steady-state, be considered to be operated in the glow regime.² We will, however, treat the transient development of a neutral gas towards this steady-state. This process, in which a neutral gas becomes conducting, is called *breakdown* or *ignition*.

Breakdown involves the multiplication of electrons in avalanches. As such, the so called multiplication factor $M = e^{\alpha d}$ is a parameter that can be used to characterise breakdown. The Paschen curve shows the minimum voltage V_b required for breakdown at a given value of pd . M is approximately $1/\gamma$ at the Paschen curve and exceeds this for voltages V above the curve. These voltages, for which $V/V_b > 1$, are called over-voltages.

The multiplication factor determines how fast the discharge will develop. In the extreme case that $M > 10^8$ (i.e. $\alpha d \approx 20$, which is called Meek's criterion [13]), somewhere in the volume between the electrodes an electron avalanche will create a localised space charge region that concentrates the electric field and drives the development of a conducting *streamer* channel [17, 18]. In that case, secondary emission at the surface is unimportant and breakdown happens quickly and in an inhomogeneous fashion.

The breakdown processes considered in this thesis take place at relatively low over-voltages and streamers do therefore not occur. Nevertheless, space charges that alter the electric field, and thereby displace ionisation regions, generally play an significant role in the development of the discharge. The geometry of the discharge vessel is important, as it defines the electric field. Furthermore, if dielectric surfaces are present, these can charge and affect the electric field as well. Finally, in some cases the cathode is heated to thermal

²In some of the discharges described in this thesis, the cathode is heated and thermal emission plays an important role. Nevertheless, the discharge resembles a glow more than an arc.

emission temperatures, which renders secondary emission as a source of electrons relatively unimportant. In such conditions, Paschen curves are of limited use and a more elaborate description is needed.

1.2 Gas discharge modelling

Experimental physics provides essential ingredients to the understanding of natural phenomena, such as gas discharges: experimental observations lead to theories and these theories can be tested and improved by additional observations. Theories can be formulated in mathematical equations and these can be manipulated and provide new insights.

This approach however has limits: often a quantity of interest cannot be observed directly and needs to be inferred via an interpretation that introduces assumptions. Moreover, when many physical processes conspire to create observed phenomena, it can be difficult to provide an analytical solution to the riddle they pose.

Numerical modelling provides a way to complement experiments and theory by producing a solution to the complete set of equations that is believed to describe the system. As opposed to experimental observations, all quantities can be known and one can test how they influence one another by artificially manipulating them. The observable quantities can be directly compared to the experimental data and this can increase the confidence in the validity of the model. Finally, model results can inspire new experiments and help interpret observations.

The following pages treat in some detail some of nowadays' most common approaches in discharge modelling.³ It is generally recognised that, in principle, the so called *Boltzmann equation*, together with the Poisson equation for the electric field and suitable boundary conditions, describes the physics of many discharges completely. In practice, however, the Boltzmann equation is unwieldy and cannot be solved without making significant simplifications to it.

After a brief introduction to the Boltzmann equation, the remainder of this section deals with the most common approaches in simplifying it and thereby introduces the various types of models used in later chapters in this thesis.

1.2.1 The Boltzmann equation

Any model of a gas discharge must be build upon a microscopic description of the particles in the discharge. Following this 'bottom-up' method in creating or analysing a model ensures that the limiting assumptions of the model become clear.

The majority of gas discharge models is built upon the Boltzmann equation. This equation results from the notion of a grand canonical ensemble, the Liouville equation in statistical mechanics, and the assumption that the particle ensemble under consideration is

³Approaches that are not treated, as they bear little relevance to this thesis, are the convective scheme [19], many body tree methods [20] and Direct Simulation Monte Carlo [21].

sufficiently large to ensure that statistical fluctuations are small enough to be neglected. Sequences of collisions are assumed to be Markovian and these interactions between particles are short-ranged and brief and do not involve more than two particles at once.⁴

The Boltzmann equation describes the evolution of the density $f(\mathbf{r}, \mathbf{u}, t)$ of a single particle species in the phase space spanned by configuration space \mathbf{r} and velocity space \mathbf{u} . An often used form of the equation reads [12]:

$$\frac{\partial f}{\partial t} + \nabla_x \cdot \mathbf{u}f + \nabla_u \cdot \mathbf{a}f = \left(\frac{\delta f}{\delta t} \right)_{\text{CR}} \quad (1.1)$$

The left hand side reflects the flow of the particles in phase space, while subject to macroscopic forces that cause the acceleration \mathbf{a} of the species. One can think of gravity and electro-magnetic forces. The right hand side of the equation is abstractly written as $(\delta f / \delta t)_{\text{CR}}$ and denotes the effect that the microscopic collisions and radiation have on the phase space density function.

For central and magnetic forces, the flow in phase space is divergence free (Liouville's theorem), and this allows equation (1.1) to be written in a more convenient form:

$$\frac{\partial f}{\partial t} + \mathbf{u} \cdot \nabla_x f + \mathbf{a} \cdot \nabla_u f = \left(\frac{\delta f}{\delta t} \right)_{\text{CR}} \quad (1.2)$$

Coupling multiple Boltzmann equations for the different species together via their right hand side is necessary to describe a discharge. However, we note here that at present this seven-dimensional equation cannot be solved completely for any practical application, even for a single species. State of the art methods allow the solution of a reduced form in which only two or at most three dimensions are retained.

Special Solutions

The solution to the Boltzmann equation for a given position in space and moment in time is a velocity distribution function. If this function is isotropic in a first order approximation (i.e. particles do not move in a beam-like fashion), one can make the substitution $\varepsilon = \frac{1}{2}mv^2$, with ε the energy and m the mass of the species, and solve the equation for $f(\varepsilon)$, the so called energy distribution function (edf). This function is especially important for electrons and the abbreviation *eedf* is therefore commonly used to denote the *electron energy distribution function*.

For various special situations an explicit expression can be found for the eedf: in the case of an electron gas in thermal equilibrium and in absence of any macroscopic forces, the eedf is called Maxwellian:

$$f = C\sqrt{\varepsilon} \exp\left(-\frac{\varepsilon}{k_B T}\right) \quad (1.3)$$

⁴Especially the assumption that interactions are short ranged and binary seems limiting: for instance, long range Coulomb interaction between charged particles are important in ionised gases. Nevertheless, often the interaction range is limited due to shielding and this effect can be used to fit these interactions into the theory.

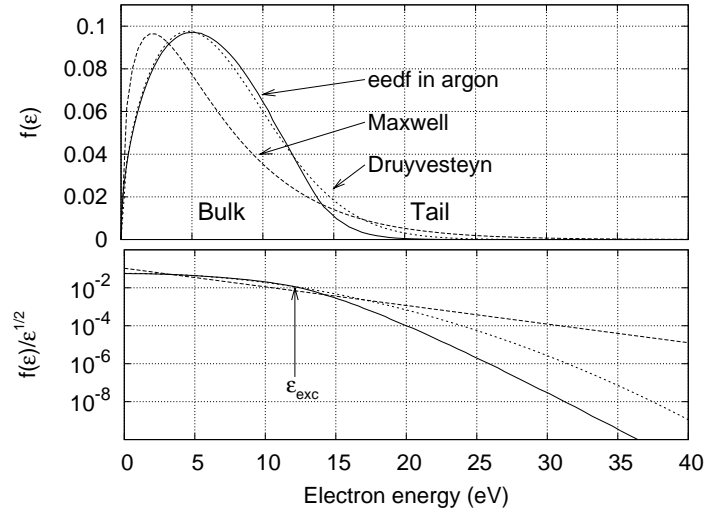


Figure 1.5: Illustration of the typical shape of an electron energy distribution function. This eedf is the one found in argon for an electric field of 100 Td, by solving the Boltzmann equation via a two-term expansion (see section 1.2.2) for the cross sections shown in figure 1.6. The top graph shows $f(\varepsilon)$ on a linear scale, the bottom graph shows $f(\varepsilon)/\sqrt{\varepsilon}$ on a logarithmic scale. For comparison also a Maxwellian distribution with the same mean energy and a fitted Druyvesteyn distribution are shown. Notice that in the bottom graph a Maxwellian eedf is a straight line.

with T the temperature and k_B the Boltzmann constant. It needs to be noted that the concept of temperature is only correct in the case that the distribution is Maxwellian. When the deviation from the Maxwellian distribution is moderate, the term ‘temperature’ can still be used, but T should be considered to be an ‘effective’ temperature, which is really more a measure for the mean energy via $\bar{\varepsilon} = \frac{3}{2}k_B T$.

For electrons another special solution is interesting: in an electric field E , if only elastic collisions are assumed to happen and the path length λ between them is constant, the eedf is the one found by Druyvesteyn [9]:

$$f = C\sqrt{\varepsilon} \exp\left(-\frac{3m_e \varepsilon^2}{M \varepsilon_0^2}\right) \quad (1.4)$$

with $\varepsilon_0 = eE\lambda$ and M the mass of the background gas species. Compared to the Maxwell distribution, the slope of the tail of the Druyvesteyn distributions is steeper.

In figure 1.5, the eedf is plotted for electrons in a homogeneous field of 100 Td in argon.⁵ For comparison, the Maxwellian distribution with the same mean energy is also shown, as well as a fitted Druyvesteyn distribution.

⁵The *Townsend* (Td) is a unit for the reduced electric field strength E/N , with N the density of the gas. 1 Td corresponds to 10^{-17} Vcm². The quantity E/p , with p the pressure, is also referred to as reduced electric field strength. In literature its unit is commonly Vcm⁻¹Torr⁻¹, with 1 Torr = 133 Pa. At room temperature, via the ideal gas law, 1 Td corresponds to 0.32 Vcm⁻¹Torr⁻¹.

1.2.2 Expansion methods

A common approach to obtain a direct solution of the electron Boltzmann equation is via expansion of $f(\mathbf{u})$ in a series of orthogonal base functions [12]. In many cases it is possible to choose the functions such that the coefficients in the series will quickly tend to zero. In those cases, the series can be truncated after a few terms. Substitution of this series allows the Boltzmann equation to be written as a small set of differential equations for the coefficients of the expansion, which can be solved with standard techniques.

For electrons, a good choice of base functions can be found by considering the following: since the mass of electrons is small compared to that of atoms, an elastic collision will have an effect on the direction of the velocity vector of an electron, but hardly on the magnitude. Therefore, if the majority of collisions is elastic, their effect consists of a redistribution of the velocity vectors over spherical surfaces in velocity space. Furthermore, in case the reduced electric field is not too high, only a small directional component is added to this isotropic distribution of velocity vectors. This holds if the energy gained between two collisions is small compared to the mean energy.

Having noted this, a suitable series of functions is formed by the so called spherical harmonics [12]:

$$f = \sum_{lms} f_{lms}(\mathbf{x}, u, t) Y_{lms}, \quad (1.5)$$

with

$$Y_{lms} = P_l^m(\cos \theta) (\delta_{0s} \cos m\phi + \delta_{1s} \sin m\phi) \quad (1.6)$$

and $P_l^m(\cos \theta)$ the well-known Legendre polynomial. f_{000} represents the isotropic form of f and the next terms in (1.5) represent different anisotropies. For a relatively small reduced electric field and mostly elastic collisions it can be assumed that the distribution is only slightly anisotropic and the series can be truncated after the second term:

$$f = f_0 + \mathbf{f}_1 \cdot \frac{\mathbf{u}}{u} \quad (1.7)$$

with f_0 a short notation for f_{000} and \mathbf{f}_1 a vector consisting of the components: $f_{1x} = f_{110}$, $f_{1y} = f_{111}$ and $f_{1z} = f_{100}$. Furthermore, u is the absolute value of \mathbf{u} .

This form of f can be substituted in the Boltzmann equation and, after some algebraic manipulation, four first order coupled differential equations result [12, 22]:

$$\begin{aligned} \frac{\partial f_0}{\partial t} + \frac{u}{3} \nabla \cdot \mathbf{f}_1 + \frac{1}{3u^2} \frac{\partial}{\partial u} (u^2 \mathbf{a} \cdot \mathbf{f}_1) &= \frac{\delta f_0}{\delta t} \\ \frac{\partial \mathbf{f}_1}{\partial t} + u \nabla f_0 + \mathbf{a} \frac{\partial f_0}{\partial u} &= \frac{\delta \mathbf{f}_1}{\delta t} \end{aligned} \quad (1.8)$$

We note that these equations are often solved for a homogeneous and time-independent field, in what is called the *local field approximation*. It assumes that the effect of spatial motion is negligible compared to the effects that collisions have on the edf. This can be

considered the case if the collisions are frequent and effective in dissipating the energy that is locally gained in the field.

If this assumption is valid, \mathbf{f}_1 is symmetric around the direction of this field and one can focus on the component along this direction. The equations above can then be combined in a second order differential equation, which is a balance equation for f along the energy axis [23]. Its solution can be used to determine reaction rate coefficients and transport coefficients as a function of the reduced electric field, and can, for instance, be used as an input to fluid models. An example of the eedf obtained in such a way is shown in figure 1.5.

1.2.3 Fluid methods

Fluid models are models in which the various discharge species are described in terms of average, hydrodynamic quantities such as density, momentum and energy. By taking velocity moments [12] of the Boltzmann equation (1.2) one arrives at conservation laws for these quantities. For example, integrating the equation over velocity space results in the first moment, the *density balance equation*:

$$\frac{\partial n}{\partial t} + \nabla \cdot \mathbf{\Gamma} = S \quad (1.9)$$

with $\mathbf{\Gamma} = n\mathbf{v}$ a flux, \mathbf{v} the average velocity and S the source term due to the various reactions in which the species are created or destroyed.

The second moment, the *momentum balance equation*, is obtained by multiplying equation (1.2) by $m\mathbf{v}$ and integrating it over velocity space:

$$\frac{\partial nm\mathbf{v}}{\partial t} + \nabla \cdot (nm\mathbf{v}\mathbf{v}) = -\nabla \cdot \mathcal{P} + qn\mathbf{E} + \mathbf{R} \quad (1.10)$$

with \mathcal{P} the pressure tensor, q and m the charge and mass of the species, \mathbf{E} the electric field and $\mathbf{R} = nm\mathbf{v}\nu_m$ the momentum source due to momentum transfer collisions with other species, with ν_m the collision frequency.

Multiplication with $\varepsilon = \frac{1}{2}mv^2$ and integration over velocity space results in the third moment, the *energy balance equation*:

$$\frac{\partial n\varepsilon}{\partial t} + \nabla \cdot \mathbf{q} = qn\mathbf{E} \cdot \mathbf{v} + S_\varepsilon \quad (1.11)$$

with $\mathbf{q} = n\varepsilon\mathbf{v}$ the heat flow vector. The first term on the right hand side represents the work done by the electric field and the second term S_ε the energy lost or gained in reactions.

Each moment contains a parameter that can be obtained from the next, such as the flux $\mathbf{\Gamma}$ in the density balance equation, which can be obtained from the momentum balance equation. Assumptions need to be introduced in order to truncate this series. It is quite common to do this after the second or third moment and to specify the shape of the edf and use this to determine the coefficients in the balance equations.

The fluid model employed for the calculations presented in this thesis is based on the first three moments of the Boltzmann equation and, furthermore, makes some simplifying

assumptions concerning the momentum and energy balance equation. This will be treated in section 5.2. Here we let it suffice to say that the momentum balance equation is reduced to the so called *drift-diffusion equation*:

$$\mathbf{\Gamma} = \pm\mu\mathbf{E}n - D\nabla n \quad (1.12)$$

where $\mu = q/(m\nu_m)$ represents the mobility and $D = u^2/(3\nu_m)$ the diffusion coefficient. The \pm sign in the drift term indicates whether the sign of the charge q is positive or negative. The advantage of this form resides in the fact that these transport coefficients can be measured directly in a so called drift tube experiment or can be obtained from the direct solution to the Boltzmann equation via a two term expansion as treated in section 1.2.2.

As such, the transport coefficients μ and D , and the reaction rate coefficients k that occur in the source term S can be expressed as functions of the local reduced electric field E/N . As was mentioned in the previous section, this local field approximation assumes that the effect of collisions on the edf is dominant over the effect of spatial motion.

In reality it is not uncommon for this equilibration to not occur on the length and time scales that are characteristic for the discharge. Commonly, the light electrons are the first to suffer from this. If the effect is small, it can be alleviated by solving the energy balance equation and expressing the transport and reaction rate coefficients as functions of the mean energy of the particles. This approach is taken in the simulations described in the chapters 5, 6 and 7. If the effect is large, another method of solution needs to be found.

We furthermore recall that it was assumed in the above equations that the species' properties are isotropic. The reduced electric field E/N introduces anisotropies in the edf of the species and for too high values of E/N one cannot expect the fluid model to describe the species correctly anymore.

1.2.4 Sampling methods

A completely different approach in modelling discharges is obtained by following individual particles through a gas [24, 25]. Their trajectories are calculated using Newton's laws and microscopic interactions between particles are described by a *Monte Carlo method*, in which random numbers are used to determine the outcome of these individual collisions.

Most discharges contain too many particles to be able to explicitly follow them in a computer program. Instead, a smaller set of so called simulation particles is followed and this sample is taken to be representative of all particles in the discharge. As is shown in reference [26], this method is indeed a way to solve the Boltzmann equation. The method is capable of treating species behaviour with a minimal amount of assumptions, at the expense, however, of significant calculation times.

Chapter 2 is entirely devoted to the theory and implementation of such a simulation and this method is explained more fully there.

1.2.5 Combinations of the above

Of the modelling methods described above, fluid models are often most attractive to use for the description of a complete discharge system. The main reason for this is that they are capable of modelling complex systems while keeping runtime limited.

As was indicated above, fluid models incorporate assumptions that are often not on par with the behaviour of some species, mostly the electrons. For this reason, the so called *Particle-In-Cell* models seem to be a good choice of model instead. They use the sampling method described above in combination with a self-consistent description of the electric field and thereby create a very detailed and complete description of the discharge. The large calculation times are however an obstruction to their usage.

In a case when the assumptions of a fluid model are valid for the majority of the species but fail for one or just a few, it is worthwhile to consider a description of these species with another model and combine this with a fluid model of the remaining species. Typically the electrons can be described by directly solving the Boltzmann equation for them or by using a sampling method. The latter type of model will be the subject of chapter 3 in this thesis.

1.3 Electron locality

In the previous text it was already mentioned that, under certain conditions, the electrons do not experience a sufficient number of collisions to be in equilibrium with the local electric field. This could express itself in phenomena such as striations and does affect the validity of fluid models. Below, we will quantify this non-locality.

An electron loses a certain amount of energy in each collisional process. If the amount of energy that an electron gains from the electric field is dissipated in collisions that happen on a small temporal and spatial scale, one can consider the electrons to be in equilibrium with the local field. In order to define what these temporal and spatial scales are, one has to consider relevant length and time scales of the discharge and compare these to those of the electrons.

The length scale that characterises the discharge is typically the smallest gradient length Λ_E of the electric field and has the smallest size R of the discharge vessel as the upper limit. Furthermore, the spatial resolution δ that one uses to investigate the discharge, either experimentally or numerically, can define a length scale. Temporal non-locality is connected to the rate ν_E at which the field changes.

The electrons are characterised by their energy relaxation length λ_ϵ and frequency ν_ϵ . These represent the typical length and time scales over which an electron loses a substantial part of its energy in collisions. λ_ϵ and ν_ϵ are given by [22]:

$$\lambda_\epsilon = \lambda_0 \sqrt{\frac{\nu_m}{\nu_\epsilon}} \quad \text{and} \quad \nu_\epsilon = \frac{2m_e}{M} \nu_m + \nu_i \quad (1.13)$$

with λ_0 the mean free path of the electrons, ν_m the collision frequency for momentum transfer and ν_i the inelastic collision frequency. The mean free path is calculated by

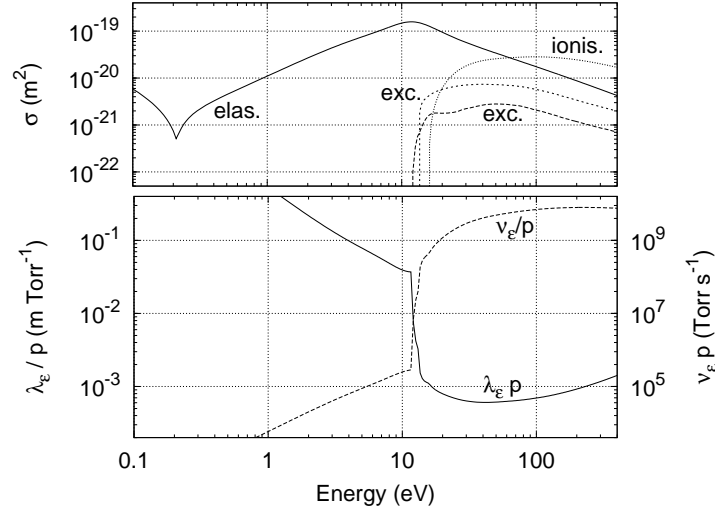


Figure 1.6: *Top graph:* cross sections in argon for elastic collisions, for excitation to two effective excited states (see section 5.2.4) and for ionisation. *Bottom graph:* the electron energy equilibration length and frequency, calculated from these cross sections by means of equation (1.13).

$\lambda_0 = 1/n\sigma_m$ from the gas density n and the total summed cross section σ_m of all processes. Similarly, $\nu_m = n\sigma_m u$ and $\nu_i = n\sigma_i u$, with σ_i the sum of the cross sections of all inelastic processes. Since σ_m and σ_i are energy dependent, λ_ϵ and ν_ϵ are generally strong functions of the electron energy. This complicates the definition of relaxation lengths and times for an entire eedf, as it is necessary to consider the energy range that is covered by the eedf.

As an example, figure 1.6 shows the various cross sections of electrons in argon and the λ_ϵ and ν_ϵ that are derived from those as a function of energy. Due to the large mass ratio of electrons and argon atoms, energy transfer in elastic collisions is inefficient and this is reflected in the long equilibration length and time scale for electrons with an energy below the first excitation level ϵ_{exc} .

A consequence of this is that if, for example, electrons leave the cathode with a low energy and gain energy in the electric field, they will only experience inelastic collisions after they have traversed a potential drop of approximately 12 eV. This effect causes the Aston dark space in figure 1.2 and similar effects are important in the formation of striations. The length scale introduced by this effect is $\Lambda = \epsilon_{\text{exc}}/eE$.

To summarise, it is thus required that $\lambda_\epsilon \ll \Lambda_E$ and $\nu_\epsilon \gg \nu_E$ for the eedf to be in equilibrium with the local field. Unfortunately, λ_ϵ and ν_ϵ are well defined for individual energies, but vary significantly within an eedf. In argon electrons typically first need to gain ϵ_{exc} before they lose this energy. The length over which this happens is ϵ_{exc}/eE and thus forms a lower limit of the estimate for the equilibration length. Plots such as those in figure 1.6 can help to obtain more insight in whether electron behaviour is local or not, for a given gas pressure.

1.4 This thesis

This introduction in discharges and models of discharges has given a flavour of what will be the subjects of the following chapters. Furthermore, as the title already gives away, the major theme of this thesis is the description of transient processes in gas discharges. Transient refers here to the breakdown phase of gas discharges, during which a neutral gas evolves towards a steady-state discharge.

One part of the work presented in this thesis consists of the development of a Monte Carlo model to describe the electrons in a way that introduces only few assumptions. This code has been coupled to the fluid model *md2d* that was developed by Gerjan Hagelaar [27]. The *md2d* code has since seen a significant reimplemention in the C++ computer language to allow code components to be shared with the *Plasimo* framework [28, 29, 30].

The Monte Carlo model is described in chapter 2 and the hybrid fluid-particle code that followed from coupling the Monte Carlo code to *md2d* is treated in chapter 3. An application of the hybrid code is formed by the description of breakdown between two parabolic electrodes in chapter 4.

Before this code was finished, some investigations were made of breakdown in fluorescent lamps by means of the fluid model, using the reaction rates and electron transport coefficients obtained from a Boltzmann solver. This work is treated in the chapters 5 and 6. Furthermore, the steady-state behaviour of discharge called a ‘plasma needle’ has been investigated with this model. Since this work is quite unrelated to the rest of this thesis, this is described in the last chapter, chapter 7.

As can be seen from this description, roughly this text can be divided into two parts: chapters 2 and 3 deal with code development and chapters 4 till 7 deal with the application of the various codes to various plasmas.

Bibliography

- [1] J. Tyndall. *Lessons in Electricity*. Longmans, Green and Co., London, 1875-6.
- [2] L. Graetz. *Handbuch der Elektrizität und des Magnetismus*. Verlag von Johann Ambrosius Barth, Leipzig, 1918. Band I.
- [3] J. J. Thomson. *The Discharge of Electricity Through Gases*. Archibald Constable & Co., Westminster, 1898.
- [4] F. Paschen. Ueber die zum Funkenübergang in Luft, Wasserstoff und Kohlensäure bei verschiedenen Drucken erforderliche Potentialdifferenz. *Wied. Ann.*, 37:69–96, 1889.
- [5] J. S. Townsend. *The Theory of Ionization of Gases by Collision*. Constable & Company Ltd., London, 1910.
- [6] S. B. Brown. *Basic Data of Plasma Physics*. The Technology Press of MIT and John Wiley & Sons, 1959.
- [7] K. T. Compton and I. Langmuir. Electrical discharges in gases part I. Survey of fundamental processes. *Rev. Mod. Phys.*, 2(2):123–242, 1930.

- [8] I. Langmuir and K. T. Compton. Electrical discharges in gases part II. Fundamental phenomena in electrical discharges. *Rev. Mod. Phys.*, 3(2):191–257, 1931.
- [9] M. J. Druyvesteyn and F. M. Penning. The mechanism of electrical discharges in gases of low pressure. *Rev. Mod. Phys.*, 12(2):87–176, 1940.
- [10] E. W. McDaniel. *Collision Phenomena in Ionized Gases*. Wiley, New York, 1964.
- [11] A. von Engel. *Ionized Gases*. Oxford University Press, London, 1965.
- [12] I. P. Shkarofsky, T. W. Johnston, and M. P. Bachynski. *The Particle Kinetics of Plasmas*. Addison-Wesley, 1966.
- [13] Yu. P. Raizer. *Gas Discharge Physics*. Springer, Berlin, 1991.
- [14] N. St. J. Braithwaite. Introduction to gas discharges. *Plasma Sources Sci. Technol.*, 9:517–527, 2000.
- [15] D. Šijačić. *Spatio-Temporal Pattern Formation in a Semiconductor-Gas-Discharge System*. PhD thesis, Eindhoven University of Technology, The Netherlands, 2004.
- [16] K. T. Compton, Louis A. Turner, and W. H. McCurdy. Theory and experiments relating to the striated glow discharge in mercury vapor. *Phys. Rev.*, 24(6):597–615, 1924.
- [17] L. B. Loeb and J. M. Meek. *The Mechanism of the Electric Spark*. Clarendon Press, Oxford, 1941.
- [18] A. N. Lagarkov and I. M. Rutkevich. *Ionization Waves in Electrical Breakdown of Gases*. Springer, Berlin, 1994.
- [19] T. J. Sommerer, W. N. G. Hitchon, and J. E. Lawler. Self-consistent kinetic model of the cathode fall of a glow discharge. *Phys. Rev. A*, 39(12):6356–6366, 1989.
- [20] S. Pfalzner and P. Gibbon. *Many Body Tree Methods in Physics*. Cambridge University Press, New York, 1996.
- [21] G. A. Bird. *Molecular Gas Dynamics and the Direct Simulation of Gas Flows*. Oxford University Press, 1994.
- [22] U. Kortshagen, C. Busch, and L. D. Tsendid. Review article: On simplifying approaches to the solution of the Boltzmann equation in spatially inhomogeneous plasmas. *Plasma Sources Sci. Technol.*, 5(1):1–17, 1996.
- [23] C. M. Ferreira and J. Loureiro. Electron kinetics in atomic and molecular plasmas. *Plasma Sources Sci. Technol.*, 9(4):528–540, 2000.
- [24] R. W. Hockney and J. W. Eastwood. *Computer Simulation using Particles*. Adam Hilger, 1988.
- [25] C. K. Birdsall and A. B. Langdon. *Plasma Physics via Computer Simulation*. Adam Hilger, 1991.
- [26] S. Longo. Monte Carlo models of electron and ion transport in non-equilibrium plasmas. *Plasma Sources Sci. Technol.*, 9(4):468–476, 2000.
- [27] G. J. M. Hagelaar. *Modeling of Microdischarges for Display Technology*. PhD thesis, Eindhoven University of Technology, The Netherlands, 2000.

- [28] J. van Dijk. *Modelling of Plasma Light Sources: an object-oriented approach*. PhD thesis, Eindhoven University of Technology, The Netherlands, 2001.
- [29] B. Hartgers. *Modelling of a Fluorescent Lamp Plasma*. PhD thesis, Eindhoven University of Technology, The Netherlands, 2003.
- [30] H. W. P. van der Heijden. *Modelling of Radiative Transfer in Light Sources*. PhD thesis, Eindhoven University of Technology, The Netherlands, 2003.

Theory and implementation of a Monte Carlo code

Abstract. A Monte Carlo code has been written to simulate the behaviour of species in a gas discharge. Particles are assumed to experience only binary collisions with the background gas particles. The basic assumption of the Monte Carlo method is therefore that the path of a particle can be considered to consist of the free flight, interrupted by instantaneous collisions. The theory that describes the trajectory, the type of collision and the result of the collision is treated in the first part of this chapter. The second part deals with the description of the code design and implementation. The choices that have been made in the design have resulted in a flexible code that can be used independently or as a component in other models.

2.1 Introduction

In the most general sense Monte Carlo (MC) methods are numerical methods that employ random number sequences to perform statistical simulations. The application range of MC methods is very large: solutions to problems with a probabilistic or a deterministic nature can both be approximated with these methods. One must be able to express the relevant mechanisms in terms of well defined probability distribution functions, according to which random numbers will be sampled. If sufficiently many of these properly distributed random numbers are sampled, the outcome of the simulations will provide a good estimate for the quantity of interest.

A classical example^a of a Monte Carlo experiment is the one that G.L.L. Comte de Buffon did in 1777 to determine the value of π . He drew a number of parallel lines, a distance d apart. Subsequently he dropped N needles of length l (with $l \leq d$) on the paper and counted the number R of needles intersecting a line. π is then approximated by $2lN/dR$.

A numerical MC simulation to determine the value of π could be done in the following way: use two random numbers that have been taken out of a uniform distribution on $[0, 1)$ to generate a coordinate (x, y) of a point on a unit square. Generate N of these points and determine the number R of these that satisfy the inequality $x^2 + y^2 < 1$, that is, determine how many of them fall within the first quadrant of the unit circle. For a large enough number of points, $4R/N$ will approach π .

In a very similar way, MC methods can be used to determine the integrals of very complex, possibly multi-dimensional functions.

^a<http://www.geocities.com/CollegePark/Quad/2435/buffon.html>

As in these examples, the concept of an MC simulation in plasma physics is relatively straightforward: the paths of particles in a discharge are calculated by considering their ballistic movement and the collisions they make with other particles. Since it is usually not possible to follow all the particles, only a limited number of them is treated and the behaviour of these simulation particles is taken to be representative for all the particles in the discharge.

Random numbers are used to determine the time between collisions and the type and outcome of collisions. The distributions of the random numbers are shaped such that they reproduce the analytical expressions that describe the physics under consideration. If a sufficient number of simulation particles is followed for a sufficient number of collision processes, quantities like the energy distribution of the particles and rates of processes can be obtained from the history of the simulation particles paths.

MC methods are computationally very expensive: tracking particles through many free paths and collisions is something that can reasonably be done with today's desktop computers¹ for particle numbers that range typically up to the order of 10^5 . If one uses a cluster

¹At the moment of writing this theses, the author runs calculations on a machine based on an AMD Athlon™ 64 FX-51 processor, working at a clock-speed of 2200 MHz, having an L2 cache of 1024 kByte and

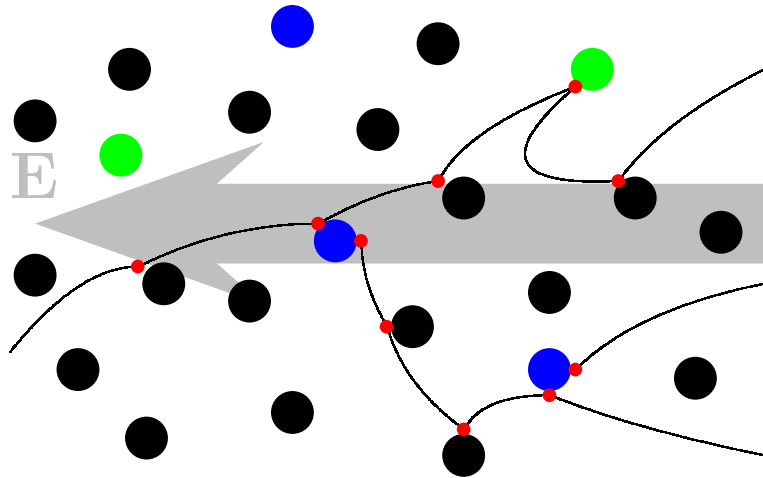


Figure 2.1: An impression of the path that an electron follows through a gas. It gains energy in the electric field E and loses this in excitation and ionisation collisions. In an ionisation event, another free electron is generated.

of machines, this number can be stretched to 10^7 . Nevertheless, this number is generally significantly smaller than the real number of particles present in plasmas. There are, for example, in the order of 10^{12} electrons in a compact fluorescent lamp during steady-state operation. Because of the disparity between the number of simulation particles and real particles, one has to deal with statistical noise in the output of MC simulations.

Despite these disadvantages, MC models have much to offer: details on the behaviour of groups of particles about which other models can only make assumptions. As such, they are often employed to validate such assumptions or to provide improved data for these other models. Specifically, one can think of (e.g. local field) assumptions made for reaction rate coefficients and transport coefficients in fluid models.

A Boltzmann solver can, in principle, also be used for validation or to provide these data. However, the complexity of the Boltzmann equation makes such a calculation feasible only for configurations that have a high degree of spatial symmetry. MC simulations do not suffer from this disadvantage and can be used as an alternative.

For situations in which the gradients in the fields are high, it is even possible that fluid model assumptions start to fail for certain species (often these are the electrons, although in certain devices these can be the ions [1]). In such a case, the fluid model can be coupled to an MC calculation in order to describe those aspects of the species' behaviour for which the fluid model fails. Such *hybrid fluid-particle models* are the subject of chapter 3 in this thesis.

When the fluid equations fail for all the species of interest, one has to think of a completely kinetic approach and consider Particle-In-Cell (PIC) or Direct Simulation Monte Carlo (DSMC) models to describe a discharge. Although a little more will be said about

1 GByte of RAM.

PIC models in chapter 3, these models are outside the scope of this thesis.

In this chapter we treat the theory and implementation of an MC code. In section 2.2 the theory is treated that is necessary to describe the path of a single particle through the discharge. In section 2.3 the implementation is treated of a versatile MC simulation program based on this theory.

2.2 Theory

The applications of MC codes typically consist of those gas discharges in which one or more species are far from thermodynamic equilibrium. This is generally the case when collisions are infrequent and therefore not effective in the exchange of energy and momentum between particles. As a result of this, one can safely make the assumption that collisions are brief compared to the time between collisions.

By making this assumption, it is possible to subdivide the treatment of a particle's path in *free flight*, during which the particle is subject to macroscopic forces, and *binary collisions*, which interrupt free flight. In these collisions, the velocity vectors of the particles change and new particles might be created and old ones lost.

This subdivision in free flight and binary collisions allows the treatment of a particle's path to consist of the following ingredients:

- the free flight time of a particle is to be determined from the total sum of cross sections for all processes that a particle can experience.
- during free flight, the equations of motion for the particle need to be solved in order to calculate its trajectory.
- at the end of the free flight, a process needs to be selected based on the relative contribution of its cross section to the sum of all cross sections.
- for the selected process, the effect of the collision on the velocity vectors of the particles and the loss and generation of new particles need to be described.

This scheme is illustrated in figure 2.2. Typically, first the time t_c at which the next collision will take place is determined. Subsequently, the trajectory of the particle is calculated by integrating the equations of motion over small discrete time-steps Δt , which are at maximum a user-defined δt in size. During this ballistic motion it is checked whether the particle is still in the discharge vessel.

When the time for a collision has arrived, the type of collision is chosen. Typically the set of possible collisions consists of various types, such as: *elastic collisions*, in which only kinetic energy and momentum are exchanged; *inelastic collisions*, in which also the state of one of the particles is changed, leading to an increase or decrease of total kinetic energy; *ionisation collisions*, in which an incident electron transfers enough energy to an atom to free one of the electrons from its orbit and leave an ion behind.

When the collision type has been chosen, it can be evaluated. This consist of applying a scattering model to the velocity vectors of the two particles and, in case the process is

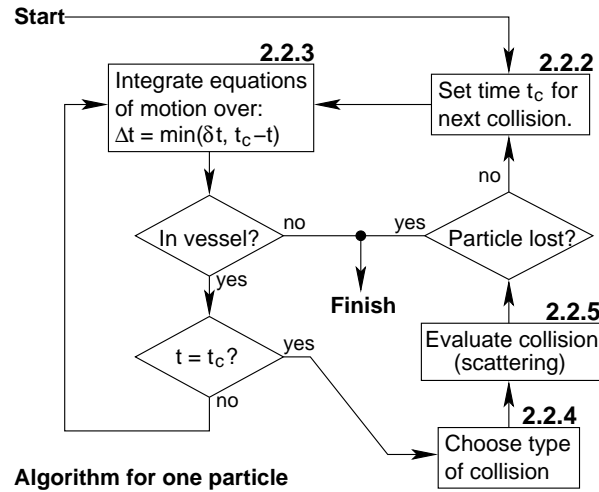


Figure 2.2: Outline of the algorithm that is used to follow the path of a single particle through the background gas. See the text for an explanation. The numbers next to the boxes refer to the section in which this aspect of the particle’s path is treated.

inelastic, accounting for kinetic energy being converted into potential energy. Furthermore, particles might be lost or new ones created.

In the following we will treat the equations that describe these components of the path of a particle and construct the expressions in which random numbers are used to sample the relevant distribution functions. However, first we will say a few words about random numbers.

2.2.1 Random numbers

A valid question to start with is: “Is 2 a random number?” [2]. The answer is that there is no such thing as an individual random number; instead it is necessary to speak about sequences of random numbers. Although a lot more can be said about this, for our purpose it will suffice to think of random numbers in terms of sequences of numbers in which each number was obtained merely by chance. Any number in the sequence has nothing to do with the other numbers of the sequence and each number has a specified probability of falling in any given range of values [2].

In fact, if the sequence of numbers is not random at all, but seems to be random, it will suit the purpose of the MC method in this document.² This allows us to use a so called *pseudo-random* number generator that produces such sequences in an algorithmic and thus deterministic: when the term ‘random number sequences’ is used in this document, actually ‘sequences of numbers which display apparent randomness’ are meant. One advantage of

²The requirements of random number generators depend on the application: in the generators used in cryptology it is important that each number in the sequence is really unpredictable. In Monte Carlo methods, equidistribution is a more relevant property.

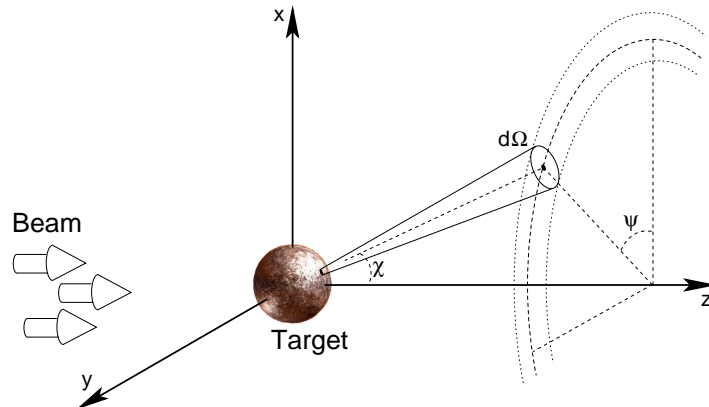


Figure 2.3: Illustration of coordinates used to describe scattering. A beam of homogeneous flux density scatters onto a target. The fraction of particles falling into the solid angle $d\Omega(\chi, \psi)$ is measured to determine the differential cross-section $Q(\varepsilon, \Omega)$.

using pseudo-random numbers is that the properties of the distribution of numbers in the sequence are well known. Another advantage is that the same sequence of numbers can be generated, which makes debugging of code easier.

When MC methods are used, solutions are often expressed in the form of integrals. Intuitively it is clear that the integral is probed by a sequence of points that has good properties of equidistribution within the domain of integration, this approximation yields a satisfactory representation of the integral [3]. Much more than the real randomness of the random numbers it is important that small sub-sequences are therefore distributed in a uniform way over their range.

In the following, random numbers are designated with the symbol r_n . The subscript n represents the sequence out of which the random number is sampled. In section 2.3.2, some properties of the random number generator used in the MC code are listed.

2.2.2 Free path

A simulation particle will collide with a certain target species at some moment in time and at a certain place. In order to describe this, a quantity called *cross section* is important.

Imagine an experiment in which a uniform beam of particles with energy ε scatters onto a target in the origin of the coordinate system (see figure 2.3). A detector is placed at a certain, adjustable angle to the incident beam and measures the number of particles that reaches it. In this way we can determine the differential cross section $Q(\varepsilon, \Omega)$, defined such that $Q(\varepsilon, \Omega)d\Omega$ is the number of particles per unit time that falls into the solid angle $d\Omega(\chi, \psi)$ per unit flux density of the incoming beam [4]. The unit of $Q(\varepsilon, \Omega)d\Omega$ is surface area.

If one integrates $Q(\varepsilon, \Omega)$ over all solid angles, one obtains the so called *total cross*

section:

$$\sigma(\varepsilon) = \int_{4\pi} Q(\varepsilon, \Omega) d\Omega \quad (2.1)$$

which can be thought of as the effective area that the target forms perpendicular to the direction of the beam.

In Monte Carlo methods for plasma physics, the target can be considered to be spherically symmetric and therefore the differential cross section does not depend on the azimuthal angle ψ . One can replace $\int_{4\pi} Q(\varepsilon, \Omega) d\Omega$ by $2\pi \int_0^\pi Q(\varepsilon, \chi) \sin \chi d\chi$.

Mean free path length

Now consider a beam of particles that traverses a thin slice of gas. The thickness of this slice is dx and the density of the gas is n . A unit area of this slice contains ndx atoms. Each of these atoms presents an area σ perpendicular to the direction of the beam and therefore the fraction of the area on which incident particles scatter is σndx .

If we extend this picture to a stack of a slices, the fraction $p(x)$ of particles that has not been scattered after having traversed a distance x is described by:

$$dp(x) = -n\sigma p(x) dx \quad (2.2)$$

Solving this differential equation, taking $p(0) = 1$ and assuming that $n\sigma$ is constant along the path of the particle, leads to:

$$p(x) = \exp(-n\sigma x) \quad (2.3)$$

The average of this distribution is:

$$\lambda_0 = \frac{\int x \exp(-n\sigma x) dx}{\int \exp(-n\sigma x) dx} = \frac{1}{n\sigma} \quad (2.4)$$

which is the mean free path of the particles. This quantity can easily be generalised for situations in which N_T different target species with densities n_i are present. In such a more realistic case, various collisional processes between the simulation particle species and the different target species can occur. The collisional process j of the N_{Pi} collision types with target species i has a cross section, denoted by σ_{ij} . The mean free path is given by:

$$\lambda_0 = \left(\sum_{i=1}^{N_T} \sum_{j=1}^{N_{Pi}} \sigma_{ij}(\varepsilon) n_i \right)^{-1} \quad (2.5)$$

The function $p(x)$ in equation (2.3) can also be interpreted as the *probability* that a particle did not collide after having travelled a distance x . The probability $c(x)$ that a particle will collide after having travelled a distance x is simply $c(x) = 1 - p(x)$:

$$c(x) = 1 - \exp\left(-\frac{x}{\lambda_0}\right) \quad (2.6)$$

By equating this distribution to a random number $r_1 \in [0, 1)$ and inverting the expression (see section 2.A.3 for the probability theory used here), we can generate a random value of the free path length of a simulation particle:

$$\lambda = c^{-1}(r_1) = -\lambda_0 \ln(1 - r_1) \quad (2.7)$$

The practical application of the above equations in a computer program is complicated by the fact that the path S of a particle can be curved: in that case one needs to integrate the distance traversed along this path until it is equal to the predetermined free path length:

$$\int_S \mathbf{e}_t \cdot d\mathbf{x} = \lambda = -\lambda_0 \ln(1 - r_1) \quad (2.8)$$

with \mathbf{e}_t the unit vector tangent to S . Taking into account that λ_0 can change along the curve leads to the general expression [5]:

$$\int_S \lambda_0^{-1}(\mathbf{x}, \varepsilon) \mathbf{e}_t \cdot d\mathbf{x} = -\ln(1 - r_1) \quad (2.9)$$

Note that, although exact, this last expression requires a lookup of $n(\mathbf{x})$ and $\sigma(\varepsilon)$ for each time-step. For this, ε needs to be calculated as well.

If the path-integration method is such that the particle travels along a straight line during each discrete time-step, one can avoid integrating the free path along the curve. Instead, by considering if the following is true, one can determine whether a collision needs to be evaluated at the end of the path segment that started at \mathbf{x}_i and ended at \mathbf{x}_{i+1} :

$$|\mathbf{x}_{i+1} - \mathbf{x}_i| > -\lambda_0 \ln(1 - r_1) \quad (2.10)$$

It is essential here that the path segment is sufficiently small, such that the chance of more than one collisions will be negligible.

Collision frequency

Instead of determining the distance a particular simulation particle travels before it undergoes a collision, it is also possible to determine how long it will take before the particle will collide. The mean free flight time t_0 is the inverse of the total mean collision frequency ν_0 :

$$\nu_0 = \sqrt{\frac{2\varepsilon}{m}} \sum_{i=1}^{N_T} \sum_{j=1}^{N_{pi}} \sigma_{ij}(\varepsilon) n_i(\mathbf{x}) \quad (2.11)$$

Similar to equation (2.3), the probability that a particle will travel during a time t without a collision is:

$$p(t) = \exp(-\nu_0 t) \quad (2.12)$$

This expression is based on the assumption that ν_0 is constant during the free flight of the particle. The time between collisions can be obtained from a random number r_1 :

$$\Delta t_{\text{collision}} = -\frac{1}{\nu_0(\varepsilon)} \ln(1 - r_1) \quad (2.13)$$

The equivalent of expression (2.10), which tells whether a collision needs to be evaluated after a time-step Δt , is:

$$\Delta t > -\frac{1}{\nu_0(\varepsilon)} \ln(1 - r_1) \quad (2.14)$$

Here it is again necessary to choose Δt sufficiently small, such that the chance of two collisions per time-step is negligible.

2.2.3 Equations of motion

Between collisions the particles will move freely, perhaps influenced by electric and magnetic fields (the gravitational force can be neglected in most cases). The motion of a particle is specified in phase space by the place and velocity vectors: (\mathbf{x}, \mathbf{u}) . The evolution of the particles phase space coordinates are governed by the equation of motion:

$$\frac{d^2\mathbf{x}}{dt^2} = \frac{\mathbf{F}}{m} \quad (2.15)$$

in which m is the mass of the particle and $\mathbf{F} = q\mathbf{E}$ the force on a particle with charge q in an electric field $\mathbf{E}(\mathbf{x})$. The velocity is written as $\mathbf{u} = d\mathbf{x}/dt$.

This equation can be discretised in time using a central difference method: let $t_i = i\Delta t$, with Δt the integration time-step, then the time derivatives of \mathbf{x} can be written as:

$$\frac{d\mathbf{x}(t_i)}{dt} \approx \frac{\mathbf{x}(t_{i+1}) - \mathbf{x}(t_i)}{\Delta t} \quad (2.16)$$

$$\frac{d^2\mathbf{x}(t_i)}{dt^2} \approx \frac{\mathbf{x}(t_{i+1}) - 2\mathbf{x}(t_i) + \mathbf{x}(t_{i-1}))}{\Delta t^2} \quad (2.17)$$

Considering the approximate signs to be equalities, substitution into equation (2.15) and rewriting gives:

$$\mathbf{x}(t_{i+1}) = \mathbf{x}(t_i) + \mathbf{u}(t_i)\Delta t + \frac{\mathbf{F}(t_i)}{2m}\Delta t^2 \quad (2.18)$$

$$\mathbf{u}(t_{i+1}) = \mathbf{u}(t_i) + \frac{\mathbf{F}(t_i) + \mathbf{F}(t_{i+1})}{2} \frac{\Delta t}{m} \quad (2.19)$$

We note that this is only one of the many possible discretisation schemes. Another popular scheme is the so called leap-frog scheme [6]:

$$\mathbf{x}(t_{i+1}) = \mathbf{x}(t_i) + \mathbf{u}(t_{i+\frac{1}{2}})\Delta t \quad (2.20)$$

$$\mathbf{u}(t_{i+\frac{3}{2}}) = \mathbf{u}(t_{i+\frac{1}{2}}) + \frac{\mathbf{F}(t_{i+1})\Delta t}{m} \quad (2.21)$$

which has the advantage of requiring less operations, but suffers from the disadvantage of having \mathbf{x} and \mathbf{v} staggered in time. In practice this means that, for example when a collision needs to be evaluated, one needs to synchronise the place and velocity vectors by integrating one of them over half a time-step. Another scheme, suitable for when magnetic fields are present, is the Boris scheme. Please refer to reference [6] for details.

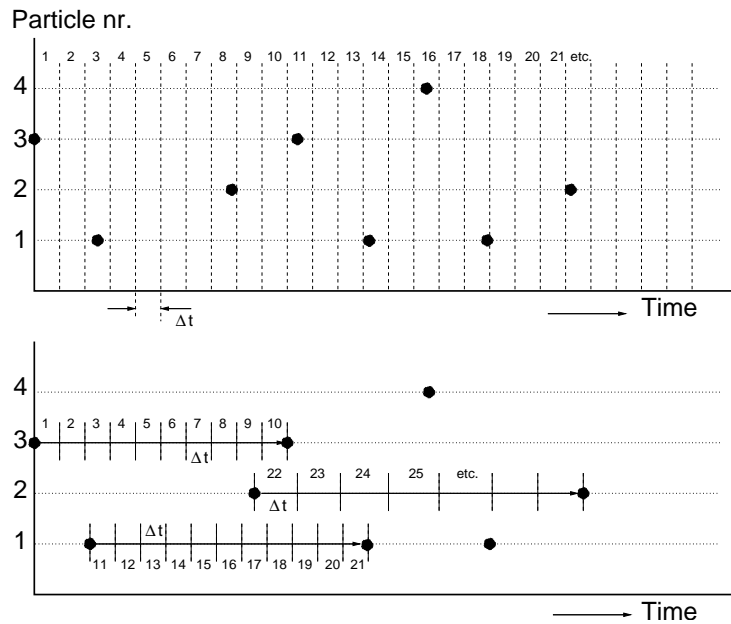


Figure 2.4: Illustration of two schemes for advancing particles in time. The solid circles indicate collision moments, the numbers indicate subsequent time-steps. *Top figure:* in this scheme the particles are synchronously advanced in time. For every time-step all the particles are moved over Δt and for some of them a collision is evaluated. *Bottom figure:* in this scheme particles are advanced separately. The particle's equations of motion are integrated till the next collision moment, the collision is evaluated and the next collision marker is set. Only then attention is shifted to the next particle, for which a similar sequence of events is evaluated. The advantage of this scheme resides partially in the fact that a different Δt can be used for each particle.

Schemes for advancing many particles

The MC model usually follows a large number of particles. There are different ways to alternately treat the paths of all these particles while time advances. The following three methods are common. For the first two it is assumed that immediately after a collision the moment in time for the next one is determined.

- The top part of the figure 2.4 illustrates one of the most straightforward ways: at each time-step, for each simulation particle the equations of motion are integrated over the size Δt of this time-step. Before integrating the equation of motion, it is checked whether the particle was determined to collide in that time-step. If this is the case (indicated with the solid circles in the figure), the path of the particle is integrated till the moment of the collision. Then, the collision is evaluated and the moment in time of the next collision event for that particle is already calculated. Finally, the path is integrated till the end of the time-step. Note that this scheme complies with a PIC scheme [6], as at the end of each time-step one can calculate the density fields of the particles for usage in the Poisson solver.

- The bottom part of figure 2.4 shows a more elaborate way to advance the particles: imagine a pointer that slides along the time axis. At some moment it moves across a solid circle (in the figure this happens right at the beginning of the time axis). For the particle in question (particle number 3 in the figure) the equations of motion are integrated from this time until the next collision. Then the collision is evaluated and the next moment of collision is calculated. When this is done, the pointer slides further along the time axis, until it hits a next collision marker (now particle number 1). Again the equations of motion are integrated until this collision, the collision is evaluated and the marker for the next collision is set, etc.

Contrary to the previous manner of progressing particles, the time-step of integration can be determined specifically for the particle under consideration, depending on its velocity. A disadvantage of this approach is that each particle has its own time. When collecting statistics, such as for determining the eedf, these times need to be synchronised.

- A third manner (not shown in the figure) of following the particles along their paths is to not set the collision times, but to evaluate by means of equation (2.10) or (2.14) what the chance on a collision is at the end of each time-step. This approach is mainly worthwhile if the mean free path length changes significantly along the free path of a particle due to changes in density and cross sections. The disadvantage of this approach is that the time-steps must be so small that the chance on two collisions during one time-step is negligible. Furthermore, the fact that densities and cross sections need to be looked up and the energy of the particle needs to be calculated at each time-step puts a significant burden on computation time.

2.2.4 Selecting the process

From all the processes that a particle can experience given its energy, one process needs to be selected at the end of the free flight. The manner in which this is done needs to reproduce the collision frequencies of the various processes i correctly, i.e. according to:

$$\nu_i(\varepsilon) = \left(\frac{2\varepsilon}{m}\right)^{1/2} \sigma_i(\varepsilon)n(\mathbf{x}) \quad (2.22)$$

This can be accomplished by generating a cumulative table of these collision frequencies for the particle with energy ε . The last entry in this table is the *total* collision frequency $\nu_0(\varepsilon)$. By scaling the table with ν_0 , one can now draw a random number r_2 to select the n^{th} process such that:

$$\frac{1}{\nu_0} \sum_{i=1}^n \nu_i \leq r_2 < \frac{1}{\nu_0} \sum_{i=1}^{n+1} \nu_i \quad (2.23)$$

This sampling method is a more general version of the rejection method that is treated in appendix 2.A.3.

Null Collision technique

In general the question *when* a particle will collide is easier to answer than *where* it will collide. The simple reason is that one does not need to calculate the length of the displacement of the particle but can just consider moments in time, as is done in the many-particle schemes above. Still, the expressions (2.13) and (2.23) have the clear disadvantage that they assume that ν_0 is constant during the free flight of the particle.

An improvement that is benign to computation time is formed by a method first introduced by Skullerud [7]. In equation (2.13) the total collision frequency ν_0 is replaced by the maximum collision frequency ν_{\max} for all energies and densities that can occur in the discharge volume V :

$$\nu_{\max} = \max_{\mathbf{x} \in V, 0 \leq \varepsilon \leq \varepsilon_{\max}} \left[\left(\frac{2\varepsilon}{m} \right)^{1/2} \sum_{i=1}^{N_T} \sum_{j=1}^{p_i} n_i(\mathbf{x}) \sigma_{ij}(\varepsilon) \right] \quad (2.24)$$

By using ν_{\max} to determine the free flight times of particles, the mean collision frequency is obviously overestimated. This can be compensated for by introducing an extra collision process, the *null collision*. This null collision does not alter the particle's velocity: if selected, effectively the particle does not collide at all. In equation (2.23) it is now possible that r_2 is so large that this equation is not satisfied for any n . In that case the null-process has been chosen.

In figure 2.5 the idea is illustrated for the simplified case of a constant background particle density: the horizontal line corresponds to the maximum collision frequency, which follows from the maximum in the sum of frequencies for all collision processes. Suppose now that a simulation particle did just collide at time t . The moment in time in which a new collision needs to be evaluated is determined by (cf. equation (2.13)):

$$t_{\text{collision}} = t - \frac{1}{\nu_{\max}} \ln(1 - r_1) \quad (2.25)$$

The particle's way through the gas is determined by integrating the equation of motion numerically until $t_{\text{collision}}$ is reached. Depending on the kinetic energy of the particle at that moment, it is determined whether the particle will experience a real collision or the null collision. Only at this point a lookup needs to be done for the properties of the particle and of the environment in the vicinity of the particle.

The efficiency of the null collision technique is dependent on the shape of the collision frequency curves. To take the fictional case of figure 2.5 as an example: there is one large peak in the collision frequency which determines ν_{\max} in equation (2.25). Due to this peak, the number of times that particles will undergo a null-collision is relatively large.

This problem can be partially circumvented by dividing the energy and density space up in different regions [8]. If this is done in such a way that within each region the null collision contribution to the maximum collision frequency stays relatively small, the efficiency of the null-collision method can be improved. This is illustrated in figure 2.6

Introducing ranges brings the disadvantage that particles can cross energy range boundaries and have their collision times misestimated. If the particle moves into an energy

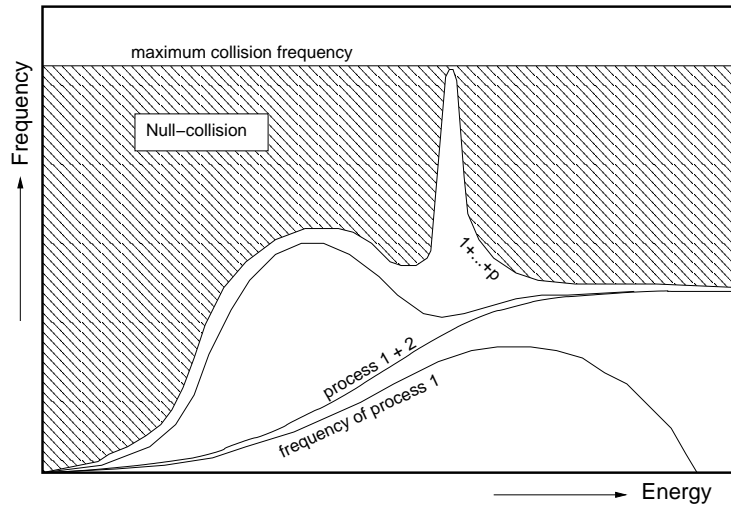


Figure 2.5: Schematic illustration of the concept of a null-collision. Refer to the text for details.

region where the maximum collision frequency is higher, a mistake is made in the moment at which a collision is to be evaluated.

2.2.5 Scattering

In MC simulations in plasma physics, one treats the question *whether* a particle is going to collide separately from *how* it is going to collide. Looking at equation (2.1) suggests that these two questions can indeed be answered individually by splitting $Q(\varepsilon, \chi)$ into two quantities $\sigma(\varepsilon)$ and $I(\varepsilon, \chi)$. If this is done such that:

$$2\pi \int_0^\pi I(\varepsilon, \chi) \sin \chi d\chi = 1 \quad (2.26)$$

then the quantity $\sigma(\varepsilon)$ is a measure for the chance that a particle scatters at all. The quantity $I(\varepsilon, \chi)d\chi$ tells what the probability is that the particle, if scattered, is scattered into the range $d\chi$ centred around χ . The term ‘differential cross section’ will from here on be used to denote $I(\varepsilon, \chi)$, rather than $Q(\varepsilon, \chi)$.

As mentioned before, collisions are assumed to happen instantaneously. Therefore, a collision event only results in a change in the velocity vectors of the particle. By considering the collision in the centre of mass frame of the two colliding particles, only the rotation of the relative velocity vector \mathbf{u}_r needs to be considered to describe the collision. Two angles are needed for this (see appendix 2.B). Furthermore, if the collision is inelastic, the energy loss needs to be subtracted from the kinetic energy of the reduced mass.

The scattering angle χ follows from the differential cross section $I(\varepsilon, \chi)$. For central force fields between the two colliding particles, the distribution of the azimuthal angle ψ is isotropic. The probability distribution of ψ can therefore be taken to be uniform on $[0, 2\pi)$

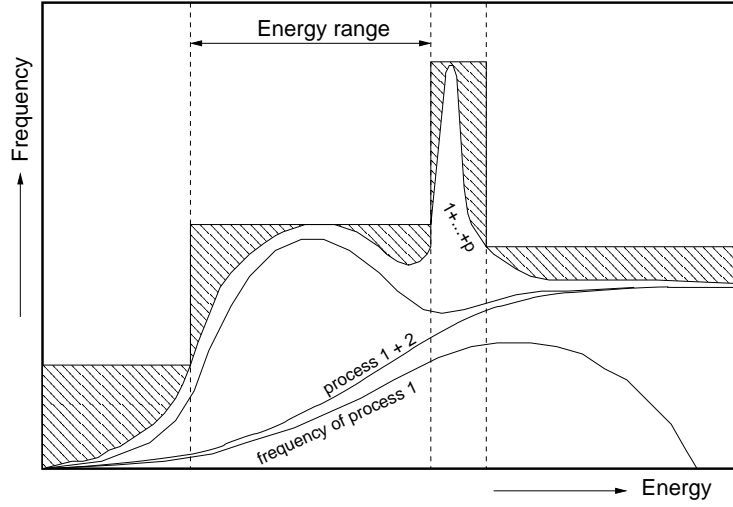


Figure 2.6: Improvement of the efficiency of the null-collision method by introducing ranges with their own null-collision frequency (cf. figure 2.5).

and is generated with a random number r_3 taken out of a uniform distribution on $[0, 1)$:

$$\psi = 2\pi r_3 \quad (2.27)$$

Following the theory in appendix 2.A, a random number r_4 can be used to generate a random scattering angle χ by solving the following equation for χ :

$$r_4 = 2\pi \int_0^\chi I(\varepsilon, \chi') \sin \chi' d\chi' \quad (2.28)$$

The precise form of $I(\varepsilon, \chi)$ is determined by the nature of the collision and needs to be considered for every species pair and collision type separately.

Relation between centre of mass frame and laboratory frame

Before we proceed with common expressions for the differential cross section, we note that the scattering angle χ in the centre of mass frame is different from the corresponding angle χ_0 in the laboratory frame (see figure 2.7). The differential cross sections in the two frames are related via:

$$I(\varepsilon, \chi_0) \sin \chi_0 d\chi_0 = I(\varepsilon, \chi) \sin \chi d\chi \quad (2.29)$$

If one solves this for $I(\varepsilon, \chi_0)$, one obtains [9]:

$$I(\varepsilon, \chi_0) = \frac{\left(1 + 2\frac{m_1}{m_2} \cos \chi + \left(\frac{m_1}{m_2}\right)^2\right)^{3/2}}{1 + \frac{m_1}{m_2} \cos \chi} I(\varepsilon, \chi) \quad (2.30)$$

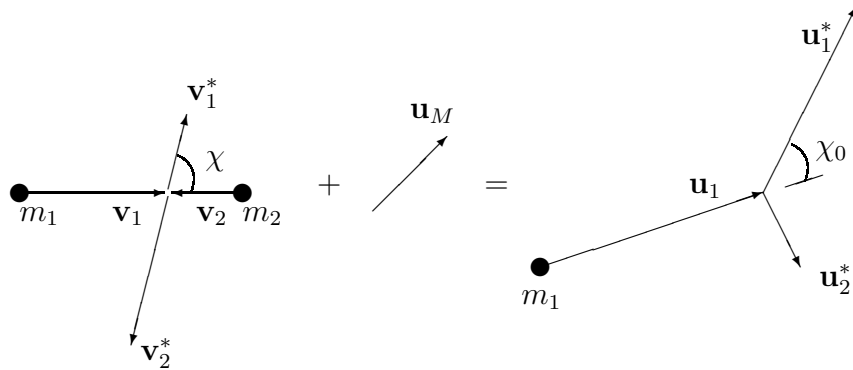


Figure 2.7: Change in angle χ in going from the centre of mass frame to the laboratory frame: by vector-addition of the centre of mass velocity \mathbf{u}_M to the velocities of the particles with respect to the centre of mass frame (on the left), one obtains the velocities in the laboratory frame of reference (on the right). For clarity the vector \mathbf{u}_2 has been omitted on the right hand side.

In the present implementation of the MC code it is assumed that the differential cross section is known in the centre of mass frame. Since the collision is evaluated in this frame, above expression is not used.

In the following, some commonly used expressions for the differential cross section are given and equation (2.28) will be inverted analytically for these. Often, one can take these expressions as good estimates for the scattering dynamics of very specific processes. The most simple case, isotropic scattering, will be the first one considered.

Isotropic scattering

In so called hard sphere collisions the scattering is isotropic on the unit sphere: $I(\varepsilon, \chi)$ is independent of ε and takes the following form:

$$I(\varepsilon, \chi) = \frac{1}{4\pi} \quad (2.31)$$

Substituting equation (2.31) into equation (2.28) and solving for χ results in:

$$\cos \chi = 1 - 2r_4 \quad (2.32)$$

which allows one to generate the scattering angle χ by means of a random number r_4 .

Elastic scattering, Born's approximation

In many processes the scattering is not isotropic, but rather has a larger probability in the forward direction. Often the extent of this forward scattering is dependent on the energy ε of the scattering particle.

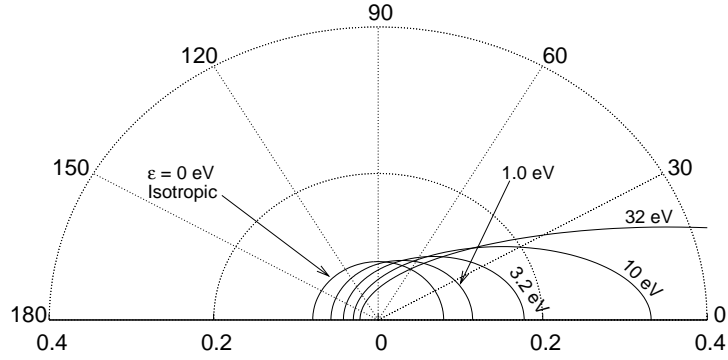


Figure 2.8: Polar plot of $I(\varepsilon, \chi)$ for the Surendra scattering notation (equation (2.36)) for several values of the incident electron energy ε . Note that for $\varepsilon = 0$ scattering is isotropic.

For elastic collisions of electrons with atoms, Born's approximation [10] can be used:

$$I(\varepsilon, \chi) = \frac{\eta(\eta + 1)}{\pi(2\eta + 1 - \cos \chi)^2} \quad (2.33)$$

in which η is a Coulomb screening parameter:

$$\eta = \frac{10.9Z^{2/3}}{\varepsilon} \quad (2.34)$$

with ε here in units of eV. Z is the atom number of the atom involved in the collision. For low energies scattering is isotropic and indeed for higher energies it gets increasingly forwardly directed. Substituting (2.33) in (2.28) and solving for χ leads to:

$$\chi = \arccos \left(\frac{\eta + 1 - (2\eta + 1)r_4}{\eta + 1 - r_4} \right) \quad (2.35)$$

which gives χ as a function of r_4 .

Surendra's approximation

An often used expression for the differential cross section is the one by Surendra et al. [11], based on screened Coulomb scattering:

$$I(\varepsilon, \chi) = \frac{\varepsilon}{4\pi[1 + \varepsilon \sin^2(\chi/2)] \ln(1 + \varepsilon)} \quad (2.36)$$

As before, to generate an angle χ by means of a random number r_4 , equation (2.31) is substituted into equation (2.28) and inverted [6, 12]:

$$\chi = \arccos \left(\frac{2 + \varepsilon - 2(1 + \varepsilon)r_4}{\varepsilon} \right) \quad (2.37)$$

In figure 2.8 a plot is given of $I(\varepsilon, \chi)$ for several values of ε .

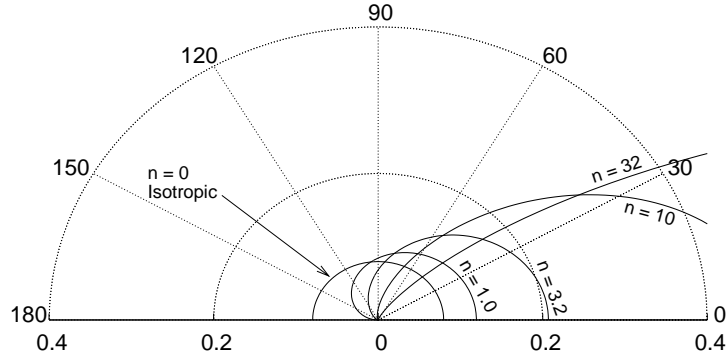


Figure 2.9: Polar plot of $I(\varepsilon, \chi)$ for the Kushner scattering notation (equation (2.40)) for several values of n . Note that for $n = 0$ scattering is isotropic.

Okhrimovskyy's approximation

In an atomic gas, differential cross sections for electron neutral interactions can be described with an expression derived by Okhrimovskyy, Bogaerts and Gijbels [13]:

$$I(\varepsilon, \chi) = \frac{1}{4\pi} \frac{1 + 8\varepsilon}{(1 + 4\varepsilon - 4\varepsilon \cos(\chi))^2} \quad (2.38)$$

with $\varepsilon = \varepsilon/E_0$, ε the energy in units of eV and $E_0 = 27.21$ eV the atomic unit of energy. For low energies scattering is isotropic, for higher energies it becomes increasingly forward directed. Compared to the Surendra approximation, the scattering angle shows a larger probability of being directed forward. Substituting (2.38) in (2.28) and solving for χ leads to:

$$\chi = \arccos \left(1 - \frac{2r_4}{1 + 8\varepsilon(1 - r_4)} \right) \quad (2.39)$$

which can again directly be used to generate χ from a random number r_4 .

Kushner's approximation

A general expression for the differential cross section for forward scattering is [14, 8]:

$$I(\varepsilon, \chi) = \frac{n + 2}{8\pi} \cos^n(\chi/2) \quad (2.40)$$

in which $n = n(\varepsilon)$ is a function of ε and the factor preceding the cosine is for normalisation. Note that for $n = 0$ equation (2.40) reduces to equation (2.31) and the scattering is isotropic. In figure 2.9 a plot is given of $I(\varepsilon, \chi)$ for several values of n . In order to use this equation, an expression for $n(\varepsilon)$ can be generated to fit the amount of forward scattering to experimental data.

To get to an equation that expresses χ as a function of a random number r_4 , we substitute the differential cross-section (2.40) into equation (2.28):

$$r_4 = \frac{n(\varepsilon) + 2}{4} \int_0^\chi \cos^{n(\varepsilon)}(\chi'/2) \sin \chi' d\chi' \quad (2.41)$$

rewriting (double angle formula) leads to:

$$r_4 = \frac{n(\varepsilon) + 2}{2} \int_0^\chi \cos^{n(\varepsilon)+1}(\chi'/2) \sin(\chi'/2) d\chi' \quad (2.42)$$

integration yields the expression which relates χ to r_4 :

$$r_4 = 1 - \cos^{n(\varepsilon)+2}(\chi/2) \quad (2.43)$$

and finally inversion brings us to the required expression:

$$\chi = 2 \arccos \left((1 - r_4)^{\frac{1}{n(\varepsilon)+2}} \right) \quad (2.44)$$

Note that for $n = 0$ this can be rewritten to the form of equation (2.32).

Ionisation

Compared to collisions that are binary on both sides of the reaction equation, ionisation collisions require some extra attention as far as the ejected electron is concerned. In literature one finds several methods to determine the direction and energy of the electrons after the collision. However, the complete dynamics of an ionisation process is poorly known and it is therefore necessary to make some assumptions.

As far as the energy of the two electrons is concerned, the empirical expression found by Opal et al. [15] is often used. The excess energy of the incident electron compared to the ionisation potential E_i is partitioned between the scattered incident electron and the ejected electron according to a distribution function $I(\varepsilon_e, \varepsilon)$. This describes the probability of producing an ejected electron with energy ε_e for a given incident electron energy ε :

$$I(\varepsilon_e, \varepsilon) = \frac{1}{\bar{E} \arctan \left[(\varepsilon - E_i) / 2\bar{E} \right]} \quad (2.45)$$

where \bar{E} is a gas-dependent parameter, the value of which is listed in [15] for several gases.

Inversion of the integral of the cumulative distribution of (2.45) allows one to sample this distribution with a random number $r_5 \in [0, 1)$:

$$\varepsilon_e = \bar{E} \tan \left[r_5 \arctan \left(\frac{\varepsilon - E_i}{2\bar{E}} \right) \right] \quad (2.46)$$

Assuming that the ion does not recoil, the energy ε_s of the scattered electron is $\varepsilon_s = \varepsilon - E_i - \varepsilon_e$. Note that if the excess energy is small, it is likely to be equally divided

between the two electrons, whereas for large excess energies the incident electrons is likely to keep most of it.

Given the energies of the electrons after the collision, the directions of the electrons remain to be calculated. In [12] it is assumed that the ion keeps the same velocity as the neutral atom before the collision and the electrons are both scattered through the angles χ and ϕ resulting from the equation (2.37) and (2.27) respectively. It is however not clear how this scheme conserves momentum.

Another approach, by Boeuf and Marode [16], uses the energies determined from equation (2.46) to come to expressions for the scattering angles of the two electrons. The interaction with the atom is ignored and the collision is treated as a collision of two electrons, one of which has zero velocity. From energy and momentum conservation it follows that the velocities of the scattered and ejected electron velocities are perpendicular. Furthermore, by fixing the amount of energy that each electron gets, the scattering angle of one of the electrons is found to be:

$$\chi_s = \arccos \sqrt{\frac{\varepsilon_s}{\varepsilon - E_i}} \quad (2.47)$$

and the angle of the other is simply $\chi_e = \chi_s - \pi/2$. This approach is followed in the implementation of the present MC code.

Result of a collision in the laboratory frame

Given the theory of the previous sections we are able to calculate the new velocities of the two particles involved in a binary collision: the collision itself is best described in the centre of mass frame of reference of the two colliding particles (see appendix 2.B). In order to get there, the centre of mass velocity \mathbf{u}_M and the relative velocity \mathbf{u}_r need to be determined:

$$\mathbf{u}_M = \frac{m_1 \mathbf{u}_1 + m_2 \mathbf{u}_2}{m_1 + m_2} \quad (2.48)$$

$$\mathbf{u}_r = \mathbf{u}_1 - \mathbf{u}_2$$

Then, the relative velocity needs to be rotated over χ and ψ . The expression for obtaining the new relative velocity vector \mathbf{u}_r^* from the \mathbf{u}_r and the two angles χ and ψ is derived in in appendix 2.C, with as a result:

$$\mathbf{u}_r^* = u_r \begin{pmatrix} \cos \theta \cos \varphi \sin \chi \cos \psi - \sin \varphi \sin \chi \sin \psi + \sin \theta \cos \varphi \cos \chi \\ \cos \theta \sin \varphi \sin \chi \cos \psi + \cos \varphi \sin \chi \sin \psi + \sin \theta \sin \varphi \cos \chi \\ \cos \theta \cos \chi - \sin \theta \sin \chi \cos \psi \end{pmatrix} \quad (2.49)$$

with u_r , θ and φ the spherical coordinates of \mathbf{u}_r in the laboratory frame.

If the collision is inelastic, the magnitude of the relative velocity will change, resulting from a change in the kinetic energy $\varepsilon_r = \frac{1}{2}m_r u_r^2$ within the centre of mass frame of reference,

with $m_r = \frac{m_1 m_2}{m_1 + m_2}$ the reduced mass of the system. The change in direction can be treated separately from the change in magnitude and therefore it is possible to scale its magnitude:

$$\mathbf{u}_r^* = \sqrt{\frac{\varepsilon_r + \varepsilon_p}{\varepsilon_r}} \mathbf{u}_r \quad (2.50)$$

with ε_p the energy that becomes available (positive) or is needed (negative) in the inelastic collision.

After rotation and, if the collision is inelastic, scaling of the relative velocity, the new particle velocities are obtained from:

$$\begin{aligned} \mathbf{u}_1^* &= \mathbf{u}_M + \frac{m_2}{m_1 + m_2} \mathbf{u}_r^* \\ \mathbf{u}_2^* &= \mathbf{u}_M - \frac{m_1}{m_1 + m_2} \mathbf{u}_r^* \end{aligned} \quad (2.51)$$

which concludes the evaluation of a collision.

Limit cases

To get insight in the result of collisions in the laboratory frame, it is instructive to calculate the angle χ_0 for several mass ratios of the colliding particles. This is done here by working out the trigonometry related to the vector additions as shown in figure 2.7 on page 33.

For the special case in which the target particle has zero velocity relative to the laboratory frame, χ_0 relates to χ according to [9]:

$$\tan \chi_0 = \frac{\sin \chi}{m_1/m_2 + \cos \chi} \quad (2.52)$$

Interesting are then the limit cases for the mass ratios of the particles:

$$m_1 \ll m_2 \quad \chi_0 = \chi \quad (2.53)$$

$$m_1 = m_2 \quad \chi_0 = \frac{\chi}{2} \quad (2.54)$$

$$m_1 \gg m_2 \quad \chi_0 \sim \frac{\sin \chi}{m_1/m_2} \quad (2.55)$$

Note that the limit case $m_1 \ll m_2$ is often employed in MC simulations, in combination with the assumption that the target has zero velocity. In that case the electron velocity and the relative velocity of the particles coincide and one does not need to calculate the centre of mass velocities (2.48). Often one does account for energy exchange in elastic recoil, which depends on the mass ratio of the two particles involved and on the scattering angle:

$$\mathbf{u}_1^* = \mathbf{u}_1 \sqrt{1 - 2 \frac{m_1}{m_2} (1 - \cos \chi_0)} \quad (2.56)$$

Although this approach is computationally less demanding, we use the equations (2.48)–(2.51) in our model.

2.3 Code design and implementation

The language in which the MC method is implemented is C++ [17]. This is an object oriented language that has been chosen for the models that are being developed in the Elementary Processes in Gas Discharges (EPG) group at Eindhoven University of Technology. More information on this choice can be found in [18, chapter 2 and 3] and [19, chapter 3]. In the following text, the design and the resulting structure of the code is treated. Firstly, the concept of classes and objects is illustrated, which is done to introduce some nomenclature that is needed in later parts of this chapter. We will by no means attempt to give a complete overview of the powerful language constructs of C++. One is advised to refer to [17, 20, 18, 19] for more details on object oriented programming and its usage in plasma simulations.

2.3.1 Classes and objects

In an object oriented language, definitions of data *and* functionality are brought together in a so called *class*. An *object* is an ontic expression of a class: one can think of a class as a blueprint and of the object as one of the realisations of this blueprint. Various objects interact when the program is running. As such, a C++ program is organised in more or less independent structures, which are often related to the components of the system it describes.

An example of what could be defined by a class is the concept of a particle (atom, molecule, electron or ion). Data-members include properties such as the particle's mass, charge, position and velocity. An example of a function-member would be a function that can calculate the kinetic energy of the particle from its velocity. Using this blueprint, one can construct various objects of this type to represent actual simulation particles like electrons.

Realising that there are many particles of the same species, one can fine-tune the definition of a particle by noting that individual particles are characterised by intrinsic and extrinsic properties. Intrinsic properties, like mass and charge, are the same for particles of the same species. Extrinsic properties, like position and velocity, are unique for each individual particle. In this way, a real-world particle can be represented by a shared reference to an object describing to which species it belongs and an object containing its extrinsic properties.

To make the concept of a class more concrete, let us consider the C++ code in listing 2.1 on the next page, which defines the intrinsic properties of a particle in the class named *mcSpecies*. The first thing one notes are the keywords *public* and *private* that divide the class in two blocks. Private members are members that are accessible to this class only. Public members are accessible to the code of other classes as well. The private members are, as it were, encapsulated in the class and could be improved without affecting the interface, i.e. public part, of the class. Note that by convention the names of the private data members are prefixed by *m_*.

The first public member in this class is of a special type: the *constructor* is a function

Listing 2.1:: *mcSpecies* class declaration

```
class mcSpecies
{
  public:
    /** Constructor. */
    mcSpecies(const plNode& node)
    {
      m_name = node("Name");
      m_mass = node("Mass")["kg"];
      m_qnr = node("ChargeNr");
      m_q = m_qnr*Constant::ElementaryCharge;
    }
    /** Accessor: returns the species mass in kg. */
    double M() const { return m_mass; }
    /** Returns the species charge in C. */
    double Q() const { return m_q; }
    /** Returns the name of the species. */
    const std::string& Name() const { return m_name; }
  private:
    /** Species name. */
    std::string m_name;
    /** Species mass in kg. */
    double m_mass;
    /** Species charge in units of the elementary charge. */
    int m_qnr;
    /** Species charge in C. */
    double m_q;
};
```

that carries the name of the class and is called when an object of that type is constructed. In this case it receives as an argument a data object named *node* of the type *plNode*. From this data object it copies the relevant data to the private members and thereby initialises the object. An object of the type *mcSpecies* is typically created as follows:

```
mcSpecies electrons(input_node);
```

The remaining public members in this example are the so called *accessors*, which provide public access to the values of the private data members. Since in this case the accessors provide only read-only access to the private data members, it is guaranteed that the species properties cannot be accidentally modified by erroneous code outside the class. A typical mistake that can be prevented by this is: **if** (*electrons.M()*=0.0) {...}, which tries to set (=) the species mass to zero instead of checking (==) whether the mass is zero.

Particles and species are obvious examples of objects. Perhaps less obvious is a class for binary processes. An object of such a class contains knowledge on the reaction format and on the total and differential cross section of the process it describes. For example a *DoApply()* function-member of the class could take two particles as arguments and calculates their new velocities based on the scattering model. In fact, the reaction format, the total

cross section and the scattering model can each be represented by a separate classes, as will be seen in section 2.3.5.

Object oriented programming encompasses many more advanced features than those illustrated above. A very important one that should be mentioned here is ‘inheritance’. By deriving one class from another, the derived class inherits the properties of the base class. This allows the common features of several classes to be put into one base class and then derive the various more specific classes from it. An example of this would be the implementation of the scattering model, as will also be treated in section 2.3.5.

An important benefit to object oriented programming is that the code becomes modular. Each module (i.e. class) can be re-used, often even outside the application-range it was originally intended for. The interface of the class definition is accessible to outside code, whereas it is guaranteed that private members cannot be accessed by any code but the class’ code itself. Furthermore, when the structure of the code is well-designed, separate classes can be tested individually or in small subsets of the complete code.

2.3.2 Random number generator

The random number generator used in the MC code described in this document is named ‘Mersenne-Twister’ [21] and has been obtained from the url listed in reference [22]. Internally it generates an integer in the range $[0, 2^{32} - 1]$ and divides this by 2^{32} to obtain a number in $[0, 1)$. The periodicity of this generator is $2^{19937} - 1$.

More details, as well as the results of various tests can be found in the references [21, 22, 23, 24]. The generator is mainly meant for MC simulations: it is fast and has good properties of equidistribution. Furthermore, the license of the code allows it to be used freely since 2001.

The original code has been cast in the form of a class *RandMT*. The main feature of this class is that an *()*-operator is defined that returns the next random number in the sequence. Furthermore, each new instant of the *RandMT* class bootstraps its generator with a different seed. As such, each *RandMT* object that is present in a running code generates a different sequence of random numbers.

2.3.3 Structure of the Monte Carlo code

In section 2.3.1 an example has been given of how the particle properties can be represented by means of a class definition. The entire MC module is in fact a collection of classes and specific interactions between these classes. The general structure of the code is depicted in figure 2.10.

Below we will consider the individual building blocks in figure 2.10 separately. The class that binds the simulation together has the whimsical name *mcFlightControl*, as it oversees flight and collisions of the simulation particles. The discussion of this class in section 2.3.8 will complete the overview of the model.

Note that listings are only given when this is beneficial to the discussion of the class under consideration. Furthermore, for reasons of terseness, the complete set of arguments

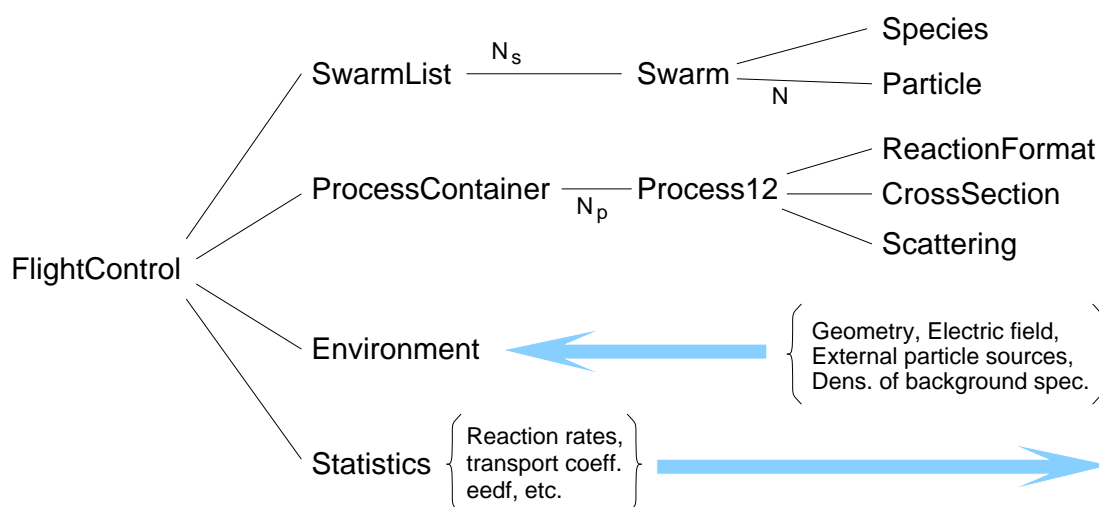


Figure 2.10: Overview of the general structure of the MC code treated in this chapter. Each node in the tree corresponds to a class in the code. A connection labelled with N between two classes indicates that the class on the left hand side is a container for the class on the right hand side. The large arrows indicate input and output to the code from and to external client code respectively.

and the return value of functions will not be listed in this text.

2.3.4 Species, particles and swarms

Typically, an MC simulation follows thousands or even millions of individual particles, which belong to a small number of species. It would be a waste of storage space to let each individual particle keep a copy of its intrinsic properties. Therefore the ‘Flyweight design pattern’ [20] has been used for the implementation of the species and particle properties. Following this pattern, the intrinsic properties are stored in one single instance of a dedicated class *mcSpecies* (listing 2.1). For each individual simulation, each particle is represented by an object of the class *mcParticle*, which stores a reference to the *mcSpecies* object of the species type to which the particle belongs.

This design strongly supports the introduction of a ‘particle container’ that contains all particles that belong to a given species. This container is responsible for the creation of the (unique) object that represents the particle’s intrinsic properties, as well as for the creation and deletion of individual particles. Such a container shall be appropriately referred to as a *swarm*.

Listing 2.2 shows the declaration of the *mcSwarm* class. Note that, for reasons of clarity, only those members and comments are shown that are relevant for the following discussion. Furthermore, the actual implementation of the member functions is not shown. This is common for C++, where declarations are listed in so called header files (carrying the extension *.h*) and the implementation typically resides in the corresponding source file

(with the extension `.cpp`).

One can see that the simulation particles are stored in a container object `m_activep` of the type `std::set` that is provided by the standard library of C++. The functions `AddParticle()` and `DeActivate()` control the addition and removal of particles from the container and are typically called when particles get created or destroyed in reactions.

The memory allocation involved in the construction of a particle is a time-consuming process, so another particle set `m_ppool` is provided in which deactivated particles are stored.³ Creating a new particle means simply fetching a particle from this set and setting its properties (like position, velocity and weight) correctly. Two more sets can be found in the listing: `m_justdied` and `m_newborn` are the containers where particles are temporarily stored, immediately after deactivation and creation respectively. This is necessary to solve initialisation and container index invalidation issues. The function member `flush_pools()` removes particles from the two transitional containers into `m_ppool` and `m_activep`.

Since we do not want to limit ourselves to just one type of simulation particle, the `mcSwarmList` is another container that has been defined to contain various swarms. Apart from the swarm(s) of simulation particles, this container is also used to store the so called `mcDensitySwarm` objects, i.e. the swarms of particles that are not actively followed by means of the MC method. These background particles are typically defined by a density field and do not need to be represented by actual simulation particles, except for when a collision needs to be evaluated. In that case, a background particle is sampled from the density field: the function `SamplePart()` returns a particle at the required location. The velocity of this particle is sampled from the energy distribution (typically Maxwellian with a given temperature) of the background gas.

2.3.5 Processes

As has become clear in section 2.2, the description of binary processes contains the larger part of the physics of an MC simulation. For the conditions for which the model will be applied, the path of a particle can be considered to consist of a free flight, interrupted by instantaneous collisions. For determining the free flight time, the total cross section is required, whereas for the evaluation of a collision, the differential cross section or scattering model is necessary.

It is a logical consequence of this two-fold structure to divide the implementation of a process in these two parts as well: in figure 2.10 the class `mcProcess12` has among its members objects of the classes `mcScattering` and `mcCrossSec`. The former class has a function `DoScatter(double6 theta, double6 phi, double eps)` that modifies `theta` and `phi` to contain two random angles for the given energy `eps`. These angles are used by another function member, `Scatter()`, to work out the changes in the velocities of the particles that participate in the process. The `mcCrossSec` class has data members that allow its `()`-operator to return the cross section at a given energy.

³If one studies the code carefully, one will see that actually pointers to particle objects are being stored in the various containers. This prevents copying particle objects from one container to the next and thereby decreases the workload to moving relatively small pointer objects around.

Listing 2.2: *mcSwarm* class declaration. For clarity, the code that is not relevant for the text has been omitted from this listing.

```

class mcSwarm
{
public:
    /** Constructor of a swarm of species s. */
    mcSwarm(const mdSpeciesBase& s, const std::string& type);
    /** Adds a particle to the container, having a position pos, a velocity
     * vel and a statistical weight weight. */
    mcParticle& AddParticle(double t, const mcGeomVector<3>& pos,
        const mcGeomVector<3>& vel, double weight);
    /** Returns a reference to the set of active particles. */
    const std::set<mcParticle*>& activep() const { return m_activep; }
    /** Puts the particle on the shortlist m_justdied of particles that
     * need to be removed from m_activep. Note that this is only done when
     * flush_pools () is called. */
    void DeActivate(mcParticle* part);
    /** Add particles in the list m_newborn to the active particles list
     * m_activep. Remove those that have an entry in m_justdied from
     * m_activep and move them to the m_ppool. */
    void flush_pools ();
    /** Samples a particle from the swarm at location loc*/
    mcParticle& SamplePart(const mcGeomVector<3>& loc);
protected:
    /** Set of active particles. */
    std::set<mcParticle*> m_activep;
    /** List of particles that has just been born and which have to be
     * added to m_activep the next time flush_pools () is called. */
    std::set<mcParticle*> m_newborn;
    /** List of particles that has just been inactivated. */
    std::set<mcParticle*> m_justdied;
    /** The pool of inactive particles. This is used by the member
     * CreateParticle () to efficiently obtain new or previously
     * inactivated particles. */
    std::set<mcParticle*> m_ppool;
    /** The species of the particles in this swarm. */
    const mdSpecies& m_spec;
    /** The swarm type. */
    const std::string m_type;
    /** This member adds a particle to the particle container m_activep. If
     * the particle pool is not empty, the particle is fetched from there,
     * otherwise a new particle is returned and a number of particles is
     * added to the pool for later usage. */
    mcParticle* CreateParticle ();
};

```



Since generally many processes are applicable to a species, it is necessary to have a way of defining which species participate in a process and what the produced species are. All this information is contained in the reaction equation and as such this concept has its counterpart in the code in the form of a class *mcReactionFormat*. The constructor of this class parses a reaction equation that the user has given as input. It checks for charge conservation and makes sure that all the species are actually known to the code.

Together, *mcReactionFormat*, *mcScattering* and *mcCrossSec* are thus the major components of the *mcProcess12* class. This class has furthermore a member function *Apply()* that takes a simulation particle as an argument and evaluates a collision for it. This function thus samples a target particle out of an appropriate swarm, calls the *Apply()* member of the *mcScattering* object to calculate the new velocities of the particles and, in case particles are destructed or constructed in the collision, calls the *DeActivate()* or *AddParticle()* members of the relevant swarms.

To contain the various processes that are treated by the model in one object, the class *mcProcessContainer* is defined. This class contains the functionality to calculate the total cross section and collision frequency for a particle, and can evaluate equation (2.23) for the particle. As such it contains, for example, a member function *DoCollision()*, which selects a collision type and calls the *Apply()* function of the *mcProcess* object in question.

The *mcProcess* class contains data objects that store the cross section and frequency data in a form that is suitable to find their values quickly for a given energy and target species density. The concept of energy ranges, as illustrated in figure 2.6 on page 32 is for example implemented by arranging the cross section and frequency containers appropriately.

Polymorphism

There are various types of processes and scattering models. One would like the user to be able to combine the various process types with available scattering models as he/she wishes, by specifying this in the input-file of the program. To allow for this flexibility, the concepts of *polymorphism* and *abstract factory design* are used. These concepts are well explained in [18, chapter 3], here we will give only a general description.

It was mentioned before that classes can be derived from each other, allowing for general functionality in a base class and more specific functionality in the various derived classes. In fact it is possible to define *virtual* functions in an *abstract base class* but refrain from implementing them there. These functions are instead implemented in a *derived class*. The base class is called abstract, since a derived class is actually required for the implementation of the virtual function. For example, the *DoApply()* function in the *mcScattering* class is such a virtual function. Classes that are derived from this class are for example *mcIsotropicScattering* and *mcSurendraScattering*. These respectively implement the equations (2.32) and (2.37) in their own *DoApply()* implementations.

The important benefit of designing code this way is that one can make use of the polymorphism capabilities of C++: it is possible to construct an object of the derived class, but refer to it with a pointer to the base class. Code can then call the virtual function of the base class, without having to know which derived class implements this function. As such,

Listing 2.3: Example of an input-file section that defines a process. Note that the structure of the input resembles the way the code is organised.

```

Process {
  Type          12_14
  Name          "e-Ar ground_to_4s collision"
  Relation       "Ar + e -> Ar* + e"
  DeltaEnergy   -11.6*eV
  CrossSection {
    Type          LookupTable
    eps0          11.6*eV
    XMultiplicator 1*eV
    YMultiplicator 1*m^2
    LuTable       "crossec/argon/ground_to_4s.lut"
  }
  Scattering   {
    Type          Surendra
  }
}

```

the code that uses a scattering model needs to know only about the base class interface. The decision of which class implements the virtual functions of the *mcScattering* base class can follow from information in an input-file that is read before an *mcScattering* object is constructed. By using polymorphism, one can extend the code by creating new scattering implementations, without having to modify the code that uses these implementations.

To make the flexibility even more complete: by using abstract factory functions and self-registering objects [18, chapter 3], it is possible to write classes that implement the virtual functions and compile them separately from the core code. The library thus created is as plug-in to the core code.

With these techniques, the process code has been set up in such a way that the type of the process, the scattering model and the cross section are implemented as plug-ins. At the moment of writing this thesis, the following implementations exist: for the process type these are the process types listed on page 22, for the scattering model these are the ones treated in section 2.2.5, and for the cross sections these are implementations that either parse a function, read a lookup table from file or implement a constant cross section. An input-file section that defines a process thus looks like given in listing 2.3. Note that the keyword *Type* is used to determine which plug-in will be used. In this example, *12_14* is the designation used for an inelastic process.

2.3.6 Environment

The collection of classes that has been described up till now contains almost everything that is necessary for an MC simulation: particles have been described, as well as the way in which they are organised in objects of the type *mcSwarm*. Furthermore the complete description of binary processes is captured in the *mcProcessContainer* and its members.

Apart from the control over the simulation, which will be described in the section on the *mcFlightControl* class below, only a definition of the discharge vessel, the electric field and background gases needs to be given.

It is the purpose of the code to be generic enough to be used as a component of various models. As such, especially these quantities that define the ‘environment’ in which the simulation particles move are not known and only some general statements can be made about them. As has become clear in the preceding text, this lack of information can be dealt with in the form of abstract base classes with virtual members that are only implemented in derived classes.

The present MC base code therefore contains a class *mcEnvironment* with mostly virtual member declarations. These members, which must be implemented in a derived class, provide all the information that is necessary to describe the path and collisions of the simulation particles completely: *InsideVessel()* is a function that returns a boolean value for a given position to indicate whether this position is inside the discharge region. *Efield()* gives back the electric field vector at a given position. *AddDensitySwarms()* is a function that adds one object of the type *mcDensitySwarm* for each background species to the *mcSwarmList*. Finally, the two virtual members *InjectFirstParticles()* and *InjectParticles()* are functions that are called at the beginning of a simulation and at each time-step respectively. As their names suggest, they can inject simulation particles into a swarm of interest and can thereby account for particle sources that are not self-consistently treated in the MC code.

2.3.7 Statistics

Similar to the environment of simulation particles in the MC simulation, also the data that need to be obtained from the simulation is something that is dictated by the client of the MC code.

To accomplish this, the following virtual members are defined in the *mcStatistics* class: *AtCollision()*, as the name suggests, is at each collision event and thereby receives information on which process occurred and what the present state of the simulation particle is. *AtMove()* is called each time the particle’s path is integrated over a certain time interval. Furthermore, *DoUpdate()* is called at each time-step and can collect information on a more global level.

Via these functions, the client code has significant access to the information conveyed in the MC simulation, without the core MC code having to know what the client code is interested in.

2.3.8 FlightControl

The code that binds together all the components that have been described in the above text is contained in the class *mcFlightControl*. Less initialisation and conclusion of a calculation, the algorithm that needs to be implemented can be considered a nested loop over subsequent time-steps, over all swarms containing simulation particles, and finally over

each simulation particle in those swarms. In the most inner loop each particle has its path advanced and if necessary, a collision is evaluated for it.

In section 2.2.3 it was already described how alternating between various particles when stepping through time can be implemented. The three methods mentioned there have been implemented in the present code. In the following we will treat control over the number of simulation particles. Then the definition of the *mcFlightControl* class is treated and the implementation of a few important member functions are given to complete this overview of the MC code.

Control over particle numbers

In order to keep the workload limited, it is necessary to have some method of control over the number of simulation particles. This is accomplished by a user-defined maximum number of simulation particles per swarm. If this number is exceeded, the swarm is resized by a factor $\xi \in (0, 1]$: for each simulation particle a random number r is drawn. If $r > \xi$, the particle is deactivated. Otherwise, its weight is multiplied by $1/\xi$.

This method can be refined by applying it only to those particles that impose a burden on the computational workload without having a large influence on the output. One can, for example, only consider those particles with a kinetic energy that is lower than a certain value [25, 26, 27].

Implementation

An object of the *mcFlightControl* class will be a member of client code that wants to use an MC simulation in its calculations. As such, the interface of the *mcFlightControl* class needs to provide the functionality that is necessary to run the simulation.

This functionality starts with the construction of an *mcFlightControl* object by calling the constructor:

```
mcFlightControl(const plNode& node,  
                mcEnvironment& _environment,  
                mcStatistics & _stat);
```

which receives a data object of the type *plNode* that contains the data that is provided by the user in an input file. Furthermore, it receives references to objects of the *mcEnvironment* and *mcStatistics* classes. As mentioned earlier, these are seen by the *mcFlightControl* class as abstract base classes, whereas the client code provides its own implementation of the virtual functions in derived classes that are not visible to *mcFlightControl*. The constructor uses the information provided via its arguments to set up the structure that is depicted in figure 2.10 on page 42. This involves the creation and initialisation of the specific set of objects that is required for the simulation. This structure is mainly defined by the input file that is provided by the user: see for example the section of input in listing 2.3 on page 46.

After construction, the client code can call the various *mcFlightControl* member functions to control and execute the MC simulation. For uniformity with other models, the interface

of the *mcFlightControl* class has been set up to comply with the functionality that time-dependent models in the Plasimo framework generally offer. This is best illustrated by listing the manner in which such a time-dependent model is run:⁴

```

void Run()
{
    Prepare();
    while ( CanGo() && !Finished() ) {
        Proceed();
        if (OutputNeedsUpdate())
            UpdateOutput();
    }
    EndReport();
}

```

The function *Prepare()* sets the time and time-step and calls the *InjectFirstParticles()* function of the environment object. The function *CanGo()* always returns true and *Finished()* checks whether the time exceeds the predetermined total simulation time.

The actual work is done in the function *Proceed()*. In condensed form, it is listed in listing 2.4. One can see that during each time-step new particles can be injected by the environment. Subsequently, for each swarm containing simulation particles, one of the move functions is called. Which move function is used was determined during construction of the *mcFlightControl* object. If the move mode is asynchronous (see the bottom panel of figure 2.4 on page 28), the individual times of the particles need to be synchronised in case the statistics class wants to extract information. At the end of a time-step, the *mcEnvironment* member *RemoveParticles()* is called. In chapter 3 it will become clear why it is necessary for the environment to have the possibility to remove simulation particles.

In order to complete the picture of this main loop, the implementation of the function *MoveAsynchronous()* is also given in listing 2.4. Note that, contrary to *Proceed()*, this is a private function, i.e. it is not exposed to the interface of the class, as there is no need for the client code to directly access it.

In this function we see a loop over all particles in the swarm that this function receives in its argument list. A check is done if the global time *m_t* exceeds the collision time of the particle, accessed via the accessor function *Tc()* provided by the *mcParticle* class. Only if this is true, the inner code of the function is executed. In that case, the particle is moved over small time-steps of at most *m_dtmax* until the time of collision is reached. The *Move()* function returns a boolean that tells if the particle is still inside the discharge region. If that is not the case, the particle is deactivated. Coming out of the **while**-loop, it is thus possible that the particle does not exist anymore. If the particle does exist, a collision is evaluated for it, and if it still exists after this collision, a new collision time is set for it.

This concludes the treatment of the implementation of the Monte Carlo code. In chapter 3 this code will be used in conjunction with a fluid code to improve its description of the electron behaviour in discharges.

⁴This patch of code is taken from Plasimo's *plModelBase* class.

Listing 2.4: Condensed form of the *Proceed()* and *Move_Asynchronous()* functions.

```
void mcFlightControl::Proceed()
{
    // Ask the environment to inject particles :
    m_env.InjectParticles(m_t, m_dt, (*m_swl));
    // Now have all particle swarms fly:
    for (mcSwarmList::PSwarms::const_iterator
         i=m_swl->PartSwarms().begin(); i!=m_swl->PartSwarms().end(); ++i)
    {
        switch (m_movemode)
        {
            case synchronous: Move_Synchronous(**i); break;
            case asynchronous: Move_Asynchronous(**i); break;
            case nonull: Move_NoNull(**i); break;
        }
        (*i)->flush_pools(); // particles may have been created or destroyed.
    }
    // Let the statistics class extract information.
    if (m_stat.NeedUpdate())
    {
        if (m_movemode == asynchronous) Synchronise();
        m_stat.Update();
    }
    // Allow environment to remove redundant particles.
    m_env.RemoveParticles(m_t, (*m_swl), m_prc->FirstEps0());
    // Increase global time.
    m_t += m_dt;
}

void mcFlightControl::Move_Asynchronous(mcParticleSwarm& swarm)
{
    const mcSwarm::PartSet::const_iterator end=swarm.activep().end();
    for (mcSwarm::PartSet::const_iterator j=swarm.activep().begin(); j!=end; ++j)
    {
        mcParticle& p = **j;
        // If the time at which the particle is scheduled to collide is smaller
        // than the simulation time, a collision is to be evaluated.
        if (p.Tc()<m_t)
        {
            // Move particle to the next collision moment.
            while (p.Tc()>p.Time())
            {
                const double dtmove = std::min(m_dtmax,(p.Tc()-p.Time()));
                if (!m_env.Move(dtmove,p)) p.DeActivate();
                m_stat.AtMove(dtmove,p);
            }
            // Evaluate collision .
            if (p.Exist()) m_prc->DoCollision(p,(*m_swl),m_stat);
            // Set new time for collision .
            if (p.Exist()) p.Tc() -= log(1.0-rnd())/m_prc->Range(p.E()).MaxFreq();
        }
    }
}
```

Acknowledgments

The author would like to thank Mark Kushner for the valuable explanations he gave on Monte Carlo methods in Urbana-Champaign (Illinois, US), May 2002. Furthermore, the author would like to acknowledge C++ poet Jan van Dijk for contributing immensely to the present structure of the Monte Carlo code.

References

- [1] G. J. M. Hagelaar, J. Bareilles, L. Garrigues, and J. P. Boeuf. Two-dimensional model of a stationary plasma thruster. *J. Appl. Phys.*, 91(9):5592–5598, 2002.
- [2] D. E. Knuth. *The Art of Computer Programming*, volume 2. Addison-Wesley, 1983.
- [3] S. K. Zaremba. *Studies in Applied Mathematics 3*, chapter The Mathematical Basis of Monte Carlo and Quasi Monte Carlo Methods. Society for Industrial and Applied Mathematics, 1969.
- [4] P. T. Matthews. *Introduction to Quantum Mechanics*. McGraw-Hill, second edition, 1968.
- [5] Z. Donkó. Hybrid model of a rectangular hollow cathode discharge. *Phys. Rev. E*, 57(6):7126–7137, 1998.
- [6] C. K. Birdsall and A. B. Langdon. *Plasma Physics via Computer Simulation*. Adam Hilger, 1991.
- [7] H. R. Skullerud. The stochastic computer simulation of ion motion in a gas subjected to a constant electric field. *Brit. J. Appl. Phys. (J. Phys. D.)*, 1(11):1567–1568, 1968.
- [8] M. J. Kushner. Private communication, Urbana-Champaign, Illinois, US, May 2002.
- [9] J. L. Delcroix. *Plasma Physics*, volume 1. John Wiley & Sons Ltd., 1965.
- [10] N. F. Mott and H. S. W. Massey. *The Theory of Atomic Collisions*. Oxford University Press, 3rd edition, 1965.
- [11] M. Surendra, D. B. Graves, and G. M. Jellum. Self-consistent model of a direct-current glow discharge: Treatment of fast electrons. *Phys. Rev. A*, 41(2):1112–1125, 1990.
- [12] V. Vahedi and M. Surendra. A Monte Carlo collision model for the particle-in-cell method: applications to argon and oxygen discharges. *Comp. Phys. Comm.*, 87(1-2):179–198, 1995.
- [13] A. Okhrimovskyy, A. Bogaerts, and R. Gijbels. Electron anisotropic scattering in gases: A formula for Monte Carlo simulations. *Phys. Rev. E*, 65:037402, 2002.
- [14] R. Kinder and M. J. Kushner. Non-collisional heating and electron energy distributions in magnetically enhanced inductively coupled and helicon plasma sources. *J. Appl. Phys.*, 90(8):3699–3712, 2001.
- [15] C. B. Opal, W. K. Peterson, and E. C. Beaty. Measurement of secondary-electron spectra produced by electron impact ionization of a number of simple gases. *The Journal of Chemical Physics*, 55(8):4100–4106, 1971.
- [16] J. P. Boeuf and E. Marode. A Monte Carlo analysis of an electron swarm in a non-uniform field: the cathode region of a glow discharge. *J. Phys. D: Appl. Phys.*, 15:2169–2187, 1982.

- [17] B. Stroustrup. *The C++ Programming Language*. Addison-Wesley, 3rd edition, 1997.
- [18] J. van Dijk. *Modelling of Plasma Light Sources: an object-oriented approach*. PhD thesis, Eindhoven University of Technology, The Netherlands, 2001.
- [19] B. Hartgers. *Modelling of a Fluorescent Lamp Plasma*. PhD thesis, Eindhoven University of Technology, The Netherlands, 2003.
- [20] E. Gamma, R. Helm, R. Johnson, and J. Vlissides. *Design Patterns: elements of reusable object-oriented software*. Addison-Wesley Publishing Company, 1995.
- [21] M. Matsumoto and T. Nishimura. Mersenne twister: A 623-dimensionally equidistributed uniform pseudorandom number generator. *ACM Trans. on Modeling and Computer Simulation*, 8(1):3–30, 1988.
- [22] Mersenne Twister homepage. <http://www.math.sci.hiroshima-u.ac.jp/~m-mat/MT/emt.html>, validity of url last checked on August 4th 2005.
- [23] M. Matsumoto and T. Nishimura. A nonempirical test on the weight of pseudorandom number generators. In K. T. Fang, F. J. Hickernel, and H. Niederreiter, editors, *Monte Carlo and Quasi-Monte Carlo methods*. Springer-Verlag, 2000.
- [24] M. Matsumoto and T. Nishimura. Sum-discrepancy test on pseudorandom number generators. *Mathematics and Computers in Simulation*, 62:431–442, 2003.
- [25] Annemie Bogaerts, Renaat Gijbels, and Wim Goedheer. Hybrid modeling of a capacitively coupled radio frequency glow discharge in argon: Combined Monte Carlo and fluid model. *Jpn. J. Appl. Phys.*, 38:4404–4415, 1999.
- [26] Annemie Bogaerts, Renaat Gijbels, and Wim Goedheer. Improved hybrid Monte Carlo-fluid model for the electrical characteristics in an analytical radio-frequency glow discharge in argon. *J. Anal. At. Spectrom.*, 16(7):750–755, 2001.
- [27] M. J. Kushner. Private communication, Ames, Iowa, US, February 2005.

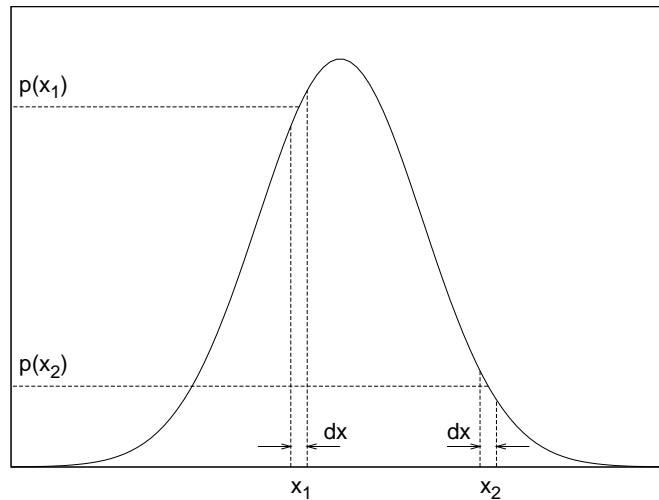


Figure 2.11: An example of a probability distribution $p(x)$.

2.A Probability calculus

2.A.1 Probability distribution

A probability distribution $p(x)dx$ (see figure 2.11) defines the likelihood of observing x in the infinitesimal interval dx . $p(x)$ must have the following properties:

$$p(x) \geq 0 \tag{2.57}$$

and:

$$\int_0^{\infty} p(x)dx = 1 \tag{2.58}$$

in which $[0, \infty)$ is the range on which $p(x)$ is defined. Note that this could be any other interval $[a, b]$, in which case the integration of equation (2.58) should range from a to b .

2.A.2 Cumulative distribution

The cumulative distribution $c(x)$ of the probability distribution $p(x)$ is defined as follows (see the right hand side of figure 2.12 on page 55) is defined as follows:

$$c(x) = \int_0^x p(x)dx \tag{2.59}$$

Note that $p(x) = \frac{d}{dx}c(x)$ and that $c(0) = 0$ and $c(\infty) = 1$. Furthermore, $c(x)$ is an monotonically increasing function of x .

2.A.3 Sampling of $p(x)$ with random numbers

In Monte Carlo methods random numbers have to be generated according to certain distributions representing the physics of the process under consideration. These distributions are generally different from the uniform distribution on $[0, 1)$ or $[0, 1]$ which is spawned by a regular pseudo-random number generator. The uniform distribution of the random number generator should somehow be transformed to the required distribution. Based on how well-behaved the distribution function is, one can choose different ways to do this.

Inversion of $c(x)$

With the definition of $c(x)$ we have created a mapping of $p(x)$ to the interval $[0, 1)$. The inverse mapping can be used to sample the distribution $p(x)$ with a random number r which is taken from a uniform distribution on the interval $[0, 1)$:

$$r = c(x) \tag{2.60}$$

and thus:

$$x = c^{-1}(r) \tag{2.61}$$

By using equation (2.61) to generate values of x out of random numbers r , one creates a set that is distributed according to the distribution function $p(x)$. This can be seen from figure 2.12 and by looking at two equally spaced intervals dx_1 and dx_2 : if many random numbers are selected from a uniform distribution on $[0, 1)$, the number of them that fall in the interval dr_1 divided by the number in dr_2 equals the ratio of the probability distribution at x_1 and x_2 :

$$\frac{dr_1}{dr_2} = \frac{\frac{d}{dx}c(x)|_{x=x_1}}{\frac{d}{dx}c(x)|_{x=x_2}} = \frac{p(x_1)}{p(x_2)} \tag{2.62}$$

This method is the most favourable method to employ if an analytic expression can be found for c^{-1} . If this is not the case one can fall back to the following, numerically more expensive, method.

Rejection method

If $c(x)$ is not easily invertible, one has to use other methods to generate the probability distribution function $p(x)$ from random numbers. One of these methods is known under the name ‘rejection method’.

The idea is the following: one uses a random number r_1 to choose an x out of the range $[a, b]$ on which x is defined:

$$x = a + (b - a)r_1 \tag{2.63}$$

For this x one calculates $p(x)/p_{max}$. Here, p_{max} is the largest value of $p(x)$ on the interval $[a, b]$. If this maximum is not known one may overestimate it. However, this will result in

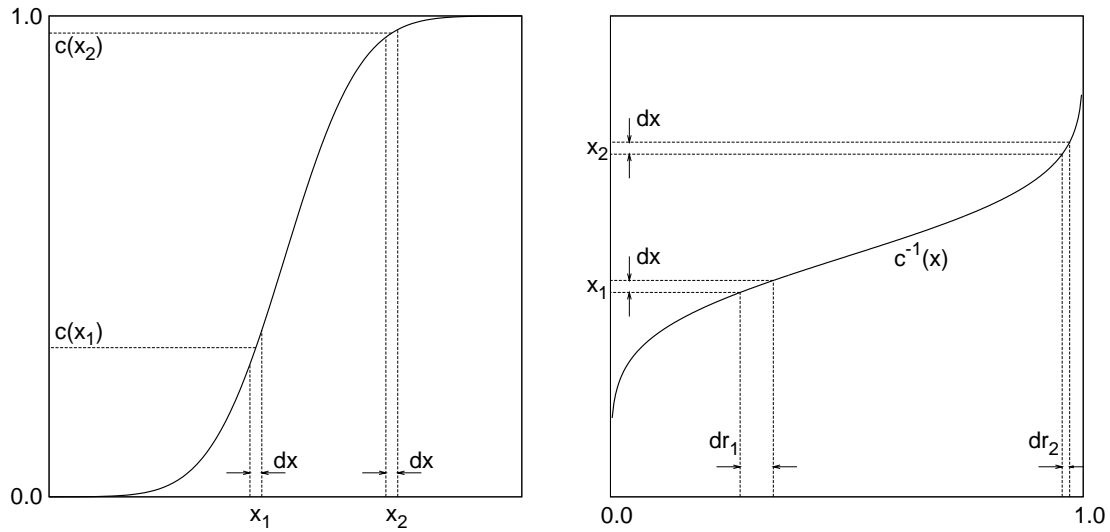


Figure 2.12: An example of the cumulative probability distribution $c(x)$ of the probability distribution function $p(x)$ of figure 2.11 and the inverse $c^{-1}(x)$.

an increase in computation costs. Subsequently it is decided whether x will be accepted or not by means of a new random number r_2 :

$$\begin{cases} r_2 < \frac{p(x)}{p_{max}} & \text{accept } x \\ r_2 \geq \frac{p(x)}{p_{max}} & \text{reject } x \end{cases} \quad (2.64)$$

if x is rejected the same procedure is applied again until an x is accepted.

In a graphical representation this method can be envisioned as choosing a point with coordinates $(a + (b - a)r_1, p_{max}r_2)$ in the graph of x versus $p(x)$ and testing whether this point lies above or under the probability distribution $p(x)$. The efficiency of this method can be defined as the number of combination of r_1 and r_2 that is accepted, divided by the total number of random numbers. This is the area under the curve of $p(x)$ divided by the total area in the graph under p_{max} :

$$\frac{1}{b - a} \int_a^b \frac{p(x)}{p_{max}} dx \quad (2.65)$$

2.B Centre of mass frame

Consider two particles with masses m_1 and m_2 , and with velocities \mathbf{u}_1 and \mathbf{u}_2 in a fixed frame of reference, which we will call the laboratory frame. The total mass, momentum

and kinetic energy are given by:

$$M = m_1 + m_2 \quad (2.66)$$

$$\mathbf{p} = m_1 \mathbf{u}_1 + m_2 \mathbf{u}_2 \quad (2.67)$$

$$\varepsilon = \frac{1}{2} m_1 u_1^2 + \frac{1}{2} m_2 u_2^2 \quad (2.68)$$

For such particle pairs, the centre of mass velocity \mathbf{u}_M is defined as:

$$\mathbf{u}_M = \frac{\mathbf{p}}{M} = \frac{m_1 \mathbf{u}_1 + m_2 \mathbf{u}_2}{m_1 + m_2} \quad (2.69)$$

Furthermore we denote the *relative* velocity of the species pair as \mathbf{u}_r :

$$\mathbf{u}_r = \mathbf{u}_1 - \mathbf{u}_2 \quad (2.70)$$

This set of equations can be inverted to obtain expressions for the velocities \mathbf{u}_1 and \mathbf{u}_2 in terms of the centre of mass and relative velocities:

$$\mathbf{u}_1 = \mathbf{u}_M + \frac{m_2}{m_1 + m_2} \mathbf{u}_r \quad (2.71)$$

$$\mathbf{u}_2 = \mathbf{u}_M - \frac{m_1}{m_1 + m_2} \mathbf{u}_r$$

By substitution of these expressions into equation (2.68) it follows that the total kinetic energy can be expressed as:

$$\varepsilon = \frac{1}{2} M u_M^2 + \frac{1}{2} m_r u_r^2 \quad (2.72)$$

where the reduced mass has been defined as:

$$m_r = \frac{m_1 m_2}{m_1 + m_2} \quad (2.73)$$

The centre of mass frame of reference is obtained by attaching a frame to the centre of mass. Let's denote velocities relative to this frame with the symbol \mathbf{v} (instead of the \mathbf{u} used for the laboratory frame). By definition the centre of mass velocity in this frame is zero: $\mathbf{v}_M = 0$. The velocities of the two particles are given by:

$$\mathbf{v}_1 = + \frac{m_2}{m_1 + m_2} \mathbf{u}_r \quad (2.74)$$

$$\mathbf{v}_2 = - \frac{m_1}{m_1 + m_2} \mathbf{u}_r \quad (2.75)$$

As one can see, the particles always move in opposite directions in the centre of mass frame. Also note that the relative velocity does not depend on the frame of reference: $\mathbf{u}_r = \mathbf{v}_r$. Within the centre of mass frame the total momentum of the particles is zero:

$$\mathbf{p}_M = m_1 \mathbf{v}_1 + m_2 \mathbf{v}_2 = 0 \quad (2.76)$$

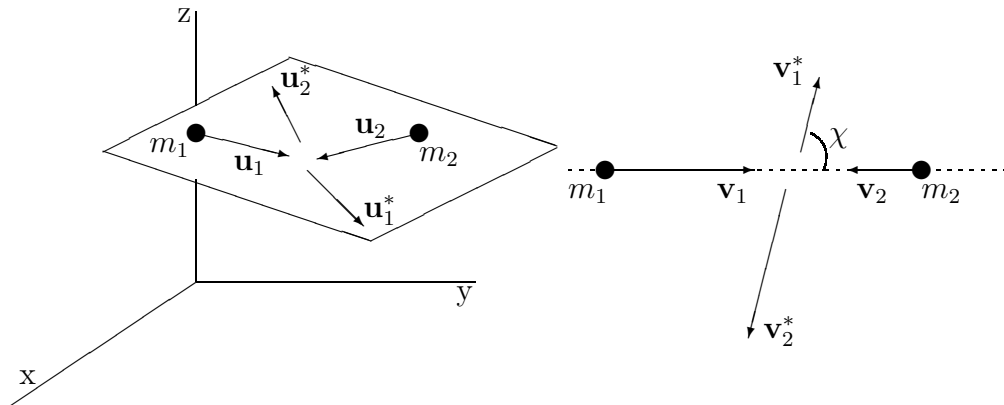


Figure 2.13: *On the left:* a schematic illustration of a collision in the laboratory frame of reference. The particles move in a plain throughout the collision process. *On the right:* the collision process in the centre of mass frame of reference, with the angle χ over which the particles scatter.

If we assume that the two particles form an isolated system, conservation of momentum says that \mathbf{p} must be constant. Furthermore, if the force between the two particles is a central force, it can be proven [9] that the particles will move in a fixed plain within the laboratory frame (refer to figure 2.13 for an illustration): the velocities before a collision \mathbf{v}_1 and \mathbf{v}_2 , as well as the velocities \mathbf{v}_1^* and \mathbf{v}_2^* after the collision — for the occasion decorated with an asterix — lie in a plane. In this two dimensional space a collision can only change the magnitude and direction of the relative velocity \mathbf{v}_r . The change in direction of the relative velocity, measured in the centre of mass frame, is denoted with the angle χ .

2.C Scattering matrix

Imagine a frame of reference in which the initial relative velocity \mathbf{u}_r lies along the z-axis and the final relative velocity \mathbf{u}_r^* has been turned over the angles χ and ψ . Mark this centre of mass frame with the symbol ζ . Furthermore, mark the laboratory frame with the symbol η (see figure 2.14 to aid in creating a mental picture). Note that the plane spanned by \mathbf{u}_r and \mathbf{u}_r^* in frame ζ is in fact the collision plane (see also figure 2.13a).

In order to relate the change in velocity (which is known in frame ζ) to the change of the velocity in the laboratory frame η , some linear algebra can be used: the components of the initial velocity in frame ζ need to be calculated from those in frame η . Subsequently the vector can be rotated within the frame ζ to obtain the new velocity. The components of this new velocity then need to be calculated for frame η from the components which are known now in frame ζ .

The tool needed for these calculations is transformation matrices. Since the origins of the two frames of reference coincide, these matrices are special cases: rotation matrices.

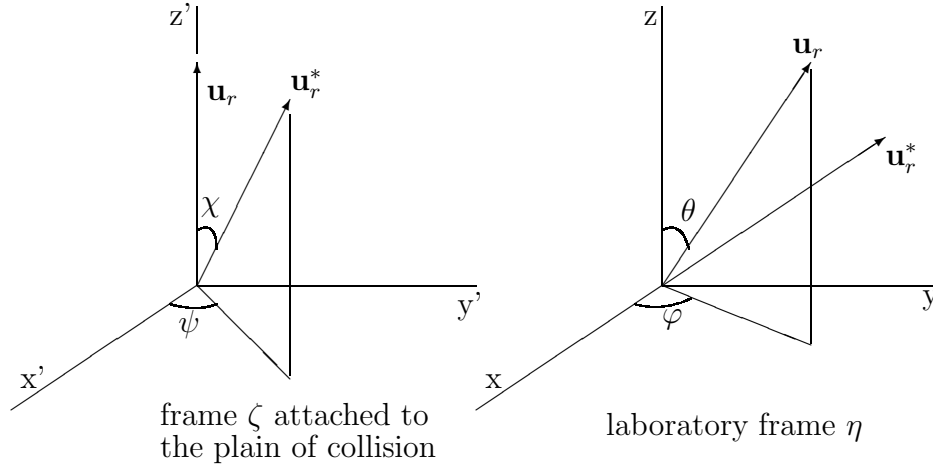


Figure 2.14: The frames of reference that are important in the treatment of collisional dynamics. The initial and final velocities \mathbf{u}_r and \mathbf{u}_r^* are shown. The angles θ and φ give the position of \mathbf{u}_r in the laboratory frame and the angles χ and ψ the position of \mathbf{u}_r^* in a frame, where \mathbf{u}_r lies along the z -axis.

The process of transforming frame η to frame ζ can be considered to consist of two rotations: one around the z -axis over an angle φ (refer to figure 2.14) and a subsequent one around the new y -axis over an angle θ . Doing those two rotations results in a new frame of reference in which the velocity vector is aligned with the z -axis: frame ζ :

$$\mathbf{u}_\zeta = {}_\zeta\mathcal{A}_\eta \mathbf{u}_\eta \quad (2.77)$$

in which \mathbf{u}_η indicates that the component of \mathbf{u}_r are expressed relative to frame η (and similar for \mathbf{u}_ζ in frame ζ). ${}_\zeta\mathcal{A}_\eta$ is the rotation matrix from frame η to frame ζ . Given the previous remark that the rotation can be thought to be composed of two subsequent rotations, ${}_\zeta\mathcal{A}_\eta$ is:

$${}_\zeta\mathcal{A}_\eta = \begin{pmatrix} \cos \theta & 0 & -\sin \theta \\ 0 & 1 & 0 \\ \sin \theta & 0 & \cos \theta \end{pmatrix} \begin{pmatrix} \cos \varphi & \sin \varphi & 0 \\ -\sin \varphi & \cos \varphi & 0 \\ 0 & 0 & 1 \end{pmatrix}$$

and thus:

$${}_\zeta\mathcal{A}_\eta = \begin{pmatrix} \cos \theta \cos \varphi & \cos \theta \sin \varphi & -\sin \varphi \\ -\sin \varphi & \cos \varphi & 0 \\ \sin \theta \cos \varphi & \sin \theta \sin \varphi & \cos \theta \end{pmatrix} \quad (2.78)$$

After this transformation, the vector needs to be rotated over the angles χ and ψ that have been obtained by working out the details of the collisional process. Since the matrix only needs to work on the z -component of the velocity, this is simply done with the following matrix:

$$\mathcal{R}_\zeta = \begin{pmatrix} 0 & 0 & \sin \chi \cos \psi \\ 0 & 0 & \sin \chi \sin \psi \\ 0 & 0 & \cos \chi \end{pmatrix} \quad (2.79)$$

The transformation back ${}_{\eta}\mathcal{A}_{\zeta}$ is the inverse of ${}_{\zeta}\mathcal{A}_{\eta}$:

$${}_{\zeta}\mathcal{A}_{\eta}^{-1} = \begin{pmatrix} \cos \theta \cos \varphi & -\sin \varphi & \sin \theta \cos \varphi \\ \cos \theta \sin \varphi & \cos \varphi & \sin \theta \sin \varphi \\ -\sin \theta & 0 & \cos \theta \end{pmatrix} \quad (2.80)$$

The total operation is now described by:

$$\mathbf{u}_r^* = {}_{\eta}\mathcal{A}_{\zeta}^{-1} \mathcal{R}_{\zeta} {}_{\zeta}\mathcal{A}_{\eta} \mathbf{u}_r \quad (2.81)$$

Or written fully:⁵

$$\mathbf{u}_r^* = \mathbf{u}_{\eta}^* = u_r \begin{pmatrix} \cos \theta \cos \varphi \sin \chi \cos \psi - \sin \varphi \sin \chi \sin \psi + \sin \theta \cos \varphi \cos \chi \\ \cos \theta \sin \varphi \sin \chi \cos \psi + \cos \varphi \sin \chi \sin \psi + \sin \theta \sin \varphi \cos \chi \\ \cos \theta \cos \chi - \sin \theta \sin \chi \cos \psi \end{pmatrix} \quad (2.82)$$

with u_r the magnitude of the vector \mathbf{u}_r .

⁵Note that in equation (2.82) the absolute value u_r of the velocity \mathbf{u}_r has been taken out of the several rotation operations. This is valid since ${}_{\zeta}\mathcal{A}_{\eta}$ is a unary matrix.

3

Coupling a fluid and a Monte Carlo code

Abstract. The Monte Carlo code described in chapter [2](#) has been coupled to the fluid code md2d to improve the description of non-local electron behaviour via the reaction rates in this fluid model. The resulting hybrid code is capable of modelling transient phenomena like breakdown of gas discharges. The first part of this chapter deals with the analysis of the ways in which a Monte Carlo treatment of electrons can improve a fluid model. The second part of the chapter describes the details of the coupling between the two existing codes.

3.1 Introduction

The Monte Carlo (MC) model described in chapter 2 contains all the details that are needed to describe discharges in which only the electron properties evolve and where the electric field and densities of different species can be considered to be known. This stand-alone usage of the MC method is useful for investigation of the electron kinetics and to validate the essential aspects of fluid models (see for example [1, 2, 3, 4]). However, it cannot be expected to give a self-consistent model of a discharge. For that one needs to add descriptions of the behaviour of other species and for the electric field.

There are several ways to use the powerful MC method in conjunction with other model components to form a self-consistent model. In the following we briefly mention the Particle-In-Cell (PIC) model [5, 6], and then continue by developing a hybrid fluid – Monte Carlo model.

In a PIC model (see figure 3.1), all species with evolving densities are described using the MC method. The space charge density is directly calculated from the densities of charged simulation particles. A method to project them on a computational grid is used to obtain the densities. These are then used to calculate the electric field with the Poisson equation. As a result one obtains the electric force on the individual simulation particles self-consistently.

PIC models are very attractive, because, by describing the species kinetically, they incorporate few assumptions. However, they are computationally demanding: for example, if statistics is poor, the fluctuations in the space charge density will cause a considerable noise in the electric field. Since the energy of particles depends on the square of the electric field, the artificial field fluctuations will lead to heating. In order to reduce this so-called numerical heating, one needs to have a sufficient number of simulation particles per grid cell. Furthermore, for the simulation to be stable, the grid cell size must be smaller than the Debye length and the time-step must be less than the inverse plasma frequency [5].

When the discharge conditions allow the description of most species with a fluid model, it becomes interesting to construct a so-called hybrid model, in which the MC method is coupled to a fluid model. In the following we will investigate the various manners in which this can be accomplished. Subsequently we will continue to develop our own hybrid code, in which aspects of the electron behaviour are described by means of the MC method.

3.2 Coupling Monte Carlo and fluid models

Although a brief introduction into fluid codes was already given in section 1.2.3, we will consider the equations of the fluid model here once more. The entire model is described in section 5.2 and in reference [7]. Subsequently, we will consider the ways of coupling the fluid code with the MC model. Since similar equations were used by the various authors that have worked on hybrid codes [8, 9, 10, 11, 12, 13, 14, 15, 16, 17, 18, 19, 20, 21, 22, 23, 24, 25, 26, 27, 28, 29, 30, 31], we will discuss some of the approaches described in literature.

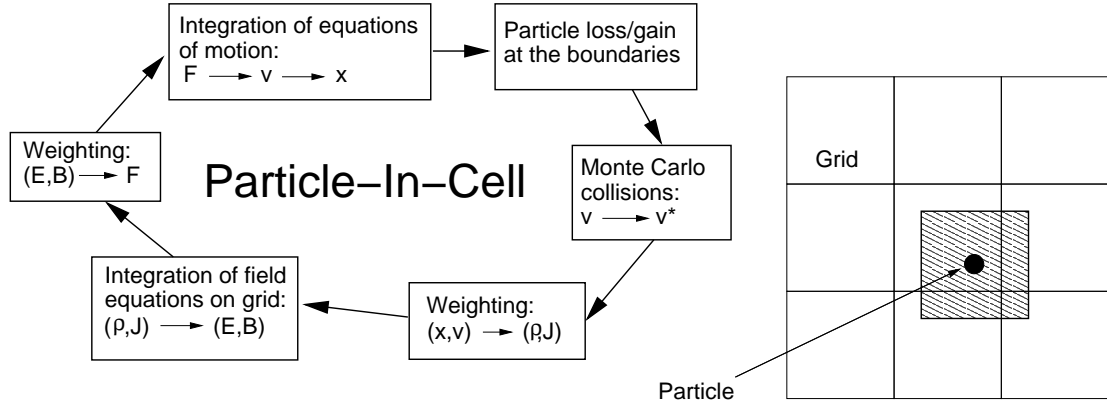


Figure 3.1: The Particle-In-Cell scheme [6]. The paths of individual simulation particles are calculated by integrating their equations of motion and using the MC method to describe collisions. At each time-step the densities and fluxes of charged particles are projected on a grid and the electric and magnetic field are calculated from these grid data. The fields are used to determine the force on the individual particles in the next time-step. In the right hand part of the figure a method is illustrated in which a particle is smeared out and contributes to the density in four grid cells.

3.2.1 Basic fluid model

We recall (see section 1.2.3) that the general structure of a fluid model consists of a set of balance equations that describes the conservation of particles, momentum and energy, in combination with the Poisson equation to self-consistently describe the electric field.

In case of the fluid model that we use in the hybrid code, the balance equations are as follows. The particle balance equation of species p is:

$$\frac{\partial n_p}{\partial t} + \nabla \cdot \mathbf{\Gamma}_p = S_p \quad (3.1)$$

in which n_p is the density and $\mathbf{\Gamma}_p$ is the flux density of the species. S_p the source of the species due to the reactions r , such as excitation and ionisation:

$$S_p = \sum_r c_{r,p} R_{r,p} = \sum_r c_{r,p} (k_r \prod_i n_i) \quad (3.2)$$

in which $R_{r,p}$ is the reaction rate and $c_{r,p}$ the stoichiometric number of particles of type p created or lost in the reaction of type r . The reaction rate depends on the product of the densities n_i of the reacting species via the reaction rate coefficient k_r .

The flux $\mathbf{\Gamma}_p$ follows from the drift diffusion equation, which is a condensed form of the momentum balance equation:

$$\mathbf{\Gamma}_p = \pm \mu_p \mathbf{E} n_p - D_p \nabla n_p \quad (3.3)$$

where μ_p represents the mobility and D_p the diffusion coefficient of the species p . The \pm sign in the drift term indicates whether the sign of the charge q_p of the species is positive or negative.

The transport coefficients, μ_p and D_p , and the reaction rates k_r are required in order to solve this set of balance equations. All these parameters generally are functions of the energy of the species under consideration. For the heavy particles the energy is assumed to be a function of the magnitude E/p of the local reduced electric field. The parameters $\mu_p(E/p)$ and $D_p(E/p)$ can be found in literature for many species. For the electrons these data can be obtained from a Boltzmann solver, as treated in section 1.2.2.

This local field approximation (see also section 1.2), in which coefficients are a function of the local electric field only, is often not satisfactory for the electrons. Instead, allowance for transport of electron energy is made by adding a balance equation for the electron energy density $n_e\bar{\varepsilon}$:

$$\frac{\partial(n_e\bar{\varepsilon})}{\partial t} + \nabla \cdot \mathbf{\Gamma}_{\bar{\varepsilon}} = S_{\bar{\varepsilon}} \quad (3.4)$$

in which $\bar{\varepsilon}$ is the average energy of the electrons, $\mathbf{\Gamma}_{\bar{\varepsilon}}$ is the associated flux density, which can be written as a drift-diffusion flux, and $S_{\bar{\varepsilon}}$ includes the energy gained or lost in reactions and by motion in the electric field. With this addition, the various electron-related coefficients in the equations (3.1) and (3.3) can be written as functions of the mean electron energy instead of the reduced electric field.

Addition of the last equation is a large improvement to the descriptive power of a fluid model. Nevertheless, the fact that specific discharge features, such as striations, cannot be reproduced with a fluid model suggests that these models are not capable of describing the non-local electron properties properly.

3.2.2 Input from Monte Carlo

By coupling the MC method for the electrons to the fluid model, assumptions concerning the shape of the electron energy distribution function (eedf) and its relation to local properties and/or the mean electron energy can be circumvented. Ideally, one would like to describe the electrons entirely by means of the MC method, such that it delivers both the electron density and reaction rates. This density can then be used in the Poisson equation and the electron density balance equation is not required anymore. The MC calculations of the reaction rates remove the need for an electron energy equation and lookup tables for the reaction rate coefficients.

This method comes close to a PIC model and indeed requires large numbers of simulation particles to prevent space charge fluctuations from causing artificial heating. Since this leads to a non-practical, computational expensive model, we have to look for alternatives.

The assumptions on the eedf are mainly contained in the transport coefficients and reaction rates. These quantities are, therefore, the next best candidates for input from the MC method. The reaction rates R_r are the most important: non-local behaviour mainly manifests itself by the effect of electrons gaining energy in a different place than where they again deposit it in inelastic reactions.

By not obtaining the electron transport coefficients from the MC model, a mistake is made in the $\nabla \cdot \mathbf{\Gamma}_e$ term in equation (3.1). The source term S_e is correct since the transport of energy is correctly described in the MC model. It will depend on the specific discharge

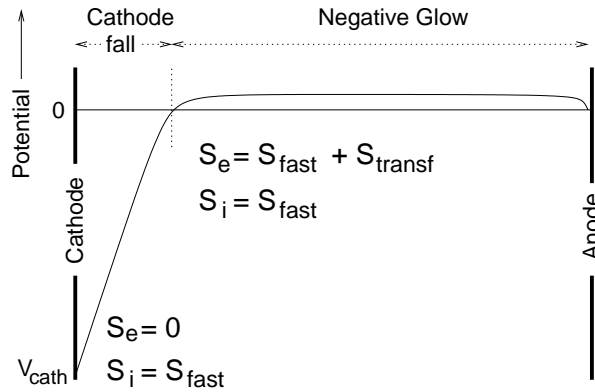


Figure 3.2: Illustration of the manner in which electron sources in the fluid model are treated by Surendra et al. [8]. Refer to the text for more detail.

conditions which term prevails in a certain region and how much the true transport coefficients differ from those obtained in the local field approximation

3.2.3 Hybrid models in literature

The choice of which electrons must be followed in the MC code depends, on the one hand, on the quantities that will be communicated back to the fluid model. On the other hand, the type of discharge under consideration is important, as it might allow for certain assumptions to be made. These assumptions can limit the number of simulation particles that are required drastically. Below we will consider some approaches taken in literature.

Direct current discharges

The early hybrid models described in the references [8, 9] were focused on DC glow discharges. In these discharges the fluid model equations are especially inapt in the cathode fall region where electrons created in secondary emission processes are accelerated across the sheath.

Surendra et al. [8] constructed a one-dimensional model of such a DC glow discharge. They divided the discharge in a cathode fall and negative glow region and treated the electrons differently for these regions. This is illustrated in figure 3.2: a balance equation was solved for the slow electrons, whereas a kinetic model was used for the secondary electrons and their progeny. In the cathode fall (defined by the region in which $V < 0$) these fast electrons gave rise to a source term S_{fast} in the ion balance equation. This term did not appear in the electron balance equation, since the electrons created in the cathode fall were by definition labelled to be fast electrons as well. Once electrons reached the negative glow (defined by $V \geq 0$), they were transferred to the fluid model at the moment that their kinetic energy dropped below the excitation energy of the first excited state of the background gas. In the negative glow the electron source term thus contained a term

S_{fast} due to ionisation by fast electrons and a term S_{transf} due to the electrons that were transferred from the kinetic model to the fluid model. The slow electrons were not capable of ionising anymore and did therefore not contribute in any source term.

In this model the density of fast electrons was furthermore considered low compared to that of the slow electrons and did therefore not add to the space charge density in the Poisson equation. The diffusion coefficients of electrons and ions were assumed constant and the mobilities were taken to be functions of the local reduced electric field.

In a next paper, Surendra et al. [9] extended their initial model by also solving the electron energy equation for the slow electrons in the negative glow region. Without treating more electrons with the MC method, the slow electrons could thereby also undergo inelastic processes. This resulted in a better description of the anode glow.

Schoenbach et al. [10] constructed a one-dimensional model of a steady-state glow discharge, in which they first described the positive column by means of a fluid model. The resulting charge and current densities were then used as a boundary condition for the hybrid cathode fall model. The electric field in the cathode fall was obtained via an iterative procedure, in which reaction rates and fluxes of the electrons were obtained from an MC model and used to integrate the balance equations from the positive column towards the cathode. The cathode was assumed to be positioned at that location where the ratio of electron and ion flux was equal to the secondary emission coefficient. Given this cathode position, the Poisson equation could be solved.

In a model similar to that described by Surendra et al., Bogaerts et al. [12] did include the fast electron density in the Poisson equation. Furthermore, in a next paper [13], they improved this glow discharge model further by treating two spatial dimensions and by adding MC descriptions of the fast ions and neutrals in the cathode fall region.

As it has become clear, the DC glow discharge favours a geometrical criterion that dictates which electrons need to be subjected to the MC treatment. This is possible because the time-independent nature of the discharge makes an a priori identification of the high field region of the discharge possible. A single electron can traverse this region once and can then be transferred to the slow electron group.

Alternating current discharges

In the case of a time-dependent discharge, it is often not possible to define geometrical criteria for which electrons to follow. Slow electrons in a low field region at one moment in time might feel this field to become high later. These electrons can then obtain energy and become fast electrons.

Sommerer and Kushner [15] developed a one-dimensional model of a radio-frequency (rf) discharge. The initial electrons were injected in the MC model at randomly distributed locations between the electrodes and followed as a function of space and phase in the rf cycle. The collision frequencies were used to determine the electron mobility and, via the Einstein relation, the diffusion coefficient. The eedf was collected in order to generate reaction rate coefficients. These data were used in a fluid model consisting of various density balance equations, fluxes in the drift-diffusion approximation, and the Poisson

equation. The MC and fluid model alternately calculated through a number of rf cycles and communicated their data back and forth until they jointly converged.

This Hybrid Plasma Equipment Model (HPEM) has been developed substantially after the publication of [15]. Among these developments are that the model has become two-dimensional [16] and implemented for parallel processing [19].

In a model of another rf discharge, Bogaerts et al. [25, 26, 27, 29] described the electrons created in secondary emission processes at the cathode and their progeny. The excitation and ionisation sources as a function of space and time in the rf cycle were communicated to the fluid model and used as source terms in the various balance equation. When convergence was reached in the fluid model, the MC model was called for another such iteration. This process was repeated until the fluid and MC code had converged together.

In the subsequent versions of this model, first, in [25], all electrons were followed during two rf cycles and were assumed to be thermalised in this period. Then, in [26, 27], the electrons were followed over a larger number of rf periods, until their total (kinetic and potential) energy dropped below the lowest excitation potential of the background gas. When this happened, these electrons were transferred to the fluid model. Since they could still gain energy in later times, the slow electron group contributed to the source term via reaction rates that were specified as a function of the mean electron energy, obtained by means of solving the electron energy balance equation. Later again, in [29], all electrons were described using the MC method and it was thereby correctly accounted for that slow electrons could become fast again. To keep the number of simulation particles within reasonable limits, the subset of simulation particles with an energy lower than a certain threshold was rescaled every now and then.

Transient discharges

Transient discharges have mainly been the domain of PIC simulations and only a few papers could be found in which hybrid models are applied to the transient development of discharges. As is the case with rf discharges, it is not straightforward to define criteria that can be used to limit the number of simulation particles.

Boeuf and Pitchford [11] created a two-dimensional hybrid model of a pseudospark discharge. In this model, they followed the electrons originating from the cathode and their progeny. The electrons were assumed to release their energy on a time scale that is short compared to the evolution of the discharge. The resulting steady-state source terms were used in the balance equations in the fluid model and scaled by the secondary emission source between subsequent MC updates.

Kushner et al. developed a two-dimensional hybrid model to describe the evolution of a dielectric barrier discharge [30] and the ignition of a high intensity discharge lamp [31]. In these models, electrons emanating from the cathode and their progeny were followed until their kinetic energy dropped below a user-defined threshold. At that moment they were transferred to the fluid model, in which they were described by a balance and electron energy equation. Both the electrons in the MC model and the electrons in the fluid model contributed to the source terms.

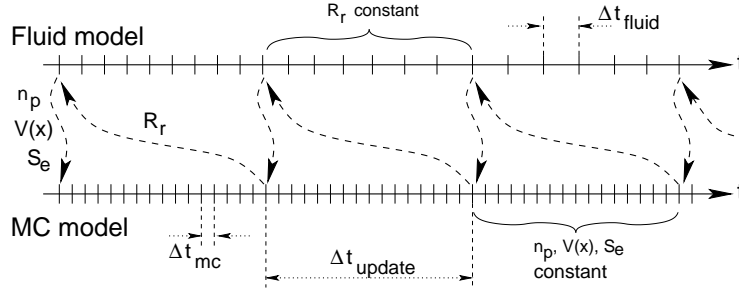


Figure 3.3: The communication between the fluid and the MC models as a function of time. Shown are the time axes for both models. At one moment, the fluid model communicates the background species densities n_p , the potential field $V(\mathbf{x})$ and the independent electron source S_e to the MC module. This then follows a number of simulation particles for a time Δt_{update} , collects statistics for the various reaction rates R_r and communicates them back to the fluid model. After solving the fluid model equations for the same Δt_{update} with these R_r , the process is repeated with new data for the MC module.

3.3 The md2d-mc hybrid model

In this section we describe the coupling between the fluid code *md2d* and the MC code that was described in chapter 2. We will not treat the md2d code in detail here, but let it suffice to say that the main equations have been given earlier in this chapter, in section 3.2.1. For a detailed description, please refer to reference [32] or section 5.2 in this thesis.

The hybrid code is set up such that the MC code follows electrons that originate from ‘independent’ sources: sources that the electrons do not cause themselves. These include, for instance, ion induced secondary emission at surfaces and Penning reactions in the volume of the discharge. The electrons and their offspring are followed until a criterion is met that allows them to be removed from the MC simulation.

The MC simulation yields reaction rates for the electron induced reactions. Also the electron transport coefficients or the electron flux can, in principle, be obtained from the MC module. However, in the present model this is not implemented yet and instead a local field approximation is used for these coefficients. The electron energy equation is not solved in the hybrid model.

Our hybrid model is a time-dependent model. At regular intervals, communication takes place between the two sub-models (see figure 3.3). The fluid model communicates the electric field, species densities and the independent electron sources to the MC module. The MC module returns the reaction rates that have been averaged over the period since the last update.

The user defines the time between updates and the amount of simulation particles injected between two updates in the MC module. The first quantity needs to be based on an estimate of how quickly quantities change within the fluid model. The second quantity allows control over the quality of the statistics that is collected in the interval.

Simulation electrons are typically ‘deactivated’ when they reach boundaries or when

their total energy drops below the excitation potential of the background gas. The lifetime of electrons can exceed Δt_{update} , since simulation particles are retained in memory from one update to the next.

In the following, we will treat the present implementation of the coupling between the fluid and MC code in more detail. The general design of that part of the MC code that facilitates the communication was illustrated in figure 2.10 on page 42 and treated in section 2.3. The MC client code needs to provide its own classes, derived from the abstract base classes *mcEnvironment* and *mcStatistics* that are present in the MC base code. With these classes the client code can construct an object of the type *mcFlightControl* and run and control the MC module.

In the following we treat these aspects in three subtopics: communication to the MC code (fluid→MC), communication back to the fluid model (fluid←MC) and control of the MC simulation. We note that the implementation of the coupling between the two models has been designed in a modular fashion. Any component of the coupling can therefore easily be improved, quite independent of other components.

3.3.1 Fluid → MC communication

In order to follow simulation particles through a discharge, the MC code needs to receive information about this discharge from its client code. This is provided via the *mcEnvironment* class (see section 2.3.6). The information consists of the following aspects: (1) a way to determine if a location is inside or outside the discharge region, (2) the electric field value at a given position and (3) the sources of simulation particle at the beginning and during the simulation.

The first two aspects are strongly related to the distinct descriptions of space that are used in the fluid simulation and in the MC simulation. The fluid simulation uses a two-dimensional grid to describe the variation of quantities as a function of discrete points in space, whereas the MC simulation allows particles to move through a continuous space. An often used component of the coupling is therefore the code that translates the continuous MC coordinates to indices on the fluid grid.

The numerical grid used in md2d is depicted in figure 3.4. As it can be seen in the figure, it is two-dimensional, structured and rectangular, and it is based on a matrix of numbers. Each number represents a type of material, in which zero is per definition the discharge region. From the material grid thus constructed, a nodal point grid is derived. Nodal points lie at the corners of material cells and form the centres of the control volumes. The value of scalar quantities such as the electric potential and species densities are known at these nodal point positions.

Discharge region

As stated before, one of the important tasks of the code that provides coupling between the two codes is to answer the question whether a position (x, y) of a simulation particle is inside the discharge region or not. The index (i, j) of the material cell in which this

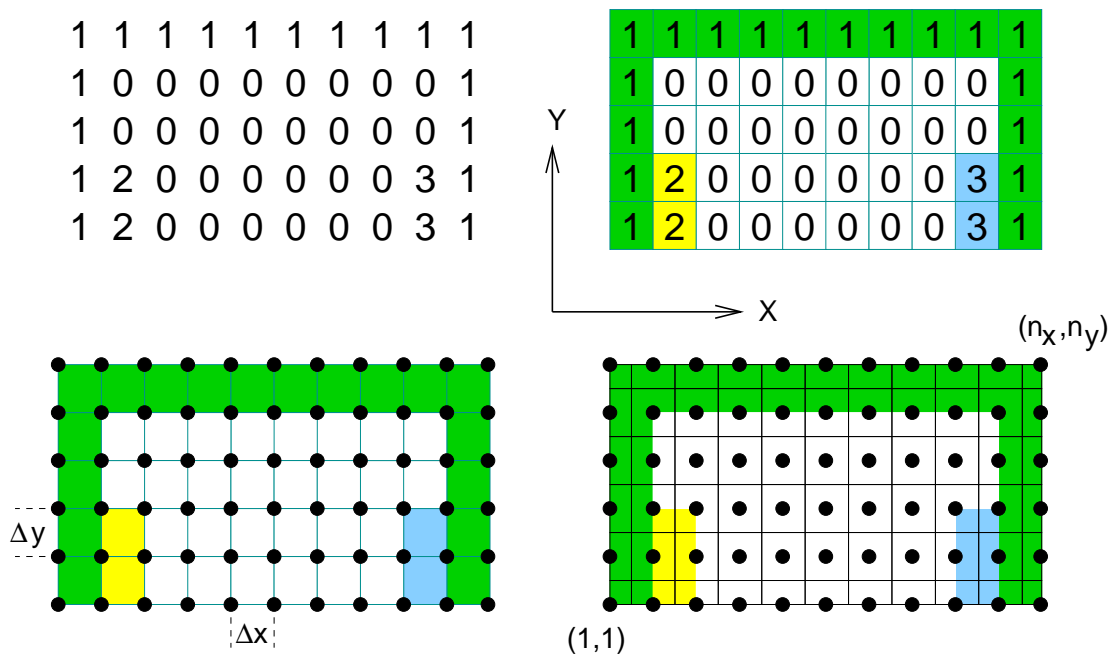


Figure 3.4: The construction of the md2d control volume grid [7, 33]. *Top left:* an example of a matrix of numbers, as specified by the user. *Top right:* each number represents one **material cell**, where the number 0 is reserved for the discharge region. *Bottom left:* at the corner of each material cell a nodal point is put. *Bottom right:* around the nodal points **control volumes** are constructed. Note that for the 10×5 matrix of numbers, an 11×6 control volume grid is constructed. Furthermore, internal material boundaries lie midway in the control volume and cross the nodal point. In case of a cylindrical geometry, the rotational axis lies at the bottom of the grid and the coordinate y in the figure represents the radial direction.

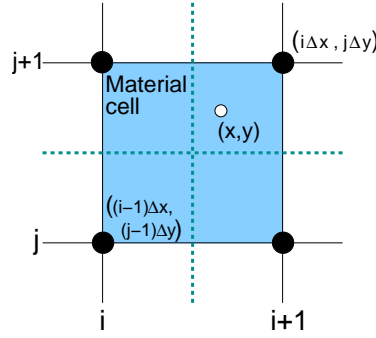


Figure 3.5: The coordinates used in the bilinear interpolation scheme for the electric field. The black dots represent the nodal points at which the electric potential is known. The open circle is an arbitrary location at which the electric field needs to be calculated.

position lies is determined according to:

$$\begin{aligned} (i-1)\Delta x &\leq x < i\Delta x \\ (j-1)\Delta y &\leq y < j\Delta y \end{aligned} \quad (3.5)$$

in which $i \in (1, n_x)$ and $j \in (1, n_y)$, with n_x and n_y the number of grid cells in horizontal and vertical direction respectively. Δx and Δy are the horizontal and vertical lengths of the grid cells. After finding the index (i, j) , it is checked whether the material index for this cell is equal to zero in order to determine whether (x, y) lies within the discharge region.

Note that finding the control volume or material cell to which a position belongs is an operation that is often executed during the MC part of the simulation. In the case of a rectangular, structured grid this is an easy task, as the inequality (3.5) shows. If the grid is more complicated, the number of operations necessary to determine in which volume a position is located can be quite substantial and detrimental to the run-time of the simulation. In such a case, it might be worthwhile to construct an intermediate rectangular grid to and from which fluid model quantities are interpolated [34, 31, 30].

Electric field

To calculate the electric field at the position (x, y) of a particle, an interpolation is necessary between the values known at the nodal points in the proximity of the particle's position. We used a bilinear interpolation scheme for this [35]. Here the value $\varphi(x, y)$ of the potential is interpolated from the values known at the four surrounding nodal points (see figure 3.5). Since the nodal points lie at the corners of a material cell, the index of the material cell (i, j) in which the position (x, y) lies is determined. $\varphi(x, y)$ is represented by:

$$\varphi(x, y) = a_{i,j} + b_{i,j}x + c_{i,j}y + d_{i,j}xy \quad (3.6)$$

The matrices of coefficient $a_{i,j}$, $b_{i,j}$, $c_{i,j}$ and $d_{i,j}$ are calculated after the Poisson equation has been solved, and subsequently are repeatedly used to calculate the electric field at desired

positions by first looking up in which material cell (i, j) the particle is and subsequently evaluating equation (3.7) for the corresponding coefficients.

The advantage of this interpolation scheme is that the electric field components E_x and E_y can be calculated directly from the coefficients by taking the partial derivatives of a equation (3.6), resulting in:

$$\begin{aligned} E_x &= -b_{i,j} - d_{i,j}y \\ E_y &= -c_{i,j} - d_{i,j}x \end{aligned} \quad (3.7)$$

for any coordinate (x, y) in material cell (i, j) .

Background densities

The *mcEnvironment* member *AddDensitySwarms()* is called once during the construction of the *mcFlightControl* object. It creates density swarms that contain references to the density fields of the various background particles in the fluid code. These swarms are added to the *mcSwarmList* and are updated each time that the *Prepare()* member of *mcFlightControl* is called at the beginning of a new update.

When a density is needed at a certain position, it is determined in which control volume the position is located (similar to (3.5), but shifted half a cell in x - and y -direction) and the density that is known at the nodal point is then taken to represent the density in the entire control volume that surrounds the nodal point.

Electron sources

Apart from the electron source that the MC code calculates self-consistently, such as electron impact ionisation, there are the independent sources that have to be provided to the MC module. The *mcEnvironment* class provides two functions to allow MC client code to inject particles in the simulation: *InjectFirstParticles* is called at the beginning of a simulation and *InjectParticles* is called at each time-step during the simulation.

In the present implementation of the hybrid code the user is allowed to specify how many particles he/she wants to have injected during each MC call. Furthermore, the user can choose between two manners of distributing the injected particles:

Globally: the volume and surface sources are integrated to give a global number of particles for the period over which the MC code will run. Together with the required number of simulation particles, this determines the weight of the simulation particles. Subsequently, via a rejection method (see section 2.A.3), particles are injected. This results in equally weighted particles that are distributed across the discharge region according to the magnitude of the sources.

Per element: the total number of particles to be injected is a fixed number for all surface and volume elements. The weight of each particle depends on the magnitude of the source for each element. This results in a distribution of particles that is homogeneous across the discharge region. However, their weights are chosen such that they reflect the magnitude of the source in each grid element. This method is useful if particles,

which originate from regions where the source is low, do play an important role in the discharge.

A lower limit of one for the injected particle weight can be specified. In simulations of breakdown (such as in chapter 4) initially the number of real electrons can indeed be smaller than the number one can simulate. By limiting the weight to a minimum of one, the noise that is seen is actually real noise [36]. Furthermore, computation time is reduced this way.

The independent electron sources are known at nodal points, but apply for the control volume or surface element around that nodal point. When particles are injected in an element, the exact position within the element is generated by means of random numbers. As such, within one element, particles are injected homogeneously.

Tossing electrons

As it has become clear in section 3.2.3, sometimes criteria can be defined for when to stop following a simulation electron, as it will not contribute anymore to the inelastic reaction rates that result from the MC simulation. Since we only obtain reaction rates from the MC module, the threshold ε_{exc} of the lowest excited level of the background gas can be used as a criterion. For that, the total energy of the electron is compared to this excitation energy ε_{exc} .

The *mcEnvironment* member *RemoveParticles()* is called every MC time-step. In the hybrid code implementation, it loops over all simulation particles and deactivates a particle if $\varepsilon + e(V_{\text{max}} - V_p) < \varepsilon_{\text{exc}}$. Here ε is the kinetic energy of the particle, V_{max} is the maximum of the potential in the discharge region and V_p is the potential at the particle's position.

We note that in the case that super-elastic collisions are possible, the lowest threshold is negative and electrons are never removed. Furthermore, it is assumed that the electric field, at a later time, does not heat particles that have reached the location for which the criterion is valid. This last point needs to be considered for each discharge separately.

3.3.2 Fluid ← MC communication

As said earlier, the present code only calculates reaction rates and returns them to the fluid model. For each reaction r that an electron can experience in the MC code, a matrix R_r of size $n_x \times n_y$ is constructed to collect the reaction rate during the runtime of the MC module. One of the following three methods can be chosen by the user:

At collision: the *AtCollision()* member of the *mcStatistics* is called each time a collision is evaluated. The code in this function first determines the index (i, j) of the control volume cell in which the collision took place and subsequently increases the number at this index in the reaction rate matrix R_r of this process r according to:

$$R_r(i, j) := R_r(i, j) + \frac{w}{V_{i,j} \Delta t_{\text{update}}} \quad (3.8)$$

in which w is the weight of the particle that caused the reaction to happen, $V_{i,j}$ the volume of the control volume cell and Δt_{update} the simulation time over which the reaction rate R_r is collected. The disadvantage of this approach is that the statistics obtained for $S_r(i, j)$ will be poor for infrequent collisions.

At move: the second method solves this issue by exploiting the fact that the chance that a certain collision will happen in a time-step does on average add up to the actual number of times the collision will be evaluated: at each time-step over which the particle is moved, the function *AtMove()* is called and adds a contribution to $R_r(i, j)$:

$$R_r(i, j) := R_r(i, j) + \frac{w\nu_r\Delta t_{\text{mc}}}{V_{i,j}\Delta t_{\text{update}}} \quad (3.9)$$

with $\nu_r = n\sigma_r u$ the frequency of process r , n the local target species density, σ_r the cross section, u the velocity of the electron and Δt_{mc} the time-step over which the particle was moved. We note here that this procedure involves a large number of lookups of various quantities, and thereby counteracts the efficiency gain that was intended by using the null collision technique.

Via the eedf: the third method reduces the increased workload of the previous method by collecting the eedf in each control volume via the *AtMove()* function. Instead of having to lookup local densities and the cross sections of each process, now only the energy of the electron needs to be calculated during this function call. At the end of the period over which statistics were collected, the eedf is convolved with the cross sections of the various processes to obtain reaction rates. Furthermore, it could be possible to also calculate the transport coefficients μ_e and D_e from the eedf and the set of cross sections. For this it would be necessary to follow all particles though.

3.3.3 Control of the Monte Carlo module

As shown in figure 3.3, the MC code is called at regular intervals Δt_{update} . Each time before the MC code is started, the *mcEnvironment* object needs to be updated. This, for example, involves recalculating the coefficients in equation (3.6). Furthermore, some quantities need to be reset to zero, such as the fields R_r in the *mcStatistics* object.

The MC code is then prepared and run as indicated in the algorithm on page 49. The *Prepare()* function gets Δt_{update} as an argument, so that the particles' weights can be determined when they are injected during runtime. Furthermore, the *mcStatistics* class implementation of the hybrid code contains a function *PostProcessData()* that, for example, calculates the rates from the eedfs that have been collected.

Apart from these steps, the control over the code is done as specified by the user in the various input options he/she specified. These included the number of particles to be injected per MC run, the time interval of the MC run, the maximum number of simulation particles allowed, etc.

3.4 Conclusions

A time-dependent, two-dimensional, hybrid fluid–particle code has been developed, based on an existing fluid model and the MC model described in chapter 2. In this code electrons are followed by means of the MC method and the resulting reaction rates are used in the source terms of the various balance equations in the fluid model. The fluid and MC models are alternately executed and keep the data that they obtained from each other at the beginning of an execution period constant during this period.

Acknowledgments

The author would like to thank Mark Kushner and Gerjan Hagelaar for the discussion on the implementation of fluid–particle codes in Ames (Iowa, US), February 2005 and Toulouse (France), December 2004, respectively.

References

- [1] G. L. Braglia. The diffusion and drift of electrons in gases. a Monte-Carlo simulation. *Fysica*, 92C:91–112, 1977.
- [2] J. P. Verboncoeur, G. J. Parker, B. M. Penetrante, and W. L. Morgan. Comparison of collision rates in particle-in-cell, Monte Carlo, and Boltzmann codes. *J. Appl. Phys.*, 80(3):1299–1303, 1996.
- [3] G. J. M. Hagelaar and G. M. W. Kroesen. A Monte Carlo modelling study of the electrons in the microdischarges in plasma addressed liquid crystal displays. *Plasma Sources Sci. Technol.*, 9(4):605–614, 2000.
- [4] A. Shvydky, V. P. Nagorny, and V. N. Khudik. Electron avalanche sliding along a dielectric surface. *J. Phys. D: Appl. Phys.*, 37(21):2996–2999, 2004.
- [5] R. W. Hockney and J. W. Eastwood. *Computer Simulation using Particles*. Adam Hilger, 1988.
- [6] C. K. Birdsall and A. B. Langdon. *Plasma Physics via Computer Simulation*. Adam Hilger, 1991.
- [7] G. J. M. Hagelaar. *Modeling of Microdischarges for Display Technology*. PhD thesis, Eindhoven University of Technology, The Netherlands, 2000.
- [8] M. Surendra, D. B. Graves, and G. M. Jellum. Self-consistent model of a direct-current glow discharge: Treatment of fast electrons. *Phys. Rev. A*, 41(2):1112–1125, 1990.
- [9] M. Surendra, D. B. Graves, and L. S. Plano. Self-consistent dc glow-discharge simulations applied to diamond film deposition reactors. *J. Appl. Phys.*, 71(10):5189–5198, 1991.
- [10] Karl H. Schoenbach, Hao Chen, and G. Schaefer. A model of dc glow discharges with abnormal cathode fall. *J. Appl. Phys.*, 67(1):154–162, 1990.

- [11] J. P. Boeuf and L. C. Pitchford. Pseudospark discharged via computer simulation. *IEEE Trans. on Plasma Science*, 19(2):286–296, 1991.
- [12] A. Bogaerts, R. Gijbels, and W. J. Goedheer. Hybrid Monte Carlo-fluid model of a direct current glow discharge. *J. Appl. Phys.*, 78(4):2233–2241, 1995.
- [13] A. Bogaerts, R. Gijbels, and W.J. Goedheer. Two-dimensional model of a direct current glow discharge: description of the electrons, argon ions, and fast argon atoms. *Anal. Chem.*, 68:2296–2303, 1996.
- [14] A. Bogaerts. *Mathematical Modeling of a Direct Current Glow Discharge in Argon*. PhD thesis, Universiteit Antwerpen, 1996.
- [15] T. J. Sommerer and M. J. Kushner. Numerical investigation of the kinetics and chemistry of rf glow discharge plasmas sustained in He, N₂, O₂, He/N₂/O₂, He/CF₄/O₂, and SiH₄/NH₃ using a Monte Carlo-fluid hybrid model. *J. Appl. Phys.*, 71(4):1654–1673, 1991.
- [16] M. Grapperhaus P. L. G. Ventzek and M. J. Kushner. Investigation of electron source and ion flux uniformity in high plasma density inductively plasma tools using 2-dimensional modeling. *J. Vac. Science Tech. B*, 12(1):461–477, 1994.
- [17] S. Rauf and M. J. Kushner. A model for non-collisional heating in inductively coupled plasma processing sources. *J. Appl. Phys.*, 81(9):5966–5974, 1997.
- [18] R. Kinder and M. J. Kushner. Non-collisional heating and electron energy distributions in magnetically enhanced inductively coupled and helicon plasma sources. *J. Appl. Phys.*, 90(8):3699–3712, 2001.
- [19] P. Subramonium and M. J. Kushner. Two-dimensional modeling of long-term transients in inductively coupled plasmas using moderate computational parallelism I. ar pulsed plasmas. *J. Vac. Sci. Technol., A* 20(2):313–323, 2002.
- [20] A. V. Vasenkov and M. J. Kushner. Electron energy distributions and anomalous skin depth effects in high-plasma-density inductively coupled discharges. *Phys. Rev. E*, 66:066411, 2002.
- [21] G. J. M. Hagelaar, J. Bareilles, L. Garrigues, and J. P. Boeuf. Role of anomalous electron transport in a stationary plasma thruster simulation. *J. Appl. Phys.*, 93(1):67–75, 2003.
- [22] Z. Donkó. Hybrid model of a rectangular hollow cathode discharge. *Phys. Rev. E*, 57(6):7126–7137, 1998.
- [23] K. Kutasi and Z. Donkó. Hybrid model of a plane-parallel hollow-cathode discharge. *J. Phys. D: Appl. Phys.*, 33(9):1081–1089, 2000.
- [24] K. Kutasi, P. Hartmann, and Z. Donkó. Self-consistent modelling of helium discharges: investigation of the role of He₂⁺ ions. *J. Phys. D: Appl. Phys.*, 34(23):3368–3377, 2001.
- [25] Annemie Bogaerts, Renaat Gijbels, and Wim Goedheer. Hybrid modeling of a capacitively coupled radio frequency glow discharge in argon: Combined Monte Carlo and fluid model. *Jpn. J. Appl. Phys.*, 38:4404–4415, 1999.
- [26] Annemie Bogaerts, Min Yan, Renaat Gijbels, and Wim Goedheer. Modeling of ionization of argon in an analytical capacitively coupled radio-frequency glow discharge. *J. Appl. Phys.*, 86(6):2990–3001, 1999.

- [27] Annemie Bogaerts and Renaat Gijbels. Monte Carlo model for the argon ions and fast argon atoms in a radio-frequency discharge. *IEEE Trans. on Plasma Science*, 27(5):1406–1415, 1999.
- [28] Annemie Bogaerts. Comprehensive modelling network for dc glow discharges in argon. *Plasma Sources Sci. Technol.*, 8:210–229, 1999.
- [29] Annemie Bogaerts, Renaat Gijbels, and Wim Goedheer. Improved hybrid Monte Carlo-fluid model for the electrical characteristics in an analytical radio-frequency glow discharge in argon. *J. Anal. At. Spectrom.*, 16(7):750–755, 2001.
- [30] M. J. Kushner. Modeling of microdischarge devices: Pyramidal structures. *J. Appl. Phys.*, 95(3):846–858, 2004.
- [31] A. Bhoj and M. J. Kushner. Avalanche processes in an idealized lamp: II. modeling of breakdown in Ar/Xe electric discharges. *J. Phys. D: Appl. Phys.*, 37:2510–2526, 2004.
- [32] G. J. M. Hagelaar, M. H. Klein, R. J. M. M. Snijkers, and G. M. W. Kroesen. Energy loss mechanisms in the microdischarges in plasma display panels. *J. Appl. Phys.*, 89(4):2033–2039, 2001.
- [33] G. J. M. Hagelaar. Private communication, Toulouse, France, November 2001.
- [34] M. J. Kushner. Private communication, Ames, Iowa, US, February 2005.
- [35] G. J. M. Hagelaar. Private communication, Toulouse, France, December 2004.
- [36] A. Shvydky. Private communication, Toledo, Ohio, US, February 2005.

A numerical description of breakdown between two parabolic electrodes in argon

Abstract. In this chapter a fluid code and a hybrid fluid-particle code are applied to an experimental setup used for breakdown research. The setup consist of two cylindrically symmetric parabolic electrodes, with their tips separated by 3.3 mm in a 3.5 Torr argon environment. A voltage pulse was applied with a rise-time of $25 \mu\text{s}$, followed by a period at a constant voltage of 350 V. Experimental observations of the light emitted by the discharge showed a stratified pre-breakdown light flash in the runup period. After the applied voltage had risen above the 300 V static breakdown voltage, a light front was observed to appear near the anode, cross the discharge gap towards the cathode and spread over its surface. The pre-breakdown flash is modelled with the hybrid model. It is caused by the charges that remained in the volume from previous pulses. The model results reproduce striations in the electron energy and density, which are found to occur due to the specific electric field configuration of the electrodes in the discharge chamber. The crossing of the light front is described with both the fluid and the hybrid model. Ionisation avalanches that start at the cathode due to secondary electrons cause a space charge that is largest near the anode and starts to effect the electric field there first. This extends the anode potential towards the cathode and is observed as a moving front. The results of both models correspond qualitatively with experimental observations.

4.1 Introduction

Breakdown is the process through which an electrically insulating gas becomes conducting under the influence of an applied electric field. This process is studied in many contexts, such as, for example, high altitude sprites and lightning [1], coronas and streamers used in gas purification [2, 3, 4], plasma displays [5], lighting [6, 7], spark discharges for switching [8] and for ultraviolet generation [9, 10].

Despite the relevance of the subject to many applications, a general theory has not been formed yet: generally, the microscopic processes that occur during breakdown are well understood. However, how these processes conspire to the specific discharge evolution is hard to predict. This situation is mitigated by the fact that the numerical data for individual processes is often poorly known.

Based on an understanding of microscopic processes, Townsend [11] did formulate a theory for breakdown in gas at pressure p , between two parallel plates separated by a distance d . Although of fundamental importance, this theory is only applicable for a restricted range of the pd product of typically 0.1 – 100 Torr cm and for simple electrode geometries.

Descriptions of breakdown do exist [12, 13, 14] for situations in which pd is either very low or very high or in which the applied voltage is much greater than the breakdown voltage. In these cases the discharge evolution is highly transient and localised in space, which makes it a challenge to measure quantities with sufficient spatio-temporal resolution [15, 16] and to describe these processes numerically [17]. Ongoing debates deal with the question whether stochastic processes play a role [4] and whether photo-ionisation is essential for the discharge development [18].

Another complication might be formed by the presence of dielectric materials and complex electrode arrangements, even outside the discharge vessel. The former can collect a surface charge and thereby alter the electric field configuration [5, 6, 19]. The latter can determine the field before the discharge produces enough space charge to shield these influences [6, 7]. These processes can dominate the evolution of the ionisation regions and will therefore have to be accounted for in models.

As a part of an ongoing effort to describe breakdown in different systems [20, 6, 19, 21], a numerical model has been developed to describe the complex interaction of the electric field with charges, both on surfaces and in the discharge volume. This model consists of a two-dimensional fluid model, which has recently been expanded with a Monte Carlo description for the electrons. By means of this addition, the non-local and non-equilibrium electron behaviour that one might find in certain discharge conditions can be taken into account correctly.

In this chapter we will apply this model to a discharge system that has been developed by Wagenaars and Bowden [19, 21] to study breakdown in a low pressure discharge. In the future this setup will be used to test high-resolution electric field measurements using Stark-spectroscopy techniques. The purpose of this chapter therefore consists in the first place of obtaining a better understanding of such a system. In the second place, comparison with experimental results gives a means a validation of the model and provides a way to

interpret experimental observations.

In the following we will first treat the experimental setup and describe high speed camera observations of the light emitted by the discharge during breakdown. Then the model will be treated and the simulation results are described. Finally, in the discussion, we will compare the model results to experimental observations and draw conclusions concerning the validity of the model.

4.1.1 Experimental setup and iCCD images

The experimental setup [19, 21] consisted of two cylindrically symmetric electrodes with a parabolic cross section and a tip-curvature that is equivalent to a radius of 4 mm. The electrodes were positioned with their symmetry axes aligned and with their tips separated by 3.3 mm. This electrode arrangement was placed in a vacuum chamber with a volume of approximately 31, filled with 99.999 % pure argon at 3.5 Torr.

For the experimental results that are considered here, the cathode was kept at ground potential and the anode was driven at a voltage that linearly increased from 0 V till 350 V in 25 μ s, remained at this potential for 50 μ s and then reduced to 0 V again in 25 μ s. The off-time between such pulses was 2 ms. The discharge vessel itself was kept at ground potential. The static breakdown voltage of this setup was measured to be 300 V.

The measurements done on this system consisted of iCCD camera observations of the discharge during breakdown [19, 21]. Images were taken with an exposure time of 100 ns for typically 3000 subsequent breakdown pulses. The images at fixed phases during the pulses were accumulated in order to obtain a clear image. This was possible because the breakdown process was reproducible and showed little jitter.

Already during the rise-time of the applied potential, before the static breakdown voltage was reached, a brief flash of light was observed in the region close to the anode. This *pre-breakdown light flash* is shown in figure 4.1. The emission is stratified in the pictures shown here. However, whether striations were observed was found to be dependent on conditions such as rise-time of the applied voltage. Also, the extent of the light along the anode surface varied depending on experimental conditions.

At a later time, when the static breakdown voltage had been reached, light was again observed near the anode. This is shown in figure 4.2. This light emitted by the *ionisation front* increased in intensity, crossed the gap and, when it reached the cathode, spread over its surface.

Both the pre-breakdown flash and the evolution of the ionisation front will be considered in the following sections.

4.2 The models

The fluid model that we used for the simulations has in general terms already been described in section 1.2.3 and 3.2.1. For more detail, please refer to section 5.2. Similarly, for the description of the hybrid fluid-particle model, refer to chapter 3.

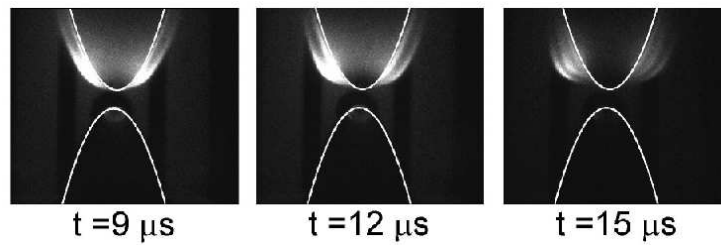


Figure 4.1: Experimentally observed emission patterns of the pre-breakdown light flash, taken from reference [21]. This light near the anode is observed before the static breakdown voltage has been reached and is visible during approximately $10 \mu\text{s}$. It can be seen that the discharge is stratified. Note that these are line-of-sight emission patterns and that all photons from the visual spectrum ($350 - 850 \text{ nm}$) contributed to these images.

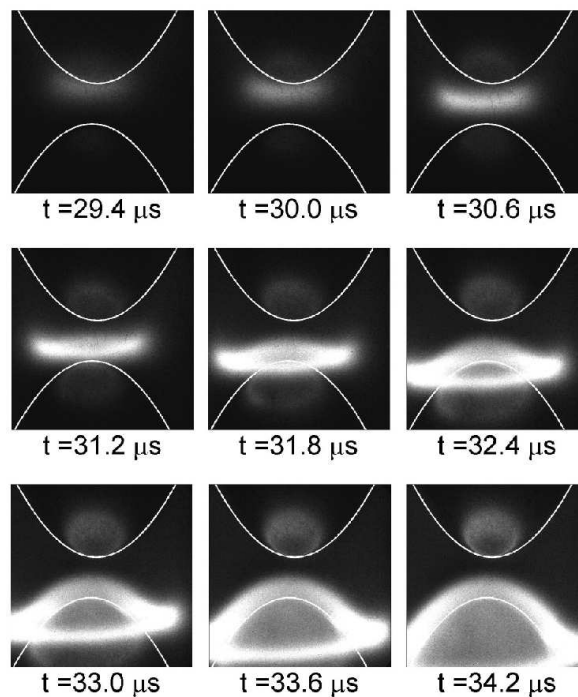


Figure 4.2: Experimentally observed emission patterns of the ionisation front that crosses the gap between the two electrodes, taken from reference [21]. The top electrode is anode and the bottom electrode is cathode. Note that these are line-of-sight emission patterns and that all photons from the visual spectrum ($350 - 850 \text{ nm}$) contributed to these images. These figures depict a smaller area than those in figure 4.1 and the grey scale is not the same: the pre-breakdown flash is approximately 10 times less intense than the light emitted by this ionisation wave. The light within the top electrode contour is not plasma emission but a reflection of it.

Table 4.1: The transport coefficients used in the hybrid model. The mobilities of the charged species were specified in the form of lookup tables as a function of the reduced electric field strength.

Species p	μ_p (Torr cm ² V ⁻¹ s ⁻¹)	D_p (Torr cm ² s ⁻¹)
e	$f(E/p)$ [24]	2×10^5 [25]
Ar*	-	64.0 [26]
Ar**	-	64.0 [26]
Ar ⁺	$f(E/p)$ [27]	Einstein relation

The set of species and reactions that was taken into account in the fluid model is described in detail in section 5.2.4. The only difference with these data is the pressure of the background gas, which is here set to 3.5 Torr.

The transport and reaction data for the hybrid model are summarised in the tables 4.1 and 4.2 respectively. The electron mobility is a function of the reduced electric field and the diffusion coefficient is taken to be constant. This forms a better approximation than taking it to be a function of the reduced electric field, as that would lead to unrealistic back-diffusion fluxes in e.g. a cathode fall [22].

The set of reactions in which electrons participate has been limited to direct impact excitation and ionisation only. The differential cross section models were chosen in correspondence with remarks concerning them in reference [23]. The rates for these reactions are calculated by means of the MC module and communicated to the fluid model as described in section 3.3 and illustrated in figure 3.3 on page 68. The time Δt_{update} between two MC updates is set to 5 ns in order to well resolve the time scale of the discharge evolution.

The two-dimensional cylindrical geometry is represented by a rectangular grid. In the case of the fluid simulations, the control volumes measure $110 \times 110 \mu\text{m}^2$ in the $r - z$ plane and the total grid is 4.33 cm in axial direction and 2.40 cm in radial direction, centred around the discharge gap. For the hybrid simulations of the pre-breakdown flash, the grid extends 4.0 cm in radial direction and consists of control volumes of $250 \times 250 \mu\text{m}^2$. An electrode is placed at $r = 4.0$ cm to account for the influence of the discharge vessel. We note that in the experimental setup the walls are at a larger distance, but expect no qualitative differences in the simulation results because of this. For the hybrid simulation of the ionisation front, a smaller grid of 3.50 cm in axial direction and 1.15 cm in radial direction is used.

4.2.1 Model applicability

Before treating the model results, it is worthwhile to consider the expected range of applicability of the fluid model and the hybrid model. As described in chapter 1, the locality of the electron behaviour forms a key parameter for the validity of a fluid model.

Electronic excitation and ionisation form the only effective mechanisms for an electron

Table 4.2: Reaction rates and rate coefficients used in the hybrid model. In case the rate is calculated by the MC module, the reference refers to the literature from which the cross section was obtained.

Nr.	Reaction	Rate (scattering model) or coeff.	Ref.
0	$\text{Ar} + e \rightarrow \text{Ar} + e$	R_r from MC (Isotropic, eqn. (2.31))	[23]
1	$\text{Ar} + e \rightarrow \text{Ar}^* + e$	R_r from MC (Surendra, eqn. (2.36))	[28]
2	$\text{Ar} + e \rightarrow \text{Ar}^{**} + e$	R_r from MC (Surendra, eqn. (2.36))	[28]
3	$\text{Ar} + e \rightarrow \text{Ar}^+ + 2e$	R_r from MC (Surendra, eqn. (2.36))	[23]
4	$\text{Ar}^* + \text{Ar}^* \rightarrow \text{Ar}^+ + \text{Ar} + e$	$k_r = 1.2 \cdot 10^{-9} \text{ cm}^3 \text{ s}^{-1}$	[29]
5	$\text{Ar}^* + \text{Ar}^{**} \rightarrow \text{Ar}^+ + \text{Ar} + e$	$k_r = 1.2 \cdot 10^{-9} \text{ cm}^3 \text{ s}^{-1}$	[29]
6	$\text{Ar}^{**} + \text{Ar}^{**} \rightarrow \text{Ar}^+ + \text{Ar} + e$	$k_r = 1.2 \cdot 10^{-9} \text{ cm}^3 \text{ s}^{-1}$	[29]
7	$\text{Ar}^{**} \rightarrow \text{Ar}^* + h\nu$	$k_r = 3.0 \cdot 10^7 \text{ s}^{-1}$	[6]

to lose energy in an atomic gas such as argon. An electron can therefore only lose energy if it has an energy that is higher than the excitation potential ε_{exc} of argon. As a result, the length scale $\Lambda = \varepsilon_{\text{exc}}/eE$, over which an electron gains this energy in an electric field E , sets a lower limit for the energy relaxation length. Furthermore, due to the mean free path length between collisions, an electron will not lose its energy instantly when it has reached the threshold, but will on average travel over λ_ε , as given by equation (1.13) on page 14.

The length scale Λ is in the order of $100 \mu\text{m}$ at the axis of the system when the full potential has been applied. In argon at 3.5 Torr, at energies above $\varepsilon_{\text{exc}} \approx 12 \text{ eV}$, λ_ε is in the order of $100 \mu\text{m}$ (see figure 1.6 on page 15). Considering the size of the system and the extent of the emission patterns in figure 4.2, the gradient length in the electric field is roughly estimated to be $500 \mu\text{m}$. Within this gradient length, the electron will both gain and lose energy and can therefore be described locally. This suggests that a fluid model is applicable during the crossing of the ionisation front.

However, at the time of the pre-breakdown flash, when the voltage is still rising, Λ is larger and the electron behaviour can be expected to exhibit non-local behaviour, which will not be captured by the fluid model.

4.3 Pre-breakdown light flash

In this section we treat the model results for the runup phase of the applied voltage, during which the pre-breakdown flash is observed. In this phase, the electric field is not high enough to cause a significant multiplication of electrons. Furthermore, the electron behaviour is expected to be non-local. Therefore, the emphasis lies on the results obtained with the hybrid model.

4.3.1 Results

In reference [21], Wagenaars et al. suggest that the pre-breakdown light flash is caused by charges leftover from previous discharges. These charges could either have remained in the volume or at the dielectric surfaces that support the electrodes. In recent work, not yet published at the moment of writing this thesis, more detailed measurements have confirmed the hypothesis that the charges remaining in the volume cause the pre-breakdown flash. The charges gathered on the dielectric materials were found to be unimportant.

The hybrid simulations were started with a homogeneous fluid background density of electrons and ions of 10^6 cm^{-3} . It was found that in these simulations this value is not important for the qualitative results: the electron density is too low to modify the field and the electrons do therefore not influence one another.

In the MC module simulation electrons of equal weight were injected across the grid to represent this homogeneous density. Their velocities were distributed isotropically and their energies according to a Maxwellian energy distribution function with a mean energy of 1 eV.

The top part of figure 4.3 shows the MC electron energy and density at three instants in time, starting at $3 \mu\text{s}$ after the applied voltage began to rise. One can see that layers of alternately low and high mean electron energy are present close to the anode. The electron density shows similar layers, with a high density at the positions where the energy is low due to flux conservation. For comparison, the results of similar calculations done with the fluid model are shown in the bottom part of this figure. Due to the assumptions that are made concerning the electron energy distribution function and the corresponding reaction rate coefficients, striations cannot be found in the fluid model results.

The electrons that are caused by ion induced secondary emission at the cathode surface can also contribute to the pre-breakdown flash. To investigate whether this group of electrons is important as compared to those that were already present in the volume, simulations were carried out for the condition in which no initial electrons were injected. As such, simulation electrons only resulted from secondary emission at the cathode.

The simulation showed that only electrons present in the volume are important for the pre-breakdown flash. Due to the low mobility of the ions and the fact that only a fraction of 0.07 produces secondary electrons, the electron density due to these ions was several orders lower than of the electrons already present in the volume.

4.3.2 Discussion

Both the fluid and the hybrid simulations predict the phenomenon of the pre-breakdown light flash: we found a qualitative agreement with the experimental observations. The presence of striations and quantitative agreement are the main topics addressed in this discussion.

Striations are typically expected when a mono-energetic group of electrons originates from a specific location in the discharge. This can for example be at the cathode, where secondary electrons all have approximately the same energy. From such a region these

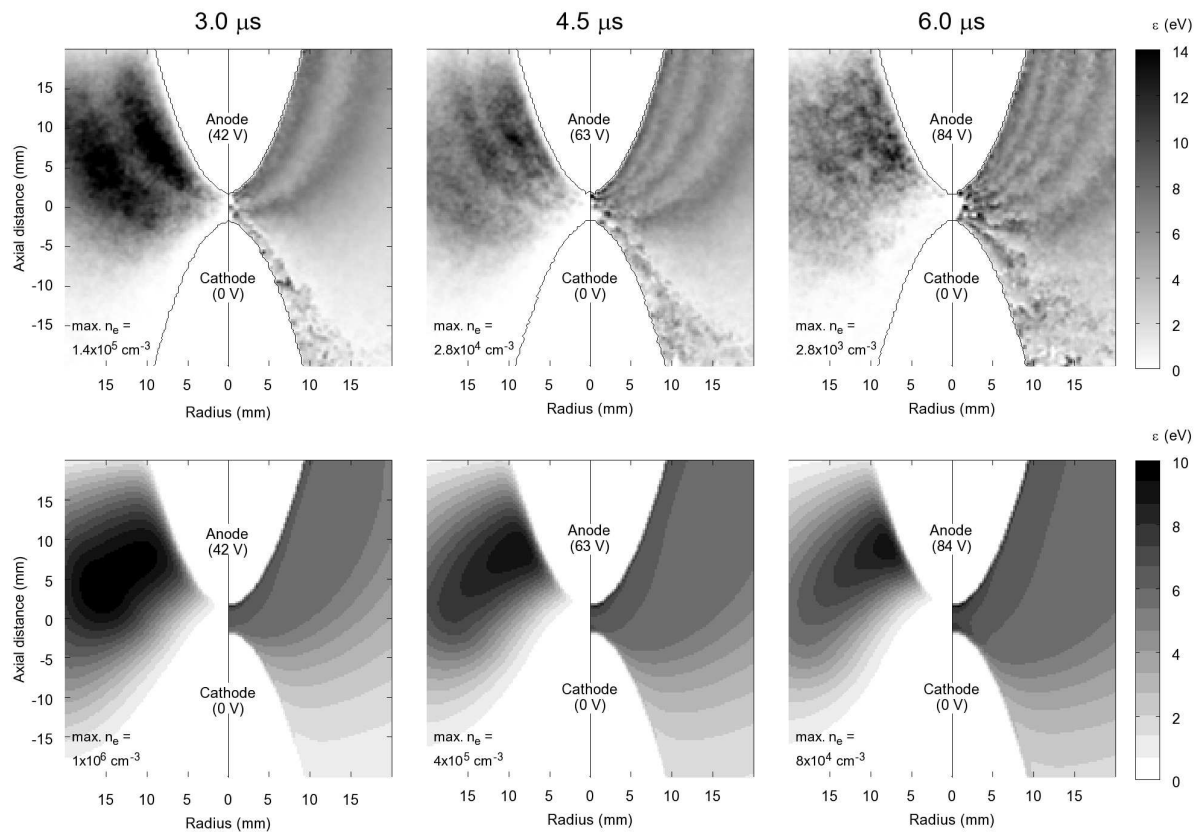


Figure 4.3: *At the top:* hybrid model results for the electron density (in each plot at the left) and mean electron energy (in each plot at the right) for three instants in time before the static breakdown voltage has been reached. The grey scale coding for the mean energy is indicated next to the bar on the right, whereas for the densities the maximum of each plot is indicated in its bottom corner. Note that the computational grid extends to a radius of 4cm and is only partially shown here. *At the bottom:* now calculated with the fluid model. No stratified structure is present in these data, which indeed cannot be expected in fluid model results. Nevertheless, the number of electrons that reaches the anode shows a maximum in time and these simulations thus also confirm the occurrence of the pre-breakdown flash. Note that in the bottom plot the grey scale contains discrete levels of grey in order to visualise contour levels in these data.

electrons synchronously accelerate in the field and reach the excitation potential of the background gas at a well-defined distance from their starting point. The excitation rate will be high locally, after which the electrons have lost their energy and need to traverse another distance to repeat this process. The light emitted when the excited atoms fall back to a lower state forms a stratified structure.

In the present configuration, the electrons that are present in the volume when the voltage first starts to rise have a low energy, since they were not heated in the field during the 2 ms period of zero applied potential. However, they are spread out in the discharge volume and it seems that they cannot appear with similar energies in well-defined regions in space. It is therefore surprising that striations are observed in the experimental data, and are reproduced in the simulations results treated above.

However, due to the specific geometry of the electrodes in the vacuum chamber, the largest fields are found near the electrodes. If one starts with an electron density that is approximately homogeneous, most electrons will be in a low field region. These electrons will drift towards the anode and gain little energy until they are close to the anode where the field is higher. Although there is a spread in the electron energy, the electrons will start to gain energy in the same region in space close to the anode and lose it after they have reached approximately $\varepsilon_{exc} \approx 12$ eV.

Therefore, for this electric field geometry and rise-time of the applied voltage, conditions are such that the electron energy becomes sufficiently synchronised in space to give rise to a stratified structure.

The hybrid model is successful in the prediction of striations. But the timing of the pre-breakdown flash does not correspond with experimental observations. This may be caused by the fact that the initial density of electrons is unknown and assumed to be homogeneous in the simulations. Furthermore, the numerical grid represents a volume smaller than the actual discharge volume. The drift velocity of electrons in a field of 10 Vcm^{-1} is approximately $1 \text{ cm } \mu\text{s}^{-1}$ for this argon pressure. The time scale associated with this has the same magnitude as the time scale of the pre-breakdown flash and therefore the discrepancy could indeed be caused by the electrons being further away initially.

4.4 Crossing of ionisation front

In this section the ionisation wave evolution will be considered. This wave occurs after the applied voltage reaches the static breakdown voltage of the setup. The discharge is then self-sustained and does not rely on background ionisation anymore. It will evolve to a structure containing a cathode sheath and a glow discharge region.

4.4.1 Results

In the following, the emphasis lies on the fluid model results, but some hybrid model results will be considered as well.

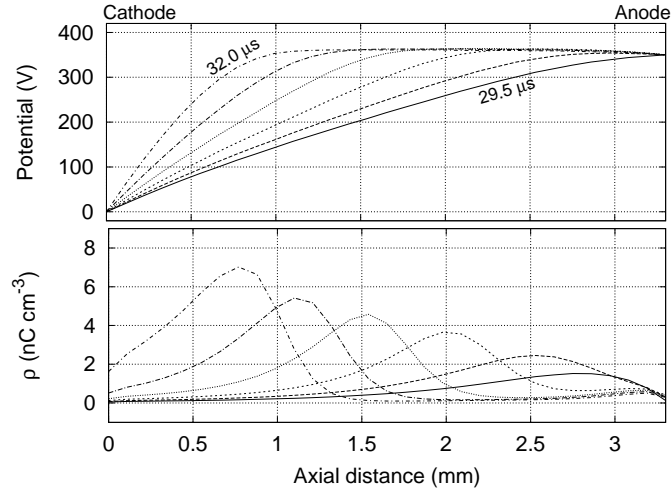


Figure 4.4: The calculated electric potential and space charge density at the axis of the setup for various instants in time during the crossing of the ionisation front.

Fluid model

In order to approximate the timing of the crossing of the ionisation front shown in figure 4.2, the initial electrons and ion densities were chosen to be a homogeneous 10^6 cm^{-3} . We will come back to this choice in the discussion section.

The behaviour of the light pattern shown in figure 4.2 can be explained by the effect of ionisation avalanches that are initiated by secondary electrons at the cathode. Initially there are no significant space charges and the avalanches move in the field that is determined by the two electrodes. Since the avalanches grow towards the anode, the electron density will be largest near the anode and the first observable light from excited species is seen in this region. Also in this region, the space charge density will first reach a value that is large enough to modify the field (this is illustrated in figure 4.4). When this happens, the potential of the anode extends towards the cathode. As a result, the region with a high field is compressed towards the cathode and electrons will generate avalanches over a lesser distance. Light now originates from that part of the high field region closest to the anode. The continuation of this process appears as a light front moving from anode to cathode.

Once the cathode is reached, this one-dimensional picture does not suffice to explain the observed phenomena any longer. At the axis, a cathode fall and negative glow have been established, but, at a larger radius, the ionisation front has not yet reached the cathode and can continue to travel towards it. This is illustrated in figure 4.5 where the electric field and space charge density are now shown in a two-dimensional representation. One can see that the cathode sheath extends along the surface and that the low field region, which is at approximately the anode potential, spreads in radial direction.

The axial velocity of the ionisation front was $1.0 \times 10^3 \text{ ms}^{-1}$, compared to $1.8 \times 10^3 \text{ ms}^{-1}$ in the experiments. Furthermore, the ionisation front in figure 4.2 appears to be more extended in radial direction than is observed in the simulation results in figure 4.5.

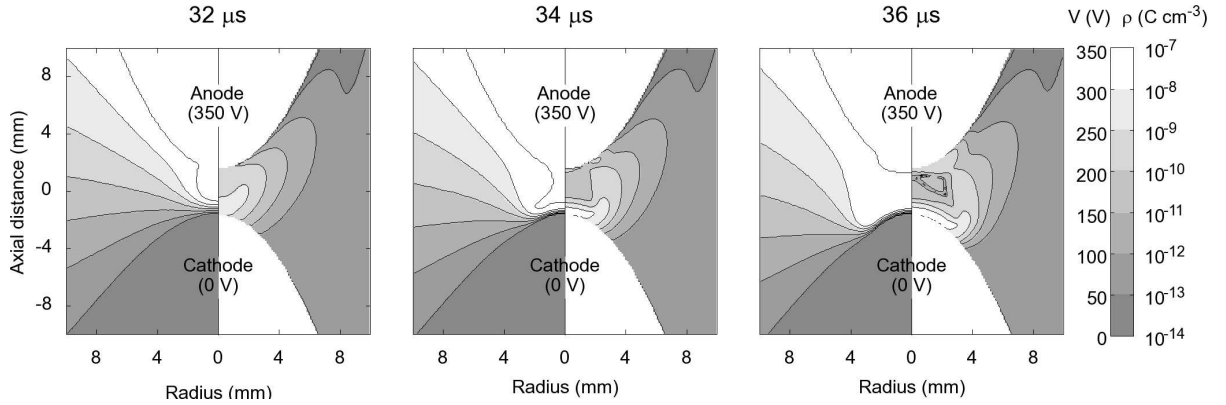


Figure 4.5: The calculated electric potential (in each plot at the left) and space charge density (in each plot at the right) for three instants in time after the ionisation wave has crossed the discharge gap and ‘spreads’ over the cathode surface.

Hybrid model

The results obtained with the hybrid simulation exhibit the same qualitative behaviour as those described above for the fluid model. In the following, some aspects of the hybrid simulation are considered in more detail.

Figure 4.6 shows the number of electrons and the mean electron energy as calculated in the MC module. Here, the number of electrons is the number of simulation electrons times their mean weight. For this simulation the weight of the simulation particles had a minimum of 1.0. Since the total number of electrons allowed in the simulation was 64000, the mean weight only started to increase after $27 \mu\text{s}$. It is possible to allow simulation particles weights that are smaller than 1.0, but this yields the same curves as the ones shown in figure 4.6. Although the data presented here contains more noise up to $27 \mu\text{s}$, this noise can be considered physical.

The time during which the ionisation front crosses the gap between the tips of the electrodes is clearly visible in figure 4.6: due to the fact that the potential drop is compressed in a smaller region, the mean energy of the electrons rises. From this figure the speed of the ionisation front is calculated to be $1 \times 10^3 \text{ ms}^{-1}$.

After the front has reached the cathode, the cathode surface occupied by the discharge becomes larger and the total electron number increases sharply. Due to the fact that the potential drop is now located across a thin sheath, most simulation electrons are in a low field region. The mean energy of all electrons drops due to this effect, but the mean electron energy in the sheath does reach values up to 70 eV, like in the fluid model.

4.4.2 Discussion

The simulation results presented above are qualitatively consistent with the experimentally observed emission. A quantitative agreement does not exist and the reason for this is likely

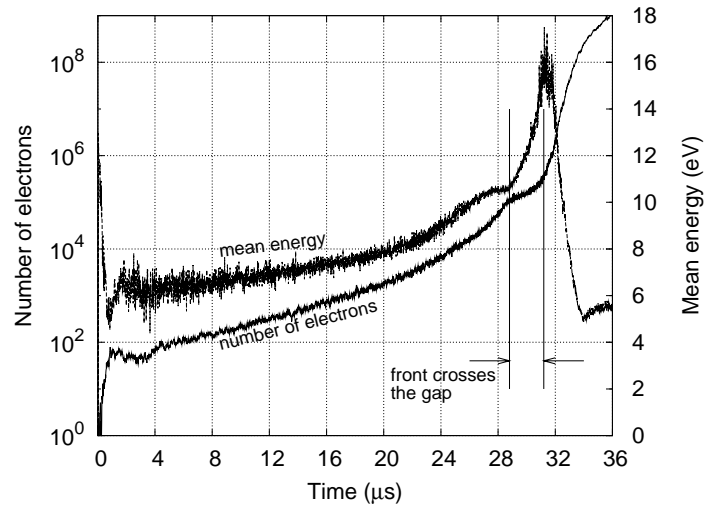


Figure 4.6: The total number and the mean energy of the electrons represented in the MC module. The number of electrons is the number of simulation electrons times their mean weight. This weight is 1.0 up till $27 \mu\text{s}$, since the maximum number of simulation particles of 64000 was only reached then.

to be found in the initial density profile of electrons and ions remaining from a previous pulse. Lacking a good estimate of this density profile, the value of 10^6 cm^{-3} is based on reproducing the timing at which the ionisation front started to move from anode to cathode. Another quantity that could have been varied to reproduce this timing is the secondary emission coefficient of the cathode surface.

Both the initial ion density and the secondary emission coefficient affect the flux of electrons away from the cathode surface. These electrons are responsible for the buildup of space charge near the anode. The time at which this space charge density is first high enough to modify the electric field is therefore determined by the secondary electron flux.

If the initial ion density is inhomogeneous and differs from 10^6 cm^{-3} , the flux of ions that reaches that cathode surface as a function of time can be substantially different from the present model flux. Also, the secondary emission coefficient is not well known. It generally depends strongly on the quality of the electrode surface and can differ by several 10 % from the assumed value of 0.07.

Both the secondary emission coefficient and the initial densities of electrons and ions were varied. These variations affected both the time at which the ionisation front started to move, as well as the speed of the ionisation front. Typically, both an earlier onset of the motion of the ionisation front and an increased speed of this front were found for a higher secondary emission coefficient and for a higher initial electron and ion density.

Lacking data on these quantities, we cannot expect a quantitative agreement. This situation can be improved by trying to obtain better estimates of the background ionisation density profile remaining from previous pulses. This could for example be done by means of afterglow simulations, but is outside the scope of this chapter.

4.5 Conclusions

In this chapter numerical simulations were presented of a setup that is used to study breakdown of low pressure discharges. In experimental observations of light emission by the discharge, two phenomena were observed: in the first place, a pre-breakdown light flash occurred near the anode at a time before the static breakdown voltage was reached. In the second place, at a voltage higher than the breakdown voltage, a light front was observed to cross the gap between the anode and the cathode.

Breakdown was investigated with a fluid and a hybrid fluid-MC model. Both models predicted the appearance of the pre-breakdown flash and the subsequent appearance and crossing of a localised ionisation front as the first stages in the full breakdown of the system.

The hybrid model result reproduced the pre-breakdown flash and its striated appearance: electrons that remained in the discharge volume after a previous discharge pulse drift towards the anode when a potential is applied to it. Due to the specific geometry of the setup, the electric field is such that electrons arrive at similar positions with approximately the same energy. This synchronisation of the space-dependent electron energy can explain the observed striations.

The model results for the period in which the ionisation front crosses the gap between the two electrodes is qualitatively consistent with experimental observations. A quantitative agreement cannot be expected due to the fact that quantities such as the initial electron and ion density distributions are not known.

Acknowledgments

The author would like to thank Erik Wagenaars and Mark Bowden for the many useful discussions and for the experimental figures.

References

- [1] E. M. Bazelyan and Yu. P. Raizer. *Lightning Physics and Lightning Protection*. Institute of Physics, Bristol, 2000.
- [2] E. M. van Veldhuizen, editor. *Electrical Discharges for Environmental Purposes: fundamentals and applications*. Nova Science Publishers, 2000.
- [3] M. Arrayás, U. Ebert, and W. Hundsdorfer. Spontaneous branching of anode-directed streamers between planar electrodes. *Phys. Rev. Letters*, 88, 2002.
- [4] A. Rocco, U. Ebert, and W. Hundsdorfer. Branching of negative streamers in free flight. *Phys. Rev. E*, 66:035102(R), 2002.
- [5] G. J. M. Hagelaar, G. M. W. Kroesen, U. van Slooten, and H. Schreuders. Modeling of the microdischarges in plasma addressed liquid crystal displays. *J. Appl. Phys.*, 88(5):2252–2262, 2000.

- [6] W. J. M. Brok, J. van Dijk, M. D. Bowden, J. J. A. M. van der Mullen, and G. M. W. Kroesen. A model study of propagation of the first ionisation wave during breakdown in a straight tube containing argon. *J. Phys. D: Appl. Phys.*, 36(16):1967–1979, 2003.
- [7] A. Bhoj and M. J. Kushner. Avalanche processes in an idealized lamp: II. modeling of breakdown in Ar/Xe electric discharges. *J. Phys. D: Appl. Phys.*, 37:2510–2526, 2004.
- [8] B. H. P. Broks, J. Hendriks, W. J. M. Brok, G. J. H. Brussaards, and J. J. A. M. van der Mullen. Plasma physical model of the photoconductively switches spark gap. In *Proceedings of the XXVIIth International Conference on Phenomena in Ionized Gases (ICPIG)*, Eindhoven, the Netherlands, 2005.
- [9] J. P. Boeuf and L. C. Pitchford. Pseudospark discharged via computer simulation. *IEEE Trans. on Plasma Science*, 19(2):286–296, 1991.
- [10] E. R. Kieft, J. J. A. M. van der Mullen, G. M. W. Kroesen, V. Banine, and K. N. Koshelev. Collective thomson scattering experiments on a tin vapor discharge in the prepinch phase. *Phys. Rev. E*, 70(5):056413, 2004.
- [11] J. S. Townsend. *The Theory of Ionization of Gases by Collision*. Constable & Company Ltd., London, 1910.
- [12] L. B. Loeb and J. M. Meek. *The Mechanism of the Electric Spark*. Clarendon Press, Oxford, 1941.
- [13] H. Raether. *Electron Avalanches and Breakdown in Gases*. Butterworths, London, 1964.
- [14] A. N. Lagarkov and I. M. Rutkevich. *Ionization Waves in Electrical Breakdown of Gases*. Springer, Berlin, 1994.
- [15] E. M. van Veldhuizen and W. R. Rutgers. Pulsed positive corona streamer propagation and branching. *J. Phys. D: Appl. Phys.*, 35:2169–2179, 2002.
- [16] T. M. P. Briels, E. M. van Veldhuizen, and U. Ebert. Branching of positive discharge streamers in air at varying pressures. *IEEE Trans. on Plasma Science*, 33(2):264–265, 2005.
- [17] C. Montijn, B. Meulenbroek, U. Ebert, and W. Hundsdorfer. Numerical simulations and conformal mapping analysis of growing and branching negative discharge streamers. *IEEE Trans. on Plasma Science*, 33(2):260–261, 2005.
- [18] S. V. Pancheshnyi, S. M. Starikovskaia, and A. Yu. Starikovskii. Role of photoionization processes in propagation of cathode-directed streamer. *J. Phys. D: Appl. Phys.*, 34(1):105–115, 2001.
- [19] M. D. Bowden, E. Wagenaars, Tao Jiang, W. J. M. Brok, and M. F. Gendre. Measurements of plasma breakdown. *J. of High Temp. Mat. Processes*, 8(4):483–498, 2004.
- [20] M. F. Gendre, M. D. Bowden, H. Haverlag, H. C. M. van den Nieuwenhuizen, J. Gielen, and G. M. W. Kroesen. Optical study of pre-breakdown processes in compact fluorescent lamps. In S. De Benedictis and G. Dilecce, editors, *Proceedings of Frontiers in Low Temperature Plasma Diagnostics V*, pages 295–298, 2003.
- [21] E. Wagenaars, M. D. Bowden, and G. M. W. Kroesen. Plasma emission imaging of a low-pressure argon breakdown. *Plasma Sources Sci. Technol.*, 14(2):342–350, 2005.
- [22] G. J. M. Hagelaar. Private communication, Toulouse, France, December 2004.

- [23] A. V. Phelps and Z. Lj. Petrović. Review article: Cold-cathode discharges and breakdown in argon: surface and gas phase production of secondary electrons. *Plasma Sources Sci. Technol.*, 8:R21–R44, 1999.
- [24] BOLSIG, Boltzmann solver for the siglo-series 1.0. CPA Toulouse & Kinema Software, 1996.
- [25] A. Bogaerts, R. Gijbels, and W. J. Goedheer. Hybrid Monte Carlo-fluid model of a direct current glow discharge. *J. Appl. Phys.*, 78(4):2233–2241, 1995.
- [26] I. S. Grigoriev and E. Z. Meilikhov, editors. *Handbook of Physical Quantities*. CRC, Boca Raton, FL, 1997.
- [27] H. W. Ellis, R. Y. Pai, E. W. McDaniel, E. A. Mason, and L. A. Viehland. Transport properties of gaseous ions over a wide energy range. *Atomic Data and Nuclear Data Tables*, 17(3):177, 1976.
- [28] K. Tachibana. Excitation of the $1s_5$, $1s_4$, $1s_3$ and $1s_2$ levels of argon by low-energy electrons. *Phys. Rev. A*, 34(2):1007–1015, 1986.
- [29] A. N. Klucharev and V. Vujnovic. Chemi-ionization in thermal-energy binary collisions of optically excited atoms. *Physics Reports*, 185(2):55–81, 1990.

Model study of propagation of the first ionisation wave during breakdown in a straight tube containing argon

Abstract. The mechanisms responsible for the propagation of the first anode directed ionisation wave that occurs in a straight discharge tube during breakdown are studied by means of a fluid model. The discharge tube contains argon at a pressure of a few Torr and is operated at a dc voltage with the cathode heated to thermal electron emission temperature. The two-dimensional model incorporates continuity and momentum equations for the electrons, for several effective excited states and for the ions, a balance equation for the electron energy and the Poisson equation. The model is capable of describing the first ionisation front in a way that is qualitatively consistent with observations made in experiments. The mechanisms behind the breakdown evolution are investigated by considering the temporal and spatial evolution of the quantities described by the model. Previously, researchers have described this breakdown evolution in terms of an RC-line circuit. The validity of this picture is surveyed by considering the distribution of charges within the lamp. The effect of control parameters on the breakdown process and the assumptions that affect the validity of the model for later stages in breakdown are considered.

5.1 Introduction

Gas discharges are widely used for lighting purposes [1, 2, 3] and are the subject of extensive research in this context. The research efforts range from application directed development to more academic research into the fundamental processes that occur in gas discharges. Although much has been understood about the gas discharges used in low pressure lighting technology, many phenomena still lack a satisfactory explanation. This is even the case for seemingly simple systems, such as a cylindrical tube containing just one noble gas. Most notably many questions are still to be answered about the mechanisms related to the breakdown of the gas.

Breakdown is the process in which a gas changes from being electrically isolating to being electrically conducting. This highly transient process involves the creation of charge carriers as a result of various processes such as electron impact ionisation and secondary emission. These processes often take place in a moving region. The displacement of such an ionisation region occurs at speeds that lie in the range of $10^3 - 10^6 \text{ m s}^{-1}$.

The nature of the mechanisms involved in breakdown has attracted much attention throughout the history of plasma physics [4, 5]. Breakdown of a low current and low pressure ($\sim 10^2 - 10^4 \text{ Pa}$) discharge between two parallel plates is rather well understood nowadays and can be described by Townsend theory [4] and predicted using Paschen curves [6]. However, for systems with different geometries, higher pressure and/or a non-uniform electric field, breakdown mechanisms are less well understood.

Breakdown is important for many applications of plasma physics. Some examples of applications in which breakdown is an issue are: coronas used in pollution control [7], plasma display panels [8], (re)ignition of high intensity discharge lamps [9], hollow cathode devices for extreme ultraviolet production [10] and improvement of fluorescent lamps [11]. Recent research focusing on what happens on breakdown time scales has involved mostly theory and modelling. With sufficiently fast experimental techniques becoming available now, experimental efforts on small time and spatial scales are expected to be performed in the near future [12]. These experiments are expected to shed light on (among others) the magnitude of the electric field in the breakdown front, providing valuable data for gaining a theoretical insight into breakdown mechanisms and for validation of existing models.

In the research described in this chapter, we use a simulation based on a fluid model to study breakdown in a straight cylindrical tube, which is reminiscent of the tubes used in compact fluorescent lamps (cfl). Breakdown in such systems has been previously studied [13, 14, 15, 16, 11] and it has become clear that the tube wall and the electrical environment of the lamp play an integral role in the initial phases of the breakdown process. Although the explanation offered by these studies provides a consistent picture of the process, there are a number of aspects that are still only poorly understood. These include, mainly, the influence of the reaction kinetics in the discharge gas and its capability to transport charges. The aim of this research is to compare the results of the simulations with previously reported results and to use detailed output of the simulation to gain further insights into breakdown phenomena.

In the above-mentioned breakdown studies the important breakdown phases have been

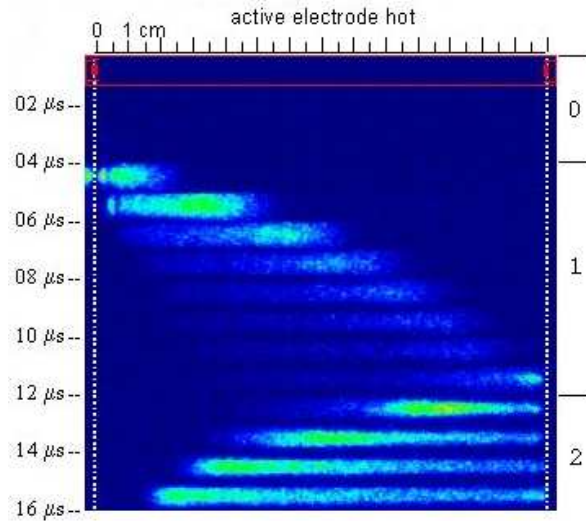


Figure 5.1: Experimentally observed emission pattern of a lamp during the first $16 \mu\text{s}$ of the breakdown phase [17]. The applied voltage is -400 V ; the cathode filament is heated by a 230 mA current that resulted from 3 V across the two lead wires. On the right hand side of the figure the time scales is divided into three parts indicating different phases: *phase 0*: little activity is observed during the rise in applied voltage. *phase 1*: an ionisation front crosses from cathode to anode. *phase 2*: a ‘return-stroke’ moves back from anode to cathode.

identified. These can be seen clearly in the results of an optical emission measurement [17] shown in figure 5.1. Typically a number of phases are observed: when the applied dc voltage has reached its final value, an ionisation front starts moving from cathode to anode (phase 1 in the figure). Subsequently a ‘return-stroke’ is observed, moving back to the cathode (phase 2). After these two phases, which take in the order of $\sim 10 \mu\text{s}$, the light intensity emitted by the tube will increase throughout the tube. Depending on the conditions, less pronounced ionisation waves are observed to travel backwards and forward in the tube. Stable and distinct striations are often easily seen in the emission pattern. The emitted light intensity increases until the voltage across the tube drops sharply and the current through the tube increases. Depending on the voltage, this point of electrical breakdown is reached up to $\sim 60 \mu\text{s}$ after the voltage was first applied.

Various researchers have addressed some of the phenomena occurring in breakdown in long tubes: Bartholomeczyk [13] discovered that the discharge begins with ionisation of the gas near the electrode. Nedospasov and Novik [14] were the first to realize the importance of the surface charge deposited on the wall: in their paper they describe that, starting at the active electrode, subsequent sections of the wall are charged to the electrode potential. The electric field is concentrated mainly between the cloud of plasma and the adjacent section of the wall. The plasma is extended along the tube due to new ionisation in the region of strong field. This process can be envisioned in terms of the distributed RC-line as shown in figure 5.2: the resistors represent the discharge gas that conducts the current from the cathode to the different sections of the wall. The capacitors represent the

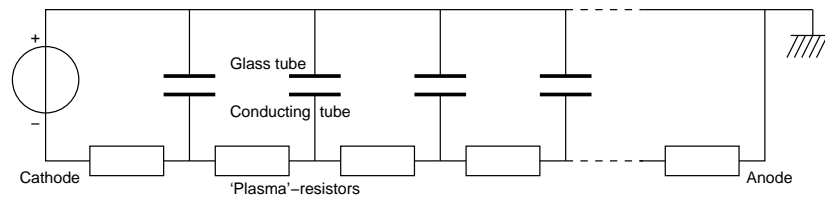


Figure 5.2: The equivalent circuit of the lamp during breakdown is a transmission line [14]: starting at the cathode at the left the subsequent capacitors are charged. The values of the ‘plasma’-resistors are strongly dependent on time [11] since the local number of electrons in the discharge gas depends on the passage of the ionisation wavefront.

capacitance between the wall and the metal tube at ground potential around the lamp. Tunitskii [15] and Abramov and Mazan’ko [16] critically survey the different views on discharge formation in long tubes as presented in the literature up till then. In the latter reference a model is proposed that confirms the RC-line picture and the fact that, initially only the active electrode and the environment of the tube play a role in the discharge formation. Horstman and Oude Lansink [11] performed measurements on the surface charge as well as on the speed of the ionisation front. In their description of the process they take into account the time dependence of the resistance of the discharge gas. At present, emission and surface charge measurements are performed by Gendre et al. [17] in a related project at our institute.

In this chapter, we will continue the research outlined above. We use a fluid model to study the breakdown phase in which the first ionisation front moves from the cathode to the anode (i.e. phase 1 in figure 5.1). Fluid models distinguish themselves from other modelling techniques by their low computational costs. Because of this feature it is worthwhile to consider the applicability of such a model to investigate breakdown in long tubes. It will be shown that it is capable of producing a picture that is qualitatively consistent with observations. The limitations in the applicability of a fluid model will be explored in order to be able to make statements on how to improve the numerical description of the breakdown process in long tubes.

This chapter is organised as follows: in the next section, the model we use is described, together with the system under consideration and the input data to the model. In section 5.3, we present simulation results on the temporal and spatial evolution of relevant quantities and on the influence of several control parameters on the breakdown process. Section 5.4 contains a discussion of these results and their interpretation and finally, in section 5.5, we summarise the main results presented in this chapter.

5.2 Description of the model

The model employed in this study is a two-dimensional fluid model that was originally developed to describe the plasmas used in display technology, such as plasma addressed liquid crystal (PALC) and plasma display panel (PDP). Since breakdown in long tubes

forms an application different from the one the model was originally developed for, we will discuss the main equations and assumptions of the model below. A complete description of the model is given in [8, 18]. Models based on similar equations have been employed by previous authors earlier (see e.g. [19, 20, 21, 22]).

5.2.1 Volume description

A fluid model can be based on balance equations derived from the Boltzmann transport equation. This equation describes the spatial and temporal development of the phase space density $f_p(\mathbf{x}, \mathbf{u})$ of an ensemble of equal particles of type p :

$$\frac{\partial f_p}{\partial t} + \nabla_x \cdot \mathbf{u} f_p + \nabla_u \cdot \mathbf{a} f_p = \left(\frac{\delta f_p}{\delta t} \right)_{\text{CR}} \quad (5.1)$$

in which \mathbf{a} is the acceleration of the particles under the influence of external forces. The subscript CR signifies the influence of collisions and radiation. Moments are taken from this equation in order to be able to approximate its solution. The first moment is obtained by integration of the above equation over velocity space. The resulting expression describes the continuity of particle species p in terms of its density n_p , flux $\mathbf{\Gamma}_p$ and source S_p as a function of time and space:

$$\frac{\partial n_p}{\partial t} + \nabla \cdot \mathbf{\Gamma}_p = S_p \quad (5.2)$$

The second moment of the Boltzmann transport equation is arrived at by multiplying equation (5.1) with the species' momentum $m_p \mathbf{u}_p$ and integrating it over velocity space. The resulting equation is called the momentum balance equation:

$$\frac{\partial n_p m_p \mathbf{u}_p}{\partial t} + \nabla \cdot (n_p m_p \mathbf{u}_p \mathbf{u}_p) = -\nabla \cdot \mathcal{P}_p + q_p n_p \mathbf{E} + \mathbf{R}_p \quad (5.3)$$

in which \mathcal{P}_p is the pressure tensor, q_p the charge of species p , \mathbf{E} the electric field and $\mathbf{R}_p = n_p m_p \mathbf{u}_p \nu_m$ the momentum source due to momentum transfer collisions with a frequency ν_m , based on the interactions with the background gas. The time-dependent term in equation (5.3) can be assumed to be zero, since collision frequencies are much larger than the inverse of the time scales involved in the application described in this contribution. The second term on the left hand side can be neglected, since there is no convective flow and since drift (i.e. directed) motion is assumed to be smaller than random motion. Furthermore, viscous dissipation can be neglected and the pressure can be assumed isotropic since the motion of particles is randomised by collisions. This allows the tensor \mathcal{P}_p to be replaced by the scalar pressure p_p . The pressure is related to the density n_p and the temperature T_p of the species p via $p_p = n_p k_B T_p$, in which k_B is the Boltzmann constant. Equation (5.3) can now be rewritten by combining the first and second term on the right hand side into a drift flux, and the first and third term into a diffusive flux. The resulting expression is the well known drift-diffusion equation:

$$\mathbf{\Gamma}_p = \pm \mu_p \mathbf{E} n_p - D_p \nabla n_p \quad (5.4)$$

where $\mu_p = e/(m_p\nu_m)$ represents the mobility and $D_p = \mathbf{u}_p^2/(3\nu_m)$ the diffusion coefficient of any of the species p described in the model. Here, e is the elementary charge and the \pm sign in the drift term indicates whether the sign of the charge q_p is positive or negative.

The source term S_p in equation (5.2) is obtained by considering the volume reactions in which particles are created or lost:

$$S_p = \sum_r c_{r,p} R_{r,p} = \sum_r \left[c_{r,p} k_r \prod_i n_i \right] \quad (5.5)$$

in which $R_{r,p}$ is the reaction rate and $c_{r,p}$ the stoichiometric number of particles of type p created or lost in the reaction of type r . The reaction rate depends on the densities n_i of the reacting species via the reaction coefficient k_r .

In the above equations the mobilities μ_p , the diffusion coefficients D_p and the reaction rates k_r are required in order to solve the equations. All these parameters generally are functions of the energy of the species under consideration. For the heavy particles the energy is assumed to be a function of the magnitude E/p of the local reduced electric field. The parameters $\mu_p(E/p)$ and $D_p(E/p)$ can be found in literature for many species. For the heavy charged particle species (the ions) we use the Einstein relation to link the diffusion to the mobility:

$$D_p = \frac{k_B T_p \mu_p}{e} \quad (5.6)$$

For the ions the temperature that is used in above equation is assumed to be dependent on the local electric field E according to [23]:

$$k_B T_p = k_B T_g + \frac{m_p + m_g}{5m_p + 3m_g} m_g (\mu_p E)^2 \quad (5.7)$$

where the subscript p denotes the ion under consideration and g the neutral gas. m is the mass of the species.

Due to the small mass of electrons as compared with the heavy particles, the assumption that the energy is directly related to the local field is often not valid for the electrons. Instead the electron related parameters are expressed as functions of the average energy $\bar{\varepsilon}$ of the electrons: $\mu_p(\bar{\varepsilon})$, $D_p(\bar{\varepsilon})$. Since, for the majority of the reactions considered, the electron is the most energetic particle, the reaction rate is also a function of the average electron energy for these reactions: $k_r(\bar{\varepsilon})$. The energy of the heavy species is neglected in the reaction rates. The average electron energy results from an energy balance equation:

$$\frac{\partial(n_e \bar{\varepsilon})}{\partial t} + \nabla \cdot \mathbf{\Gamma}_{\bar{\varepsilon}} = S_{\bar{\varepsilon}} \quad (5.8)$$

By assuming that the electron velocity distribution is isotropic we can relate the energy to a temperature by: $k_B T_e = \frac{2}{3} \bar{\varepsilon}$. This allows the Einstein relation (5.6) to be used for the electrons as well. In equation (5.8) the electron energy flux $\mathbf{\Gamma}_{\bar{\varepsilon}}$ is obtained from [6, 21]:

$$\mathbf{\Gamma}_{\bar{\varepsilon}} = -\frac{5}{3} \mu_e \mathbf{E} n_e \bar{\varepsilon} - \frac{5}{3} n_e D_e \nabla \bar{\varepsilon} \quad (5.9)$$

in which the first term on the right hand side is the hydrodynamic flux of enthalpy and the second term the heat conduction flux. The electron energy source term in equation (5.8) is:

$$S_{\bar{\varepsilon}} = -e\Gamma_e \cdot \mathbf{E} - \sum_r c_{r,p} \varepsilon_r R_r \quad (5.10)$$

in which the first term represents heating by the electric field and the second term the energy gained or lost in the various reactions. ε_r is the energy lost in reaction r by a single electron. This loss is taken to be equal to the reaction threshold.

In addition to the particle transport, as described by the equations above, the electric field \mathbf{E} also needs to be calculated: this is done by solving the Poisson equation:

$$\nabla \cdot (\epsilon \nabla \varphi) = -\nabla \cdot (\epsilon \mathbf{E}) = -\sum_p q_p n_p \quad (5.11)$$

in which φ is the electric potential as a function of time and space and ϵ the permittivity of the medium. The space on which the Poisson equation is solved is composed of several regions, one of which is the discharge region. Other sub-regions consist of materials that can be chosen from two specific types: electrodes with a user-defined potential, and dielectrics with given permittivities ϵ .

5.2.2 Wall-interaction description

The boundary conditions for the particle transport equations represent what happens at the discharge edge. The boundary conditions used here are described in [24]. We will treat them briefly below.

For the heavy particles the flux Γ_p directed to the surface in drift-diffusion conditions is given by [25, 24]:

$$\Gamma_p \cdot \mathbf{e}_n = \pm a_p \mu_p (\mathbf{E} \cdot \mathbf{e}_n) n_p + \frac{1}{4} v_{th,p} n_p - \frac{1}{2} D_p (\nabla n_p \cdot \mathbf{e}_n) \quad (5.12)$$

where \mathbf{e}_n is the normal vector pointing towards the surface and a_p a parameter that equals one if the drift velocity $q_p \mu_p \mathbf{E}$ is directed to the wall and zero otherwise. $v_{th,p}$ is the thermal velocity of the species and is given by

$$v_{th,p} = \sqrt{\frac{8k_B T_p}{\pi m_p}} \quad (5.13)$$

with T_p the temperature given by equation (5.7) for the heavy particles and calculated from $\bar{\varepsilon}$ in the case that p represents the electrons. By using equation (5.4) for the region at the boundary, equation (5.12) can be rewritten in the form which is used in this model:

$$\Gamma_p \cdot \mathbf{e}_n = \pm (2a_p - 1) \mu_p (\mathbf{E} \cdot \mathbf{e}_n) n_p + \frac{1}{2} v_{th,p} n_p \quad (5.14)$$

For the electrons the situation is more complicated since, in addition to the terms in equation 5.12, also the flux $\mathbf{\Gamma}_\gamma$ due to secondary emission and due to thermal emission need to be taken into account:

$$\mathbf{\Gamma}_\gamma \cdot \mathbf{e}_n = (1 - a_e) \left[\mathbf{\Gamma}_t \cdot \mathbf{e}_n - \sum_p \gamma_p (\mathbf{\Gamma}_p \cdot \mathbf{e}_n) \right] \quad (5.15)$$

in which γ_p represents the yield of secondary electrons per incident ion of species p and $\mathbf{\Gamma}_p$ the flux of these ions, $\mathbf{\Gamma}_t$ is the thermal emission flux and is an input parameter to the model for electrode materials only. Merely adding (5.15) to the right hand side of equation (5.14) does, however, not result in a satisfactory expression for the electrons since in this way the secondary electrons wrongly add to the drift-diffusion flux via their contribution to n_e . Distinguishing between α -electrons coming from the bulk and γ -electrons due to secondary and thermal emission leads to the expression to be used instead of equation (5.14) for the electrons:

$$\mathbf{\Gamma}_\alpha \cdot \mathbf{e}_n = -(2a_e - 1) \mu_\alpha (\mathbf{E} \cdot \mathbf{e}_n) n_\alpha + \frac{1}{2} v_{th,e} n_\alpha \quad (5.16)$$

The sum of the two fluxes (5.15) and (5.16) is then used as the boundary condition for the total electron flux. In order to calculate the flux due to α -electrons, their density n_α needs to be known. This is obtained from the knowledge that $n_\alpha = n_e - n_\gamma$ and the following expression which results from combining (5.4) and (5.16):

$$n_\gamma = (1 - a_e) \frac{-\mathbf{\Gamma}_t \cdot \mathbf{e}_n + \sum_p \gamma_p (\mathbf{\Gamma}_p \cdot \mathbf{e}_n)}{\mu_e (\mathbf{E} \cdot \mathbf{e}_n)} \quad (5.17)$$

The contribution due to the diffusion term in equation (5.4) has been neglected here: in situations in which secondary emission is important this is a valid assumption since the field near the surface will generally be high.

For the electron energy transport equation the boundary condition results from an equivalent derivation, resulting in:

$$\begin{aligned} \mathbf{\Gamma}_\varepsilon \cdot \mathbf{e}_n = & -(2a_e - 1) \frac{5}{3} \mu_e (\mathbf{E} \cdot \mathbf{e}_n) n_\varepsilon + \frac{2}{3} v_{th,e} (n_\varepsilon - n_{\varepsilon,\gamma}) \\ & + 2(1 - a_e) \left[\bar{\varepsilon}_t (\mathbf{\Gamma}_t \cdot \mathbf{e}_n) - \sum_p \gamma_p \bar{\varepsilon}_p (\mathbf{\Gamma}_p \cdot \mathbf{e}_n) \right] \end{aligned} \quad (5.18)$$

Finally the surface charge σ on dielectric materials at time t results from charged particles striking the wall:

$$\sigma = \int_0^t \left[\sum_p q_p (\mathbf{\Gamma}_p \cdot \mathbf{e}_n) \right] dt' \quad (5.19)$$

This charge is included in the Poisson equation (5.11) as an additional term on its right hand side.

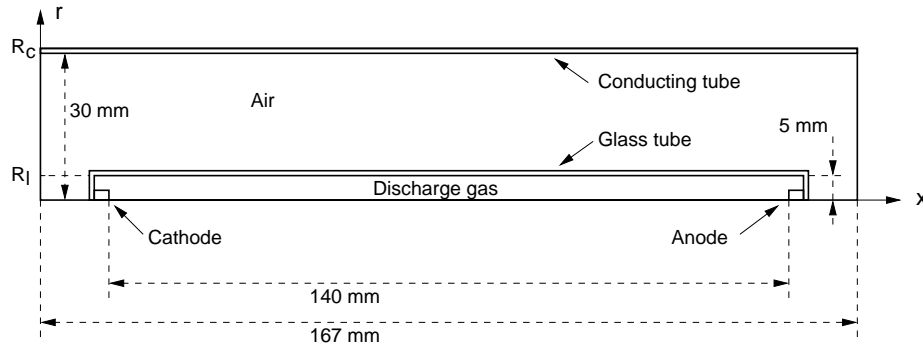


Figure 5.3: The geometry and the relevant sizes of the system under consideration. Note that the geometry is cylindrically symmetric around the x -axis.

5.2.3 System under consideration

The system to which we will apply the model is a long straight discharge tube containing argon at a pressure of a few Torr. In figure 5.3, the layout of the numerical grid describing this system is shown. This geometry is the numerical equivalent of the experimental set-up used in reference [17] and is a straight idealisation of the fairly common compact fluorescent lamp.

The lamp consists of a glass tube with an inner radius R_l of 5 mm. The distance between the electrodes is 140 mm. To have the electrical environment of the lamp well defined, it is surrounded by a conducting tube with an inner radius R_c of 30 mm, at ground potential. The lamp is driven at a dc voltage: the anode stays at ground potential, the cathode is set to a negative potential in the range of typically 300 – 600 V. The cathode is heated to a temperature at which thermal electron emission occurs in order to have a supply of electrons during the breakdown process.

The equations relating to the evolution of particle densities are solved within the discharge region (marked ‘discharge gas’ in figure 5.3). The Poisson equation is solved on the entire grid, which in addition to the discharge region thus also contains the glass envelope, two electrodes, the surrounding ‘vacuum’ and the cylinder at ground potential. This grid consists of 335×62 square grid cells.

5.2.4 Input data for the model

As mentioned earlier, the input data needed in order to solve the equations that describe the dynamics of the various particle species are the diffusion coefficients and mobilities of the various particle species and the reaction rates of the reactions considered. Since the ionisation degree is low, the density and temperature of the argon ground state atoms are assumed to be constant. The time evolution of the following species are described: two excited states Ar^* and Ar^{**} , the first ion state Ar^+ and the electrons e . The excited states are ‘effective’ states in which different levels have been lumped together, similar to the method used by Vasenkov and Kushner [26]: the four energy levels in the 4s manifold are

Table 5.1: The transport coefficients used by the model. For the electrons the coefficients are converted to be functions of the mean electron energy ε after the data is read by the model. The E/p vs. ε table that is required for this was obtained from Bolsig [27].

Species p	μ_p (Torr cm ² V ⁻¹ s ⁻¹)	D_p (Torr cm ² s ⁻¹)	Ref.
e	fig. 5.4	eq. (5.6)	[27, 25]
Ar^*	-	64.0	[28]
Ar^{**}	-	64.0	[28]
Ar^+	fig. 5.4	eq. (5.6)	[23]

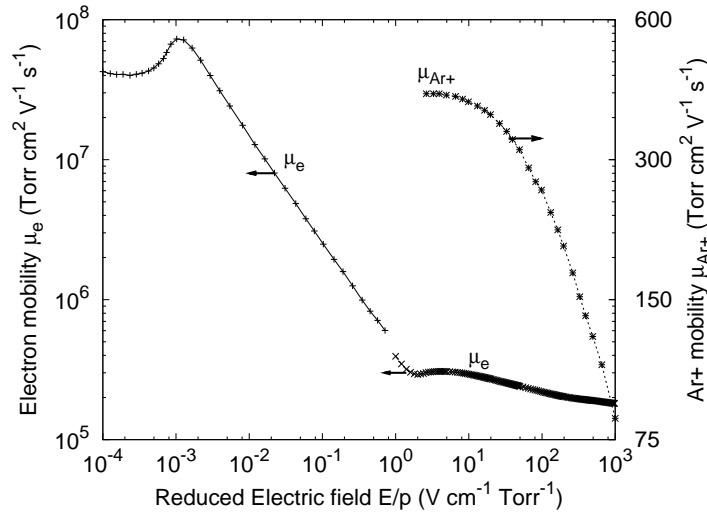


Figure 5.4: The mobility of the electrons and the argon ions. The data for the electrons originate from reference [25] for $E/p < 1.0 \text{ Vcm}^{-2}\text{Torr}^{-1}$ and from Bolsig [27] calculations for $E/p \geq 1.0 \text{ Vcm}^{-2}\text{Torr}^{-1}$. The data for the argon ions were obtained from reference [23].

represented by Ar^* and similarly Ar^{**} refers to the 4p manifold and higher energy levels.

In table 5.1 the transport coefficients used in equation (5.4) are listed for the four species considered. For the charged species the diffusion coefficient is calculated from the mobility via equation (5.6). The data for the ions have been taken from [23]. For the electrons the mobility at low reduced electric field values ($E/p \leq 1.0 \text{ Vcm}^{-2}\text{Torr}^{-1}$) was taken from [25] and for high reduced electric field values from calculations with the Boltzmann solver Bolsig [27] (figure 5.4).

The reactions considered in the model are listed in table 5.2. The rate coefficients of reaction 0 – 9 have been calculated using the electron energy distribution functions $f(E/p, \varepsilon)$ as calculated by Bolsig [27] for various reduced electric field values:

$$k_r(E/p) = \sqrt{\frac{2}{m_e}} \int_n^\infty \sigma_r(\varepsilon) f(E/p, \varepsilon) \sqrt{\varepsilon} d\varepsilon \quad (5.20)$$

Table 5.2: Reaction coefficients used by the model. The reaction rate coefficients 0 – 9 have been calculated by the Boltzmann solver Bolsig [27]. The cross sections used for this were obtained from the references listed in the table.

Nr.	Reaction	Coeff. k_r	Ref.
0	$\text{Ar} + e \rightarrow \text{Ar} + e$	refer to the text	[29]
1	$\text{Ar} + e \rightarrow \text{Ar}^* + e$	see fig. 5.5	[30]
2	$\text{Ar} + e \rightarrow \text{Ar}^{**} + e$	see fig. 5.5	[30]
3	$\text{Ar} + e \rightarrow \text{Ar}^+ + 2e$	see fig. 5.5	[29]
4	$\text{Ar}^* + e \rightarrow \text{Ar} + e$	see fig. 5.5	[30] ^a
5	$\text{Ar}^* + e \rightarrow \text{Ar}^{**} + e$	see fig. 5.5	[31]
6	$\text{Ar}^* + e \rightarrow \text{Ar}^+ + 2e$	see fig. 5.5	[32]
7	$\text{Ar}^{**} + e \rightarrow \text{Ar} + e$	see fig. 5.5	[30] ^a
8	$\text{Ar}^{**} + e \rightarrow \text{Ar}^* + e$	see fig. 5.5	[31] ^a
9	$\text{Ar}^{**} + e \rightarrow \text{Ar}^+ + 2e$	see fig. 5.5	[33]
10	$\text{Ar}^* + \text{Ar}^* \rightarrow \text{Ar}^+ + \text{Ar} + e$	$1.2 \times 10^{-9} \text{ cm}^3 \text{ s}^{-1}$	[34]
11	$\text{Ar}^* + \text{Ar}^{**} \rightarrow \text{Ar}^+ + \text{Ar} + e$	$1.2 \times 10^{-9} \text{ cm}^3 \text{ s}^{-1}$	[34]
12	$\text{Ar}^{**} + \text{Ar}^{**} \rightarrow \text{Ar}^+ + \text{Ar} + e$	$1.2 \times 10^{-9} \text{ cm}^3 \text{ s}^{-1}$	[34]
13	$\text{Ar}^* + e \rightarrow \text{Ar}_r^* + e$	$2.0 \times 10^{-7} \text{ cm}^3 \text{ s}^{-1}$	[35, 36]
14	$\text{Ar}_r^* \rightarrow \text{Ar} + h\nu$	$2.0 \times 10^6 \text{ s}^{-1}$	^b
15	$\text{Ar}^{**} \rightarrow \text{Ar}^* + h\nu$	$3.0 \times 10^7 \text{ s}^{-1}$	^b

a: from the forward reaction using microscopic reversibility.
 b: calculated using estimated free photon path lengths.

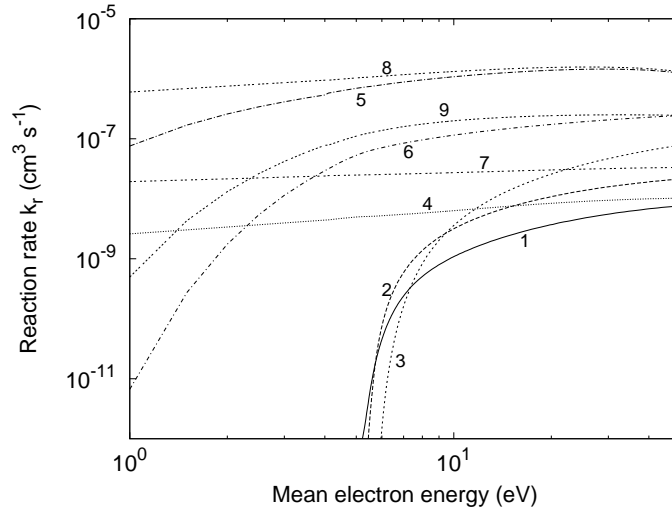


Figure 5.5: The reaction rate coefficients of the various reactions included in the model. The numbers close to the curves indicate the corresponding entry in table 5.2.

From $f(E/p, \varepsilon)$ a function has been calculated which relates the average energy $\bar{\varepsilon}$ to the reduced electric field E/p . With this expression, the reaction rates were finally written as functions of the mean electron energy: $k_r(\bar{\varepsilon})$. The cross sections $\sigma_r(\varepsilon)$ have been taken from the references listed in the table. This set is similar to the one used in [26]. The rate for reaction 0 is treated differently from those for the other reactions: the input to the model for this rate coefficient was determined by multiplying the integrand in equation (5.20) with $(2m_e/m_g)\varepsilon$ to account for the energy exchange in the elastic collisions with the stationary and homogeneous Ar background gas. The rate for this reaction is specified in units of $\text{eV s}^{-1}\text{Torr}^{-1}$, instead of cm^3s^{-1} . An increase of temperature of the background gas due to this momentum exchange is neglected.

In order to account for the loss of excited states via spontaneous emission, an approach similar to the one used in [36] has been followed: the metastable states in the 4s manifold contribute most to the electron impact cross section of the total manifold and therefore Ar^* is treated as a metastable state. In order to do account for radiation of the resonant states, an extra species Ar_r^* is introduced which represents the two non-metastable states of the 4s manifold. In reaction 13, the Ar^* state is collisionally quenched to Ar_r^* which can then fall down to the ground state via spontaneous emission in reaction 14. Ar^{**} can directly fall down via spontaneous emission to the Ar^* state in reaction 15. The effective lifetimes of the two spontaneous emission reactions have been estimated by considering the number of reabsorption events before a photon can leave the discharge region.

5.3 Simulation results

The model described above was used to study breakdown processes in the lamp shown in figure 5.3. Results are shown here for the phase in which the first ionisation front crosses the tube from cathode to anode. The suitability of the model for later phases is discussed in section 5.4. First, the physics will be considered for one specific situation. Subsequently, variations will be made to single parameters in order to study their influence on the breakdown process.

5.3.1 Breakdown evolution

The evolution of several quantities during breakdown was studied by means of one set of control parameters: the geometry as depicted in figure 5.3 and described in section 5.2.3. Furthermore, the cathode voltage was constant at -450 V and the gas pressure was 3.0 Torr . The thermal emission from the cathode was set to $1 \times 10^{17}\text{ cm}^{-2}\text{s}^{-1}$, which for an electrode with a work function of 2 eV , corresponds to a temperature of about 1000 K via the Richardson-Dushman equation [3]. This value is typical for real lamps, although it should be noted that the true flux in experiments is difficult to estimate due to the complex geometry of the electrode filament.

In order to make the link to the experimental observation depicted in figure 5.1, the time evolution of the rate of spontaneous emission from Ar^* to Ar^{**} (reaction 15) is plotted in

figure 5.6. Note that the voltage chosen above is not the same as that used in the experiment that produced figure 5.1. In the experiment, the voltage had a rise-time of $3.0\ \mu\text{s}$ and a final level of $-400\ \text{V}$. Here, we chose a voltage of $-450\ \text{V}$, without a rise-time. The reason for this was that at these settings the simulation results provided a more insightful picture of the breakdown phenomena than at the settings used in the experiment. Related to this choice was also the qualitative nature of the agreement between model and experiments. This is discussed in more detail in section 5.4.

Nedospasov and Novik [14] already showed that the charging of the wall displaces the region of strong electric field. Starting at this insight, the evolution of various plasma quantities was examined. These are shown in figures 5.7–5.12.

In figure 5.7, the amount of charge on the wall for various instants in time is shown. It can be seen that as time increased the surface charge profile extended in the tube. The effect that this charge had on the solution of the Poisson equation can be seen in figure 5.8, in which the magnitude of the field on the axis of the lamp is depicted. At $t = 0$, the Poisson equation is free of the sources and its solution shows a large field near the cathode, due to the radial symmetry introduced by the grounded cylinder around the lamp. At later times the charges in the lamp deform the field in such a way that the region of large electric field is moved within the lamp towards the anode. These charges mainly sit on the wall, although there is some net charge within the plasma as well.

The effect of the wall and volume charges is demonstrated in a different way in figure 5.9, which shows the equipotential lines on the entire computational grid for two instants in time: $t = 0.0$ and $2.0\ \mu\text{s}$. The fact that the surface charge profile develops like it does during breakdown is the result of the interplay of the effect of the surface charge with the plasma. If the field is sufficiently high, the electrons can gain enough energy to be able to experience inelastic collisions with the background gas, so that new plasma is created which facilitates the propagation. As a result, the main region of plasma production moves along with the displacement of the high field region.

Immediately after the application of the voltage, the radial profile of the electron density (which is not shown) peaks near the wall. This is caused by the strong radial field which initially initiates the breakdown between the electrode and the nearby wall. In later stages, when the ionisation front has travelled further into the tube, the plasma production becomes stronger in the centre of the tube: the radial density profile becomes first flat, falling off steeply at the wall and then tends more to parabolic.

In figure 5.10 the density of the electrons on the axis of the lamp is shown for various instants in time. It is interesting to note here that the density did indeed increase sharply at the position of the front, as expected, but also that the density remained almost constant in the part of the lamp that was already traversed by the ionisation region.

Figure 5.11 shows the mean energy of the electrons, which was about $6 - 7\ \text{eV}$ in and behind the active region. Finally figure 5.12 shows the production rate of ions. As one could already see in figure 5.6, the maximum in the reaction rates decreased as the ionisation front traversed through the lamp. This can be ascribed to the fact that the gradients in the wall charge profile and in the potential profile in the lamp are attenuated as time passes.

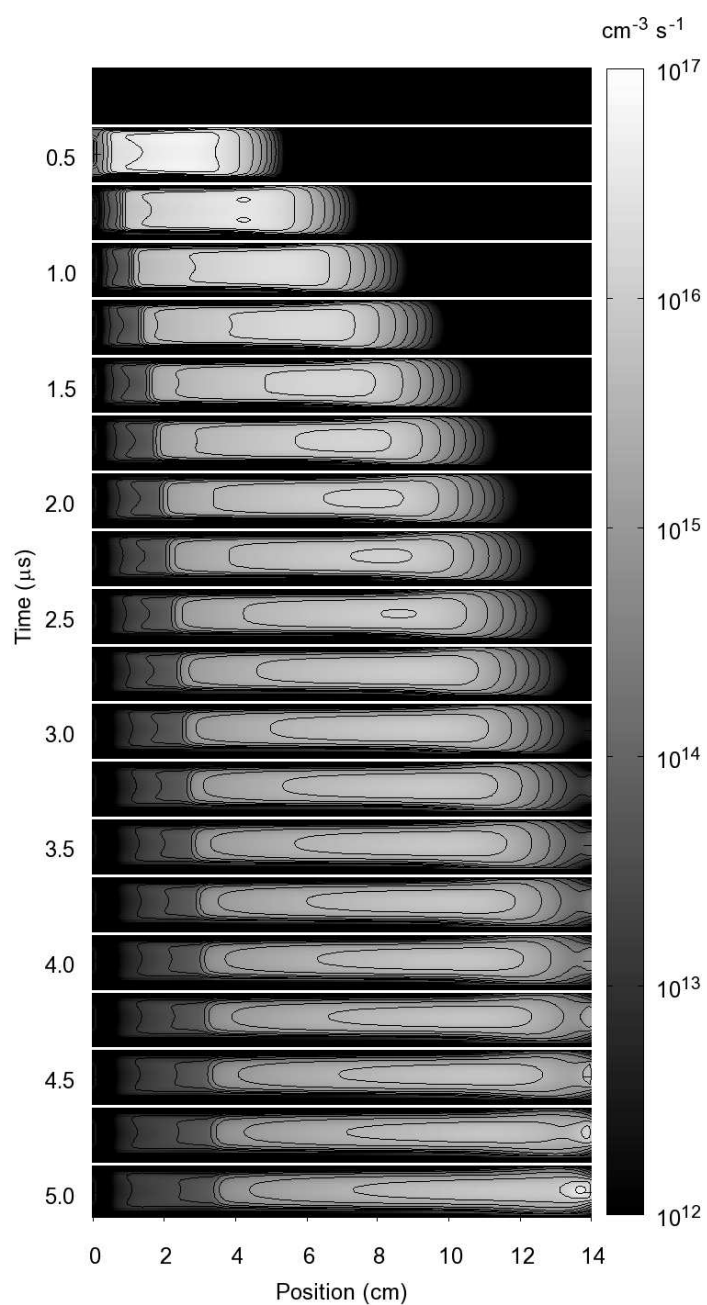


Figure 5.6: A ‘film’ of the calculated reaction rate of spontaneous emission from Ar^{**} to Ar^* in the entire tube. The subsequent frames, spaced $0.25 \mu\text{s}$ in time, are concatenated in the vertical direction. Although similar, this figure is not to be compared directly with figure 5.1 since in the experiment the voltage is different and has a rise-time of $3 \mu\text{s}$, due to technical restrictions. However, in qualitative terms the important features are the same: the velocity and the intensity of the emission profile become smaller as time passes.

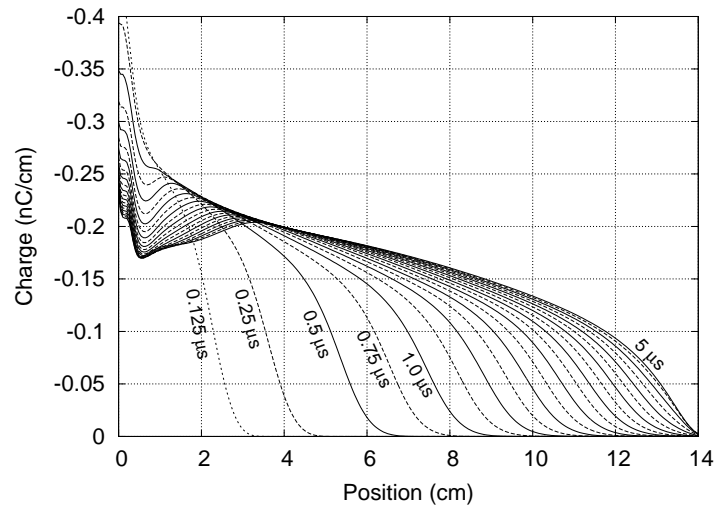


Figure 5.7: The charge per unit length deposited at the wall, for various instants in time. As time progresses the profile extends towards the anode. This is due to the fact that the active region of the discharge profile moves along with the slope in this charge profile, and deposits new electrons just in front of it.

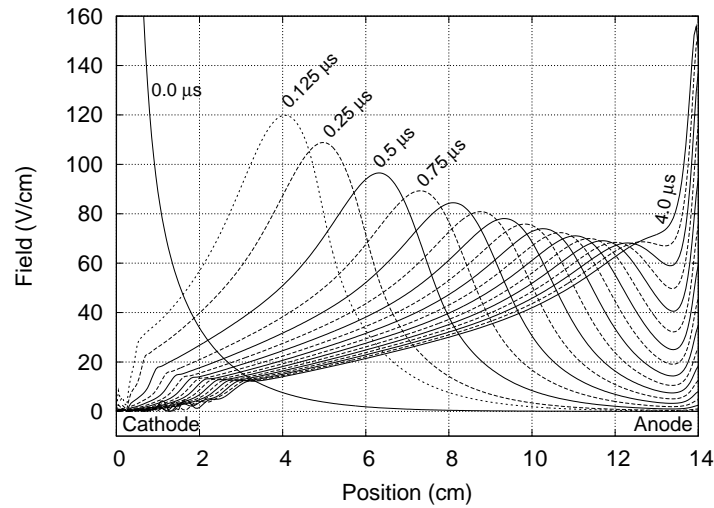


Figure 5.8: The magnitude of the electric field at the axis for various instants in time. Its evolution is mainly determined by the surface charge (cf. figure 5.7) deposited on the inner wall of the tube. The potential at $t = 0$ is not linear between the electrodes because of the radial term that arises in the sourceless Poisson (i.e. Laplace) equation due the grounded tube that surrounds the lamp.

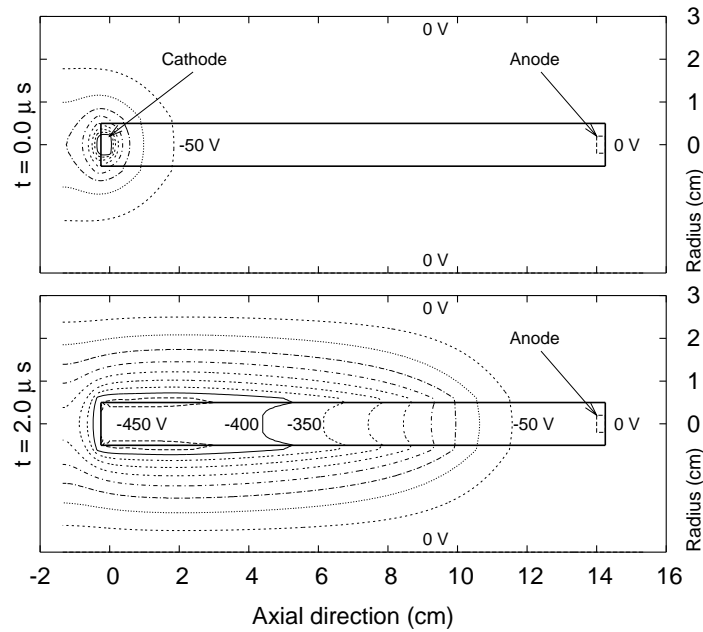


Figure 5.9: Contour plots of the electric potential on the numerical grid at $t = 0.0 \mu\text{s}$ (top) and $t = 2.0 \mu\text{s}$ (bottom). Note that in the lower plot, in the wake of the ionisation front, the potential in the tube is peaked compared to the potential at the adjacent wall. This indicates the presence of a net positive charge in the developing plasma.

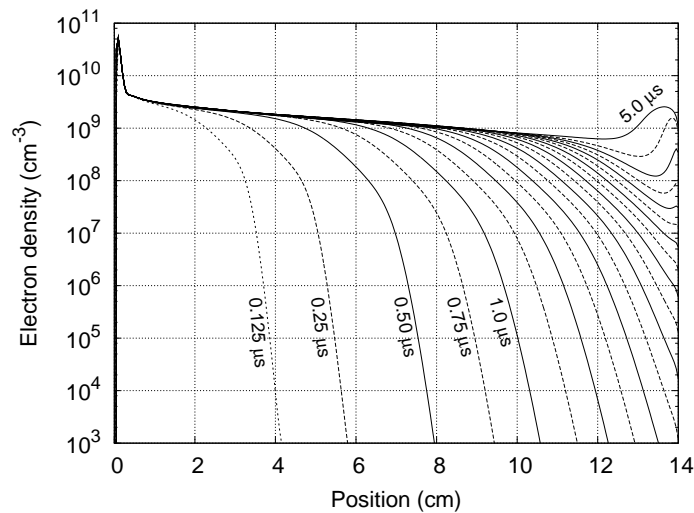


Figure 5.10: The electron density at the axis for various instants in time. One can see that the density profile extends in the tube in accordance with the displacement of the high electric field region, as observed in figure 5.8. Furthermore, in the region behind the ionisation front the density stays at a more or less constant level.

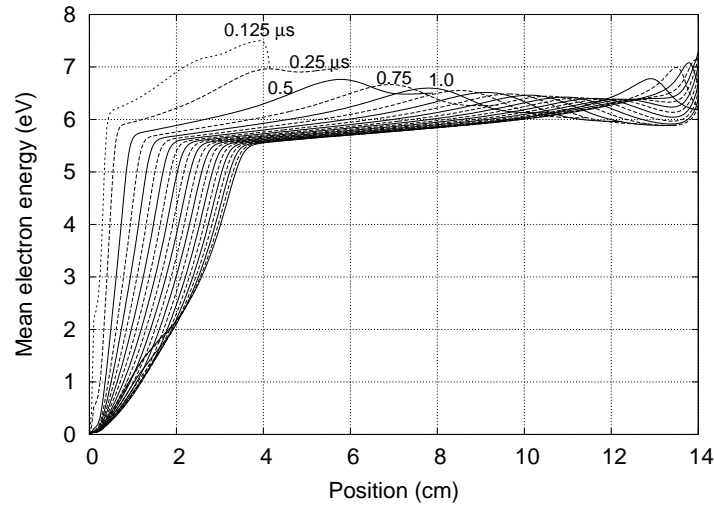


Figure 5.11: The mean electron energy at the axis for various instants in time. The part of the curves for which the corresponding electron density of figure 5.10 drops below 10^3 cm^{-3} have been omitted. For these parts the curves do not give any information since the energy density contained in the electron group is negligible there.

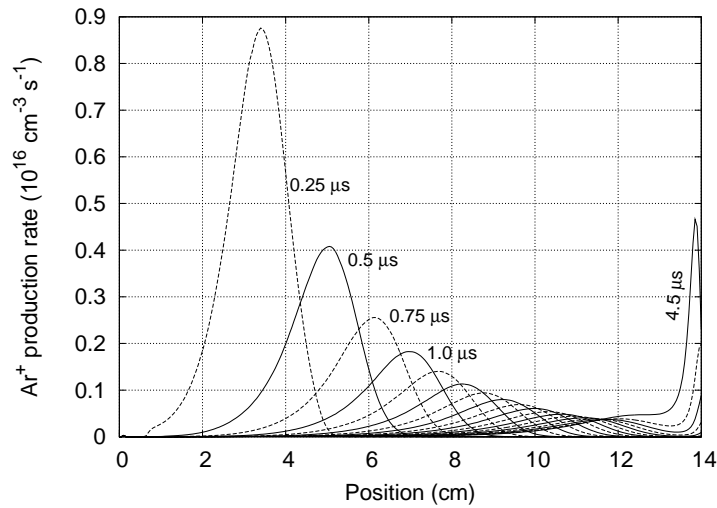


Figure 5.12: The production rate of electron-ion pairs at the axis for various instants in time. Together with figure 5.6 this figure shows that the intensity of the reactions reduces as the ionisation front progresses through the tube.

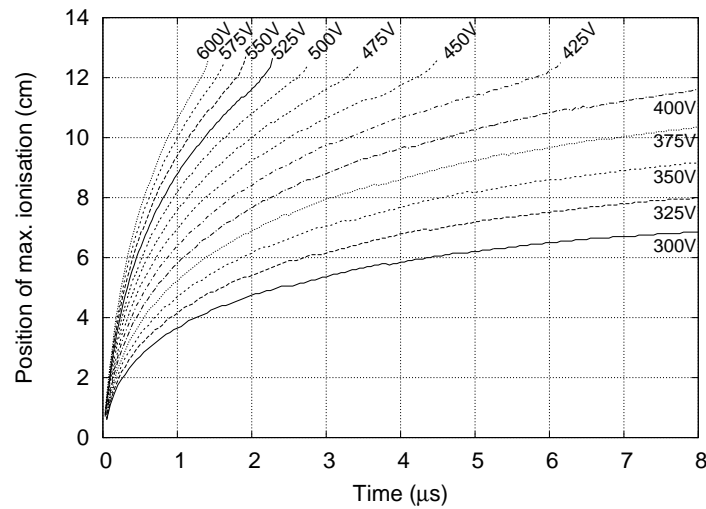


Figure 5.13: The influence of the applied cathode voltage on position of the maximum in ionisation at the axis as a function of time. From the graphs one can read that the speed of the front decreases monotonically while the front traverses through the tube. Furthermore, the speed is lower for lower applied voltages, and if the voltage is too low, the front will not make it to the anode.

5.3.2 Parameter variations

In section 5.3.1, the physics of the breakdown process was considered for one specific situation. In this section, the influence of variation of control parameters on the breakdown process is investigated. The influence of those parameters is also of technological importance since they can be altered by lamp manufacturers. Direct control parameters in the experiments are of course the voltage applied to the lamp and the thermal emission of the electrodes. The latter quantity is determined by the heating current through the electrode filaments. We repeat that, due to the complex geometry of the electrodes, the relation between heating current and thermal emission flux is difficult to establish.

In figure 5.13 the position of the maximum in electron-ion pair production is shown as a function of time for various applied voltages. The gradient in this quantity represent the velocity of the ionisation front. As can be seen, the velocity decreased monotonically for each curve, which is consistent with observations made in the experiments of which an example is shown in figure 5.1. Figure 5.13 shows that the time it took the front to cross the space between the two electrodes was smaller for higher voltages. This time, to which we will refer with the term ‘crossing time’, is shown as a function of voltage in figure 5.14. Note that if the voltage was too low, the ionisation front did not reach the anode: the lamp failed to ignite.

Figure 5.15 shows the influence of the thermal emission of the cathode on the crossing time for several applied voltages. If the thermal emission flux was too low, the crossing time tended to infinity, which means that the front did not reach the anode. The point at which this happened was quite dependent on the applied voltage. For high thermal

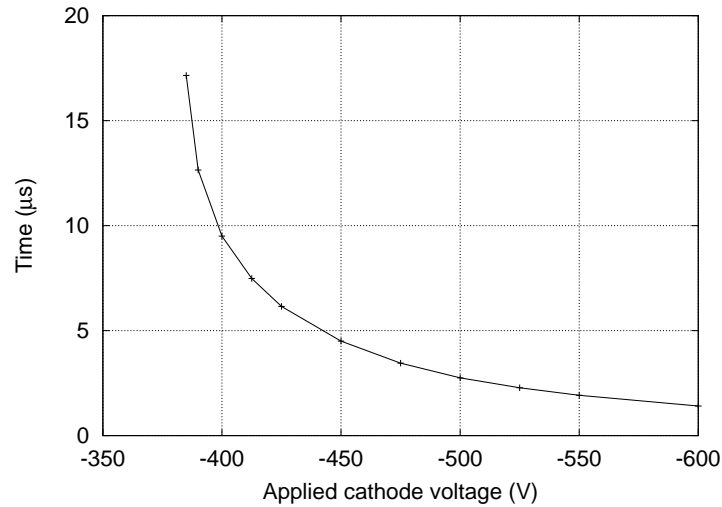


Figure 5.14: The influence of the applied cathode voltage on the crossing time (i.e. the time it takes the ionisation front to reach the anode). If the voltage is too low the front will not reach the anode: the lamp does not ignite.

emission fluxes ($> 10^{17} \text{ cm}^{-2}\text{s}^{-1}$) the behaviour was virtually independent of the flux.

The influence of the pressure of the filling gas on the crossing time is plotted in figure 5.16 and the influence of the radius R_c of the conductor is shown in figure 5.17. If the applied voltage is low, the influence of the parameter variation on the crossing time is large. For higher applied voltages, the influence remains but is less pronounced. These effects will be discussed in more detail in section 5.4.2.

5.4 Discussion

Here, the simulation results presented in the previous section are discussed. First, the analogy of the lamp with an RC-line is treated. Subsequently, the influence of control parameters is discussed. Finally, the assumptions made in the fluid model and the resulting applicability of the fluid model to breakdown in long tubes are discussed.

5.4.1 Phenomenological behaviour

As already mentioned in section 5.1 and illustrated in figure 5.2, during breakdown one can consider the configuration of a lamp within a conducting cylinder at ground potential in a first approximation as a distributed capacitor. The capacitance of a configuration of two coaxial cylinders of infinite length can be easily calculated by first imagining a third cylindrical surface S of radius r . The radially directed field \mathbf{E} at this surface is obtained

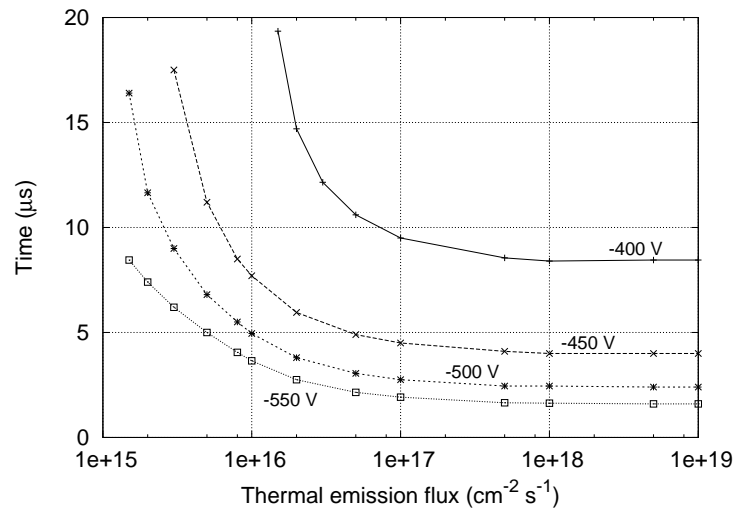


Figure 5.15: The influence of the thermal electron flux at the cathode on the crossing time. In experiments the electrode temperature is the quantity that determines the thermal emission flux, via the Richardson-Dushman equation. The temperature is regulated with a heating current through the electrode filament.

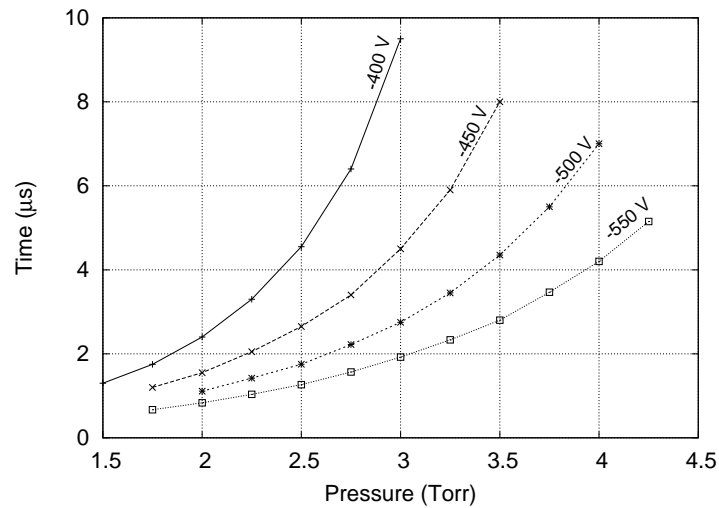


Figure 5.16: The influence of the Ar filling pressure on the crossing time.

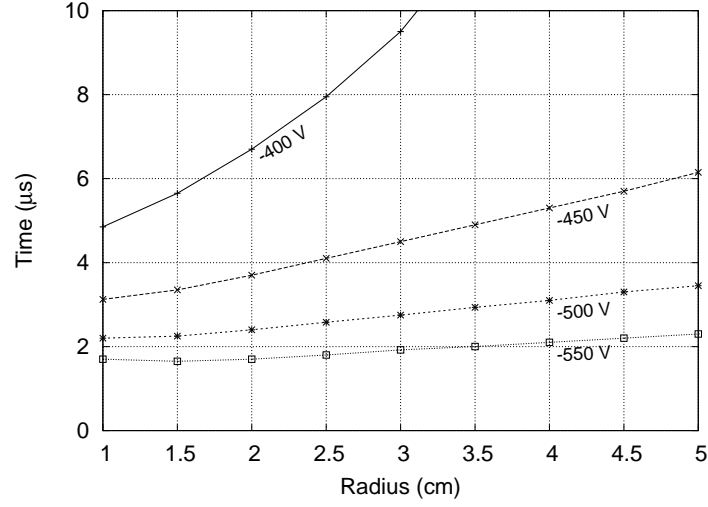


Figure 5.17: The influence of the radius R_c of the grounded tube around the lamp on the crossing time.

by applying Gauss' law to the Poisson equation:

$$\int_S \mathbf{E} \cdot d\mathbf{A} = 2\pi r E = \frac{1}{\epsilon} \frac{Q}{L} \quad (5.21)$$

$$E = \frac{1}{2\pi r \epsilon} \frac{Q}{L} \quad (5.22)$$

in which Q/L represents the charge enclosed per unit length and ϵ the dielectric permittivity of the medium between the two cylinders. The potential φ between the two cylinders results from integrating \mathbf{E} over a path connecting them:

$$\varphi = - \int_{r_1}^{r_2} \mathbf{E} \cdot d\mathbf{l} = - \frac{1}{2\pi \epsilon} \frac{Q}{L} \ln \left(\frac{r_2}{r_1} \right) \quad (5.23)$$

in which r_1 and r_2 are the radii of the inner and outer cylinders respectively. The capacitance per unit length C/L of two coaxial cylinders in the infinite length limit is the proportionality constant between Q/L and φ :

$$\frac{C}{L} = \frac{2\pi \epsilon}{\ln(r_2/r_1)} \quad (5.24)$$

Neglecting fringe fields that result from the finite extent of the tube sections and neglecting the difference in permittivity of the glass and the air between the two tubes, we can estimate the charge (in C/cm) that is necessary to bring a section of the lamp wall to the cathode potential V_C :

$$\frac{Q}{L} = \frac{C}{L} \cdot V_C = 3.1 \times 10^{-13} V_C \quad (5.25)$$

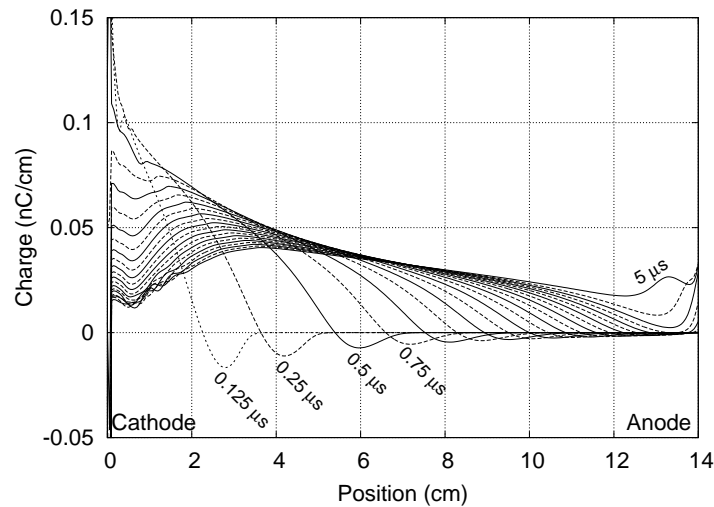


Figure 5.18: The linear charge density in the volume of the lamp, for various instants in time. One can see that the ionisation front is negatively charged and that the region it leaves behind is positively charged.

In figure 5.7 the linear charge density at the wall, as found by the model, is depicted. This figure illustrates that indeed the wall can be viewed as a distributed capacitor of which each subsequent section charges as the ionisation front moves along. The charge that is predicted by equation (5.25) for the applied cathode voltage is 0.14 nC/cm . The model predicts a larger value, as can be read from figure 5.7. This can be ascribed to the presence of a charge *within* the volume of the lamp: in the wake of the ionisation front a plasma develops which is net positive. This charge enters equation (5.21) and should thus be added to the surface charge in order to correctly describe the situation.

Figure 5.18 shows the linear charge density within the volume of the lamp. Adding a curve in this figure to the corresponding surface charge curve in figure 5.7 results in a values which match the number predicted by equation (5.25). This is illustrated as well by figure 5.19, in which the sum of all the charges within the tube is shown as a function of time. If the final level of the net charge is divided by the length of the lamp, we obtain the 0.14 nC/cm as predicted above.

In figure 5.20 an artist impression is shown of the distribution of the various charges within the lamp: during the progression of the ionisation front the inner wall of the tube is coated with electrons. Together with the induced positive charges at the shielding tube, these charges deform the field within the lamp such that the cathode potential extends towards the ionisation front. The large mobility of the electrons allows them to move faster than the ions. This results in the situation where the ionisation front itself is negatively charged and the amount of charge on the wall is larger than the induced charge in the shielding tube. A net positive plasma remains in the volume behind the ionisation front. This plasma forms a conductor that is capable of providing a current from the cathode to the ionisation front.

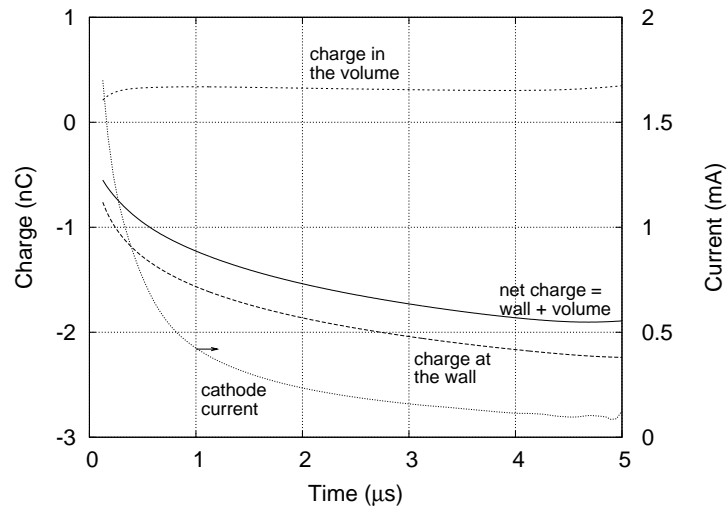


Figure 5.19: The net charge in the lamp as a function of time. Due to the fact that there is no conducting path between the cathode and the anode, the cathode current adds to the charge within the lamp.

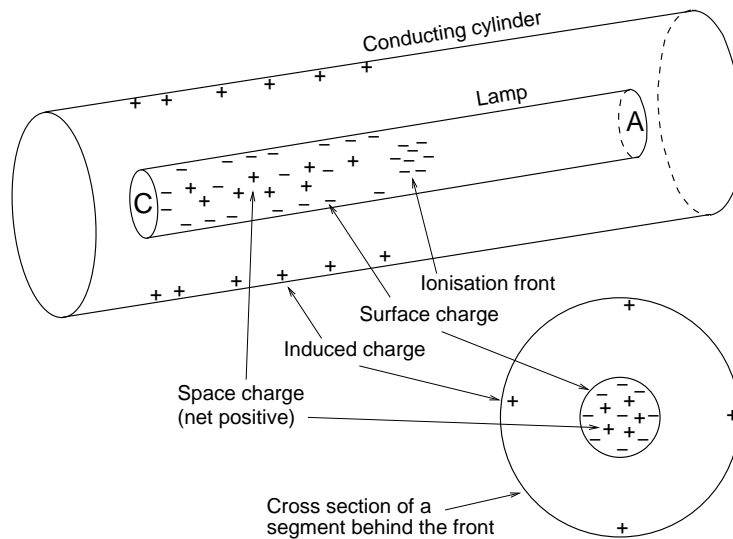


Figure 5.20: An impression of the distribution of charges in the system while the ionisation front is progressing through the tube. The charge at the inner surface of the lamp tube is larger than the induced charge in the surrounding conductor. This is a result of the fact that the positive charge in the volume should be taken into account since it cancels some of the charge at the wall.

With the picture outlined above, an observation made in recent experiments [17] can be explained. In these experiments, and indeed in the simulations (see figure 5.14), if the voltage applied to the lamp is too low, the ionisation front will not reach the anode. If this happens, it has been observed that it is more difficult to ignite the lamp up to minutes later: i.e. higher voltages are necessary to realize breakdown in the lamp than would have been the case if the previous breakdown had been successful.

This behaviour can be explained by looking at the net charge present in the lamp, both in the discharge volume and at the wall. During normal lamp operation the total amount of negative charges is equal to the sum of the positive charges. In such a case, when the discharge is switched off, the charges will diffuse and recombine. As can be seen from figure 5.19, during the first phase of breakdown, the net charge within the lamp is not equal to zero. When the breakdown process stops in this phase, the charges of opposite sign will recombine until there are no positive charges left. The remaining negative charges will eventually end up on the wall and stay there. Via equation (5.23), these charges will attenuate the potential between the cathode and the wall during a next ignition attempt, making it more difficult for the lamp to ignite.

A related observation in the experiments is that if the ionisation front does reach the anode, the lamp is guaranteed to successfully continue its path to electrical breakdown. This can be explained by noting that after the first phase is completed, a path of sufficient conductance has been established between the cathode and anode. A current now runs between the cathode and the anode of the lamp and, due to the negative current-voltage characteristics of the plasma, its conductivity will rise and with it the current through the plasma. This will happen as long as the power supply is capable of maintaining the voltage across the lamp and is capable of delivering the required current, as was the case in the experiments. In [11], a measurement of the cathode current shows this increase.

5.4.2 Influence of control parameters

The results presented in section 5.3 and the above discussion have confirmed once more that the charge buildup on the wall drives the region with the highest electric field forward. This means that the rate of surface charge deposition is the determining factor for the speed of the ionisation front: the ability of the discharge to supply the necessary electrons is essential for its evolution. There are two ways in which the electrons that will coat the wall can be generated: electrons can be supplied from the heated electrode and drift towards the active region and/or they can be produced by volume ionisation. But, as we have seen in the previous subsection, the latter generates an equal amount of positive charge and will, therefore, not directly aid the effect as illustrated in figure 5.2. Indirectly, the ions can decrease the surface charge at one position by secondary emission and thereby allow charge to be deposited at other places.

The influence of the different control parameters resides in the effect that, in one way or another, they can prevent or augment the supply of electrons to coat the wall near the active region. An increase in the applied voltage means an increase in the electric field. The reaction rates are dependent on the electric field, via the electron energy. This

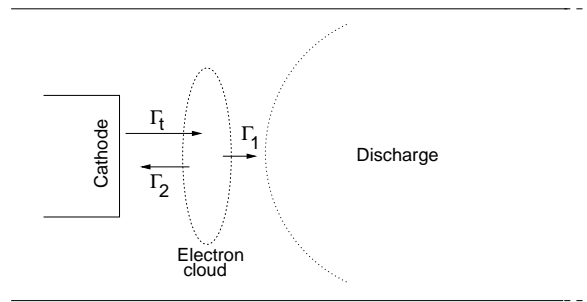


Figure 5.21: Schematic picture of the influence of the thermal emission flux Γ_t from the cathode. This flux feeds a cloud of electrons in front of the cathode. From this cloud a flux Γ_1 will go into the discharge and a flux Γ_2 will go back to the cathode. The magnitude of Γ_1 depends on the discharge conditions.

means that, for higher fields, the rate of ionisation is larger and, therefore, also the plasma conductivity: at higher applied voltages the discharge is able to transport a larger current.

In the case of the thermal emission flux of electrons from the cathode, the influence can be explained as follows. In front of the cathode a cloud of electrons (see, e.g. the peak in electron density in figure 5.10) is supplied by the given thermal emission flux Γ_t . Due to the peak in electric field which is generated by this cloud, electrons are lost to the discharge on one side and back to the cathode on the other. This is illustrated schematically in figure 5.21. The equilibrium established by those three fluxes explains why, for a high Γ_t , the influence on ignition is negligible, since only a comparably small part of this flux goes into the discharge, and how for a low Γ_t this flux is not sufficient to maintain the desired flux into the discharge. Especially in the initial moments after the application of the cathode voltage, the desired current into the discharge is large (as can be concluded from figure 5.19) and therefore, the initial development can be mitigated by an insufficient flux. Changing the radius R_c of the tube around the lamp changes the capacitance between the lamp wall and this tube. A larger radius means a smaller capacitance and, therefore, the amount of surface charge that is necessary to bring the tube wall near the cathode voltage is lower. However, as expected from the logarithmic term in equation (5.24), the influence of R_c is limited.

To our knowledge, at this moment¹ there is no experimental data available in literature to which we can directly compare the influence of the control parameters other than the applied voltage. In [14] a plot of the influence of the pressure on the speed of the ionisation front is shown. However, these data cannot be compared directly to the result shown in figure 5.16, since the time between subsequent breakdown events in the experiments did not allow sufficient deionisation of the discharge gas. Moreover, since the rate at which the discharge decays is also a function of pressure, a proper comparison between the measurements in [14] and the results presented here is difficult to establish.

¹a continuation of the work presented in [17] is expected to provide experimental data which includes the influence of the parameters varied in this chapter.

5.4.3 Validity of fluid model assumptions

In the fluid model described in section 5.2, several assumptions were made. For the argon ions the drift velocity (see figure 5.4) exceeds the thermal velocity for the magnitude of the electric field that occurs in the ionisation front. As a result the assumption of setting the second term on the right hand side of equation (5.3) to zero, in order to obtain the drift diffusion equation (5.4), is not necessarily valid. A careful consideration of the relative magnitudes of the two divergence terms in equation (5.3) shows that for the argon ions the term containing the pressure tensor does prevail. Another limiting factor for a good quantitative description of the breakdown process is the manner in which the reaction rates were determined. These reaction rate coefficients were obtained from the integral expression (5.20), which contains the cross sections for the reaction and the electron energy distribution function. In this study the electron energy distribution function was calculated using the Boltzmann solver Bolsig, which assumes a stationary and homogeneous electric field and a constant background density of ground state atoms. Furthermore, only reactions starting at the ground state are taken into account. The resulting electron energy distribution function is strongly non-Maxwellian and dependent on the exact shapes of the cross sections included in the description.

In the initial phase there is mostly a neutral background gas through which the ionisation front progresses in one direction. The assumption that only reactions starting at the ground state are important is satisfied here to a large extent, especially at the ionisation front. This is illustrated in figure 5.22, which shows the reaction rates at time $t = 2.0 \mu\text{s}$ for the parameters used in section 5.3.1: the ground state reactions 1, 2 and 3 are far more important than the remaining electron impact reactions 4–9, which start at excited states.

In the plasma behind the ionisation front, reactions such as step-wise ionisation can become important, due to the presence of metastable atoms. In figure 5.23 one can see that at one instance in time the density of Ar^* is in the order of 10^{11}cm^{-3} . Although this is small compared to the ground state density, the number of electrons in the part of the electron energy distribution function that exceeds the 4.2 eV that is necessary to ionise a metastable state is far larger than the number of those that can excite or ionise a ground state atom. In breakdown phases in which the gas in active regions of the discharge contains an appreciable density of excited species, the reaction rates might not be the correct ones any more and they need to be recalculated based upon different electron energy distribution functions.

5.4.4 Later phases in breakdown and more cfl-like systems

As mentioned earlier, the breakdown phase that is discussed in this contribution is the first one of a sequence that leads to electrical breakdown of the discharge. It is an important phase in the sense that it determines whether the lamp will break down or not and it sets the stage for later phases. The later phases, however, do exhibit an interesting amount of spatial structure in the emitted light intensity and still confront us with our lack of understanding of the complete breakdown process. Moreover, in systems like the compact

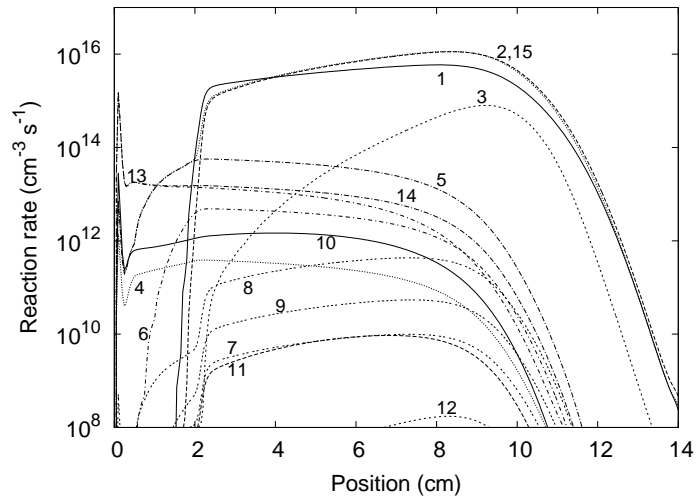


Figure 5.22: The various reaction rates at the lamp axis for $t = 2.0 \mu\text{s}$. The conditions are the same of those used to produce the figures 5.7–5.12. Refer to table 5.2 for the reaction equations that correspond to the numbers near the graphs. The electron impact reaction rates starting at the ground state are most important.

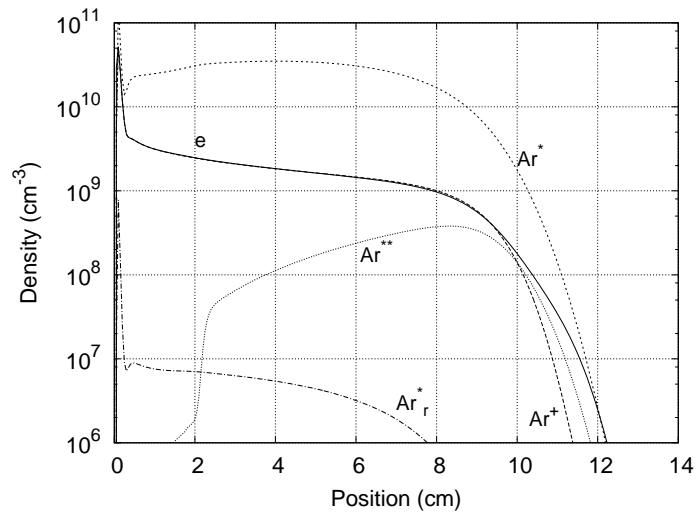


Figure 5.23: The various densities at the lamp axis for $t = 2.0 \mu\text{s}$. Note that a large amount of metastables is created. These are likely to be important in later phases in breakdown.

fluorescent lamps that are common today, two different complicating properties are added: in the first place, these lamps are generally not operated at a dc voltage but at a frequency of about 20–25 kHz. This means that, depending on the conditions, the ionisation front might not have the time to cross the tube during half a period of the ac cycle, but instead will feel the electric field reverse halfway. Secondly, compact fluorescent lamps consist of several straight parallel tubes which are connected by bridges or bends. During the breakdown process in such a lamp the electrical environment of one straight tube is influenced by what happens in the adjacent ones.

In order to use the present model to describe later phases in dc breakdown and to be able to deal with high frequency breakdown, several issues need to be dealt with. From section 5.4.3 it has become clear that the influence of an appreciable density of excited states on the electron energy distribution function needs to be described properly. Furthermore, there are indications [11] that in later phases the wall discharges partially. At present, the question of whether this effect can be solely described with a constant secondary emission coefficient is still unanswered.

5.5 Conclusions

In this chapter, we applied a fluid model to the initial phase of breakdown in long discharge tubes. The results of the numerical calculations were used to gain insight into the breakdown phenomena occurring in these tubes and to evaluate the applicability of fluid models to this breakdown.

It is shown that, starting at the cathode, subsequent sections of the inner wall become negatively charged. This surface charge electrically shields the inside of the tube and extends the cathode potential within the tube. The region with a high electric field progressed towards the anode. In this region, an active production of metastable atoms and electron-ion pairs leaves a plasma in the wake of the moving ionisation front. This plasma constitutes a conducting path between the cathode and the ionisation front, replenishing it with the electrons that are necessary to coat the wall and to ensure the progression of the ionisation front. Once the front has reached the anode, the lamp-circuit is closed and a conduction current increases the plasma density from then on.

In previous studies, the observation has been made that this breakdown process in long tubes can be seen in terms of an RC-line. This view has been evaluated and found to be useful in terms of describing the breakdown process in general terms. However, the RC-line picture is not powerful enough to be able to provide a good model of the breakdown process: in the first place, a positive charge within the volume of the discharge needs to be taken into account and predictions based on the capacitance of the system, therefore, underestimate the surface charge. In the second place, the transient and non-linear behaviour of the discharge conductivity make calculations based on the RC-line picture rather complex and impractical.

The fluid model approach gives results that are qualitatively consistent with experimental observations for the first phase of breakdown. Due to unknowns in the experimental

studies, it is hard to make a direct quantitative comparison between the simulations and experiments. The time in which the ionisation front crosses from the cathode to the anode is of the same order of magnitude as the experimentally observed time. However, it is shown that several control parameters have a significant influence on this time. Most important in these are the pressure and the flux of electrons that leaves the heated cathode. The latter parameter is especially hard to estimate in the experiments.

Finally, the assumptions made in the fluid model were evaluated. It is argued that the assumptions that lead to the reaction rate coefficients are the ones that will fail first: the rate coefficients were obtained by means of electron energy distribution functions calculated with a Boltzmann solver. In these calculations, only reactions starting at the ground state were used. This is especially valid for the ionisation front in the first phase of breakdown and, therefore, one can be quite confident with respect to the results presented in this chapter. However, in later breakdown phases the excited state densities can become sufficiently high for step-wise reactions to have an effect on the shape of the electron energy distribution function. At that point the reaction rates obtained with the electron energy distribution functions calculated with Bolsig might not be valid anymore.

Acknowledgments

We would like to acknowledge Philips Research and Philips Central Development Lamps for funding this research and providing us with experimental feedback, respectively.

References

- [1] J. Waymouth. *Electric Discharge Lamps*. MIT Press, Cambridge, 1971.
- [2] W. Elenbaas. *Light Sources*. MacMillan, London, 1972.
- [3] J. J. de Groot and J. A. J. M. van Vliet. *The High-Pressure Sodium Lamp*. Kluwer, Deventer, 1986.
- [4] J. S. Townsend. *The Theory of Ionization of Gases by Collision*. Constable & Company Ltd., London, 1910.
- [5] A. N. Lagarkov and I. M. Rutkevich. *Ionization Waves in Electrical Breakdown of Gases*. Springer, Berlin, 1994.
- [6] Yu. P. Raizer. *Gas Discharge Physics*. Springer, Berlin, 1991.
- [7] E. M. van Veldhuizen, editor. *Electrical Discharges for Environmental Purposes: fundamentals and applications*. Nova Science Publishers, 2000.
- [8] G. J. M. Hagelaar, G. M. W. Kroesen, U. van Slooten, and H. Schreuders. Modeling of the microdischarges in plasma addressed liquid crystal displays. *J. Appl. Phys.*, 88(5):2252–2262, 2000.
- [9] B. Lay, S. Rauf, and M. J. Kushner. Gap closure in a cold metal halid lamp. *IEEE Trans. on Plasma Science*, 30(1):190–191, 2002.

- [10] J. P. Boeuf and L. C. Pitchford. Pseudospark discharged via computer simulation. *IEEE Trans. on Plasma Science*, 19(2):286–296, 1991.
- [11] R. E. Horstman and F. M. Oude Lansink. The starting process in long discharge tubes. *J. Phys. D: Appl. Phys.*, 21:1130–1136, 1988.
- [12] E. Wagenaars, M. D. Bowden, and G. M. W. Kroesen. Experimental arrangement for the study of plasma breakdown. In S. De Benedictis and G. Dilecce, editors, *Proceedings of Frontiers in Low Temperature Plasma Diagnostics V*, pages 140–143, 2003.
- [13] W. Bartholomeyczky. Über den Mechanismus der Zündung langer Entladungsrohre. *Ann. der Physik*, 5:485–520, 1939.
- [14] A. V. Nedospasov and A. E. Novik. The speed of propagation of the ionization front in breakdown in long discharge tubes. *Sov. Phys. Tech. Phys.*, 5:1261–1267, 1961.
- [15] L. N. Tunitskii and E. M. Cherkasov. Discharge formation in tubes. *Sov. Phys. Tech. Phys.*, 14(12):1640–1642, 1970.
- [16] A. P. Abramov and I. P. Mazan'ko. Ionization wave during development of a discharge in long tubes. *Sov. Phys. Tech. Phys.*, 25(4):446–449, 1980.
- [17] M. F. Gendre, M. D. Bowden, H. Haverlag, H. C. M. van den Nieuwenhuizen, J. Gielen, and G. M. W. Kroesen. Optical study of pre-breakdown processes in compact fluorescent lamps. In S. De Benedictis and G. Dilecce, editors, *Proceedings of Frontiers in Low Temperature Plasma Diagnostics V*, pages 295–298, 2003.
- [18] G. J. M. Hagelaar and G. M. W. Kroesen. Speeding up fluid models for gas discharges by implicit treatment of the electron energy source term. *J. Computational Phys.*, 159:1–12, 2000.
- [19] M. Meyyappan and J. P. Kreskovsky. Glow discharge simulation through solutions to the moments of the Boltzmann transport equation. *J. Appl. Phys.*, 68(4):1506–1512, 1990.
- [20] E. Gogolides and H. H. Sawin. Continuum modelling of radio-frequency glow discharges. I. theory and results for electropositive and electronegative gases. *J. Appl. Phys.*, 72(9):3971–3987, 1992.
- [21] J. D. P. Passchier and W. J. Goedheer. A two-dimensional fluid model for an argon rf discharge. *J. Appl. Phys.*, 74(6):3744–3751, 1993.
- [22] C. Punset, J. P. Boeuf, and L. C. Pitchford. Two-dimensional simulation of an alternating current matrix plasma display cell: Cross-talk and other geometric effects. *J. Appl. Phys.*, 83(4):1884–1897, 1998.
- [23] H. W. Ellis, R. Y. Pai, E. W. McDaniel, E. A. Mason, and L. A. Viehland. Transport properties of gaseous ions over a wide energy range. *Atomic Data and Nuclear Data Tables*, 17(3):177, 1976.
- [24] G. J. M. Hagelaar, F. J. de Hoog, and G. M. W. Kroesen. Boundary conditions in fluid models of gas discharges. *Phys. Rev. E*, 62(1):1452–1454, 2000.
- [25] E. W. McDaniel. *Collision Phenomena in Ionized Gases*. Wiley, New York, 1964.
- [26] A. V. Vasenkov and M. J. Kushner. Electron energy distributions and anomalous skin depth effects in high-plasma-density inductively coupled discharges. *Phys. Rev. E*, 66:066411, 2002.

- [27] BOLSIG, Boltzmann solver for the siglo-series 1.0. CPA Toulouse & Kinema Software, 1996.
- [28] I. S. Grigoriev and E. Z. Meilikhov, editors. *Handbook of Physical Quantities*. CRC, Boca Raton, FL., 1997.
- [29] A. V. Phelps and Z. Lj. Petrović. Review article: Cold-cathode discharges and breakdown in argon: surface and gas phase production of secondary electrons. *Plasma Sources Sci. Technol.*, 8:R21–R44, 1999.
- [30] K. Tachibana. Excitation of the $1s_5$, $1s_4$, $1s_3$ and $1s_2$ levels of argon by low-energy electrons. *Phys. Rev. A*, 34(2):1007–1015, 1986.
- [31] P. Zapesochnyi and L. L. Shimon. Effective excitation cross sections of alkali-metal atoms colliding with slow electrons. *Opt. Spectrosc.*, 11(3):155–157, 1966.
- [32] R. H. McFarland and J. D. Kinney. Absolute cross sections of lithium and other alkali metal atoms for ionization by electrons. *Phys. Rev.*, 137(4A):A1058–A1061, 1965.
- [33] L. Vriens. Calculation of absolute ionisation cross sections of He, He*, He+, Ne, Ne*, Ne+, Ar, Ar*, Hg and Hg*. *Physics Letters*, 8(4):260–261, 1964.
- [34] A. N. Klucharev and V. Vujnovic. Chemi-ionization in thermal-energy binary collisions of optically excited atoms. *Physics Reports*, 185(2):55–81, 1990.
- [35] N. L. Bassett and D. J. Economou. Effect of Cl₂ additions to an argon glow discharge. *J. Appl. Phys.*, 75(4):1931–1939, 1994.
- [36] S. Ashida, C. Lee, and M. A. Lieberman. Spatially averaged (global) model of time modulated high density argon plasmas. *J. Vac. Sci. Technol.*, A 13(5):2498–2507, 1995.

Model study of dc and ac breakdown in a straight discharge tube containing argon and mercury

Abstract. Breakdown in a discharge tube is investigated by means of a fluid model for both applied dc and ac voltages. The discharge tube is similar to a compact fluorescent lamp tube, containing argon at 3 Torr and mercury at a few mTorr. For a dc voltage it was found that the minimum breakdown voltage is decreased substantially compared to a tube containing pure argon. Penning ionisation of mercury via an argon metastable state plays an important role in this effect. This is illustrated for a lamp operated on a dc voltage, where significant Penning-ionisation takes place in the wake of the ionisation front. Furthermore, the development of the surface potential of the lamp is shown to be controlled by both surface and volume charges.

Since compact fluorescent lamps are often started at a frequencies up to 100 kHz, we furthermore simulated breakdown behaviour at ac voltages and investigated the effect of the frequency on the breakdown time. Higher frequencies were found to be more effective in ensuring breakdown. The reason is that, if the applied voltage cycle is short, ions do not have sufficient time to drift towards the discharge wall to recombine there with negative surface charge.

6.1 Introduction

In the previous chapter, we presented a numerical model to study the breakdown process in long tubes containing argon at a few Torr. It was found that the spatio-temporal behaviour had a two-fold structure: upon application of a dc voltage to the cathode, first an ionisation wave moved from cathode to anode. The successful completion of this *forward-stroke* was found to be a requirement for the lamp to ignite. Then, a second ionisation wave, the *return-stroke* moved back towards the cathode again.

We discussed the processes that are responsible for evolution of the forward-stroke. The motion of this ionisation wave could be explained by considering charging of the inner surface and the effect this has on the electric field in the tube. The simulation results showed good agreement with experimental observations [1] of the light emitted by the tube during the forward stroke.

In commercial fluorescent lamps, the gas mixture contains a small fraction of saturated mercury vapour in order to make it an efficient light source. Mercury also aids the ignition process, as is known from the fact that at low temperatures (-20°C) ignition is more difficult than at higher temperatures. The mercury vapour pressure at room temperature is in the order of several mTorr.

In this chapter we continue the work presented in the previous chapter (or reference [2]) by discussing the effect of Penning ionisation on the evolution of the anode directed ionisation wave. It will be shown that this extra source of ionisation increases the electrical conductivity behind the ionisation front. This allows for a faster charging of the wall and therefore enables ignition at lower potentials.

Furthermore, whereas in chapter 5 only the forward stroke was discussed, here we will also consider the return stroke. The reason for that is that in pure argon discrepancies were seen between the simulation results and experimental observations for the second, cathode directed ionisation wave. A comparison of the numerical and experimental data [3] suggests that agreement is better for the argon-mercury mixture. This increases the confidence in the simulation results for the later phases in breakdown.

Finally, fluorescent lamps are nowadays often operated at ac voltages in the 20 – 30 kHz range. However, the frequency at which they are started lies in the range up to 100 kHz. We will consider breakdown for these alternating voltages and investigate whether the breakdown voltage is dependent on the frequency due to resonant effects that might occur between the applied voltage and the time scale at which the ionisation fronts traverse the tube.

6.2 The model

The work presented in this chapter is based on the model described in chapter 5. The difference lies in the set of species and reactions. For completeness, we will briefly treat this model and the geometry of the lamp system. Then we list the set of species and reactions.

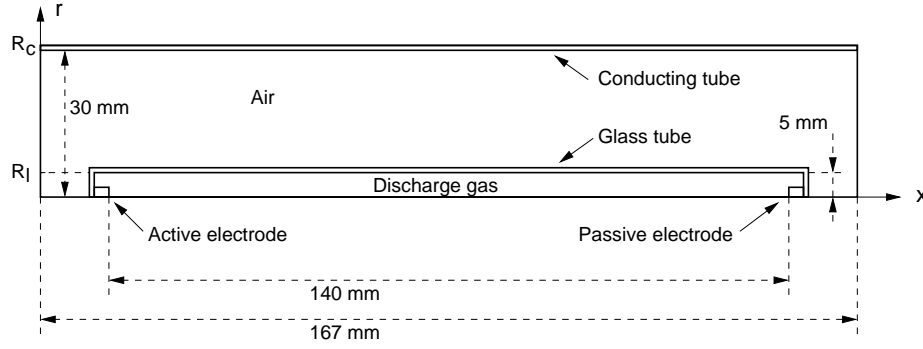


Figure 6.1: The geometry and the relevant sizes of the system under consideration. Note that the geometry is cylindrically symmetric around the x-axis.

6.2.1 Model description

The numerical model described in reference [2] and references therein is a time-dependent, two-dimensional fluid model. For a number of species the density balance equations are solved in the drift-diffusion approach:

$$\frac{\partial n_p}{\partial t} + \nabla \cdot \mathbf{\Gamma}_p = S_p \quad (6.1)$$

with:

$$\mathbf{\Gamma}_p = \pm \mu_p \mathbf{E} n_p - D_p \nabla n_p \quad (6.2)$$

where n_p is the density of species p , S_p the source of the species due to reactions, μ_p and D_p the species' mobility and diffusion coefficient respectively, and \mathbf{E} the electric field.

The Poisson equation is solved to account for the influence that the charged species have on the electric field \mathbf{E} :

$$\nabla \cdot (\epsilon \nabla \varphi) = -\nabla \cdot (\epsilon \mathbf{E}) = -\sum_p q_p n_p \quad (6.3)$$

in which φ is the electric potential as a function of time and space and ϵ the permittivity of the medium.

Furthermore, the electron energy balance equation is solved in a form similar to the balance equations above, but with an ohmic heating source term. The mean electron energy is used to determine reaction rate coefficients and electron transport coefficient from lookup tables that the model receives as input.

The boundary conditions to the various balance equations are listed completely in reference [2]. They include de-excitation of excited species and neutralisation of ions, as well as secondary and thermal electron emission. Fluxes of charged species to the dielectric boundaries of the discharge contribute to the surface charge at these boundaries.

The layout of the computational grid that is used for the simulations presented in this paper is given in reference [2]. For clarity it is again depicted in figure 6.1, which shows

that the calculation domain consist of a discharge region, a region containing dielectric materials (the glass tube and the air around it) and electrode materials. The latter consist of the active electrode on the left, the passive electrode on the right, and a tubular metal fixture outside the lamp at a radius of 3 cm, which is placed there to establish a well-defined electrical environment. The Poisson equation is solved on this entire grid and the balance equations are solved in the discharge region only.

Both the metal tube around the lamp and the passive electrode are kept at ground potential, whereas for the dc simulations the active electrode is cathode and for the ac simulations it is driven at an alternating voltage, starting as cathode. Furthermore, for dc operation the cathode is heated to a thermal emission temperature. For ac operation both electrodes are heated. Thermal emission is represented by an electron flux of $10^{17} \text{ cm}^{-2}\text{s}^{-1}$, which is based on a temperature of 1000 K and a work function of the electrode material of 2 eV via the Richardson-Dushman equation [4].

6.2.2 Species and reactions

The gas mixture consists of argon at a pressure of 3 Torr and mercury at the vapour pressure corresponding to the temperature of the lamp. At room temperature this is 1.8 mTorr. Since the ionisation degree remains low throughout the breakdown process, the densities of argon and mercury are assumed constant and no balance equations have to be solved for these species.

The time-evolutions of the following species are described: the electrons e , the excited states Ar^* and Hg^* and the ions Ar^+ and Hg^+ . Here, Ar^* is an effective state that represent the four 4s states of argon and, similarly, Hg^* represents the four 6p states of mercury. Higher states are not included in the model, as with this set of species we expect the model to capture the essential phenomena that we are interested in.

The reactions included in the model are listed in table 6.1. The rate coefficients for the electron impact excitation and ionisation collisions were obtained as a function of the mean electron energy ε from an external Boltzmann solver [5]. The cross sections needed for this were taken from [6, 7, 8, 9]. Step-wise ionisation and superelastic collisions of electrons with excited states are not included, because these are assumed to be unimportant due to the low density of excited states. The set of heavy particle reactions and corresponding reaction rates were adapted from [10]. Radiation from the $\text{Ar}(4s)$ resonant states was assumed to be effectively trapped on the time scale of the simulation and was therefore not included.

In the reaction set used in reference [2] we included a radiative reaction to be able to compare the simulation results to iCCD camera images taken of the lamp during the ignition process. A posteriori we could conclude that the calculated emission profile was proportional to direct excitation to the 4s state. Because of this observation, we chose to use the rate of reaction 1 in table 6.1 as a means of comparison between simulation and experimental results. It needs to be noted that, because we both lack spectrally resolved experimental emission data and a collisional radiative model, the comparison should not be considered conclusive.

Table 6.1: Reaction rate coefficients used in the model. $\Delta\varepsilon$ is the energy cost of the forward process. For the rate coefficients obtained by means of the Boltzmann solver [5], the references indicate which cross sections were used as input.

Nr.	Reaction	$\Delta\varepsilon$ (eV)	Coeff. k_r	Ref.
0	$\text{Ar} + e \rightarrow \text{Ar} + e$	^a	from Boltzmann solver	[6]
1	$\text{Ar} + e \rightarrow \text{Ar}^* + e$	11.6	from Boltzmann solver	[7]
2	$\text{Ar} + e \rightarrow \text{Ar}^+ + 2e$	15.8	from Boltzmann solver	[6]
3	$\text{Ar}^* + \text{Ar}^* \rightarrow \text{Ar} + e + \text{Ar}^+$	-7.4	$5 \times 10^{-10} \text{ cm}^{-3} \text{ s}^{-1}$	[10]
4	$\text{Hg} + e \rightarrow \text{Hg} + e$	^a	from Boltzmann solver	[9]
5	$\text{Hg} + e \rightarrow \text{Hg}^* + e$	5.215	from Boltzmann solver	[9]
6	$\text{Hg} + e \rightarrow \text{Hg}^+ + 2e$	10.43	from Boltzmann solver	[9]
7	$\text{Hg}^* + \text{Hg}^* \rightarrow \text{Hg} + e + \text{Hg}^+$	0.0	$4 \times 10^{-10} \text{ cm}^{-3} \text{ s}^{-1}$	[10]
8	$\text{Hg}^* \rightarrow \text{Hg} + h\nu$		$1 \times 10^6 \text{ s}^{-1}$	[10]
9	$\text{Ar}^* + \text{Hg} \rightarrow \text{Ar} + \text{Hg}^+ + e$	-1.17	$5 \times 10^{-10} \text{ cm}^{-3} \text{ s}^{-1}$	[10]
10	$\text{Ar}^* + \text{Hg}^* \rightarrow \text{Ar} + \text{Hg}^+ + e$	-6.285	$5 \times 10^{-10} \text{ cm}^{-3} \text{ s}^{-1}$	[10]
11	$\text{Ar}^+ + \text{Hg} \rightarrow \text{Ar} + \text{Hg}^+$		$1.5 \times 10^{-11} \text{ cm}^{-3} \text{ s}^{-1}$	[10]

a: energy lost in the recoil of the atom; this is specified as a function of the mean electron energy.

6.3 DC breakdown

In this section we describe the simulation results obtained with the model described above for an applied dc voltage. The effect of mercury on the breakdown process is considered. Furthermore, the results are discussed in terms of the observed shielding lengths and in terms of the calculated wall potential as compared to experimental data.

6.3.1 Results

A dc voltage of 300 V with a rise-time of $2 \mu\text{s}$ was applied to the lamp. Figure 6.2 depicts the electric field strength for various instants in time. The various phases observed in the breakdown process are described below.

From cathode to anode: forward-stroke

As was seen in the study for pure argon [2], an ionisation front first moves from the cathode (on the left) to the anode (on the right): in this *forward-stroke*, electrons in the ionisation front move in the direction of the metal fixture, as this appears to them as the closest anode. They encounter the tube wall and contribute locally to the negative surface charge at the wall close to the front. The buildup of surface charge modifies the electric field and thereby progressively extends the electric potential of the cathode further inside the tube

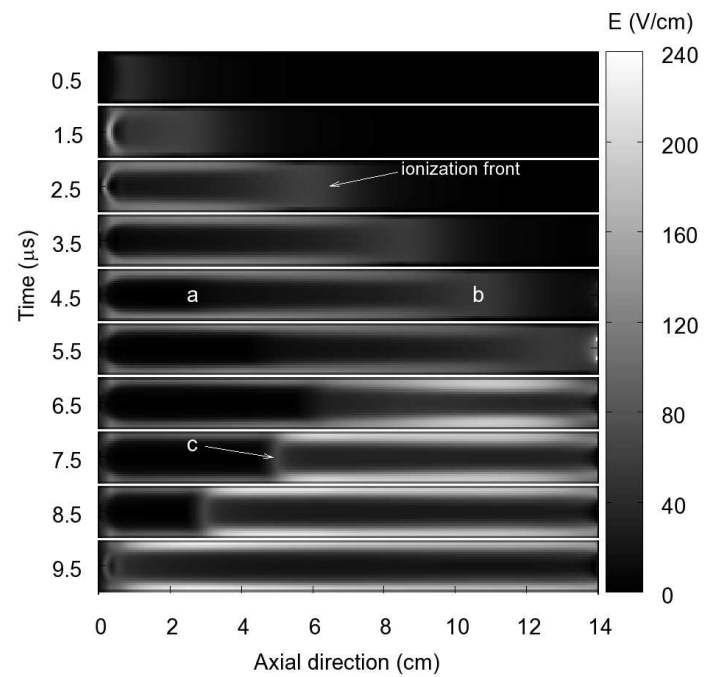


Figure 6.2: Snapshots of the electric field strength in the discharge for various instants in time. The entire diameter of the lamp is shown. Note that the scale in the horizontal direction is not the same as in the vertical direction. Refer to the text for the discussion.

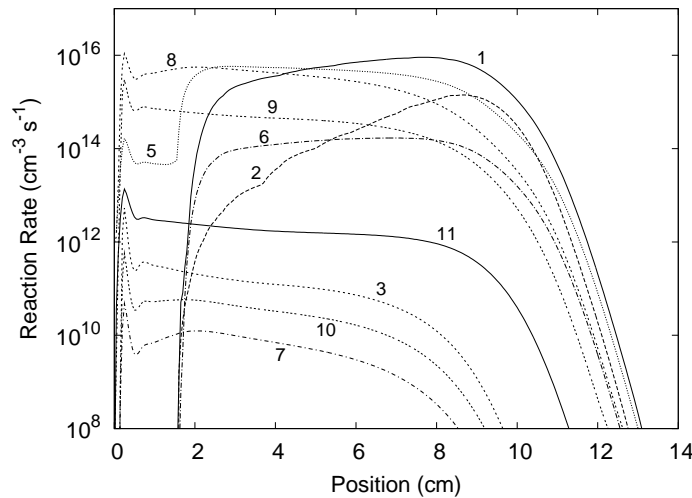


Figure 6.3: The various reaction rates at the lamp axis for $t = 4.0 \mu\text{s}$. At this time the front is at approximately 9 cm. Refer to table 6.1 for the reaction equations that correspond to the numbers near the graphs. The important ionisation reactions are reaction 2 (e-impact of Ar), 6 (e-impact of Hg) and 9 (Penning of Hg by Ar^*). Note that the latter is especially important in the wake of the wave.

towards the anode.

Although figure 6.2 does not show the direction of the field, it is clear that due to symmetry the field points in axial direction at $r = 0$. At larger values of r the radial component becomes more predominant. The field vectors have a large positive radial component in the section of tube that is marked “a” in the figure. This field configuration confines the electrons radially and thereby presents a tunnel for the electrons towards the ionisation front. In the section marked “b”, the radial component of the field is less strong and the electrons can flow towards the tube wall and form a surface charge.

In figure 6.3 the reaction rates of the reactions listed in table 6.1 are shown at the axis of the lamp for $t = 4.0 \mu\text{s}$. At this time the ionisation front had travelled to approximately 9 cm in the tube. The electron impact ionisation reactions 2 and 6 are mostly important in the front of the ionisation wave, whereas the Penning ionisation reaction 9 is of comparable magnitude in the wake of the wave.

This additional electron source keeps increasing the electron density behind the ionisation wave, as shown in figure 6.4. This, in turn, increases the conductivity behind the wave and thereby has a twofold effect: in the first place, the current that flows from cathode to the front can stay approximately constant, even though the distance between those two becomes larger. Since the velocity of the wave depends on how fast nearby sections of tube wall are charged, the ionisation wave velocity can remain constant. In the second place, due the high conductivity, only a small voltage drop exists between the cathode and the front, resulting in an virtually unreduced voltage drop across the ionisation front. The front thereby keeps its ability to ionise and produce metastable atoms and ensures a low

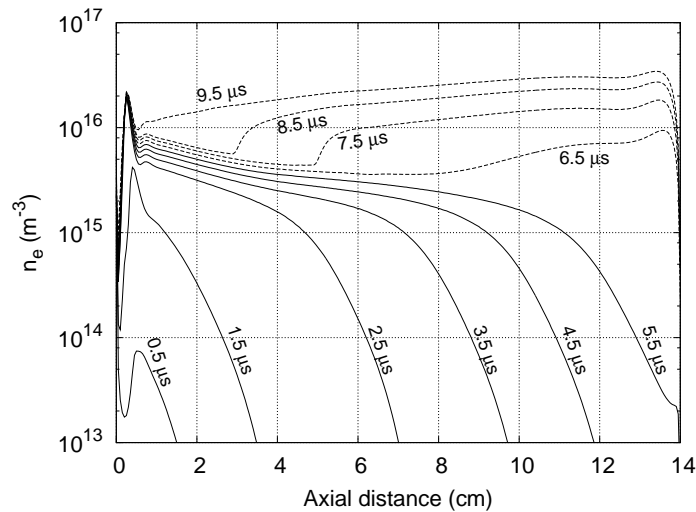


Figure 6.4: The electron density at the axis of the lamps for several instants in time. Note that it does not only increase at the position of the ionisation waves, but throughout the tube. This is due to the Penning ionisation source.

conductivity in newly traversed sections of tube.

This is in contrast to a pure argon discharge, where the conductivity from cathode to front decreases and the front slows down due to a decreased supply of unbalanced charge and due to a diminishing field strength [2].

At some distance behind the ionisation front (e.g. at “a” in figure 6.2), a region develops where the axial component of the electric field is very low and the electron temperature is approximately 1 – 2 eV as compared to 5 – 6 eV in the higher field regions (e.g. at “b”). Since the mobility of the electrons is high at low energies, even at small electric field strengths the conductivity of the discharge stays sufficient to conduct the required current to the ionisation front.

From anode to cathode: return-stroke

At approximately 5.5 μs , the anode is reached and now a *return-stroke* takes place. In pure argon the calculated development of this wave shows two clear discrepancies with experimental observations [2]: in the first place, we found that the speed is smaller than is observed experimentally. In the second place, the emitted intensity is uniform in the wake of the wave and does not show the decay that is observed in the experiments. In the present case of the argon-mercury mixture the agreement is considerably better

At the end of the forward-stroke, the entire potential drop is situated close to the anode. Ionisation rates are large in this high field region and the plasma density strongly increases (see figure 6.4). At the axis the region of high electric field displaces back towards the cathode due to the increased positive space charge near the anode. This process continues until the wave reaches the part of the tube where the electrons are relatively cold (like at

“b” in a previous instant in time).

When this happens, an interesting phenomenon can be observed in the simulations: a layer (marked “c” in figure 6.2) comes into existence and bears resemblance to the electric field and space-charge structure found in positive streamers.

Due to the difference in ionisation rates on both sides of the layer, a considerable plasma density gradient exists across it, as can be seen in figure 6.4. Since the electrons are more mobile than the ions, this results in a net negative space charge on the cathode side and a net positive space charge on the anode side. This space charge causes the ridge in the electric field.

When the return-stroke reaches the cathode, the axial field strength is approximately constant throughout the tube, except for near the cathode itself, where it is slightly stronger in the cathode fall.

Further discharge development

The final snapshot in figure 6.2 shows the rudiments of the cathode fall and the sheath at the tube wall. Further in time, this sheath will become thinner as the electron density grows. The current running through the lamp increases and will at some moment be limited by the power supply. During this buildup of the plasma density and the increase in current through the lamp, no significant spatial-temporal structure is observed in the simulation results.

6.3.2 Discussion

In the following, the above results are discussed by estimating shielding lengths of the discharge based on the Debye length and by considering the surface potential of the tube. The latter quantity was experimentally investigated in literature and the interpretation of these data can be reconsidered by means of the present model results.

Debye length

The snapshots of figure 6.2 clearly show the development of an electric field configuration that resembles a positive space-charge sheath near the wall. This is especially true for the 9.5 μs snapshot, where the field configuration is similar to a typical cathode fall and a positive column that is controlled by ambipolar diffusion.

The distance across which the space charges are shielded may be an important parameter in explaining these pictures. In order to investigate whether we can interpret them in this manner, we can consider the Debye length λ_D [11]:

$$\lambda_D = \sqrt{\frac{\epsilon_0 k_B T_e}{n_e e^2}} \quad (6.4)$$

with ϵ_0 the permittivity of free space, k_B the Boltzmann constant, T_e and n_e the temperature and density of the electrons respectively, and e the elementary charge. The Debye

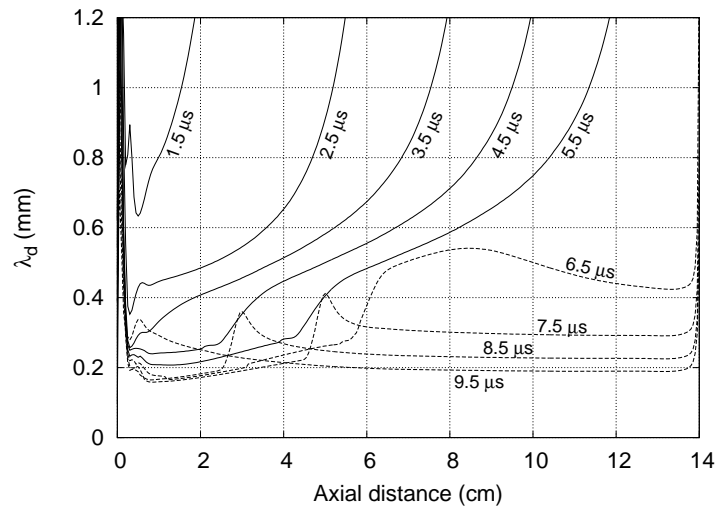


Figure 6.5: The radially averaged Debye length λ_D as a function of axial position for various instants in time.

length provides a crude estimate for the extent of a sheath, which typically measures several times λ_D [12].

In figure 6.5, the Debye length is shown as a function of axial position for various instants in time. Since both the electron energy and density vary radially, averaged values were substituted in equation (6.4).

Comparison of the lengths in figure 6.5 with the extent of the high field regions shows that they indeed measure several time λ_D . In the head of the first ionisation front λ_D is approximately 1 mm, which is one fifth of the radius of the tube. Behind the ionisation front $\lambda_D \approx 0.5$ mm and the sheath spans approximately 2.5 mm.

In the anode side of the tube, λ_D continuously decreases with time, which corresponds to the sheaths becoming thinner. On the cathode side, the return-stroke increases the electron temperature and λ_D temporarily increases with it.

Surface potential

Horstman and Oude Lansink [13], and more recently also Gendre [3], have performed electrostatic probe measurements of the potential just outside the lamp. In reference [13] the surface charge was calculated on the inside of the lamp wall from these experimental data, but the fact that a net charge exists inside the discharge volume was disregarded. The reduction in voltage that is measured when the return-stroke passes by the electrostatic probe was interpreted as a partial discharging of the wall. No physical mechanisms were proposed to explain this discharging.

In the top panel of figure 6.6 the calculated surface potential is shown as a function of time for an axial distance of 4 cm and 10 cm away from the cathode. Although the lamp in reference [13] had a different size, the qualitative picture corresponds to the measurements

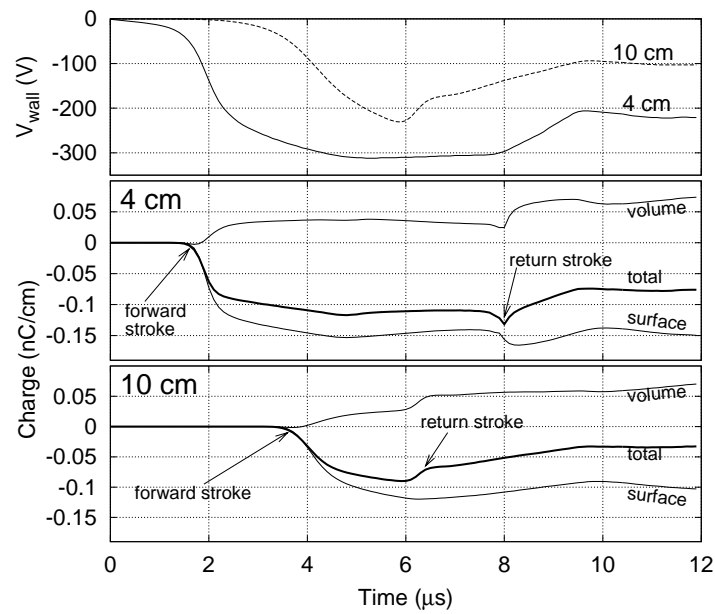


Figure 6.6: The top panel shows the wall potential as could be measured by an electrostatic probe at the axial positions 4 cm and 10 cm as a function of time. The bottom two panels show for each of these positions what the linear charge density is at the surface, in the volume, and in total. Note that both the volume and the wall charge in nearby regions contribute to the wall potential measured by an electrostatic probe.

presented in that paper. The jumps in the graphs clearly mark the passage of an ionisation front, first at 4 cm and then at 10 cm and subsequently in reverse order when the return-stroke passes these positions again.

In the two bottom panels of the figure, the linear charge density¹ at the *surface*, in the *volume* and the sum of those two are shown as a function of time for these two positions. The surface charge does fluctuate with the passage of the return-stroke, but the volume charge exhibits the largest change. It is therefore mainly the volume charge that is responsible for the fact that the net charge in a lamp section decreases and with it the absolute value of the surface potential. Assuming proportionality between the surface charge and the wall potential, as was done in reference [13], is therefore not correct.

6.4 AC breakdown

In this section we consider ac voltages and the effect of alternating potentials. We furthermore investigate the dependence of the frequency on how quickly breakdown is accomplished.

6.4.1 Results

Modern fluorescent lamp circuitry typically operates a lamp at 20–30 kHz, whereas during ignition a higher frequency up to 100 kHz is applied. The time scales associated with these frequencies are similar to the time it takes for the ionisation fronts to traverse the tube.

For the upcoming discussion we applied a trapezoidal waveform to the active electrode, because this was found to illustrate the various processes best. This in contrast to a block wave, where fast phenomena occurring after the zero crossing cannot be resolved conveniently in one overview figure. Furthermore, for a sinusoidal waveform, the continuous change in the voltage obscures visual representation of the development of the electric field. The evolution of the calculated electric field strength for this trapezoidal waveform is shown in figure 6.7. The applied frequency is 100 kHz and the amplitude 180 V.

During the first four microseconds the forward-stroke moves through the tube in the same way as in the case of a dc voltage. It charges the wall negatively and thereby extends the cathode potential towards the ionisation front. When the applied voltage becomes positive, a large potential gradient is now created between the active electrode and the nearest section of wall. The mobile electrons drift towards the powered electrode and a positive space charge is left behind. This space-charge layer extends the electrode potential along the axis, which then moves the high field at the axis a bit further away from the electrode. This process repeats itself and extends the anode potential in the tube until it has reached the location where the previous ionisation front stopped. It will not move further, since the electron density beyond that point is too low.

Due to the high mobility of the electrons, this process happens quickly. In experiments [3] it is observed as a light front that again moves away from the active electrode,

¹The linear charge density is the charge per unit length in the lamp.

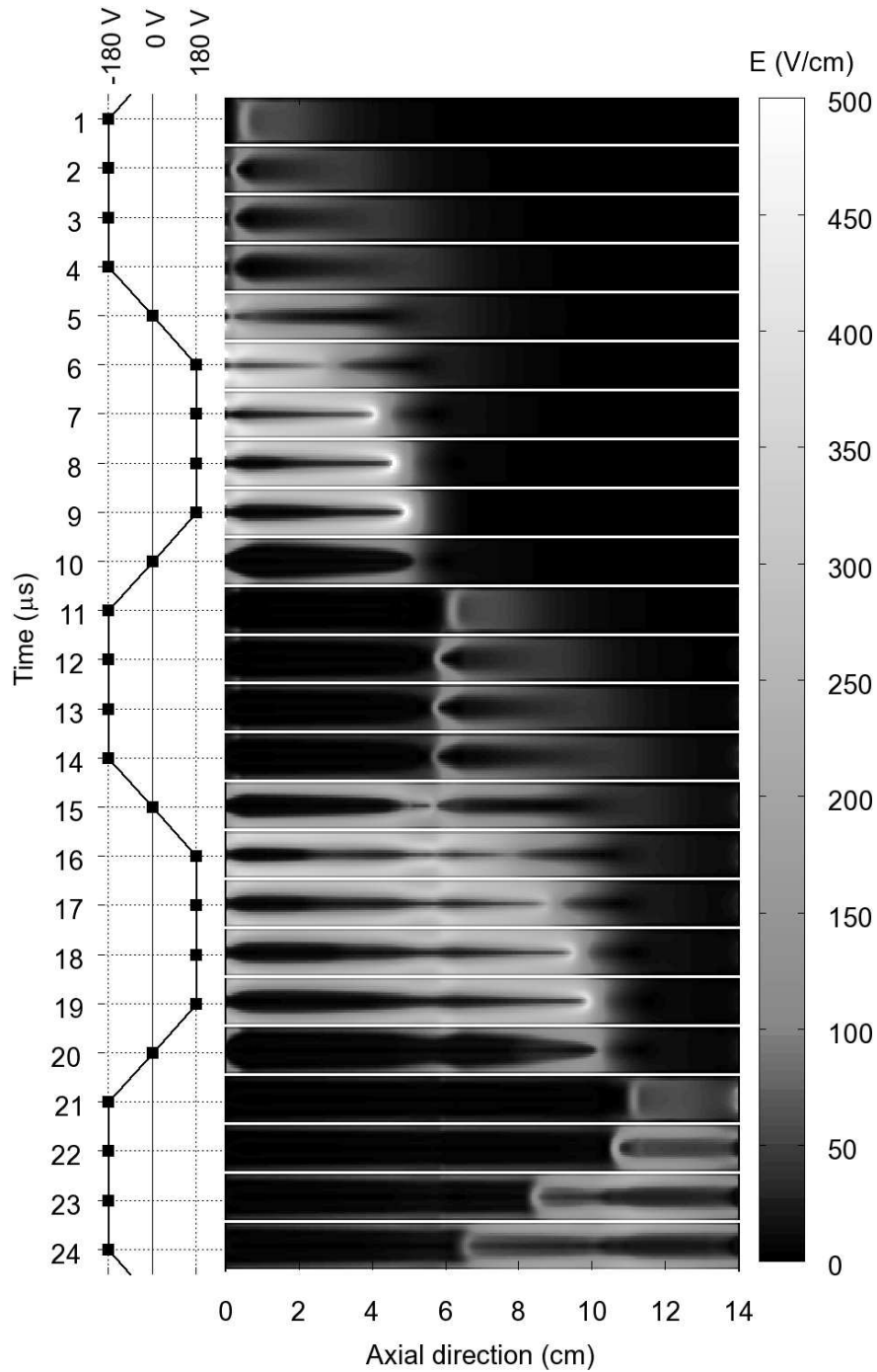


Figure 6.7: Snapshots of the electric field strength in the discharge for various instants in time. The applied voltage waveform is shown on the left hand side. Note that electric field data is mirrored in $r = 0$ to show the entire diameter of the lamp. Furthermore, the darker levels of grey have been compressed towards $E = 0$ in order to resolve the relatively small fields during the first, third and fifth half-cycle.

but is both brighter and faster than the front that was seen during the first negative half-cycle. The brightness can be explained by the fact that, due to the surface charges, higher fields are present at the same magnitude of the applied voltage. In these high fields, the excitation and ionisation rates are larger.

When the active electrode potential becomes negative again at $10\ \mu\text{s}$, the situation is similar to what it was at $4\ \mu\text{s}$, except for the fact that in the meanwhile the plasma density and conductivity have been increased substantially in this part of the tube. Indeed, the forward-stroke proceeds in the direction of the passive electrode again, as if it started from a cathode that extends in the tube.

Depending on the applied potential and the frequency, it might take several of these cycles to reach the passive electrode and close the circuit.

In figure 6.7 the first part of the return-stroke is shown. When the voltage reverses, the development of the return-stroke is interrupted by similar processes as described above and substantial spatial-temporal structure can still be seen in the experimental and numerical data. Nevertheless, as in the dc case [2], we found that the question whether the forward-stroke is successful in reaching the passive electrode is decisive for eventual ignition of the lamp.

In the description given above, the motion of the ions did not play a role. Due to the relatively low mobility of the ions, the time scale associated with their motion across the tube radius is in the order of $10\ \mu\text{s}$ in these conditions. In figure 6.7 the effect of ion motion can therefore not be observed. In the case of a lower applied frequency, the ions do discharge the negative surface charge on the inner wall during the positive half-cycle of the active electrode. This attenuates the radial electric field and results in a diminished increase in plasma density during this half-cycle. Depending on time that the ions have to reach the wall, the surface charge can stay negative or even become positive.

Breakdown time

Since a resonance effect seems to be possible between the time it takes ionisation wave to traverse the tube and the frequency of the applied voltage, it is interesting to investigate whether breakdown can be aided by the choice of frequency. We do not intend to answer this question by finding a minimum breakdown potential at a number of frequencies, since this would require a considerable number of long simulations. Instead, we investigate the time till breakdown as a function of amplitude and frequency. In these simulations a sinusoidal waveform was applied.

We recall that breakdown is ensured once the forward-stroke reaches the anode. In the dc case, the current will increase from the moment that a conducting path is established until it is limited by the external circuit. In ac breakdown the current is modulated, but does rise from one cycle to the next. Based on this observation, we took the moment at which the anode is first reached by an ionisation wave as a measure for the breakdown time. This crossing time was defined by the time that the current of the passive electrode first exceeds $0.1\ \text{mA}$.

In figure 6.8 these data are shown. A general trend can be observed of small crossing

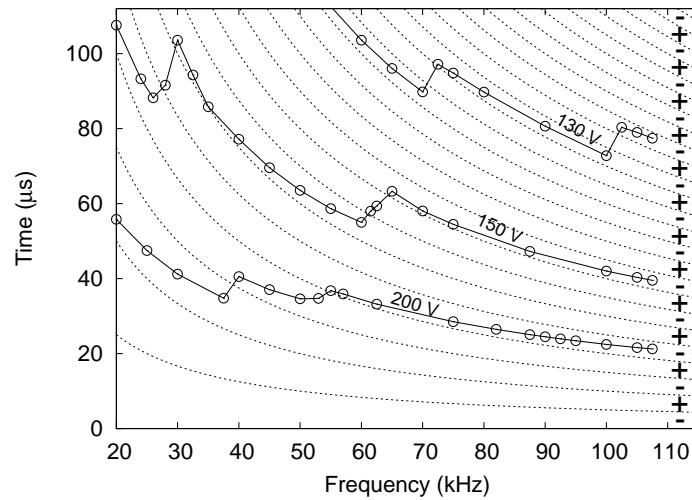


Figure 6.8: The time at which the forward-stroke first reaches the passive electrode as a function of applied frequency. The measure used to define this time is when a current larger than 0.1 mA first flows through this electrode. The thin dotted lines indicate at which time the sign of the applied potential changes. The column of pluses and minuses at the right hand side gives the sign of the potential of the active electrode.

times for high frequencies. The number of half-cycles necessary for the forward-stroke to reach the passive electrode is constant over a range of frequencies and only increments few times when going from 20 kHz to 100 kHz. Especially at a low voltage amplitude, when this number of half-cycles is large, this results in a strong decrease in crossing time for increasing frequency.

6.4.2 Discussion

In the results described above it has become clear that the number of half-cycles before the forward-stroke reaches the passive electrode is approximately constant over the 20–100 kHz range. This means that at higher frequencies it takes the forward strike a shorter time to close the circuit by establishing a conducting path between the electrodes.

Although the minimum breakdown voltage as a function of frequency cannot be obtained directly from these results, the curves in figure 6.8 suggest that for low voltages the lamp will not ignite at all if the frequency is too low. It is therefore preferable to apply a frequency higher than the steady-state operating frequency of 20 – 30 kHz to the lamp during breakdown, as is generally realised by lamp manufacturers.

The reason for this dependence of frequency can be found in the ion drift velocity: at low frequencies the ions have time to discharge the wall partially and thereby diminish the increase in plasma density during the positive part of the applied voltage cycle.

6.5 Conclusions

We used a fluid model to describe breakdown in a long straight tube, similar to a fluorescent lamp. The gas mixture consisted of argon at 3 Torr, with saturated mercury vapour at room temperature. The lamp was surrounded by a metal tube to provide a well-defined electrostatic environment. The electrodes were heated to thermal emission temperatures such that breakdown did not depend on secondary emission processes at the cathode. Both dc and ac breakdown were considered.

For dc breakdown, the development of the anode directed ionisation wave was compared to this wave in pure argon [2]. It was found that Penning ionisation of mercury by metastable argon atoms continuously increases the electron density behind the forward-stroke and thereby allows for a larger current to the ionisation front and a higher electric field in the front. This expresses itself in a more constant speed of the front as compared to in pure argon, where it slows down while traversing the tube.

The numerical description of the return-stroke showed better agreement with experimental observations than it was the case in pure argon. Having obtained more confidence in the simulation because of this, we could consider the phenomena occurring during this return-stroke. An important observation concerns the surface potential of the lamp as a function of time. In literature [13] this quantity was observed to decrease in magnitude when the return-stroke passes the location of the electrostatic probe. This was interpreted as a discharging of the surface charge on the inner wall. The simulations, however, indicate that the prime cause is an increase of net positive volume charge in the lamp and that therefore no need exists for the introduction of mechanisms that can facilitate discharging of the tube wall.

Commercial fluorescent lamps are usually started and operated on an ac voltage with a frequency of several tens of kHz. The simulated evolution of the electric field was considered for such an alternating voltage. The discharge starts with a forward-stroke, as is observed for dc voltages. If the applied frequency is high enough, this wave does not reach the anode and instead stops when the sign of the applied voltage reverses.

Due to the negative charge on the inner wall, large fields arise between the lamp wall and the active electrode when its potential becomes positive. Electrons in this region move back towards this new anode and leave positive space charge behind. This extends the electrode potential along the tube axis and causes the same to happen a bit further in the tube. This process appears as a fast wave in the direction of the passive electrode. Large radial fields are thus formed up to the point where the first wave reached. Further in the tube the electron and ion densities are too low to continue this development. The ions will eventually move towards the wall and recombine with negative surface charge. However, due to their low mobility, the extent to which this happens is dependent on the time available until the applied voltage reverses in sign again.

When the applied voltage becomes negative again, the mobile electrons quickly restore the space and surface charge configuration that was present after the previous negative half-cycle and the wave continues towards the anode.

These two processes alternate until the anode is reached. Due to the strong radial

fields during each positive half-cycle, the plasma density and conductivity of sections of tube increase substantially and this eventually result in a conducting path between the electrodes. Due to the negative current voltage characteristic of the plasma, the lamp is then sure to ignite.

A final topic treated in this paper consists of the question of whether an optimal frequency exists for the ignition of the lamp. To answer this question, the time it took for the forward-stroke to reach the passive electrode was recorded as a function of frequency. It was found that the number of half-cycles before this happens is constant over a wide range of frequencies and therefore higher frequencies are favourable for ignition.

Acknowledgments

We would like to acknowledge Philips Research and Philips Central Development Lamps for funding this research and providing us with experimental feedback, respectively.

References

- [1] M. F. Gendre, M. D. Bowden, H. Haverlag, H. C. M. van den Nieuwenhuizen, J. Gielen, and G. M. W. Kroesen. Optical study of pre-breakdown processes in compact fluorescent lamps. In S. De Benedictis and G. Dilecce, editors, *Proceedings of Frontiers in Low Temperature Plasma Diagnostics V*, pages 295–298, 2003.
- [2] W. J. M. Brok, J. van Dijk, M. D. Bowden, J. J. A. M. van der Mullen, and G. M. W. Kroesen. A model study of propagation of the first ionisation wave during breakdown in a straight tube containing argon. *J. Phys. D: Appl. Phys.*, 36(16):1967–1979, 2003.
- [3] M. F. Gendre et al. *To be submitted to J. Phys. D: Appl. Phys.*, 2005.
- [4] J. J. de Groot and J. A. J. M. van Vliet. *The High-Pressure Sodium Lamp*. Kluwer, Deventer, 1986.
- [5] G. J. M. Hagelaar. BOLSIG+, private communication, Toulouse, France, December 2004.
- [6] A. V. Phelps and Z. Lj. Petrović. Review article: Cold-cathode discharges and breakdown in argon: surface and gas phase production of secondary electrons. *Plasma Sources Sci. Technol.*, 8:R21–R44, 1999.
- [7] K. Tachibana. Excitation of the $1s_5$, $1s_4$, $1s_3$ and $1s_2$ levels of argon by low-energy electrons. *Phys. Rev. A*, 34(2):1007–1015, 1986.
- [8] A. N. Klucharev and V. Vujnovic. Chemi-ionization in thermal-energy binary collisions of optically excited atoms. *Physics Reports*, 185(2):55–81, 1990.
- [9] S. D. Rockwood. Elastic and inelastic cross sections for electron-Hg scattering from Hg transport data. *Phys. Rev. A*, 8(5):2348–2358, 1973.
- [10] B. Lay, R. S. Moss, S. Rauf, and M. J. Kushner. Breakdown processes in metal halide lamps. *Plasma Sources Sci. Technol.*, 12:8–21, 2003.

- [11] I. P. Shkarofsky, T. W. Johnston, and M. P. Bachynski. *The Particle Kinetics of Plasmas*. Addison-Wesley, 1966.
- [12] B. H. P. Broks, W. J. M. Brok, J. Remy, J. J. A. M. van der Mullen, A. Benidar, L. Bienier, and F. Salama. Numerical investigation of the discharge characteristics of the pulsed discharge nozzle. *Phys. Rev. E*, 71:036409, 2005.
- [13] R. E. Horstman and F. M. Oude Lansink. The starting process in long discharge tubes. *J. Phys. D: Appl. Phys.*, 21:1130–1136, 1988.

Numerical description of discharge characteristics of the plasma needle

Abstract. The plasma needle is a small atmospheric, non-thermal, radio-frequency discharge, generated at the tip of a needle, which can be used for localised disinfection of biological tissues. Although several experiments have characterised various qualities of the plasma needle, discharge characteristics and electrical properties are still not well known. In order to provide initial estimates on electrical properties and quantities such as particle densities, we employed a two-dimensional, time-dependent fluid model to describe the plasma needle. In this model the balance equation is solved in the drift-diffusion approach for various species and the electron energy, as well as Poisson's equation. We found that the plasma production occurs in the sheath region and results in a steady flux of reactive species outwards. Even at small ($< 0.1\%$) admixtures of N_2 to the He background, N_2^+ is the dominant ion. The electron density is typically 10^{11} cm^{-3} and the dissipated power is in the order of 10 mW. These results are consistent with the experimental data available and can give direction to the practical development of the plasma needle.

7.1 Introduction

Non-thermal atmospheric plasmas have recently attracted much attention due to their applicability in biomedical technology [1, 2]. The main characteristic of such a plasma is that the gas temperature stays low, typically not much more than a biologically compatible 310 K. The electron temperature, however, is several ten thousands Kelvin and this leads to the production of many reactive species such as excited molecules, radicals and ions. These species can react with molecules in the tissue and thereby accomplish the disinfective purpose of the device.

One of the promising non-thermal plasma devices is the recently developed plasma needle [1]. In several experimental studies, Stoffels, Kieft, et al. [3, 4] have shown it to be capable of locally killing cells and loosening them from their substrate for removal. This allows malignant cells to be disposed of in an orderly fashion, diminishing the risk of infections and damage to nearby benign cells: the cell membrane stayed intact and thus kept the potentially harmful content of the cell contained.

The active medium of the plasma needle is a small (~ 1 mm) atmospheric, non-thermal radio-frequency (rf) plasma, generated at the tip of a metal wire (see figure 7.1). The needle itself can be held as one holds a pen and is connected to a gas cylinder and a power supply via a small tube and a wire. This arrangement makes it practical as a tool in future applications such as dentistry and micro-surgery. However, before it can be considered safe and suitable for these medical applications, the plasma and its properties need to be investigated further: the interactions between the species and the interplay of the charged particles with the electric fields make the plasma a complex non-equilibrium system, which can be improved more efficiently if a theoretical description is available.

Unlike the plasma needle, theoretical descriptions do exist for other types of atmospheric, non-thermal plasmas (see e.g. reference [5, 6, 7]). These devices are in a similar manner employed for disinfection and surface treatment of materials that do not react well to vacuum or high temperatures. However, their active region is larger and does not allow for very localised treatments of surfaces.

The aim of the present research was to provide an initial numerical description for the plasma needle. This description provided estimates of important plasma properties and insight in the physical processes that determine those properties. Among these properties are species densities and the production rates for the various chemically active species, as a function of experimental settings such as the applied voltage. With these insights the plasma can be optimised for its purpose.

We used a versatile, time-dependent, two-dimensional fluid model, earlier applied in the context of plasma display panels [8] and the ignition of compact fluorescent lamps [9]. This model included the relatively terse, but appropriate set of reactions taken from dielectric barrier discharge literature [6], a cylindrically symmetric geometrical representation of the needle and a simplified description of the circuit that drives the discharge.

In this chapter we present our numerical approximation of the needle, the results of the calculations done with this model, and a discussion of these results.

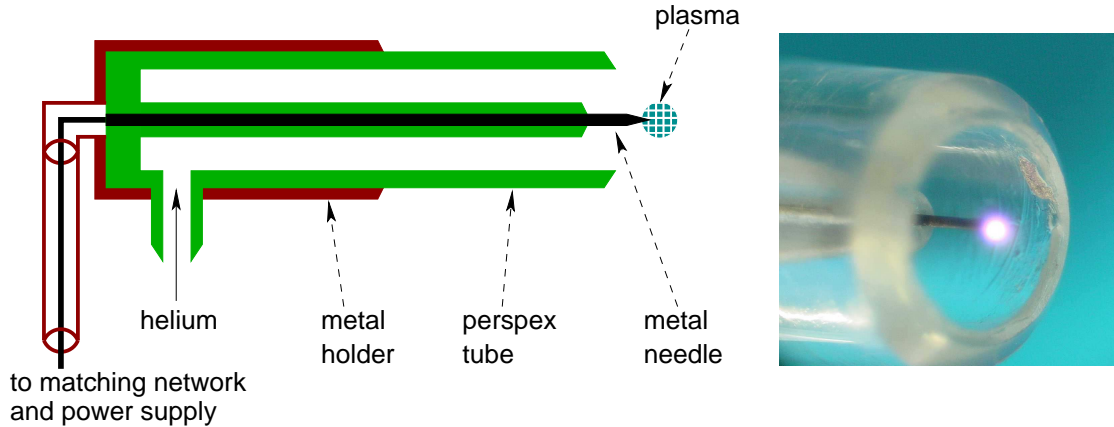


Figure 7.1: *On the left:* a schematic drawing of the plasma needle. *On the right:* a picture taken of the tip of the needle in operation. The needle itself is a sharpened metal wire with a diameter of 0.3 mm. The perspex tube around it has an inner diameter of 5 mm and serves to direct the flow of helium along the needle. The needle is isolated for a large part in order to prevent a discharge from forming within the tube. Refer to reference [10] for more details concerning the device.

7.2 The model

In this section, the model we used is described in its various aspects: the equations that were solved, the data on the various species and reactions and finally the geometry of the needle and its surroundings and the electrical circuit that drives the discharge.

7.2.1 Model description

The numerical model that was employed is described fully in reference [9] and references therein. Briefly, it is a time-dependent, two-dimensional fluid model: for a number of species (electrons, excited states and ions) the particle density balance equation is solved in the drift-diffusion approach:

$$\frac{\partial n_p}{\partial t} + \nabla \cdot \mathbf{\Gamma}_p = S_p \quad (7.1)$$

with:

$$\mathbf{\Gamma}_p = \pm \mu_p \mathbf{E} n_p - D_p \nabla n_p \quad (7.2)$$

where n_p the density of species p , S_p the source of the species due to reactions, μ_p and D_p the species' mobility and diffusion coefficient, respectively, and \mathbf{E} the electric field.

The density and temperature of the neutral background gas were assumed to be constant in time and uniform in space. The electron energy was determined by solving the electron energy balance equation in a form similar to the equations above, with an extra source term containing the electric field. Poisson's equation was solved in order to account for the influence of charged species on the electric field.

A possible deviation from a Maxwellian energy spectrum for the electrons was taken into account by constructing a set of tables for transport coefficients and reaction rate coefficients as functions of the mean electron energy. These tables were obtained from an external Boltzmann solver [11], in which it was assumed that the density of the neutral ground-state background gas was stationary and uniform, as in the fluid model itself. This assumption implies that the densities of the excited and charged species stay small compared to the density of the background gas, so that pressure gradients can be neglected.

The boundary conditions to the various balance equations are listed completely in reference [9]. They included de-excitation of excited species and neutralisation of ions, as well as secondary electron emission.

7.2.2 Species and reactions

Table 7.1 lists the set of species for which the balance equations were solved and table 7.2 gives the complete set of reactions that was used in the model. For these sets we followed the approach by Golubovskii et al. [6]. One important assumption made in their data set was that only a few excited states are needed in order to describe the discharge behaviour. For the helium atom, this means that only the metastable levels were included, lumped together in one state, denoted by He^* . For the helium molecular system, the various excimer levels were assumed to decay into the $\text{He}_2(a^3\Sigma_u^+)$ state (denoted by He_2^*) at time scales that are smaller than the breakdown time scale. While this was the case in reference [6], it is not immediately clear this assumption holds for the plasma needle that is operated at a frequency of 13.6 MHz. This will be discussed further in section 7.4. Note that no radiative transitions were explicitly included in this approach: the energy necessary to produce radiative species was included as a loss term to the electron energy equation.

Recent measurements of the plasma needle [12] showed that typically there are nitrogen impurities present in the discharge gas. The impurity density is determined by the quality of the gas in the cylinder, as well as by diffusion of air into the active region of the discharge: close to the needle tip the gas can be expected to be most pure, while further away from the tip the impurity density increases. In the experiments, the amount of nitrogen in the centre of the discharge was found to be below the detection limit of 0.5 % of a Raman-scattering technique and was only detectable at a distance further away than approximately 1.5 mm from the tip of the needle. Considering that the plasma is most dense close to the needle, where the gas is most pure, we assumed that only helium is directly electronically excited and ionised. The excitation and ionisation of N_2 are realised in heavy particle collisions only. For the calculations we used a uniform nitrogen fraction of 0.1 % and disregarded the increase of impurities with a distance from the needle tip.

7.2.3 Needle geometry and circuit

We simplified the geometry of the plasma needle to a point-plane geometry with a cylindrical symmetry (see figure 7.2), defined on a rectangular grid of typically $N_z = 100$

Table 7.1: The list of species for which the balance equation was solved, including references to the literature sources of the various coefficients.

Species	Diffusion coeff.	Mobility	Sec. emiss. coeff.
e	1	[11, 13]	
He*	[14]		[13]
He ⁺	1	[15]	[13]
He ₂ *	[14]		
He ₂ ⁺	1	[15]	[13]
N ₂ ⁺	1	[15]	[13]

1: obtained from the mobility using the Einstein relation.

control volumes in the axial direction and $N_r = 100$ control volumes in the radial direction. The dimension of each control volume was $0.05 \times 0.05 \text{ mm}^2$.

In experimental practice, the discharge is part of a circuit that includes a rf source and a matching network. The matching network serves to adapt the impedance of the plasma to the output impedance of the power supply and thereby maximise transmission of power [17]. It is outside the scope of the present chapter to fully describe the nontrivial interaction between the plasma and the matching network. Instead, only one important feature was accounted for: no net current can run, due to a capacitor in series with the discharge. Before the discharge reaches steady-state, any net current adds charge on the plates of the capacitor and will thereby contribute to a bias voltage that offsets the potential of the needle with respect to the earth potential. This bias voltage then counteracts the current and eventually reaches a steady-state level at which no net current runs. To simulate this, a single capacitor of 2 pF was modelled in series with the discharge. This relatively low value was chosen in order to minimise the time which it took for the simulation to reach steady-state.

Although not experimentally ideal, it is possible to have a matching network with inductive instead of capacitive elements in series with the needle. In such a configuration a direct current can run. This was briefly investigated in order to study the interesting confining effect of the unbiased electrical potential on the electrons.

Finally, in experiments the helium gas flow through the Perspex tube surrounding the needle was typically in the order of 2 l/min. We neglected this flow because the directed velocity due to this flow was three orders of magnitude smaller than the thermal motion of the gas atoms.

7.3 Results

The model described in section 7.2 was used to investigate various aspects of the plasma needle. In the text that follows, we first look at the case in which the needle was placed

Table 7.2: The set of reactions treated in the model, with the references to the literature from which the reaction rate coefficients were obtained.

Nr.	Reaction	Rate Coefficient	Ref.
0	$\text{He} + e \rightarrow \text{He} + e$	from Boltzmann solver	[11]
1	$\text{He} + e \rightarrow \text{He}^* + e$	from Boltzmann solver	[11]
2	$\text{He} + e \rightarrow \text{He}^+ + 2e$	from Boltzmann solver	[11]
3	$\text{He}^* + e \rightarrow \text{He}^+ + 2e$	from Boltzmann solver	[11, 16]
4	$\text{He}^* + 2\text{He} \rightarrow \text{He}_2^* + \text{He}$	$2.0 \times 10^{-34} \text{ cm}^6 \text{ s}^{-1}$	[6]
5	$\text{He}^+ + 2\text{He} \rightarrow \text{He}_2^+ + \text{He}$	$1.1 \times 10^{-31} \text{ cm}^6 \text{ s}^{-1}$	[6]
6	$\text{He}_2^* + M \rightarrow 2\text{He} + M$	10^4 s^{-1}	[6] ^a
7	$2\text{He}^* \rightarrow \text{He}_2^+ + e$	$1.5 \times 10^{-9} \text{ cm}^3 \text{ s}^{-1}$	[6]
8	$2\text{He}_2^* \rightarrow \text{He}_2^+ + 2\text{He} + e$	$1.5 \times 10^{-9} \text{ cm}^3 \text{ s}^{-1}$	[6]
9	$\text{He}_2^+ + e \rightarrow \text{He}^* + \text{He}$	$8.9 \times 10^{-9} (T_e/T_g)^{-1.5} \text{ cm}^3 \text{ s}^{-1}$	[6]
10	$\text{He}^* + \text{N}_2 \rightarrow \text{N}_2^+ + \text{He} + e$	$5.0 \times 10^{-11} \text{ cm}^3 \text{ s}^{-1}$	[6]
11	$\text{He}_2^* + \text{N}_2 \rightarrow \text{N}_2^+ + 2\text{He} + e$	$3.0 \times 10^{-11} \text{ cm}^3 \text{ s}^{-1}$	[6]
12	$\text{He}_2^+ + \text{N}_2 \rightarrow \text{N}_2^+ + \text{He}_2^*$	$1.4 \times 10^{-9} \text{ cm}^3 \text{ s}^{-1}$	[6]
13	$\text{N}_2^+ + e \rightarrow 2\text{N} \rightarrow \text{N}_2$	$4.8 \times 10^{-7} (T_e/T_g)^{-0.5} \text{ cm}^3 \text{ s}^{-1}$	[6] ^b

a: The symbol M represents an arbitrary heavy collision partner.

b: The intermediate reaction products were not described in the model.

at a distance of 3 mm from the plane and was driven by a voltage of 320 V in amplitude. This standard condition encompasses all characteristics of the needle that are also found at larger distances and yet there is no appreciable influence of the proximity of the plane. Following the study of this standard condition, we then examine the influence of parameters such as applied voltage and distance to the plane.

7.3.1 Discharge characteristics

In figure 7.3, the voltage applied to the needle and the periodic current running through the needle are shown for the standard condition ($V = 320 \text{ V}$ and $d = 3 \text{ mm}$). The steady-state bias voltage was -116 V and the dissipated power 31 mW . The total current lagged the voltage just a little less than $\pi/2$ rad, which indicates that the needle behaved almost completely capacitatively. This capacitive component is formed by the capacitance of the metal needle in its environment and gives rise to a displacement current. The discharge itself adds a small resistive component which is responsible for the dissipated power.

Figure 7.4 shows the time-averaged electron-density profile. The maximum electron density was $3 \times 10^{11} \text{ cm}^{-3}$ and the size of the discharge, measured by the distance over which the electron density dropped by one order of magnitude, was in the order of 1 mm^3 . The electron energy close to the needle was calculated to be 8 eV and dropped quickly below 1.5 eV at a distance of 0.5 mm away from the needle.

Figure 7.4 shows that the plasma exhibited a large degree of spherical symmetry between

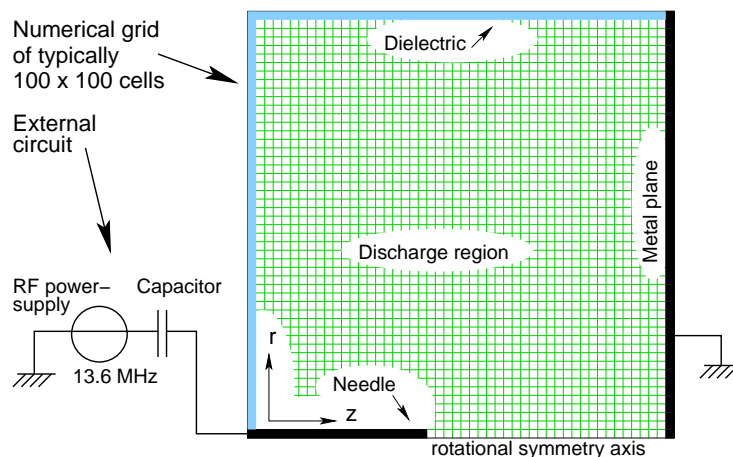


Figure 7.2: A schematic diagram of the numerical grid and the circuit driving the discharge. The discharge region was bounded on the right by a metal plane and on the left and in radial direction by a dielectric. The needle itself was located on the axis of the system. The metal plane was connected to earth and the needle to a rf power supply via a capacitor.

the needle and the plane. In the following text we will therefore consider quantities at the axis of the discharge: these quantities show similar profiles along different lines at an angle from the needle towards the plane.

The axial, time-averaged densities profiles of the various species are depicted in figure 7.5. Of the species treated by the model, only N_2^+ and the electrons existed relatively far from the needle, while the other species were found within 0.4 mm of the needle tip. In this region close to the needle, the electric field was highest and the electron energy gained in this field was mainly lost in the production of He^* via reaction 1 (in table 7.2). This energy, now contained in He^* , eventually resulted in the ionisation of N_2 , either directly through Penning ionisation in reaction 10 or via He^* (reactions 4 and 11). For the resulting N_2^+ ions, the destruction rate (reaction 13) was sufficiently low so that the main loss processes was that of ambipolar diffusion of this species outward, together with an equal number of electrons.

To give an impression on the time dependence of the reaction rates in the active region of the discharge, the rates are shown at a distance of 0.2 mm away from the tip of the needle in figure 7.6. Moving further away from the needle, all rates dropped to negligible values except for the rate of reaction 13.

The electron density and potential at the axis of the system are shown in figure 7.7 for different phases (0 , $\pi/2$, π and $3\pi/2$ radians) during the rf cycle. The electron density oscillated with the rf cycle, with an amplitude of about 0.2 mm. Unlike the electrons, the spatial modulation of the ions was negligible, due to their relatively large mass. The positive space-charge density that remained when the electrons moved away from the needle was responsible for the large cathode fall. During the anode phase, the space-charge density in front of the needle was small and did not contribute to the field appreciably.

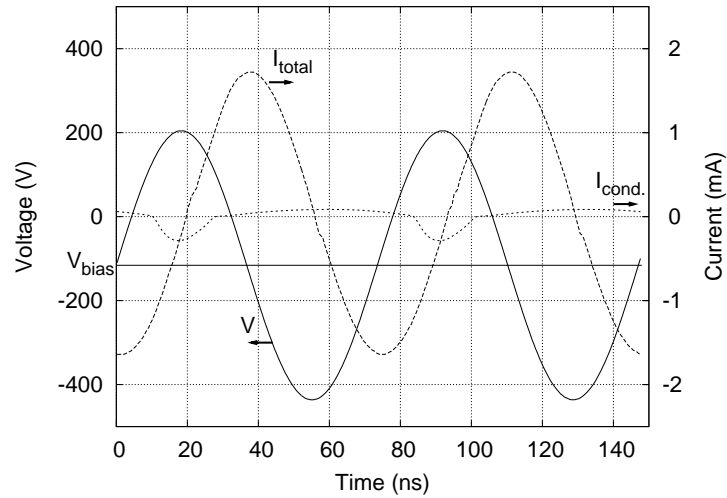


Figure 7.3: The voltage, conduction current and total (i.e. conduction plus displacement) current as a function of time during steady-state operation of the needle for the standard conditions ($V = 320$ V and $d = 3$ mm). The horizontal line at -116 V indicates the bias voltage that offsets the needle potential with respect to earth.

7.3.2 Influence of distance and applied voltage

The applied voltage and distance of the needle to the plane are the control parameters that are normally important for the application of the needle. In order to investigate their influence on the dissipated power, these quantities were varied under otherwise equal conditions.

Figure 7.8 shows the effect of the applied voltage on the power. At higher powers, the maximum electron density was higher. Furthermore, the discharge became more elongated, that is, extended itself along the needle. The discharge thereby increased the extent of its sheath along the surface of the needle and could draw more current. This is consistent with experimental observations.

In figure 7.9 the effect of the distance between needle and plane is shown. For increasing distance, the magnitude of the field close to the needle decreased, which resulted in smaller dissipated powers.

7.3.3 Effect of current restriction

As mentioned in section 7.2, the matching network of the needle often contains a capacitor in series with the needle. Before the system reaches steady-state, this capacitor generally accumulates charge and thereby introduces an offset in the average needle voltage that eventually prevents a net current from running. Instead of this configuration, it is feasible to make a matching network that contains only an inductance in series with the needle. In such a circuit, net currents do not lead to a bias voltage and this absence of bias voltage

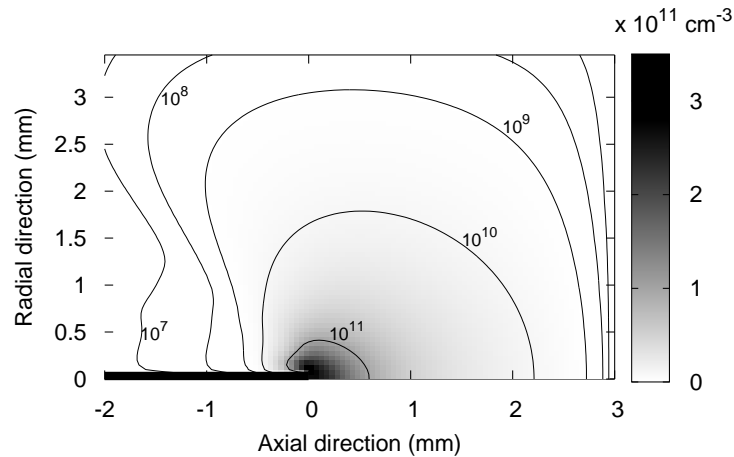


Figure 7.4: The electron-density profiles, averaged over the rf cycle, for a needle at 3 mm from a plane, driven at 320 V. The contour lines show the density at a logarithmic scale, the different levels of gray show the density at a linear scale. Note that not the entire calculation domain is shown here.

has a large effect on the steady-state field configuration.

In the unbiased situation, we found that the electric field was such that the electrons were confined to a region close to the needle, while the ions were not. Figure 7.10 shows the charged particle densities and potential for this case. One can see that the electrons did not move further away than approximately 1 mm from the tip of the needle. Beyond that distance the field pointed towards the needle during the entire rf cycle. The average potential at this distance corresponded to the absolute value of the bias voltage, as was observed in the simulation of which results are presented in figure 7.7.

This simulation also allowed us to obtain an estimate of the time scale for the discharge to reach steady-state. We applied a 10% step in the voltage from $V = 320$ V to $V = 352$ V and looked at the time that it took for the power to reach its final value within a fraction of $1/e$ of the difference between the original and final values. This was $20 \mu\text{s}$. The equilibration time scale of the discharge is thus several times these $20 \mu\text{s}$.

In a circuit containing a capacitor, a second time scale is formed by the time at which the bias voltage sets itself. Given a current of typically $1 \mu\text{A}$ in the unbiased situation and a capacitor in the order of 10 pF , the relation $I = (CdV/dt)$ predicts a time scale in the order of 1 ms for a capacitor to charge and thus for steady-state to settle.

7.4 Discussion

In the following paragraphs we will discuss the results presented in section 7.3 in terms of consistency with experimental data and in terms of what important physical processes that underly them. Also, some assumptions are discussed that could not a priori be considered correct.

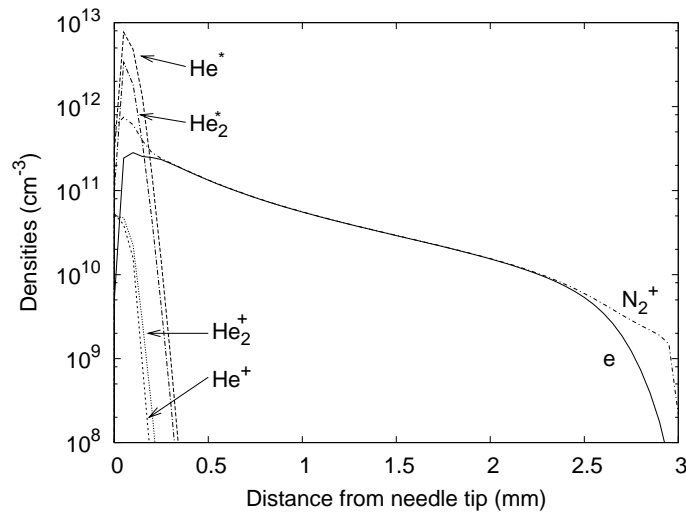


Figure 7.5: The axial, time-averaged densities of the various species as a function of the distance to the needle tip. Most species existed only close to the needle and got rapidly converted in N_2^+ ions and electrons. These then diffused outward and recombined further away from the needle.

7.4.1 Comparison to experiments

In section 7.3, simulations for the standard condition ($V = 320$ V and $d = 3$ mm) predicted that the electron density is typically of the order of 10^{11} cm^{-3} . The size of the plasma is typically 1 mm. N_2^+ was the dominant ion, even for small admixtures of nitrogen. The power dissipated in the discharge ranged from 10 – 100 mW and was strongly dependent on both the applied rf voltage and the distance of the needle to the plane.

These results do agree with the experimental data that were available at the time of writing this chapter: from the experiments [10] we know that the amplitude of the voltage applied to the needle typically ranges from 200 V to 350 V for a small, stable plasma; the (visually determined) size of the discharge is ~ 1 mm, the electron density is estimated to be $\sim 10^{11}$ cm^{-3} and the dissipated power is in the order of 100 mW.

The most directly measured quantity was the dissipated power [10] and therefore especially this quantity is a suitable parameter to compare the model with the experiments. Given the figures mentioned in [10, 18], the results shown in figure 7.8 suggest that the calculated power dissipation at the above-mentioned voltage is at most a factor of 10 too low. However, it is not exactly known how much power is dissipated in the matching network and how this depends on the distance from the needle to the plane. Due to this uncertainty, the measured power reported in [10] can be considered to be the upper limit of the power that is actually dissipated in the plasma itself. In reference [18] powers are reported in the range of 0 – 50 mW, however, here the applied voltage to the needle is not given, which makes the figures reported in this chapter unsuitable for direct comparison. In addition to the experimental uncertainties, a further reason for this discrepancy could

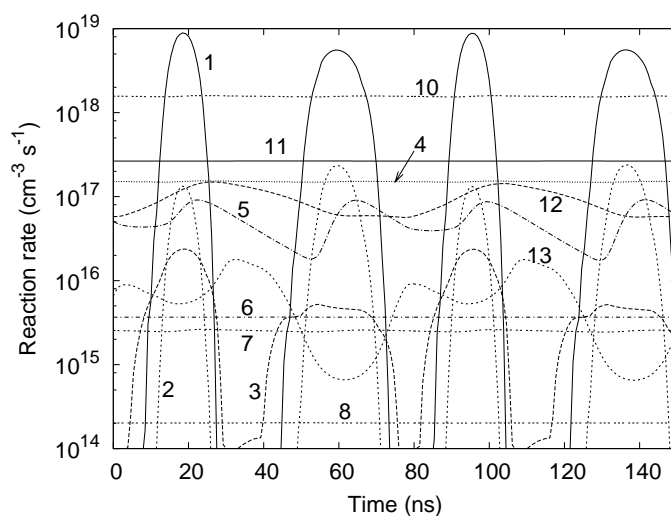


Figure 7.6: The time-dependent reaction rates at a distance of 0.2 mm from the needle tip. The numbers near the curves correspond with the numbers in table 7.2. Refer to figure 7.3 for the phase of the applied voltage as a function of time.

be that in the model the electric field at the tip of the needle is underestimated due to a limited sharpness of the needle as a result of the coarseness of the numerical grid. A higher field results in a higher ionisation rate and leads to higher electron densities and more power dissipation.

Therefore, although the measured and calculated values of the dissipated power differ, there are both experimental and computational factors which make agreement or disagreement uncertain. Further research will have to be done in order to make better conclusions on this subject.

7.4.2 Reaction kinetics

Various assumptions were made in constructing the set of reactions between the various species described by the model. The validity of several of these assumptions was treated in section 7.2. Here we discuss the others.

In the first place, we assumed that the various excimer levels of the helium molecular system decay into the $a^3\Sigma_u^+$ state over time scales that are faster than the rf period. In figure 7.6, the reaction rates are shown as a function of time in the rf cycle. Reaction number 4 is the reaction that treats the compound of reactions that eventually result in the $a^3\Sigma_u^+$ state. One can see in the figure that this reaction rate is not significantly modulated during the rf cycle. This indicates that the typical time scales involved here are longer than the rf time scale and that it is therefore reasonable to treat only this one excimer state.

Furthermore, note that in the experimental setup the gas is not uniform in its impurities: the helium flow along the needle ensures that the gas close to the needle is almost as pure as

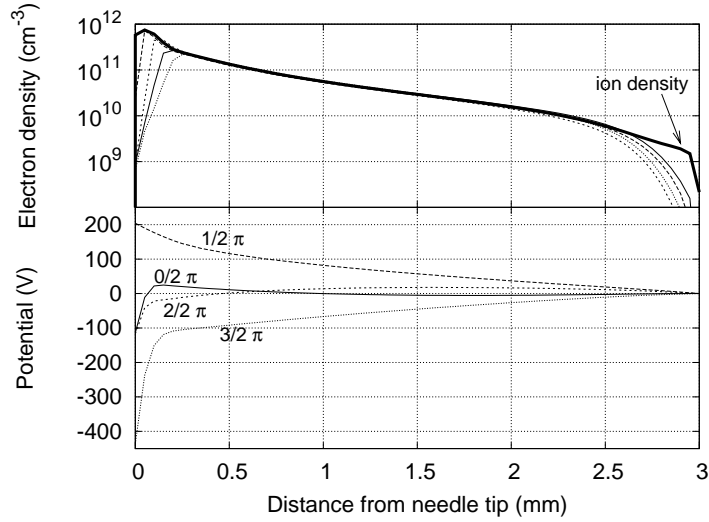


Figure 7.7: The axial electron density and the potential at four different phases during the rf cycle. The bold continuous line in the top part of the graph shows the time-averaged ion density.

that contained in the source cylinder. Further away from the needle, the purity is decreased due to inward diffusion of air and perhaps molecules from a nearby surface. Since the active plasma is confined to a region close to the needle, this disuniformity further away from the needle will not effect the results significantly.

From the results presented in section 7.3 it has become clear that only a small region close to the needle exhibits active production of species. Only N_2^+ ions and electrons can diffuse away from this region due to their relatively low recombination rates. One can consider the region close to the needle as a point source from which these species diffuse away radially with an ambipolar diffusion constant D_{amb} and are destroyed with a rate $S = kn_en_i$. After equating n_e to n_i and assuming the rate k of reaction 12 to be constant, the particle densities outside of the productions region can be described by the balance equation of n_e in spherical coordinates, for $r > 0$:

$$\nabla^2 D_{\text{amb}} n_e(r) = \frac{D_{\text{amb}}}{r^2} \frac{d}{dr} r^2 \frac{d}{dr} n_e(r) = kn_e^2 \quad (7.3)$$

Solving this equation yields:

$$n_e(r) = c \frac{2D_{\text{amb}}}{kr^2} \quad (7.4)$$

where c is a constant that depends on the density of the electron-ion pairs at the border of the production region. The decrease in density as a function of r as predicted by this equation is slower than observed in, for example, figure 7.5. One reason for this could be that both D and k are taken to be constants, while, in fact, they are dependent on the electron temperature. Depending on the distribution and nature of pollutants, N_2 and the electrons might react to form negative ions and radicals further away from the needle tip.

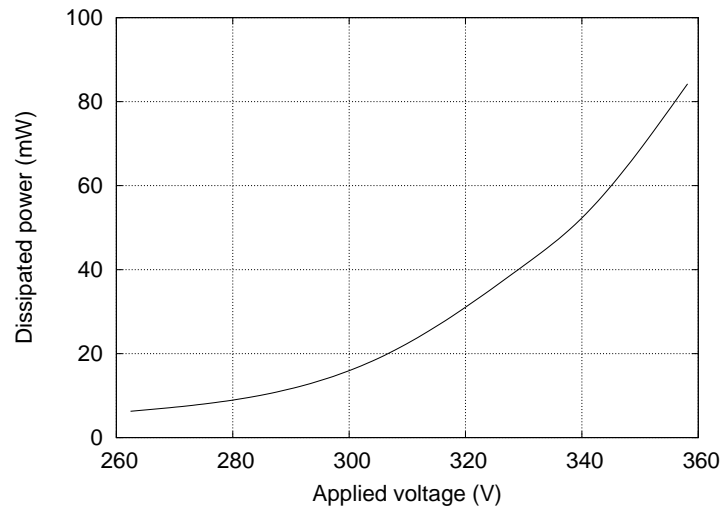


Figure 7.8: The dissipated power as a function of the applied voltage for a distance of 3.0 mm between needle and plane.

These results suggest that in a future theoretical description of the needle, a distinction can be made between the production region close to the needle and a recombination region further away from the needle. A more advanced description could exploit this by modelling the former region in more detail with a denser grid and add the latter region by adding more impurities and corresponding reactions and take the complex interaction with biological materials into account. The coupling of the two regions can be described by the outward flux of N_2^+ and electrons.

7.4.3 Effect of current restriction

A few simulations were run in which no capacitor was assumed to be in series with the needle and, therefore, a net current could run. If a capacitor is connected in series with the needle (as is the case in most matching networks), such a net current charges the capacitor and offsets the average potential of the needle. When the bias voltage is not present, the average electric field is distinctly different from the biased situation and has its effect on the discharge. Although there is no experimental data on the behaviour of the discharge in this situation, we included some numerical results that might point the way to future experiments.

If one compares figure 7.10 for the unbiased case with figure 7.7 for the biased case, one can see that the main effect of this different electric field is the confinement of electrons to a region close to the needle. Outside this region the current is carried by ions alone. A matching network based on an inductive element instead of a capacitor could accomplish this situation, perhaps offering a way to control the nature of the species arriving at a substrate.

Note that a similar situation also temporarily arises for a needle driven by a regular

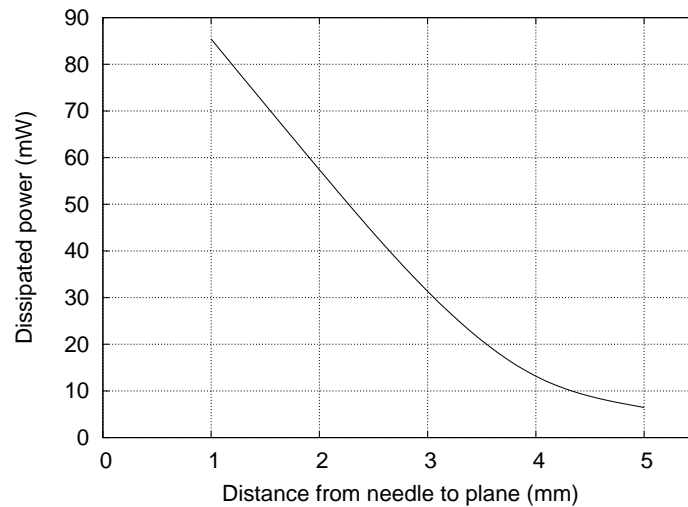


Figure 7.9: The dissipated power as a function of the distance between needle and plane for an applied voltage of 320 V.

matching network when the steady-state bias voltage of the device is suddenly altered. This can, for example, happen when one of the experimental setting is suddenly changed, or when the electrical potential of the environment alters. The time it then takes for a new steady-state to set depends on the net current and the capacitance of the matching network and was estimated to be in the order of 1 ms.

7.5 Conclusions

In this chapter we presented a first numerical description of the plasma needle. We used a two-dimensional, time-dependent fluid model and included a set of species and reactions that was designed earlier for a dielectric barrier discharge with similar conditions. This set is on the one hand detailed enough to give a realistic model of the needle and on the other hand terse enough to be able to give insight in what the important processes are. With this model, the electrical properties of the needle and the spatiotemporal evolution of quantities such as particle densities could be predicted. These insights can help in explaining observations in present experiments and in giving direction to future experiments. More experimental data will be necessary to improve and further validate the model.

This study has shown that the electron density in the plasma is typically of the order of 10^{11} cm^{-3} . The size of the plasma, measured by the distance over which the electron density dropped by one order of magnitude, is typically 1 mm. Even at small admixtures of nitrogen, N_2^+ was found to be the dominant ion. The power dissipated in the discharge ranged from 10 – 100 mW and was strongly dependent on both the applied rf voltage and the distance of the needle to the plane. For higher powers the plasma covered more surface of the needle. These findings are consistent with the few experimental data available.

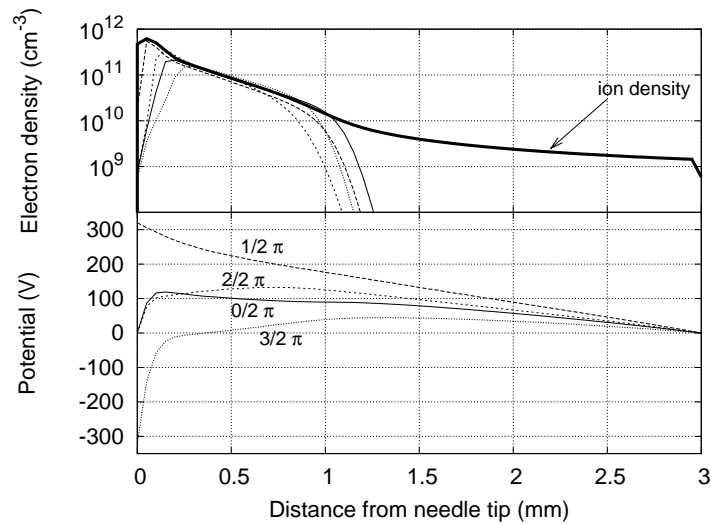


Figure 7.10: The axial electron density and the potential at four different phases during the rf cycle for the situation in which the current is not restricted by a bias voltage across a capacitor. The bold continuous line in the top part of the graph shows the time-averaged ion density. Compare with figure 7.7 for the biased situation.

The simulations showed that the reaction kinetics are most important in the sheath and that the end products of the reactions were N_2^+ ions and electrons, which diffused from this region and recombined at some distance from the needle. Future models could exploit this fact by distinguishing between the production region and the recombination region. The former could be described by a finer numerical grid and use effluxes as boundary conditions for the balance equations. The latter could be refined by including more impurities and reaction, which originate from the inward diffusion of air and of species from the treated surface.

Finally, the design of the matching network could be used for controlling the charged species densities that diffuse away from the needle: if a dc current is allowed to flow, the electrons are confined to a region close to the needle and only positive ions carry the current towards a surface.

Acknowledgments

We would like to acknowledge Philips Research for funding this investigation. Furthermore, we would like to thank Ingrid Kieft for the many useful discussions.

References

- [1] E. Stoffels, A. J. Flikweert, W. W. Stoffels, and G. M. W. Kroesen. Plasma needle: a non-destructive atmospheric plasma source for fine surface treatment of (bio)materials. *Plasma*

- Sources Sci. Technol.*, 11:383–388, 2002.
- [2] Jan van Dijk, Yasuhiro Horiuchi, and Toshiaki Makabe. Argon micro-cell plasma with applications in biomedical technology. *Bulletin of the American Physical Society*, 48(6):17, 2003.
- [3] I. E. Kieft, J. L. V. Broers, V. Caubet-Hilloutou, D. W. Slaaf, F. C. Ramaekers, and E. Stoffels. Electric discharge plasmas influence attachment of cultured CHO K1 cells. *Bioelectromagnetics*, 25(5):362–368, 2004.
- [4] E. A. Sosnin, E. Stoffels, M. V. Erofeev, I. E. Kieft, and S. E. Kunts. The effects of UV irradiation and gas plasma treatment on living mammalian cells and bacteria: a comparative approach. *IEEE Trans. on Plasma Science*, 32(4):1544–1550, 2004.
- [5] Jaeyoung Park, I. Hennins, H. W. Herrmann, and G. S. Selwyn. Discharge phenomena of an atmospheric pressure radio-frequency capacitive plasma source. *JAP*, 89(1):20–28, 2001.
- [6] Yu. B. Golubovskii, V. A. Maiorov, J. Behnke, and J. F. Behnke. Modelling of the homogeneous barrier discharge in helium at atmospheric pressure. *J. Phys. D: Appl. Phys.*, 36:39–49, 2003.
- [7] L. Mangolini, C. Anderson, J. Heberlein, and U. Kortshagen. Effects of current limitation through the dielectric in atmospheric pressure glows in helium. *J. Phys. D: Appl. Phys.*, 37:1021–1030, 2004.
- [8] G. J. M. Hagelaar, M. H. Klein, R. J. M. M. Sniijkers, and G. M. W. Kroesen. Energy loss mechanisms in the microdischarges in plasma display panels. *J. Appl. Phys.*, 89(4):2033–2039, 2001.
- [9] W. J. M. Brok, J. van Dijk, M. D. Bowden, J. J. A. M. van der Mullen, and G. M. W. Kroesen. A model study of propagation of the first ionisation wave during breakdown in a straight tube containing argon. *J. Phys. D: Appl. Phys.*, 36(16):1967–1979, 2003.
- [10] I. E. Kieft, E. P. van der Laan, and E. Stoffels. Electrical and optical characterization of the plasma needle. *New Journal of Physics*, 6:149, 2004.
- [11] BOLSIG, Boltzmann solver for the siglo-series 1.0. CPA Toulouse & Kinema Software, 1996.
- [12] I. E. Kieft, J. J. B. N. van Berkel, E. R. Kieft, and E. Stoffels. Radicals of plasma needle detected with fluorescent probe. *Plasma Processes and Polymers*, Special issue after the 16th ISPC, Taormina:295–308, 2005.
- [13] E. W. McDaniel. *Collision Phenomena in Ionized Gases*. Wiley, New York, 1964.
- [14] I. S. Grigoriev and E. Z. Meilikhov, editors. *Handbook of Physical Quantities*. CRC, Boca Raton, Fl., 1997.
- [15] H. W. Ellis, R. Y. Pai, E. W. McDaniel, E. A. Mason, and L. A. Viehland. Transport properties of gaseous ions over a wide energy range. *Atomic Data and Nuclear Data Tables*, 17(3):177, 1976.
- [16] R. K. Janev, W. D. Langer, D. E. Post Jr., and K. Evans Jr. *Elementary Processes in Hydrogen-Helium Plasmas*. Springer, Berlin, 1985.
- [17] Yu. P. Raizer, M. N. Shneider, and N. A. Yatsenko. *Radio-Frequency Capacitive Discharges*. CRC, Boca Raton, Fl., 1995.

- [18] E. Stoffels, R. E. J. Sladek, I. E. Kieft, H. Kersten, and R. Wiese. Power outflux from the plasma: an important parameter in surface processing. *Plasma Phys. Control. Fusion*, 46:B167–B177, 2004.

8

Concluding remarks

Nature shows unparalleled wisdom in its organization.

Yu. P. Raizer, *Gas Discharge Physics*, 1991.

8.1 Introduction

The work described in this thesis has a twofold nature: on the one hand, computer code was developed to treat non-local electron behaviour in discharges using the Monte Carlo method. This code was coupled to an existing fluid model in order to improve its descriptive power. On the other hand, several discharge devices were studied: a setup to study breakdown at low pressures, a fluorescent lamp and the plasma needle.

In the following we will conclude this thesis by giving a short overview of the topics treated throughout the various chapters. Please refer to the actual chapters for more detailed conclusions.

8.2 General remarks concerning the code

A Monte Carlo (MC) code has been developed to model electrons in a discharge. The design of this code allows stand-alone usage, as well as a coupling to other models. The latter has been demonstrated by coupling the MC code to the fluid code md2d. This code originated from the work of Gerjan Hagelaar [1] and has been rewritten in C++ in order to allow code components to be shared with the Plasimo project [2, 3, 4]. The combination of this fluid code with the MC code resulted in a two-dimensional and time-dependent model, capable of describing transient discharge evolution such as breakdown.

Fitting within the philosophy of the Plasimo project, the MC code is designed to be highly run-time configurable by means of its input-files and thereby incorporates few assumptions concerning the types of species and reactions that can be treated by it. Due to the modular design (which is facilitated by the C++ language), it allows for local improvements and user-defined plug-ins without affecting the integrity of the code as a whole.

Although the present code has been demonstrated to work, its development has not reached an end. Future improvements could consist of optimisation for speed and re-implementation for parallel processing. Future applications that lie within reach of the present implementation may include a coupling to the Plasimo modelling framework and a Particle-In-Cell model.

The present implementation of the hybrid fluid-MC model is applied to a setup for low pressure breakdown studies. Non-local electron behaviour that was observed in the experiments is reproduced by this code. In order to apply the hybrid model to the breakdown in fluorescent lamps, the large thermal emission electron flux emanating from the electrodes will need to be dealt with. In the present implementation the relatively cold electrons in front of the cathode use a significant amount of computer time and poor statistics result in the discharge front.

8.3 Breakdown

In the various discharges that are discussed in this thesis, breakdown plays an important role. More specifically, breakdown is studied at voltages that lie only just above the min-

imum voltage necessary for breakdown to occur. As such, Meek's criterion is not met and streamers are not formed. It was found that even for systems of which steady-state operation is well understood, the spatio-temporal process that transforms an insulating gas into a conducting discharge is a subject that has not been studied extensively. The first reason is that many applications rely on steady-state discharges that are ignited by a voltage pulse of ample magnitude. The precise way in which this happens is often not important. The second reason is that breakdown is a highly transient process and often very localised in space. Only recently the experimental and numerical technologies have become advanced enough to probe these small temporal and spatial scales.

One of the difficulties in forming a generalised description of breakdown resides in the fact that in the early stages of the discharge development many factors play a role that are of minor importance during steady-state discharge operation. Specifically these are the influence of the environment on the electric field configuration, and sources of charged particles that have either been produced externally or are preserved from a previous discharge pulse. Both aspects have been encountered in the discharges studied in this thesis.

8.3.1 Parabolic electrodes

In chapter 4, a pre-breakdown light flash is described that was observed in iCCD camera images of breakdown in a system consisting of two cylindrically symmetric electrodes with parabolic cross sections. Their tips are separated by 3.3 mm and the discharge is operated in 3.5 Torr argon.

The pre-breakdown light flash is caused by ions and electrons that remained after a previous discharge pulse. Although this background ionisation will perhaps not alter the steady-state breakdown criterion as formulated by Townsend, it can influence the temporal development of breakdown and is therefore likely to be important in the case of pulsed discharges.

It was shown that the electron behaviour is non-local during the pre-breakdown phase, which is in some conditions suggested by a stratified appearance of the light generated during this phase. This phenomenon is reproduced by the hybrid model.

8.3.2 Discharge tubes

In the chapters 5 and 6, breakdown is studied in a long discharge tube resembling the tubes used in fluorescent lighting. The tube is 14 cm long and 1 cm in diameter, contains 3 Torr of argon and (in chapter 6) a saturated mercury vapour. The discharge tube is enclosed in a metal tube to provide a well-defined electrical environment. The electrodes are heated to thermal emission temperatures.

Experiments have revealed that, on the time scale of $10\ \mu\text{s}$, ionisation waves travel from the cathode to the anode and back. It was found that the first ionisation wave is dominated by the electric field that exists between the cathode and the fixture in which the lamp is placed. During the breakdown process the discharge shields itself from this external

influence by depositing charge on the tube wall and thereby establishing an electric field that allows a current to run between the electrodes inside the lamp.

A continuous current starts to run once the first ionisation wave has crossed the lamp. After this has happened, this current keeps increasing until it is limited by the power-supply, which typically takes place several $10\ \mu\text{s}$ after the completion of the first wave. The condition that the first ionisation wave must have bridged the gap between the electrodes is also valid for ac operation.

During ac operation at a frequency in the order of 100 kHz, the time scale at which the waves travel through the tube is in the same order of magnitude as the time scale of the applied voltage. It was found that during the positive part of the voltage cycle, the electron density in the previously traversed part of the tube increases. This facilitates a restart of the first ionisation wave during the next half cycle, at the position where it stopped when the voltage reversed. This effect is more efficient at high frequencies due to the immobility of ions at small time scales. At low frequencies the ions can move towards the wall and discharge the negative charge from the wall. This lowers the field during the positive part of the cycle and thereby makes it less effective for increasing the electron and ion density.

Finally, the addition of a small amount of mercury to the argon background gas was found to have a large effect on the breakdown potential of the lamp. The reason for this is that Penning ionisation of mercury by metastable argon atoms forms an extra electron source that is active behind the high field region of the ionisation front itself. This results in a larger conductivity of the path between the electrode and the ionisation front, which allows the current that is necessary to charge the inner wall of the tube to be maintained at a smaller applied voltage.

8.4 The plasma needle

A final, odd discharge that is studied in this thesis is the plasma needle. This device is developed for future medical applications, in which the reactive species produced by the discharge interact with biological tissue. The device consists of a needle, powered by a radio-frequency source. Along the needle a flow of helium defines the operating gas. A plasma of typically $1\ \text{mm}^3$ is formed at the tip of the needle, dissipating 10 – 100 mW of energy.

One observation resulting from this study is that the discharge region in which the reactive species are produced does not coincide with the downstream region where the reactive energy is deposited. This fact can be exploited in more advanced future models by specialising the description of the particle kinetics for each region. A similar separation in the production and the reaction region was found in the so called pulsed nozzle discharge (PDN) [5]. No details have been included in this thesis about this source.

A second observation is that a small fraction of impurities in the main gas can have a profound influence on the discharge behaviour. In the case of the plasma needle this is N_2 in a He background: N_2^+ becomes the dominant ion. A similar observation is made in chapter 6, as described above. :wq

References

- [1] G. J. M. Hagelaar. *Modeling of Microdischarges for Display Technology*. PhD thesis, Eindhoven University of Technology, The Netherlands, 2000.
- [2] J. van Dijk. *Modelling of Plasma Light Sources: an object-oriented approach*. PhD thesis, Eindhoven University of Technology, The Netherlands, 2001.
- [3] B. Hartgers. *Modelling of a Fluorescent Lamp Plasma*. PhD thesis, Eindhoven University of Technology, The Netherlands, 2003.
- [4] H. W. P. van der Heijden. *Modelling of Radiative Transfer in Light Sources*. PhD thesis, Eindhoven University of Technology, The Netherlands, 2003.
- [5] B. H. P. Broks, W. J. M. Brok, J. Remy, J. J. A. M. van der Mullen, A. Benidar, L. Biennier, and F. Salama. Numerical investigation of the discharge characteristics of the pulsed discharge nozzle. *Phys. Rev. E*, 71:036409, 2005.

Summary

Gas discharges are commonly used in modern society. The most clearly visible are those found in fluorescent lamps and in plasma televisions. Less noticeable are the discharges used in the fabrication of e.g. computer chips and solar cells, in cleaning of gases and liquids, the improvement of the surface quality of materials and in satellite propulsion. In nature they are found in the forms of lightning and the polar light. In outer space the vast majority of all visible matter is in a state that resembles a discharge: a mixture of atoms and molecules, permeated with electrically charged particles.

A gas discharge is created by applying an electric potential across a neutral gas. If the resulting electric field is large enough, the force that this field exerts on charged particles will accelerate them. With the kinetic energy gained, they can separate charges from neutral atoms. This process is called ionisation and is mainly effectuated by the light electrons that collide with heavy neutral atoms. In comparison to the other charge carriers — the ions — electrons can indeed displace themselves easier through the gas and can thereby gain energy in the electric field more readily. Apart from ionisation, this energy is also used to excite atoms and molecules to higher energy states. These excited states can often lose their energy by radiating light, which gives gas discharges their typical appearance.

Contrary to a neutral gas, a gas discharge contains a myriad of different particle species: electrons, ions, atoms and molecules, in various excited states. As mentioned earlier, the first two of these are electrically charged and thus interact with each other and with external fields. The motion of all these particles, their interaction with electric fields and the exchange of energy between them, all conspire to make a discharge a complex system that is worthy of scientific study. The technological relevance of studying the fundamental principles underlying gas discharges originates from the multitude of possible applications. Without an understanding of these principles, it is difficult to improve and expand their application range.

Traditionally, this understanding is obtained by combining experimental observation with the development of a theory. However, the latter is often only possible for relatively simple discharges. With the advance of modern computer techniques, it is possible to gain an insight in more complex discharges by modelling them by computer programs. Whereas in experiments only a limited number of quantities can be measured, in numerical models it is possible to know the values of all quantities. Since assumptions underly numerical models, it is necessary to compare experimental observations with simulation

results in order to gain confidence in the correctness of the model. The combination of experiments and numerical models forms an excellent way to understand the physics of gas discharges. Although in this thesis the emphasis lies on the numerical description of discharges, comparisons are made with experimental observations where possible.

In the first part of this thesis, the theory and implementation of a so called Monte Carlo (MC) model is described. Contrary to fluid models, in which particle species are described as a continuum, in MC models the paths of individual particles are calculated. Collisions between the individual particles are simulated by means of statistical methods. The behaviour of a large number of these test particles is taken to be representative for all particles in the discharge. The number of test particles that can be simulated is typically limited by the available computer power. An MC model is especially suitable for the description of the electrons. Since electrons are often the main agents for coupling energy into the discharge, the correct description of the electrons is essential for the success of the model. A strong emphasis has been put on the flexibility of the code and its usability in combination with fluid models. As such, the MC code can be applied to a large number of gas discharges.

An existing two-dimensional and time-dependent fluid model has been expanded with this MC description for the electrons. The application range of the model, which is now a hybrid, has thereby been expanded to discharges in which the electrons are ill-described by fluid equations. Since MC models are computationally expensive, choices were made in order to describe only those electrons for which the MC method forms an improvement. In the present model, species densities and the electric field are communicated to the MC model and species sources are returned to the fluid model as a result of the MC calculations. By performing this communication repeatedly, the description of the discharge is time dependent.

This hybrid model has been used to study a gas discharge that is used for fundamental research of the ignition behaviour of gas discharges. During experiments a light flash was observed next to the positive electrode (the anode) before the applied voltage was high enough to cause the discharge to ignite. This light is described by the hybrid model, which also predicts the stratified structure of this light. It has been shown that the electrons and the ions that remained in the discharge after a previous discharge pulse play an important role in this phenomenon. The further development of the discharge, as described by the model, corresponds with the experimental observations.

The compact fluorescent lamp is the second discharge that was studied in this thesis. Again the research was aimed at understanding ignition. Although a simplified version of the commercial lamp was investigated, the important processes during the ignition process have been identified. In experiments ionisation waves were observed to travel to the anode and back. The first ionisation wave (from cathode to anode) displaces itself by charging the inner wall of the tube negatively. This charge influences the electric field in such a way that it results in a displacement of the ionisation wave towards the anode. An important conclusion that could be drawn from this study is that, if the first ionisation wave does reach the anode, the lamp will ignite in a later stage.

One of the simplifications made to the lamp is the nature of the discharge gas: in

commercial lamps the mixture consists of argon and mercury. Initially a lamp containing pure argon was studied, with the above-mentioned conclusions as a result. By also including mercury in the description of the lamp it turned out that the description of the second ionisation wave (from anode to cathode) corresponded better with the experiments than it was the case for pure argon. This allowed a second simplification, namely direct current operation of the lamp, to be replaced by the more realistic alternating current operation. From this study it could be concluded that for ac operation the successful completion of the first ionisation wave is also a requirement for the lamp to start at a later instant in time.

Finally, the numerical description of another discharge has been treated: the plasma needle. This discharge is created at the tip of a needle, at atmospheric pressure, by a radio-frequency electric field. At present this discharge is heavily studied because of its applicability in the medical field, for instance for tissue disinfection. It was shown that reactive species are predominantly created close to the tip of the needle and deposit their energy further away from the needle. Furthermore, it is shown that a small fraction of nitrogen in the helium background gas in which the discharge is operated has a large influence on the reaction kinetics. Nitrogen ions are present in larger numbers than helium ions, although helium atoms are more abundant.

In this thesis the development of a numerical model to describe the electrons in a gas discharge and the study of three different gas discharges is reported. The emphasis lies on the ignition of discharges. An insight is gained in the various mechanisms important in this process. The implementation of the numerical models forms a sound basis for further development and application in the future.

Samenvatting

Gasontladingen worden veelvuldig toegepast in de moderne maatschappij. Het meest opvallend vindt men ze terug in lichtbronnen, zoals bijvoorbeeld tl-buizen en in plasmatelevisies. Meer onttrokken aan het oog worden ze gebruikt in het fabriceren van onder meer computerchips en zonnecellen, het reinigen van gassen en vloeistoffen, het verbeteren van de eigenschappen van materiaaloppervlakken en het voortstuwen van satellieten. In de natuur worden ze teruggevonden in de vorm van bliksem en het noorderlicht. In de ruimte is zelfs het grootste deel van de zichtbare materie in een toestand die te vergelijken is met de toestand waarin een gasontlading zich bevindt: een mengsel van vrije atomen en moleculen, doorspekt met elektrisch geladen deeltjes.

Een gasontlading wordt gecreëerd door een elektrische spanning aan te brengen over een neutraal gas. Indien het resulterende elektrische veld van voldoende grootte is, zal de kracht die dit veld uitoefent op de ladingsdragers ertoe leiden dat deze versneld worden en met de opgenomen bewegingsenergie in staat zijn nieuwe ladingen los te maken uit neutrale atomen. Dit proces wordt ionisatie genoemd en wordt voornamelijk bewerkstelligd door de lichte elektronen die botsen tegen de zwaardere neutrale atomen. Elektronen kunnen zich immers makkelijker verplaatsen door het gas dan andere ladingsdragers — de ionen — en zo sneller energie opnemen uit het elektrische veld. Behalve voor ionisatie wordt deze energie ook aangewend tot het aanslaan van atomen en moleculen tot hogere energietoestanden. Deze aangeslagen toestanden kunnen veelal hun energie weer verliezen door uitzending van licht, hetgeen gasontladingen hun kenmerkende uiterlijk geeft.

In tegenstelling tot een neutraal gas bestaat een gasontlading dus uit een grote verscheidenheid aan deeltjes: elektronen, ionen, neutrale atomen en moleculen, al dan niet in aangeslagen toestand. Zoals opgemerkt zijn deze eerste twee soorten elektrisch geladen en gaan aldus een wisselwerking aan met elkaar en met externe elektrische velden. De beweging van al deze deeltjes, hun wisselwerking met het elektrische veld en de uitwisseling van energie tussen deeltjes onderling leiden tot een complexiteit die het verkrijgen van begrip tot een wetenschappelijke uitdaging verheft. Door de vele toepassingen is het ook van groot technologisch belang dat de werking van een gasontlading voldoende begrepen wordt. Zonder dit begrip tast men in het duister wat betreft het verbeteren en uitbreiden van de toepassingsmogelijkheden.

Traditioneel wordt begrip verkregen uit de wisselwerking tussen experimenten en theorievorming. Vooral dit laatste is vaak slechts mogelijk voor eenvoudige gasontladingen. Met

moderne computers en numerieke technieken wordt steeds meer de mogelijkheid geboden om inzicht in gasontladingen te verkrijgen door deze door middel van simulatieprogramma's na te bootsen. Terwijl in experimenten slechts een beperkt aantal grootheden bepaald kan worden, is het in computersimulaties mogelijk alle grootheden te kennen. Aangezien aan numerieke modellen aannames ten grondslag liggen, is het vergelijken van simulatieresultaten met experimentele waarnemingen nodig teneinde vertrouwen te winnen in de correctheid van het model. De combinatie van experimenten en numerieke modellen vormt zodoende een uitstekend middel voor het doorgronden van de fysica van gasontladingen. Hoewel in dit proefschrift de nadruk ligt op de numerieke beschrijving van gasontladingen, zijn waar mogelijk dan ook vergelijkingen gemaakt met experimentele waarnemingen.

In het eerste deel van dit proefschrift wordt de theorie achter en de verwezenlijking van een zogeheten Monte Carlo (MC) model beschreven. In tegenstelling tot een zogenaamd vloeistofmodel, waarin deeltjessoorten als een continuüm beschreven zijn, worden in een MC model de banen van afzonderlijke deeltjes door de gasontlading uitgerekend. Via statistische methoden worden botsingen met andere deeltjes nagebootst. Het gedrag van een groot, doch door computercapaciteit beperkt aantal van deze testdeeltjes is maatgevend voor het gedrag van de deeltjes in een echte ontlading. Een MC model is vooral geschikt voor de gedetailleerde beschrijving van het gedrag van elektronen. Aangezien elektronen veelal verantwoordelijk zijn voor de inkoppeling van energie en de uitwisseling van deze energie met de zwaardere deeltjes, is de correcte beschrijving van elektronen bepalend voor het succes van het model. In de ontwikkeling van het MC model is bovendien veel nadruk gelegd op flexibiliteit van de code en de bruikbaarheid van deze in combinatie met vloeistofmodellen. Als zodanig is het MC model inzetbaar voor een grote variëteit aan gasontladingen.

Een bestaand, tijdsafhankelijk en tweedimensionaal vloeistofmodel is uitgebreid met deze MC beschrijving van de elektronen. Hiermee is de toepasbaarheid van dit, nu hybride model uitgebreid naar ontladingen waarin de elektronen zich slecht laten beschrijven door vloeistofvergelijkingen. Aangezien MC methoden duur zijn wat betreft benodigde reken-tijd, zijn bij de koppeling van deze twee modellen keuzes gemaakt om voornamelijk die elektronen te beschrijven waarvoor de MC methode een verbetering biedt. In het huidige model worden deeltjesdichtheden en het elektrische veld vanuit het vloeistofmodel naar het MC model gecommuniceerd en worden deeltjesbronnen als resultaat van de MC berekeningen aan het vloeistofmodel teruggegeven. Door deze communicatie op gezette tijdstippen plaats te laten vinden is de beschrijving van de ontlading tijdsafhankelijk.

Dit hybride model is gebruikt om het starten van een gasontlading te bestuderen die gebruikt wordt voor fundamenteel onderzoek naar het ontsteekgedrag van ontladingen. In experimenten was geconstateerd dat zelfs bij een spanning die te laag is om de ontlading te starten al een lichtschijsel bij de positieve elektrode (de anode) kan worden waargenomen. Dit schijsel is beschreven met behulp van het hybride model en zelfs de gelaagde structuur ervan kon met behulp van dit model voorspeld worden. Hiermee is duidelijk geworden dat elektronen en ionen die achter zijn gebleven na een vorige ontlading een belangrijke rol spelen in dit verschijnsel. De verdere ontwikkeling van de ontlading zoals beschreven door het model strookt tevens met de experimentele waarnemingen.

Een tweede ontlading die bestudeerd is in dit proefschrift is de compacte fluorescencielamp, ook wel spaarlamp genoemd. Ook hier is het onderzoek gericht op het ontsteekgedrag. Hoewel een vereenvoudigde versie van de commerciële lamp is onderzocht, is het mogelijk gebleken de belangrijkste processen aan te wijzen die tijdens het ontsteken van de lamp een rol spelen. Zo zijn in experimenten zogeheten ionisatiegolven waargenomen die zich van de kathode naar de anode en terug verplaatsen. De eerste golf (van kathode naar anode) blijkt zich voort te sturen door het opladen van de binnenwand van de lamp met een negatieve lading. Deze lading beïnvloedt het elektrische veld op een dusdanige wijze dat dit de beweging van het ionisatiegebied in de richting van de anode tot gevolg heeft. Een belangrijke conclusie die verder getrokken kon worden is dat indien deze eerste golf in staat is de anode te bereiken, het ontsteken van de lamp op een later tijdstip succesvol zal zijn.

Eén van de vereenvoudigingen die aangebracht is in de lamp is de aard van het gas. In commerciële lampen is dit een mengsel van argon en kwik. Aanvankelijk is een lamp met puur argon bestudeerd, met de boven vernoemde conclusies als gevolg. Echter door ook kwik in de beschrijving van de lamp mee te nemen blijkt dat de numerieke uitkomsten ten aanzien van de tweede ionisatiegolf (van anode naar kathode) beter met experimenten overeenkomt dan dat voor puur argon het geval is. Hiermee kan een tweede vereenvoudiging, namelijk het bedrijven van de lamp op gelijkspanning, vervangen worden door het meer realistische wisselspanningsbedrijf. Uit deze studie is gebleken dat nog altijd het succesvol oversteken van de ionisatie golf van de actieve naar de gearde elektrode een vereiste is voor het daadwerkelijk ontsteken van de lamp op een later tijdstip.

Tot slot is de numerieke beschrijving van een ander plasma beschreven: de plasmanaald. Dit is een ontlading die opgewekt wordt aan de punt van een naald bij atmosferische druk door een radiofrequent elektrisch veld. Deze ontlading wordt momenteel veelvuldig onderzocht met het oog op de mogelijke toepasbaarheid in de medische wereld voor onder meer het zeer gelokaliseerd desinfecteren van weefsels. Uit deze studie is gebleken dat reactieve deeltjes vooral dicht bij de punt van de naald geproduceerd worden en verder van de naald aangewend kunnen worden voor het deponeren van reactie-energie. Voorts is gebleken dat een kleine fractie van stikstof in het helium gas, waarin de ontlading bedreven wordt, een grote invloed heeft op de reactiekinetiek en dat stikstof ionen in grotere getale aanwezig zijn dan de helium ionen, ondanks de overvloed van helium.

In dit proefschrift is verslag gedaan van zowel het ontwikkelen van een numeriek model voor de beschrijving van elektronen in een gasontlading als de bestudering van een drietal verschillende ontladingen. Hierbij ligt de nadruk op het ontsteken van gasontladingen en is inzicht verworven in de mechanismen die hierbij een rol spelen. De verwezenlijkte numerieke modellen vormen tevens een goede basis voor verdere toepassing en ontwikkeling in de toekomst.

Dankwoord

Dit proefschrift is het resultaat van vier jaar onderzoek onder de bezielende begeleiding van Joost van der Mullen. Ik wil hem dan ook graag bedanken voor de mix van vrijheid en sturing die hij me gedurende deze periode gegeven heeft, alsmede voor de vele uren die hij besteed heeft aan het grondig lezen van de verschillende versies van dit proefschrift.

Voorts wil ik Gerrit Kroesen en Gerrit Oversluizen bedanken voor het mogelijk maken van dit onderzoek, Marco Haverlag voor het instemmen met mijn eerste promotor te zijn en Annemie Bogaerts, Wim Goedheer, Marnix van der Wiel, Mark Kushner en Ute Ebert voor het plaatsnemen in mijn promotiecommissie en de aanwijzingen aangaande dit proefschrift.

I would like to thank Mark Kushner for welcoming me in his laboratory twice during the last four years, for boosting my understanding of discharges and the ways to describe them numerically. These visits have been inspiring and very fruitful for my research.

Ook Gerjan Hagelaar, mijn voorganger, was altijd bereid mijn vragen te beantwoorden en inzicht te verschaffen in de eigenaardigheden van computermodellen ten aanzien van de fysica. De keren dat we elkaar de laatste vier jaar ontmoet hebben waren immer inspirerend.

Graag wil ik mijn collega's bedanken voor de prettige werksfeer. In het bijzonder, Mark Bowden, Erik Wagenaars, Bart Broks, Ingrid Kieft, Danijela Šijačić en Eddie van Veldhuizen voor de vele discussies die het onderzoek interessant maakten en levendig hielden; Bart Hartgers en Kurt Garloff voor de hulp en de inzichten betreffende Linux; Jan van Dijk voor de vliegende start die hij me gegeven heeft wat betreft C++ en md2d. Ook ben ik Xiaoyan Zhu, Jérôme Remy, Misha Sorokin, Carole Maurice, Tanja Briels, Erik Kieft, Gabriela Paeva, Nienke de Vries, Maxime Gendre, Tao Jiang, Michiel van den Donker en Marc van der Velden erkentelijk. Ik wil Rina Boom, Loek Baede, Lambert Bisschops, Charlotte Groothuis, Evert Ridderhof en Huib Schouten bedanken voor alles wat zij veelal onopgemerkt bijdragen aan het onderzoek en de sfeer binnen de groep EPG.

Vervolgens wil ik de mogelijkheid aangrijpen om Tatiana and Victor te bedanken. En mijn beste vrienden, Jorn en Tanya, Dirk, Jasna en Roos, Chris en Farrah, Irina, Constanze, Alex en mijn zus Janne, bedankt voor jullie vriendschap.

Tot slot wil ik mijn ouders bedanken voor de belangstelling, voor de steun en voor de mogelijkheden die jullie mij geboden hebben. En natuurlijk mijn lieve Sveta, voor de aanmoedigingen, het begrip en de vele bijzondere momenten samen.

*Wouter Brok,
4 augustus 2005.*

Curriculum vitae

28 January 1977

Born in 's-Hertogenbosch, The Netherlands.

1989 – 1995

Maurick College, Vught, The Netherlands.

1995 – 2001

M.Sc. in Applied Physics at Eindhoven University of Technology.

Three month traineeship at the Institute of Neuroinformatics (ETH-UZ) in Zürich, Switzerland. Subject: *Neuromorphic Models for Binaural Localisation*, supervised by Dr. P.F.M.J. Verschure and Prof. R. Douglas.

Master thesis project at the High Intensity Discharge group of Philips Lighting in Eindhoven. Subject: *Model for the Electrical Behaviour of Metal Halide Lamps*, supervised by Dr. R.A.J. Keijser and Prof. G.M.W. Kroesen.

2001 – 2005

Ph.D. at the Elementary Processes in Gas Discharges group of the Department of Applied Physics at Eindhoven University of Technology. Subject: *Modelling of Transient Phenomena in Gas Discharges*, supervised by Dr. J.J.A.M. van der Mullen.

